Application of Wide Area Synchrophasor Measurements for Improved Real-Time Monitoring and Control of Power Systems

By

Dinesh Rangana Gurusinghe

A Thesis submitted to the Faculty of Graduate Studies of
The University of Manitoba
in partial fulfillment of the requirements of the degree of
DOCTOR OF PHILOSOPHY

Department of Electrical and Computer Engineering
Faculty of Engineering
University of Manitoba
Winnipeg, Manitoba

November 2016

Abstract

This thesis investigates novel ways to utilize the potential of wide area synchrophasors for improved real-time monitoring and control of power systems. The performance of phasor measurement units (PMUs) was examined at the outset, since the accuracy and consistency of synchrophasor applications heavily rely on the input measurements. Two performance class algorithms: P-class and M-class, published in the IEEE standard C37.118.1-2011 were implemented on a commercial PMU and a simple test setup was developed to evaluate it. Tests revealed some inadequacies of the M-class algorithm and remedies were suggested. Moreover, several minor inconsistencies in error limits imposed by the existing synchrophasor standard were found and reported.

Two new computationally efficient and stable algorithms for real-time estimation of transmission line parameters were developed. A third algorithm was developed to estimate parameters of series compensated lines. The proposed algorithms were validated through simulations carried out with a real-time digital simulator (RTDS^{TM}), experiments conducted using a laboratory scale test setup, and using a set of field measurements.

The second application is the prediction of transient stability status of a power system after a fault using synchrophasors. A novel algorithm, which utilizes the nature of rate of change of voltage vs. voltage deviation characteristics of the post-disturbance voltage magnitudes obtained from synchrophasors, was proposed. This algorithm is

computationally simple and fast compared to the rotor angle based methods, capable of predicting the multi-swing transient instabilities, and pinpoints the generators that become unstable first, which is very useful for emergency controls. Offline and RTDS simulations demonstrated over 99% overall success rate under both symmetrical and asymmetrical faults, and robust performance under changes in pre-disturbance loading and network topology.

Finally, a wide area response based emergency generator and load shedding scheme, which operates in conjunction with the prediction algorithm, was developed. A simple method to recognize the unstable cluster of generators using the synchronously measured voltages magnitudes is proposed and the unstable cluster is tripped if the system is predicted unstable. A frequency based load shedding scheme is applied to maintain the generation-load balance. The effectiveness of the approach was demonstrated using the RTDS based experimental test setup.

Acknowledgments

I would like to express my appreciation and thanks to my advisor Dr. Athula Rajapakse for his constant moral support, invaluable guidance, and continuous encouragement throughout the research work. It was a great privilege to work under his supervision.

I would also like to thank Dr. Krish Narendra and the technical staff at ERL Phase Power Technologies Ltd and Mr. Dean Ouellette and Mr. Rick Kuffel at RTDS Technologies Inc. for their support with providing resources, technical support, and valuable feedback. The support received from the technical staff at the Department of Electrical and Computer Engineering, especially from Mr. Erwin Dirks, is highly appreciated.

I wish to express my sincere gratitude to the Advisory Committee members for their many helpful comments and feedback to improve the quality of the thesis. The financial support received from University of Manitoba Graduate Fellowship (UMGF), Manitoba Graduate Scholarship (MGS), Mitacs-Accelerate Program, the Natural Sciences and Engineering Research Council, ERL Phase Power Technologies Ltd, and RTDS Technologies Inc. is gratefully acknowledged.

Thanks to the administrative staff of the University of Manitoba for their support in each step of this study, especially to Ms. Traci Gledhill and Ms. Amy Dario. Special

thanks to Christian Jegues, Sachintha Kariyawasam, and Kati Sidwall for the comments made to improve my writing. Also, I would like to thank all my colleagues in the Department of Electrical and Computer Engineering for their continuous encouragement and for making my years at the University of Manitoba one of the best experiences of my life.

Last but not least, I would like extend my extreme gratitude to my beloved parents for all their love and guidance throughout my life. Without them, I would not be the person who I am today. The biggest acknowledgement goes to my loving wife for her patience, understanding, and encouragements whenever I most needed them.

Dinesh Rangana Gurusinghe

November 2016

Dedication

To my beloved mother, father and my dear wife

Contents

Front Matter

Contents iv

List of Tables x

List of Figures xii

List of Symbols xvii

List of Abbreviations xix

List of Appendices xxii

1 Introduction **1**

1.1 Background 1

1.2 Synchrophasor Networks 2

1.2.1 Perception of Synchrophasor 4

1.2.2 Phasor Measurement Unit (PMU) 5

1.2.3 Phasor Data Concentrator (PDC) 6

1.2.4 Synchrophasor Communication Network 7

1.3 Synchrophasor Applications 7

1.3.1 Off-line Applications 8

1.3.2 Monitoring Applications 8

1.3.3 Protection and Control Applications 10

1.4 Transmission Line Parameters 11

1.5 Power System Stability 13

1.5.1 Power System Transient Stability 14

1.6 Power System Instability Control 15

1.7 Motivation and Objectives 17

1.8 Thesis Overview 20

2 Synchrophasor Measurement Technology 22

2.1 Introduction 22
2.2 Evolution of Synchrophasor Standards 22
2.3 Total Vector Error (TVE) 25
2.3.1 TVE, Magnitude Error and Phase Angle Error Relationship 26
2.4 Functional Model of a PMU 29
2.5 Phasor Estimation Methods 31
2.5.1 Discrete Fourier Transform (DFT) Method 31
2.5.2 Basic Least Squares (LS) Method 33
2.5.3 Iterative Least Squares Methods 34
2.6 Frequency Estimation and Measurement Reporting 36
2.6.1 Frequency Estimation 36
2.6.2 Measurement Reporting 37
2.7 Backend Performance Class Filters 38
2.7.1 Reference P-class Filter Model 38
2.7.2 Reference M-class Filter Model 41
2.8 PMU Testing 46
2.9 Improving PMU Performance 47
2.10 Concluding Remarks 48

3 Testing and Performance Enhancement of a Phasor Measurement Unit 49

3.1 Introduction 49
3.2 Proposed Improvements to M-Class Filter Model 50
3.2.1 Compensation Factor to the Reference M-Class Filter 50
3.2.2 Modified M-class Filter Model 52
3.3 PMU Test Setup 57
3.3.1 Sources of Errors in Testing 58
3.4 Test Results and Discussion 62
3.4.1 Signal Frequency Test 62

3.4.2 Measurement Bandwidth Test 64
3.4.3 Linear Frequency Ramp Test 66
3.4.4 Step Response Tests 69
3.5 Concluding Remarks 73

4 Efficient Algorithms for Real-Time Monitoring of Transmission Line Parameters 74

4.1 Introduction 74
4.2 Importance of Real-Time Line Parameters Monitoring 75
4.3 Real-Time Monitoring of Line Parameters 77
4.4 Problem of Line Parameter Estimation 79
4.5 Review of Transmission Line Parameter Estimation Algorithms 80
4.5.1 Method A [19] 80
4.5.2 Method B [20] 81
4.5.3 Method C [61] 82
4.5.4 Method D [63] 82
4.5.5 Method E [20] and Method F [65] 83
4.6 Proposed Transmission Line Parameters Estimation Algorithms 83
4.6.1 Algorithm for Estimating π −Equivalent Circuit Parameters (Algorithm 1) 84
4.6.2 Algorithm for Estimating Distributed Model Parameters (Algorithm 2) 86
4.6.3 Algorithm for Estimating Parameters of a Series Compensated Line (Algorithm 3) 88
4.6.4 Application to Other Configurations 92
4.7 Performance Validation – Simulations 93
4.7.1 Transmission Line Parameters under Ideal Conditions 95
4.7.2 Effect of Line Length under Ideal Conditions 96
4.7.3 Effect of the Degree of Compensation 96
4.7.4 Effect of the Location of Series Compensator 97

4.7.5 Effect of Unbalance 98
4.7.6 Parameter Estimation under Noisy Conditions 101
4.7.7 Data Window Length 103
4.7.8 Comparison of Computational Efficiency 104
4.8 Performance Validation – Experimental Setup 106
4.9 Line Parameter Estimation with Field Measurements 110
4.10 Sensitivity of Estimated Parameters to Measurement Errors 114
4.11 Concluding Remarks 117

5 Transient Stability Status Prediction in Power Systems 119
5.1 Introduction 119
5.2 Power System Transient Stability 120
5.3 Previous Approaches for Transient Stability Prediction 122
5.3.1 Time-Domain Simulations 122
5.3.2 Equal-Area Criterion and Its Extensions 124
5.3.3 Transient Energy Function Methods 127
5.3.4 Curve-Fitting Techniques 129
5.3.5 Swing Center Voltage Method 133
5.3.6 Machine Learning Techniques 137
5.4 Transient Stability Status Prediction using Voltage Magnitude Measurements 140
5.5 Transient Stability Status Prediction Using Post-disturbance Loci on ROCOV–ΔV Plane 143
5.6 Concluding Remarks 147

6 Prediction of Post-Disturbance Transient Stability Status of Multi-Machine Power Systems Using Synchrophasor Measurements 148
6.1 Introduction 148
6.2 Procedure for Implementing the Proposed Algorithm for a Multi-machine System 149
6.2.1 Identification of Marginally Critical Contingencies 150

6.2.2 Determination of Stability Boundary 150
6.2.3 Detection of Disturbances..... 152
6.3 Testing with TSAT Simulations..... 154
6.3.1 Base Case 155
6.3.2 Cases with Random Load/Generation Variations 156
6.4 Validation with an Experimental Setup based on Real-Time Simulations 159
6.4.1 Disturbance Detection 160
6.4.2 Performance under Symmetrical Faults..... 162
6.4.3 Performance under Asymmetrical Faults..... 171
6.4.4 Impact of the Topology Changes 172
6.5 Concluding Remarks 173

7 A Synchrophasor based Emergency Control Scheme for Mitigating Transient Instabilities 175
7.1 Introduction 175
7.2 Wide Area Transient Stability Control..... 176
7.3 Generator and Load Shedding Scheme 177
7.3.1 Recognition of Coherent Clusters of Generators 179
7.3.2 Frequency based Load Shedding..... 181
7.4 Experimental Setup for Validation..... 183
7.4.1 Example 1 : Fault on line 26-29 (25% of the length) 186
7.4.2 Example 2 : Fault on line 2-25 (50% of the length) 190
7.4.3 Example 3 : Fault on line 16-17 (95% of the length) 193
7.5 Real-World Implementation Issues 197
7.6 Concluding Remarks 198

8 Conclusions and Contributions 200
8.1 Conclusions 200
8.2 Contributions 206
8.3 Suggestions for future research 210

Appendix A 212
Appendix B 214
References 219

List of Tables

Table 2.1 PMU reporting rates [5] 38

Table 2.2 P-class filter parameters 39

Table 2.3 M-class filter parameters 42

Table 3.1 TVE and FE results of the P-class and M-class compliance 68

Table 3.2 Step change performances 72

Table 4.1 Theoretical transmission line parameters of the tie-line 95

Table 4.2 Transmission line parameters estimated by different algorithms 95

Table 4.3 Unbalanced loads connected to bus-5 and bus-6 98

Table 4.4 Parameters estimated under unbalanced conditions 100

Table 4.5 Estimated parameters under unbalanced, non-transposed conditions 100

Table 4.6 Computational complexities of different algorithms 104

Table 4.7 Computational time of different algorithms 105

Table 4.8 Parameters for the experimental transmission line setup 108

Table 4.9 Line parameters estimated under balanced condition 109

Table 4.10 Line parameters estimated under unbalanced condition 109

Table 4.11 Theoretically calculated transmission line parameters (25 ^{0}C) 110

Table 4.12 Line parameters estimated with field data 111

Table 6.1 Stability boundaries for each generator 155

Table 6.2 Prediction accuracy : Base case 156

Table 6.3 Prediction accuracy : Random cases 158

Table 6.4 Prediction accuracy for different types of faults 172

Table 6.5 Prediction accuracy under topology changes 173

Table 7.1 Load shedding locations 185

Table 7.2 Frequency settings and waiting times 186

Table 7.3 Distance matrix elements – Example 1 187

Table 7.4 Distance matrix elements – Example 2 190

Table 7.5 Distance matrix elements – Example 3 194

List of Figures

Figure 1.1 Typical architecture of a wide area synchrophasor network 3

Figure 1.2 Synchrophasor representation of a sinusoidal waveform 4

Figure 1.3 The π-equivalent model of a transmission line..... 12

Figure 1.4 Classification of power system stability [18] 14

Figure 1.5 Different options available for power system stability control [31]..... 16

Figure 2.1 Relationship between actual phasor, measured phasor and TVE..... 25

Figure 2.2 TVE as a function of magnitude and phase angle errors..... 27

Figure 2.3 TVE as a function of phase angle error for different magnitude errors 27

Figure 2.4 TVE as a function of magnitude error for different phase angle errors 28

Figure 2.5 Relationship between magnitude and phase angle errors for different TVEs . 28

Figure 2.6 The model of a typical commercial PMU with DFT based phasor extraction 29

Figure 2.7 P-class filter coefficient example 40

Figure 2.8 P-class filter response example in frequency domain 40

Figure 2.9 Frequency response mask specification for M-class filter [5]..... 41

Figure 2.10 M-class filter coefficient example 43

Figure 2.11 M-class filter magnitude response example in frequency domain 43

Figure 2.12 Revised frequency response mask specification for M-class filter [41]..... 44

Figure 2.13 M-class filter coefficient example for revised frequency response mask 45
Figure 2.14 M-class filter magnitude response example for revised frequency response mask 45
Figure 3.1 Comparison of magnitude error, phase angle error and TVE variations for reference M-class filter under signal frequency deviations with and without the compensation factor 51
Figure 3.2 Modified M-class filter coefficient example 53
Figure 3.3 Modified M-class filter response with frequency 54
Figure 3.4 Comparison of magnitude error, phase angle error and TVE variations for the modified M-class filter under signal frequency deviations 56
Figure 3.5 Operational flowchart of test setup 58
Figure 3.6 Starting delay of waveform with respect to the UTC reference 60
Figure 3.7 Steady-state current frequency response at 60 fps 63
Figure 3.8 Current magnitude and phase angle modulation response at 60 fps 65
Figure 3.9 Current signal linear frequency ramp response at 60 fps 67
Figure 3.10 Waveforms of current magnitude positive step response at 60 fps 70
Figure 3.11 Waveforms of current phase angle positive step response at 60 fps 71
Figure 4.1 The equivalent π-equivalent model of a transmission line 79
Figure 4.2 The equivalent model of a series compensated transmission line 88
Figure 4.3 The equivalent model of a series compensator at the receiving end 92
Figure 4.4 The equivalent model of a shunt reactor at the receiving end 92
Figure 4.5 Simplified two-area four generator power system 94
Figure 4.6 Variations of the errors with transmission line length 96

Figure 4.7 Variations of errors with the degree of compensation..... 97

Figure 4.8. Variations of the errors with the location of the series compensator 98

Figure 4.9. Waveforms at sending and receiving ends under unbalanced condition..... 99

Figure 4.10 Transmission line parameters at different noisy levels (algorithm 1) 101

Figure 4.11 Maximum errors under noise (SNR = 35 dB) 102

Figure 4.12 Line parameters with different data window lengths (SNR = 35 dB)..... 103

Figure 4.13 Maximum error at different data window lengths (SNR = 35 dB)..... 104

Figure 4.14 Experimental setup – Block diagram 107

Figure 4.15 Experimental setup – Actual arrangement 107

Figure 4.16 Estimations of resistances under different conditions 113

Figure 4.17 Errors in transmission line parameters with bias-errors in magnitude 115

Figure 4.18 Errors in transmission line parameters with bias-errors in phase angle 116

Figure 4.19 Variations of the error of estimated R at different X/R ratios 117

Figure 5.1 Power-angle curves for the three different conditions and areas defined in EAC..... 125

Figure 5.2 Energy-angle relationship [29] 128

Figure 5.3 Two machine system 133

Figure 5.4 Voltage phasor diagram of a two machine system 134

Figure 5.5 SCV during a power swing..... 134

Figure 5.6 Projection of Vs onto the axis of current, I..... 135

Figure 5.7 Positive sequence SCV and its derivative 136

Figure 5.8 SMIB equivalent circuit 140

Figure 5.9 SMIB system with the initial steady-state power flow solution..... 143

Figure 5.10 Variations of rotor angle and voltage magnitude following a fault..... 144

Figure 5.11 Plot of ROCOV vs. ΔV 146

Figure 6.1 Stability boundary on $ROCOV-\Delta V$ plane 151

Figure 6.2 Severe disturbance detection logic 153

Figure 6.3 RTDS and laboratory scale synchrophasor network 160

Figure 6.4 Variations of voltage magnitude and ROCOV of 6 cycles fault 162

Figure 6.5 Variations of rotor angle and voltage magnitude for a fault on line 16-17 (25% of the length) cleared by removing the line after 6 cycles 163

Figure 6.6 ROCOV vs. voltage deviation for a fault on line 16-17 (25% of the length) cleared by removing the line after 6 cycles 164

Figure 6.7 Variations of rotor angle and voltage magnitude for a fault on line 26-29 (25% of the length) cleared by removing the line after 6 cycles 165

Figure 6.8 ROCOV vs. voltage deviation for a fault on line 26-29 (25% of the length) cleared by removing the line after 6 cycles 166

Figure 6.9 Variations of rotor angle and voltage magnitude for fault on line 2-25 (50% of the length) cleared by removing the line after 6 cycles 167

Figure 6.10 ROCOV vs. voltage deviation for a fault on line 2-25 (50% of the length) cleared by removing the line after 6 cycles 168

Figure 6.11 Variations of rotor angle and voltage magnitude for fault on line 16-17 (95% of the length) cleared by removing the line after 6 cycles 169

Figure 6.12 ROCOV vs. voltage deviation for fault on line 16-17 (95% of the length) cleared by removing the line after 6 cycles 170

Figure 7.1 Overall structure of the proposed transient stability status prediction and emergency control system..... 178

Figure 7.2 Coherency cluster recognition routine (adapted from [120]) 181

Figure 7.3 Proposed load shedding scheme..... 183

Figure 7.4 Test setup for validating the synchrophasor based emergency control scheme 184

Figure 7.5 Example 1 : Variations of rotor angle, voltage magnitude and generator trip signals with the emergency control scheme..... 188

Figure 7.6 Example 1 : Comparison of frequency variations with and without load shedding scheme and load trip signals..... 189

Figure 7.7 Example 2 : Variations of rotor angle, voltage magnitude and generator trip signals with the emergency control scheme..... 191

Figure 7.8 Example 2 : Comparison of frequency variations with and without load shedding scheme and load trip signals..... 192

Figure 7.9 Example 3 : Variations of rotor angle, voltage magnitude and generator trip signals with the emergency control scheme..... 195

Figure 7.10 Example 3 : Comparison of frequency variations with and without load shedding scheme and load trip signals..... 196

List of Symbols

t	Time
f	Frequency
f_0	Power system nominal frequency (50 Hz or 60 Hz)
$Vmag$	Voltage magnitude
Δt	Sampling interval
Δf	Offset from the nominal frequency or frequency deviation
ΔV	Offset from the nominal voltage (1 pu) or voltage deviation
N_s	Sample rate (samples/cycle)
F_s	PMU reporting rate (frames/second)
ϕ	Phase angle
R	Series resistance of transmission line
X_L	Series inductive reactance of transmission line
y_c	Shunt capacitive susceptance of transmission line
Z_c	Characteristic impedance of transmission line
γ	Propagation constant of transmission line
δ	Rotor angle of the generator
ω_s	Synchronous speed of the generator

P_m	Mechanical power input the generator
P_e	Electrical power output of the generator
P_G , V_G	Generator bus active power injection and voltage set point respectively
P_L , Q_L	Load bus active and reactive power consumption respectively

List of Abbreviations

AC	**A**lternating **C**urrent
ADC	**A**nalog to **D**igital **C**onverter
ANN	**A**rtificial **N**eural **N**etwork
CCT	**C**ritical **C**learing **T**ime
COI	**C**enter **O**f **I**nertia
COMTRADE	**COM**mon format for **TRA**nsient **D**ata **E**xchange
CT	**C**urrent **T**ransformer
DAC	**D**igital to **A**nalog **C**onverter
DAE	**D**ifferential and **A**lgebraic **E**quations
DC	**D**irect **C**urrent
DFR	**D**igital **F**ault **R**ecorder
DFT	**D**iscrete **F**ourier **T**ransform
DT	**D**ecision **T**ree
EAC	**E**qual **A**rea **C**riterion
FACTS	**F**lexible **AC** **T**ransmission **S**ystem
FE	**F**requency **E**rror
FIR	**F**inite **I**mpulse **R**esponse
fps	**f**rames **p**er **s**econd

GPS	**G**lobal **P**ositioning **S**ystem
HVDC	**H**igh **V**oltage **D**irect **C**urrent
IEC	**I**nternational **E**lectrotechnical **C**ommission
IEEE	**I**nstitute of **E**lectrical and **E**lectronics **E**ngineers
IIR	**I**nfinite **I**mpulse **R**esponse
IRIG-B	**I**nter**R**ange **I**nstrumentation **G**roup **T**ime **C**ode Format **B**
KE	**K**inetic **E**nergy
LDC	**L**oad **D**ispatch **C**enter
LS	**L**east **S**quare
PDC	**P**hasor **D**ata **C**oncentrator
PE	**P**otential **E**nergy
PLL	**P**hase **L**ocked **L**oop
PMU	**P**hasor **M**easurement **U**nit
pps	**p**ulse **p**er **s**econd
PT	**P**otential **T**ransformer
RFE	**R**ate of change of **F**requency **E**rror
ROCOF	**R**ate **O**f **C**hange **O**f **F**requency
ROCOV	**R**ate **O**f **C**hange **O**f **V**oltage
RTDS	**R**eal **T**ime **D**igital **S**imulator
SCADA	**S**upervisory **C**ontrol **A**nd **D**ata **A**cquisition
SCV	**S**wing **C**enter **V**oltage
SEP	**S**table **E**quilibrium **P**oint
SMIB	**S**ingle **M**achine to **I**nfinite **B**us

SNR	**S**ignal to **N**oise **R**atio
spc	**s**amples **p**er **c**ycle
SPS	**S**pecial **P**rotection **S**ystem
SVD	**S**ingular **V**alue **D**ecomposition
SVM	**S**upport **V**ector **M**achine
TEF	**T**ransient **E**nergy **F**unction
TLS	**T**otal **L**east **S**quare
TRV	**T**ransient **R**ecovery **V**oltage
TVE	**T**otal **V**ector **E**rror
UEP	**U**nstable **E**quilibrium **P**oint
UTC	**C**oordinated **U**niversal **T**ime
WAMPaC	**W**ide **A**rea **M**onitoring, **P**rotection **a**nd **C**ontrol
WAPaC	**W**ide **A**rea **P**rotection **a**nd **C**ontrol

List of Appendices

Appendix A

Single Machine to Infinite Bus (SMIB) Test System …….212

Appendix B

IEEE 39-bus Test System ……..……. 214

Chapter 1

Introduction

This chapter presents the background, motivation, and the major research objectives. A brief review of the concepts of synchrophasor technology, synchrophasor applications, transmission line parameters, power system transient stability, and power system instability control is also provided. The chapter concludes with an overview of the organization of the thesis.

1.1 Background

A power system is designed to operate satisfactorily within the desired limits of voltage and frequency under normal conditions and to withstand a wide range of disturbances such as faults, loss of generation or large changes in loads. However, it is neither possible nor economically feasible to design a power system to be immune to all possible events; unpredicted disturbances can lead to rotor angle, frequency or voltage instabilities in a power system. The final cause of most major blackouts is some form of instability. Therefore, recognizing power system instabilities as early as possible is very important for the security of power systems [1].

Wide area monitoring, protection and control (WAMPaC) of power systems using synchrophasor measurements is emerging as a useful tool for preventing catastrophic events. WAMPaC systems enable real-time observation of an interconnected power system spread over a large geographical area [2], [3]. Since the synchrophasors are time synchronized using global time reference and updated at a faster rate, they are superior to traditional supervisory control and data acquisition (SCADA) measurements in capturing power system steady-state and dynamic behaviors [4]. Therefore, many power utilities install phasor measurement units (PMUs) at their important substations, targeting various steady-state and dynamic applications [4].

The rapid advance of synchrophasor technology and the growth of PMU installations in recent years have substantially increased the feasibility of deploying practical synchrophasor applications for improving the real-time monitoring of power systems. These synchrophasor applications can range from simple monitoring algorithms to advanced response based WAMPaC systems. With PMUs conforming to the new synchrophasor standard, IEEE C37.118.1-2011 [5], more predictable and consistent synchrophasor measurements can be obtained during the steady-state as well as under dynamic conditions. This supports the development of more accurate and reliable synchrophasor applications to enhance the real-time operation and control of power systems.

1.2 Synchrophasor Networks

A typical wide area synchrophasor network consists of PMUs and phasor data concentrators (PDCs) connected through a communication network, as shown in Figure 1.1.

The global positioning system (GPS) is used to synchronize the phasor measurements to a common time base.

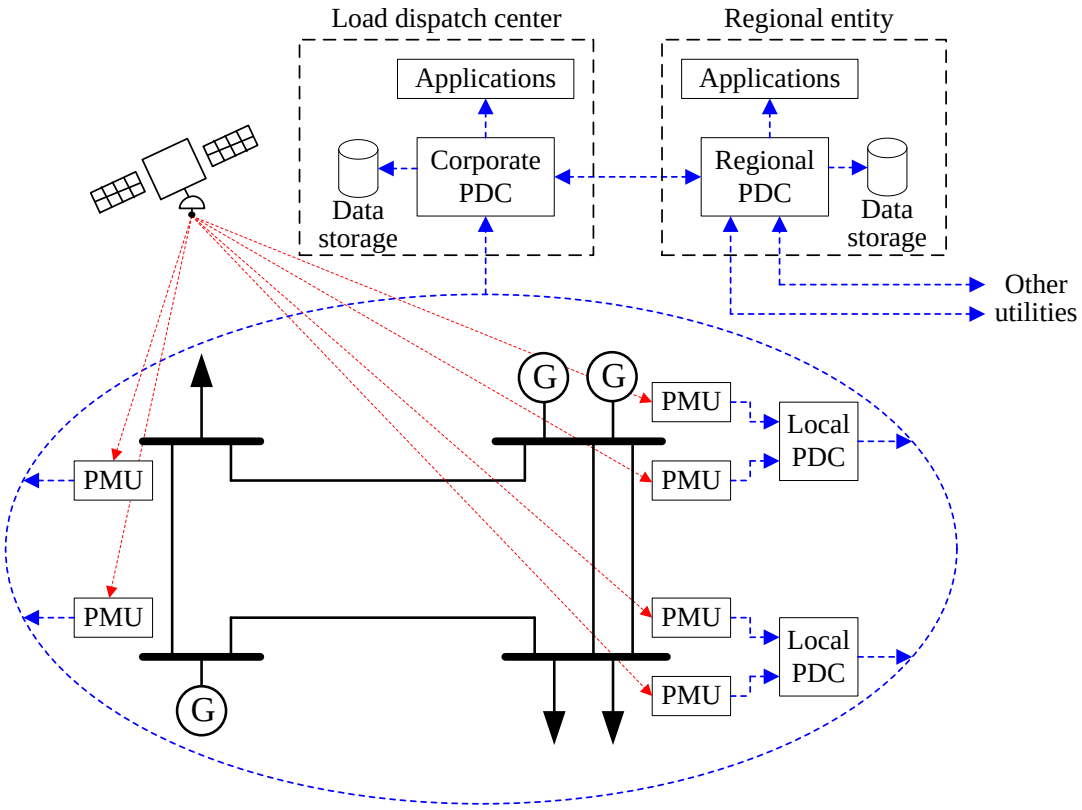

Figure 1.1 Typical architecture of a wide area synchrophasor network

Typically, several PMUs are installed in a substation, and a local PDC is deployed to collect the synchrophasor measurements in the substation. A corporate PDC at the load dispatch center (LDC) collects the data from different PMUs and local PDCs at various locations of an interconnected power system. The corporate PDCs belonging to different utilities may be further linked to higher level regional PDCs to provide a wide area view of the power system [6], [7]. These systems may use a dedicated network or a part of the corporate data network of the power utility to maintain performance, reliability and cyber security.

1.2.1 Perception of Synchrophasor

A phasor is an equivalent representation of a pure sinusoidal waveform, $x(t)$, which is fully characterized by the magnitude, phase angle, and frequency:

$$x(t) = X_m \cos(\omega t + \phi) = X_m \cos(2\pi f t + \phi) \tag{1.1}$$

where X_m is the peak amplitude and f is the signal frequency. In a phasor, the phase angle ϕ can be expressed with respect to an arbitrary reference, but in a synchrophasor, the phase angle ϕ is the offset from a reference cosine function at the nominal power system frequency f_0 (50 Hz or 60 Hz) synchronized to the coordinated universal time (UTC) as shown in Figure 1.2. The corresponding synchrophasor is represented by a complex number as,

$$\mathrm{X} = \frac{X_m}{\sqrt{2}} e^{\mathrm{j}\phi} = \frac{X_m}{\sqrt{2}} (\cos\phi + \mathrm{j}\sin\phi) = \frac{X_m}{\sqrt{2}} \angle \phi \tag{1.2}$$

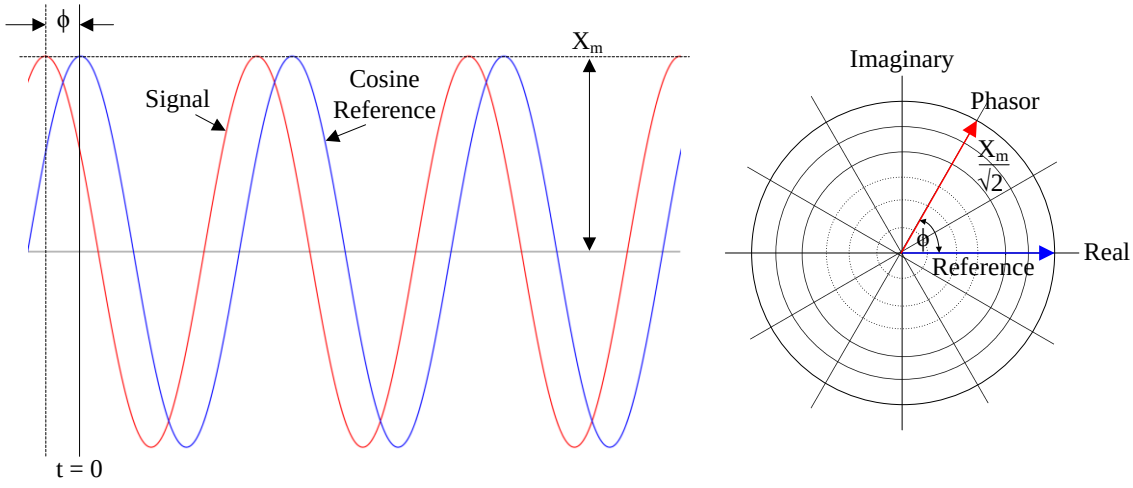

Figure 1.2 Synchrophasor representation of a sinusoidal waveform

In the general case, both the amplitude and the frequency of the sinusoid are considered as varying with time. Then, the sinusoid can be written as,

$$x(t) = X_m(t)\cos\left(2\pi\int f(t)dt + \phi\right) \tag{1.3}$$

The time varying frequency can be expressed as

$$f(t) = f_0 + \Delta f(t) \tag{1.4}$$

where f_0 is the nominal power system frequency, and $\Delta f(t)$ is an offset from the nominal frequency. The modified sinusoid can be written as,

$$x(t) = X_m(t)\cos\left[2\pi f_0 t + 2\pi\int \Delta f(t)dt + \phi\right] \tag{1.5}$$

Since $X_m(t)$ and $\Delta f(t)$ are functions of time, $x(t)$ represents a dynamic phasor. In the special case where $\Delta f(t)$ is a constant offset from f_0, then $\int \Delta f(t)dt = \Delta f t$. Thus, the general phasor can be simply represented as,

$$\mathrm{X}(t) = \frac{X_m}{\sqrt{2}}e^{\mathrm{j}(2\pi\Delta f t+\phi)} = \frac{X_m}{\sqrt{2}}\angle\{2\pi\Delta f t + \phi\} \tag{1.6}$$

A synchrophasor is attached to a time stamp which indicates the time of measurement, usually in UTC.

1.2.2 Phasor Measurement Unit (PMU)

A PMU is a device which can estimate the phasors of the voltage and current signals input to it, with all phase angles precisely referenced to a common time frame with the aid of a GPS clock. In addition to the phasors, a PMU can estimate secondary measurements such as frequency and rate of change of frequency (ROCOF) [2], [5]. The PMU measurements together with other optional analog and digital measurements are timestamped and dispatched as a data packet to the communication network at a specified

rate. The data reporting rates range from 10 to 50 frames per second (fps) in 50 Hz systems and 10 to 60 fps in 60 Hz systems [5]. Traditionally, dedicated PMUs have provided synchrophasor measurements. These PMUs are not in widespread use because they are relatively expensive, and they are only used on critical systems [8]. With advancements in signal processing hardware, PMUs are now commonly available as a functional unit within another physical unit such as power system digital fault recorder (DFR), protection relay, or a meter [5], [7]-[10].

1.2.3 Phasor Data Concentrator (PDC)

A PDC functions as a node in a synchrophasor network and collects the phasor measurements from a set of PMUs or lower-level PDCs and aligns the phasor data according to their timestamps. Collated data are then sent to local applications and upstream PDCs as a single stream. The mid-level and higher-level PDCs (corporate and regional PDCs) keep an archive for offline and historical data analysis [4], [11]. If the PMU communication network experiences abnormal delays or packet losses, some measurements can be lost. The PDC performs quality checks to detect such missing or corrupted data, flags them, and monitors the overall performance of the synchrophasor network. The PDC can be a stand-alone device or a hardware/software package integrated into other systems and devices [11].

1.2.4 Synchrophasor Communication Network

A communication network is essential for the proper functioning of wide area power system applications. Loss of communication would leave the application with insufficient information to carry out its operations. The reliability, network traffic characteristics, and latency of the communication network are the aspects critical to WAMPaC applications. In a packet-based communication network, reliability is related to the packet loss probability and bit errors. Both latency and packet-loss probability depend on network congestion. The maximum usable data-rate, which is determined by the bandwidth of the communication link, directly impacts the communication latency.

1.3 Synchrophasor Applications

The technology of synchronized phasor measurements or synchrophasors was first proposed in 1980s [2]. Researchers and engineers quickly recognized the many potential applications of synchrophasors in power system monitoring, protection, operation and control [3]. PMUs were developed and deployed on an experimental basis in actual power systems in the 1990s and commercial PMUs were then installed in power systems in North America [4]. The first documented commercial synchrophasor application was the EPRI parameter identification data acquisition system project in 1992 [12]. In this project, PMUs were placed at six different locations in the USA and were used to validate and correct power system models. Furthermore, this project was the first instance where synchrophasors were used for post-event analysis [12], [13]. Since then an exhaustive list of synchrophasor applications can be found in literature. They can be essentially catego-

rized into three groups: off-line, monitoring, and protection and control. This section lists a few applications under each category.

1.3.1 Off-line Applications

Off-line synchrophasor applications use archived synchrophasor data, and processing may be conducted days, months, or even years after the data were collected. The availability of synchrophasors enhances power system performance and improves models used in power system studies [14].

Some examples of offline synchrophasor applications include:

- Post-event analysis
- Static and dynamic system model calibration and validation
- Power plant model validation
- Load characterization
- Determination of accurate operating limits
- Power system restoration or system black start

1.3.2 Monitoring Applications

Synchrophasors are widely used for various monitoring applications, which require real-time synchrophasor measurements and immediate data processing. Time synchronized phasors at different locations aid system operators in understanding what is happening in the power system and identifying potential problems. Furthermore, synchrophasors help to evaluate, implement and assess remedial measures [14]. In literature, various

monitoring and visualization tools can be found that explore dynamic power flow, dynamic phase angle separation, real-time frequency and ROCOF displays [15]. For example, voltage magnitudes and phasor angles with respect to a user-defined reference angle can be used as input for a visualization tool and system depressed conditions can be easily identified at a glance [15].

A few synchrophasor based monitoring applications include:

- State estimation
- Wide area situational awareness
- Voltage monitoring and trending
- Frequency stability monitoring and trending
- Power oscillations detection and mode meters
- Transmission line parameters estimation
- Fault location identification
- Event detection and avoidance
- Dynamic line ratings and congestion management
- Alarming and setting system operating limits
- Resource integration

Since synchrophasors improve system operators' ability to understand and make decisions related to the power system, the United States-Canada Task Force on the August 14, 2013 Blackout recommended that all utilities enhance synchrophasor based monitoring capabilities to avoid catastrophic system failures [1].

1.3.3 Protection and Control Applications

Since synchrophasors provide system wide observability with high resolution, they can be effectively used for wide area protection and control applications. Applications include backup protection, transient stability, voltage stability, and low frequency oscillations whereas control actions can be local or centralized.

Power system backup protection can be improved with synchrophasor measurements. In literature, a number of protection applications are available [10], [12], [16]; differential protection of transmission lines, distance protection of multi-terminal transmission lines, backup zones of distance relays, and adaptive out-of-step protection are a few examples.

Power system transient instability, voltage instability, and low frequency electromechanical oscillations can be predicted/detected from synchrophasor measurements. In literature, voltage phasors are used to predict transient and voltage stabilities. Monitoring phase angle separation or voltage magnitude dropping at certain locations is commonly used to predict potential instabilities [13]. The frequency measurements are used to monitor electromechanical oscillations in power systems. In addition, the frequency measurements are used to develop a frequency monitoring network, which can detect any significant loss of generation and predict the amount of generation loss [17].

The data transfer rates required for a real-time application; depends on the application – monitoring versus protection and control, for example. Voltage stability is a slower phenomenon and thus the monitoring of voltage stability can be achieved with a slower data rate, while a faster application such as transient stability control requires faster data

transfer rates [18]. In contrast, the speed of data transfer over communication channels is less critical in the case of off-line applications.

Although literature reports on many synchrophasor applications, there is still a room for new applications, which improve power system reliability and make the power system more immune to catastrophic failures. Therefore, two areas will be investigated in this thesis: transmission line parameters estimation as a real-time monitoring application, and transient stability status prediction and emergency control as a wide area protection and control application. The next few sections will shed more insight on these applications.

1.4 Transmission Line Parameters

Electrical properties of transmission lines can be characterized by means of transmission line parameters: resistance, inductance, capacitance and conductance. The resistance is due to electrical properties of the conductor materials. The inductance and capacitance account for the effect of magnetic and electric field around the conductor. The shunt conductance is due to the effect of leakage current flowing across insulators and ionized paths in the air. As the leakage current is very small compared to the current flowing in the transmission line, shunt conductance is often neglected.

Transmission lines are represented by equivalent models with appropriate circuit parameters. Among various transmission line models, the π-equivalent model is extensively used for planning and operation studies, setting protection relays, fault location, state estimation, and numerous other applications. Figure 1.3 shows the π-equivalent model of a transmission line where electrical performances are exhibited by series resistance, series

inductive reactance and shunt capacitive susceptance. Accurate estimation of these parameters is very important for the modeling of power systems.

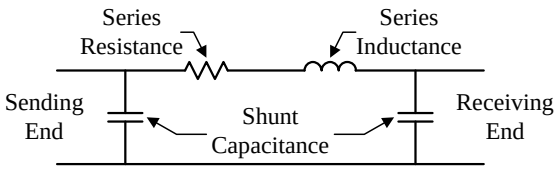

Figure 1.3 The π-equivalent model of a transmission line

Most utilities determine transmission line parameters through theoretical calculations [19]. The traditional theoretical method of calculating line parameters consider tower geometries, conductor dimensions, estimates of line length, conductor sag and other factors such as earth resistivity. Results obtained using these calculations involve a number of approximations [19]-[21] such as identical tower configuration and constant soil resistivity throughout the line. Another approach is to determine the transmission line parameters through offline tests. Although this method can give more accurate results, offline measurements require forced outages and complex wiring [19].

Transmission line parameters are affected by environmental factors and the load level. Specifically the line resistance varies with the conductor temperature, which not only depend on the load current and the ambient temperature but also on other ambient weather conditions such as wind speed and sun flux [22]-[24]. Both theoretical calculations and offline tests do not allow for the tracking of parameters when they are changing [21]. However, the accuracy of some applications such as state estimation and fault location can be improved by updating the line parameter values with changing load and environmental conditions [20]-[22]. Furthermore, if the line resistance can be accurately calcu-

lated, it can be used to estimate the mean line temperature and hence the closeness to the thermal limit.

As many power utilities increase the installation of PMUs at important substations for monitoring various aspects of the power grid [25], opportunities arise for the continuous identification of transmission line parameters. The phasor values of the voltages and currents measured at the two ends of a transmission line with proper time synchronization provide excellent information of identification its model parameters [26], [27]. Since the synchrophasor measurements have greater accuracy and accurate time synchronization than the data obtained from traditional SCADA systems, line parameters can be estimated with an improved accuracy on a continuous/real-time basis when they are changing [21].

1.5 Power System Stability

Power system stability is defined as the ability of a power system operating at a given steady-state condition to regain an equilibrium state (either return to the original operating condition or regain a new state of operating equilibrium) after being subjected to a severe disturbance [18]. The post-disturbance stability of a power system not only depends on the pre-disturbance system operating condition, but is also affected by the form of disturbance and the post-disturbance network configuration, which can be altered due to the isolation of faulted elements.

Power system stability can be classified into different categories and well-recognized classification is given in [18], where rotor angle, voltage and frequency stabilities are identified as three main categories. This classification is illustrated in Figure 1.4. Both ro-

tor angle and voltage stabilities can further be divided into small disturbance and large disturbance stabilities. The rotor angle stability is a short term phenomenon whereas the voltage and the frequency stabilities may be either a short term or a long term phenomenon as recognized in Figure 1.4. In this thesis, the large disturbance rotor angle stability phenomenon (also known as transient stability) is the focus.

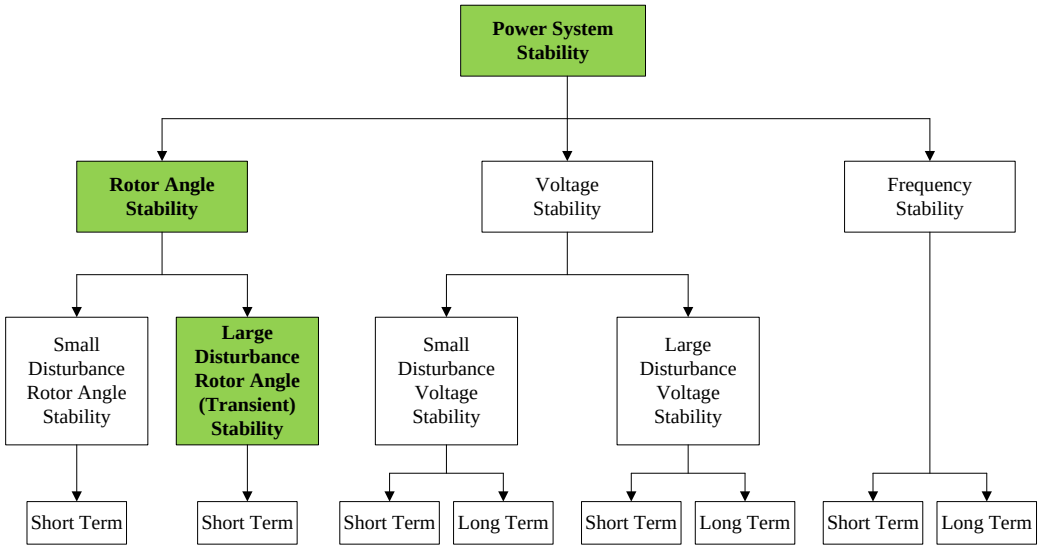

Figure 1.4 Classification of power system stability [18]

1.5.1 Power System Transient Stability

Transient stability is the ability of synchronous machines of an interconnected power system to maintain synchronism when subjected to a severe disturbance such as a short circuit on a transmission line, or disconnection of a large generator or load [18], [28], [29]. It is a fast phenomenon, and a generator or group of generators can potentially lose synchronism within a few seconds after a disturbance, depending on their mechanical inertia.

Under steady-state operation, each synchronous machine in the system has a constant rotor speed (equal to its synchronous speed), as the input mechanical torque and the output electromagnetic torque are equal and opposite. If the power system is perturbed, its equilibrium is distressed, resulting in an acceleration or deceleration of the rotor speeds of synchronous machines. Consequently, the angular positions of rotors change, resulting in an angular separation between the faster machines and the slower machines. The synchronizing torque resulting from the nonlinear power-angle relationship acts to counter the angular separation. However, an increase in angular difference beyond a certain limit results in a decrease of power transfer, causing a rapid increase in angular separation. Instability ultimately occurs when the system cannot absorb the kinetic energy corresponding to the rotor speed differences [18], [28], [29]. Eventually one or more generators could run out of synchronism from the rest of the network, damaging generators unless disconnected from the system [29], [30].

1.6 Power System Instability Control

The approaches for controlling instabilities depend on the nature of the instability, its magnitude, and available control mechanisms. The illustration of different stability controls philosophies, adapted from [31], shown in Figure 1.5 classifies the detection methods as event based and response based, and the control actions as continuous and discontinuous. They can also be classified based on the type of inputs as local or wide area control.

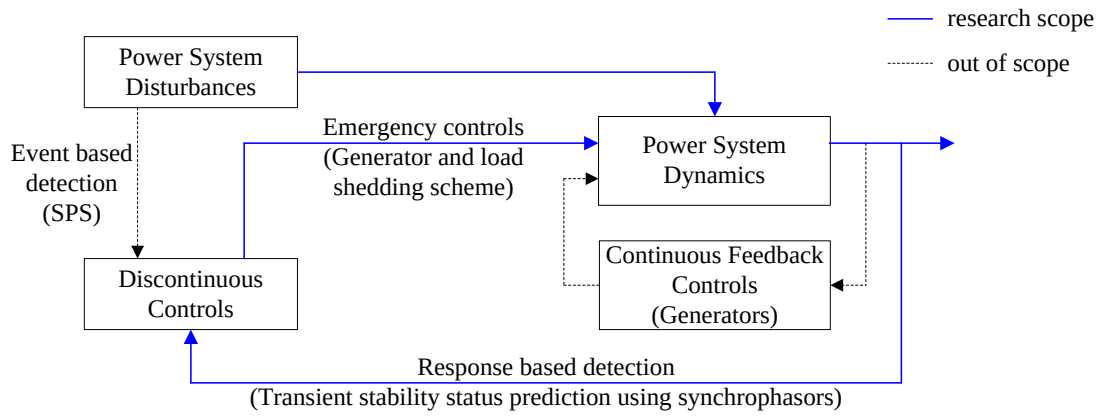

Figure 1.5 Different options available for power system stability control [31]

A power system instability may be initiated either by a small disturbance to the system such as a change in load or a large disturbance such as a fault in the system. Oscillations initiated by a small disturbance can be damped through appropriate continuous feedback controls, for example, governor or exciter control in a generator. In contrast, large disturbances may cause some form of power system instability within a very short time and it is mandated to initiate emergency control actions to arrest the situation. Possible emergency control actions include severe measures such as generator tripping, load shedding, controlled islanding, circuit switching, dynamic breaking, and generator fast valving. Depending on the availability, other actions such as fast control of flexible AC transmission system (FACTS) devices and high voltage direct current (HVDC) converters can be utilized. These emergency control actions are generally discontinuous in nature and can be initiated with the aid of event based special protection systems (SPSs) or response based WAMPaC systems.

Special protection systems are event based control systems that activate controls in response to the occurrence of some pre-identified set of disturbances which are usually

identified through extensive dynamic simulation studies. The event detection logic of an SPS can be complicated and the implementation can be expensive [31], especially when relying on many remote signals. Any modification to a SPS requires fresh system studies and significant alteration of the control logic [32]. Response based WAMPaC systems are potential alternatives for SPSs; their design can potentially be simpler and robust against minor system modifications [32]-[34].

This thesis focuses on a response based WAMPaC system to mitigate potential transient instabilities. The biggest challenge in the transient instability control problem arises from the rapid development of the instability phenomenon, thus requiring a response time in the order of 1s or less.

1.7 Motivation and Objectives

Today, many power utilities around the world install wide area synchrophasor measurement systems, targeting various WAMPaC aspects of power grid. As a result, synchrophasor measurements are becoming an integral part in many power systems, but the potential of synchrophasors for power system monitoring and control is not fully utilized, especially in the area of real-time stability control. Only a few control applications have been actually implemented in control rooms. Considerable research has been conducted in the area of detection of potential steady-state voltage stabilities using synchrophasor measurements, but only a few studies have investigated the early detection and control of potential rotor angle instabilities (or transient instabilities), possibly due to fast nature of the transient stability phenomenon. Fast recognition of instabilities provides opportunity

to initiate emergency control actions [35]. In [36]-[37], synchronously measured post-disturbance recovery voltage magnitude measurements have been used to predict the transient stability status using a support vector machine (SVM) classifier. Further, the above work establishes that use of the post-disturbance recovery voltage magnitude measurements have a strong relationship with the post-disturbance transient stability status, and enable faster and accurate predictions. Despite the reported success, training of the classifiers, and preparing the data necessary for training is a time consuming task that needs considerable expertise. This motivates the exploration of better approaches for prediction of rotor angle instabilities.

Real-time stability control applications demand high accuracy and consistency in synchrophasor measurements under dynamic conditions. It is important to understand the quality and the accuracy of measurements, based on which the extreme control actions such as load shedding are performed. The recently published IEEE Standard C37.118.1-2011 [5] provides the necessary guidelines to ensure dynamic performance of synchrophasors with two performance class filters: P-class and M-class. Practical implementation of PMUs conforming to this new standard and conformity testing are challenging tasks. Thus, the first part of this thesis examines the practical implementation of two performance class filters required to meet the dynamic performance of synchrophasor measurements, the practical methods available to evaluate PMU performances according to [5], and the typical characteristics of synchrophasor measurement errors.

The general approach used for the development of synchrophasor based monitoring and control algorithms involves theoretical formulation and verification through off-line time-domain simulations. Real-time implementation of these algorithms is only rarely re-

ported in the published literature. It is important to recognize the development issues, technical hitches in real-time implementation of the algorithms, and issues related to communication. Therefore, in this thesis, a simple steady state synchrophasor application is first investigated as a precursor to the more challenging real-time stability monitoring and control application. The chosen simple application is the real-time monitoring of transmission line parameters. Despite a number of diverse approaches reported in literature to estimate transmission line parameters, there is still a room for improvement in terms of the reliability, accuracy and efficiency of estimation.

Finally, it is important to test and verify the algorithms and their real-time implementations. As it is practically difficult to evaluate the performances of a given synchrophasor application algorithm on a real power system, the more feasible solution for validation of real-time performance is to use real-time power system simulators. The biggest advantage of this approach is that actual hardware such as PMUs and communication equipment can be interfaced with the power system simulated in a real-time simulator, and the operation of individual components as well as the integrated system can be tested methodically. This is the motivation for development of a laboratory scale synchrophasor network around a RTDS^{TM} real-time digital simulator.

Based on the above discussion, the following specific objectives can be identified:

1. Implementation of P-class and M-class dynamic performance according to the latest IEEE synchrophasor standard [5] on a practical PMU and evaluation of its performance.

2. Development and implementation of efficient algorithms for real-time monitoring of transmission line parameters, and understanding of the implementation and performance issues.
3. Development of an efficient algorithm to accurately predict the potential transient instabilities using wide area synchrophasor measurements.
4. Development of an emergency control scheme to prevent possible power system collapses due to transient instability for an example power system.
5. Development of a laboratory setup that include a real-time simulator and a synchrophasor network to evaluate the real-time performances of the proposed WAMPaC applications.

1.8 Thesis Overview

This chapter provides the introduction giving necessary background to the research, motivation, and key objectives. The rest of the thesis is organized as follows.

Chapter 2 provides the literature review related to the synchrophasor measurement technology. The review includes the development of synchrophasor standards, a typical PMU model and phasor estimation methods, the backend performance class filters, and evaluation of PMU performances.

Chapter 3 analyses the dynamic performance of a PMU. A simple test setup to measure the PMU performance is developed, and the sources of errors in the test setup are discussed. The reference P- and M-class filters provided in the latest synchrophasor stand-

ard, IEEE C37.118.1-2011 [5], are implemented, evaluated and several modifications are proposed for convenient implementation.

Real-time transmission parameters estimation is investigated in Chapter 4. The chapter proposes three new transmission line parameters estimation algorithms. The performances of the new algorithms are evaluated using a real-time digital simulator, a laboratory hardware experimental setup, and a set of field measurements obtained from a utility. The sensitivity of the parameter estimations to bias-errors in measurements is also assessed.

In Chapter 5, the problem of transient stability status prediction is investigated. The chapter reviews the existing transient stability status prediction approaches in particular the approaches that use voltage magnitude measurements. A new transient stability status prediction algorithm is introduced with the aid of a single machine to infinite bus system (SMIB).

The proposed transient stability status prediction methodology using post-disturbance voltage magnitudes is further expanded to cover multi-machine power systems in Chapter 6. This chapter describes the method of implementation, validates the proposed algorithm through offline simulations and a real-time testing.

In Chapter 7, a simple emergency control scheme is proposed to demonstrate the effectiveness of the transient stability status prediction algorithm described in Chapter 6. The effectiveness and the feasibility of the proposed emergency control scheme are validated using a real-time simulation based test-setup.

Finally, the major conclusions and a summary of main contributions are provided in Chapter 8.

Chapter 2

Synchrophasor Measurement Technology

2.1 Introduction

This chapter reviews the essential background literature related to the synchrophasor measurement technology. The development of synchrophasor standards, functional model of a typical PMU, phasor and frequency estimation methods, and backend performance class filters introduced in the latest IEEE synchrophasor standard [5] are briefly discussed. The existing methods for evaluating the steady-state and dynamic performance of PMUs are reviewed and their advantages and drawbacks are identified.

2.2 Evolution of Synchrophasor Standards

The first synchrophasor standard, IEEE Standard 1344 [38] was published in 1995. With the rapid advancement of the technology, need for an improved standard with well-defined terms and performance evaluation methods was recognized. As a result, the new

IEEE Standard C37.118-2005 [39] was introduced to replace the original standard. The concept of total vector error (TVE), compliance tests to evaluate steady-state performance, and well-defined data communication formats are some of the new features introduced in this standard [39].

In 2009, a joint task force was formed between the IEEE and the International Electrotechnical Commission (IEC) to develop a strategy to split IEEE Standard C37.118-2005 [39] into two parts. This split-up was to support harmonization with the IEC 61850 communication standard that is also capable of carrying synchrophasor information. This led to publication of IEEE Standard C37.118.1-2011 [5] for synchrophasor measurements and performances, and IEEE Standard C37.118.2-2011 [40] for synchrophasor data transfer in late 2011.

The original synchrophasor standard, IEEE Standard 1344-1995 [38], and its successor, IEEE Standard C37.118-2005 [39] played an important role in steady-state characterization of phasor measurements. However, they fell short in the aspect of PMU dynamic performance. The latest IEEE Standard C37.118.1-2011 [5] provides necessary guidelines to assure dynamic characterization of synchrophasors. It defines two classes of performances, namely, P-class and M-class. P-class is preferred for applications requiring fast response. The letter P is used since protection applications require a fast response. M-class is intended for applications demanding greater precision. The letter M is used since analytic measurements often require greater precision. However, the user has freedom to choose a performance class that matches the requirement of each application [5]. It also provides two reference filters in an annex. Furthermore, the concept of TVE and compliance tests is expanded in the new standard. In addition, it also defines the frequency error

(FE) and the rate of change of frequency error (RFE) limits for both steady-state and dynamic conditions.

The IEEE Standard 1344-1995 [38] did not support data transmission hierarchy. The messaging was strictly from a PMU to another device, such as a power system digital fault recorder (DFR). This drawback was addressed in the next revision, IEEE Standard C37.118-2005 [39], which defined a communication protocol to operate over synchrophasor networks. The communication protocol includes four types of messages, namely data, configuration, header and command frames, and it was widely used throughout the world [7]. The recent IEEE Standard C37.118.2-2011 [40] minimizes disruption to its predecessor, IEEE Standard C37.118-2005 [39] to maintain backward compatibility [7].

The first PDC guidelines, IEEE C37.244 [11] was published in 2013 as a guide, which describes performance, functional and communication needs of PDCs for power system protection, control and monitoring applications. This covers synchrophasor system needs and testing procedures for PDCs as well as functional requirements for associated interfaces with PMUs to a PDC and PDC systems. Furthermore, it includes requirements for synchronization, synchrophasor data processing, and real-time access.

In April 2014, IEEE Standard C37.118.1a [41], an amendment to IEEE C37.118.1-2011 was released to relax the M-class FE and RFE requirements and rectify minor inconsistencies as suggested in Chapter 3. Since the IEEE Standard C37.118.1-2011 [5] does not specify test procedures, different test procedures may yield different test results for the same PMU. To address that issue, the IEEE standards association conformity assessment program published the IEEE synchrophasor measurement test suite specification [42] in December 2014.

2.3 Total Vector Error (TVE)

The latest IEEE standard C37.118.1 [5] defines the total vector error (TVE) as a measure to assess the accuracy of synchrophasor measurements and it is defined as,

$$\mathrm{TVE}(n) = \frac{|\mathrm{X}_a(n) - \mathrm{X}_m(n)|}{|\mathrm{X}_a(n)|} \tag{2.1}$$

where $\mathrm{X}_a(n)$ is the actual synchrophasor and $\mathrm{X}_m(n)$ is the measured synchrophasor. The relationship between the actual phasor, the measured phasor and the TVE for an arbitrary limit, ε is shown in Figure 2.1.

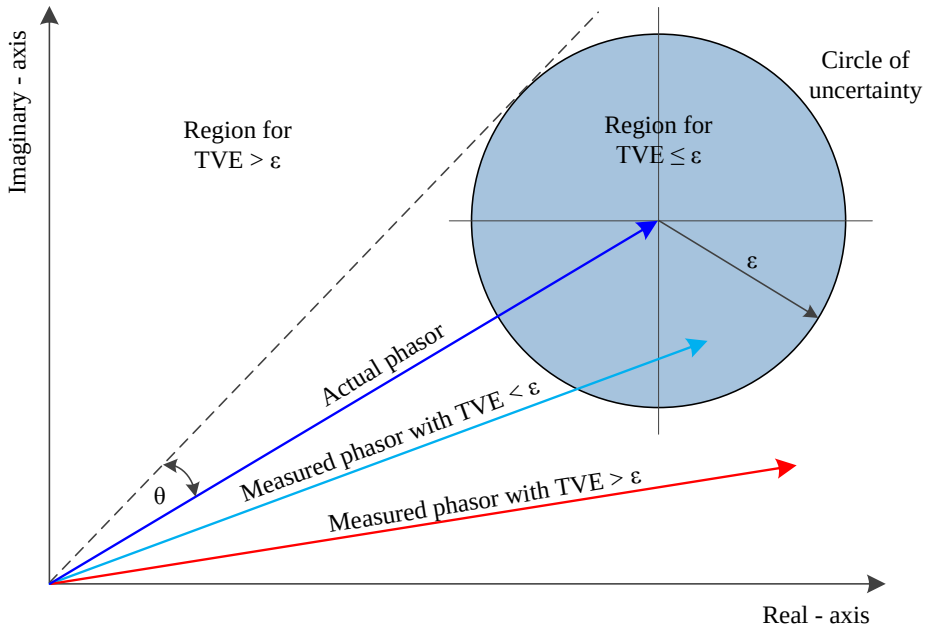

Figure 2.1 Relationship between actual phasor, measured phasor and TVE

If the end point of the measured phasor lies inside the circle of uncertainty with the radius of ε drawn at the end of the actual phasor, the measured phasor fulfills the required accuracy. The maximum error for the magnitude measurement with no phase angle error can be easily obtained from Figure 2.1, it would be ± ε. The maximum phase error, θ occurs

when the measured phasor is a tangent to the circular TVE region. As the phase angle is measured with respect to a time synchronized reference signal, timing errors creates an error in the phase angle measurement. The same timing error will result different TVE depending on the system frequency.

2.3.1 TVE, Magnitude Error and Phase Angle Error Relationship

The TVE combines the errors from both magnitude and phase angle measurements, and a relationship between the TVE, and the magnitude error λ and the phase angle error γ can be derived from (2.1) as:

$$\text{TVE} = \sqrt{2(1 \pm \lambda)(1 - \cos\gamma) + \lambda^2} \tag{2.2}$$

It is important to identify the error contributions from magnitude and phase angle in order to minimize TVE. The 3D plot in Figure 2.2 shows the relationship between the magnitude error, the phase angle error and the TVE.

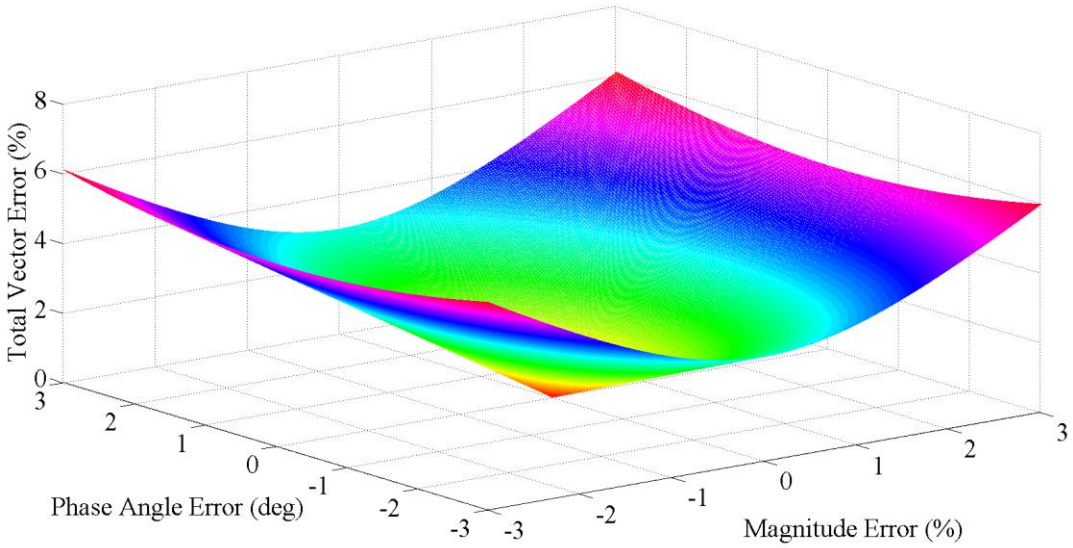

Figure 2.2 TVE as a function of magnitude and phase angle errors

Figure 2.3 illustrates the TVE as a function of the phase angle error for different magnitude errors, and Figure 2.4 shows TVE as a function of the magnitude error for different phase angle errors and Figure 2.5 displays the relationship between magnitude and phase angle errors for different TVE values.

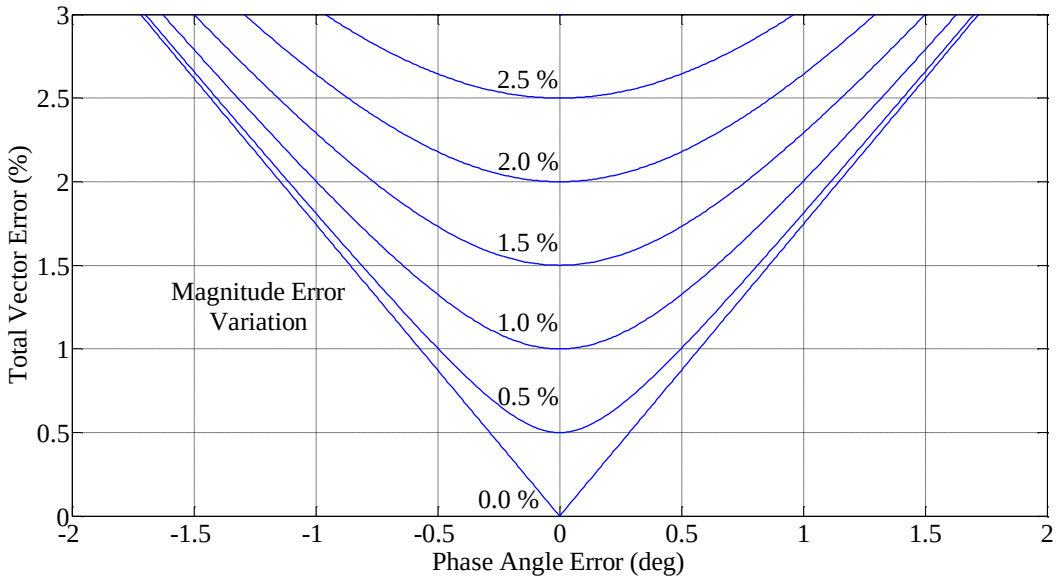

Figure 2.3 TVE as a function of phase angle error for different magnitude errors

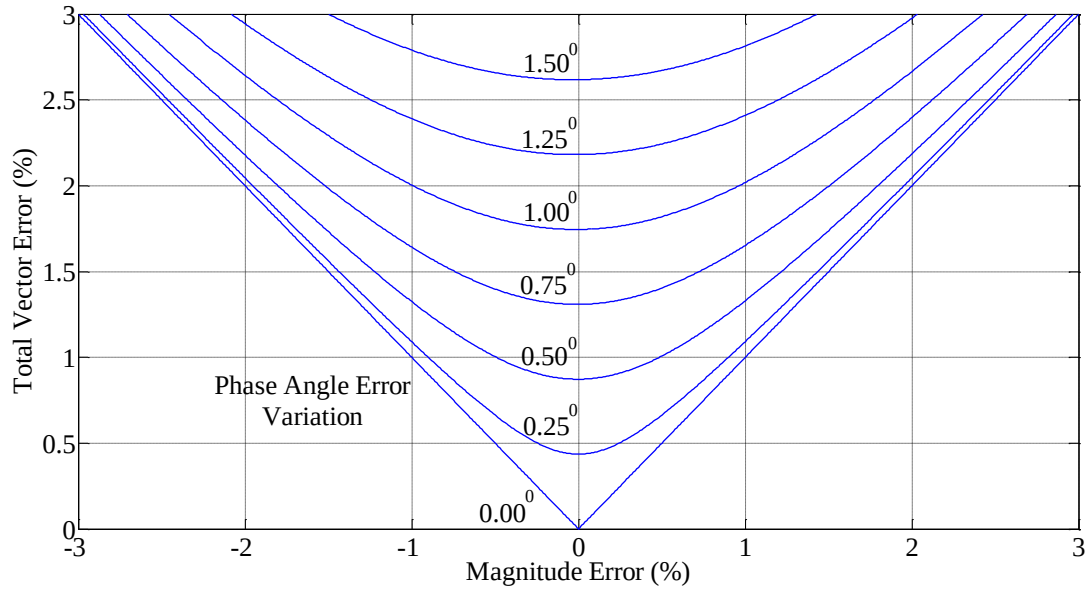

Figure 2.4 TVE as a function of magnitude error for different phase angle errors

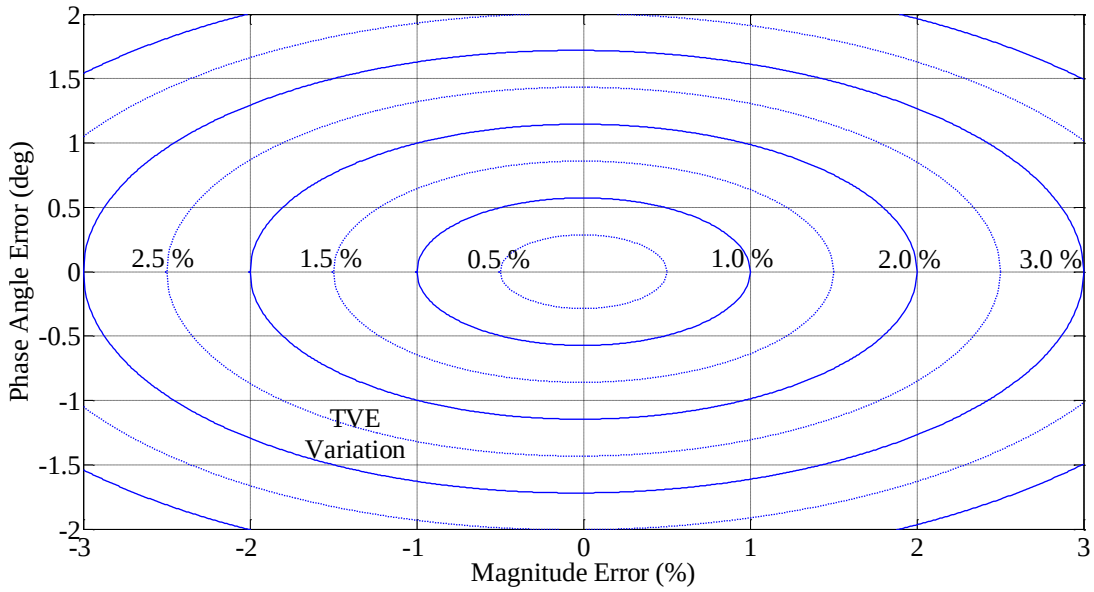

Figure 2.5 Relationship between magnitude and phase angle errors for different TVEs

If it is required to limit TVE to 1%, the maximum allowable magnitude error is ±0.01pu (when the error in phase angle is zero), and the maximum allowable error in an-

gle is ± 0.573° (when the magnitude error is zero). The timing error corresponding to ± 0.573° at 50 Hz is ±31.8 μs which at 60 Hz is only ±26.5 μs. For 3% TVE criterion, the maximum error in the magnitude is ±0.03 pu with no phase angle error and the maximum phase angle error is ±1.719°. The corresponding timing error at 50 Hz is ±95.5 μs and that at 60 Hz is ±79.6 μs. Therefore, it is essential to minimize both magnitude and phase angle errors to maintain the TVE within the appropriate accuracy limit.

2.4 Functional Model of a PMU

The process of calculation of synchrophasors in a typical commercial PMU is shown in Figure 2.6.

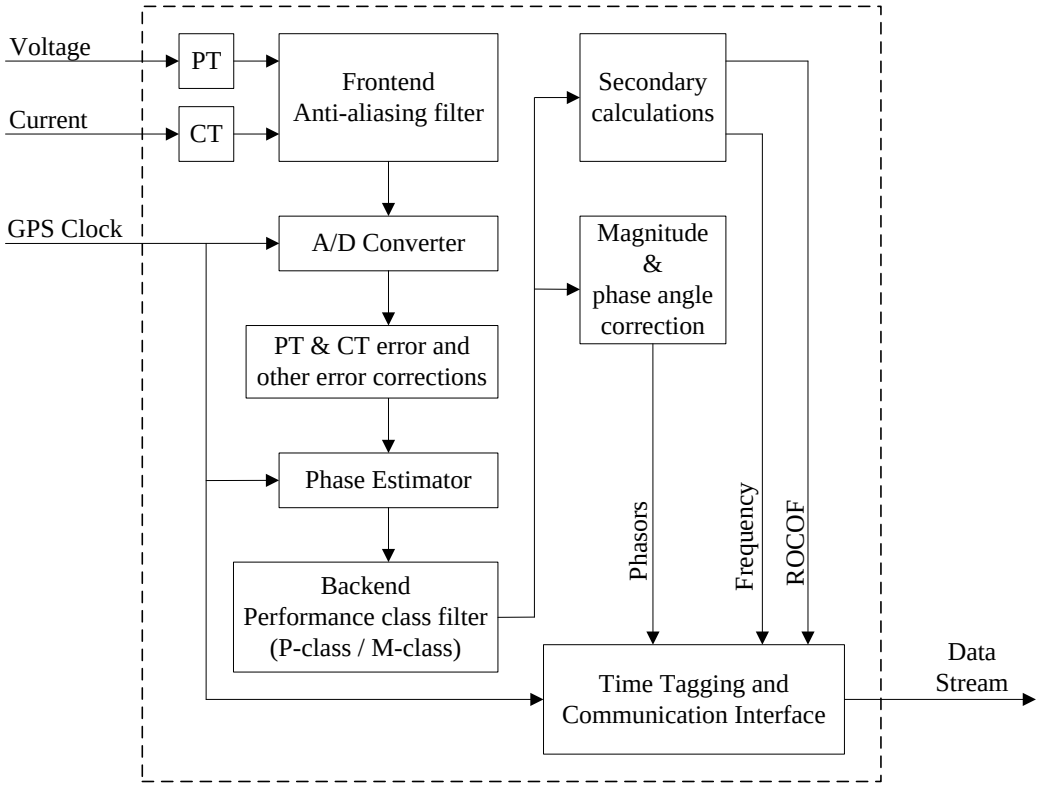

Figure 2.6 The model of a typical commercial PMU with DFT based phasor extraction

The input voltage and current signals are passed through the internal potential and current transformers (PTs & CTs), which step-down signals to a level appropriate for analog to digital converter (ADC). The stepped-down signals are passed through the frontend anti-aliasing filters so that the high frequency interference signals are eliminated before sampling. The ADC has fixed frequency sampling synchronized to a GPS clock. In order to achieve a high level of accuracy, the internal instrument transformer errors are corrected using proprietary algorithms, which are tuned through an appropriate calibration procedure. Discrete Fourier transform (DFT) and least square (LS) estimation based methods are commonly used for phasor estimation.

When the input waveforms are sinusoidal signals with fixed frequency, a PMU produces accurate output measurements. However, actual power system waveforms are far from the ideal, and thus, additional filtering is required. The backend performance class filter shown in Figure 2.6 (either P-class or M-class) is applied to the output of the phasor estimator. The characteristics of the backend filter can significantly vary from manufacturer to manufacturer, and filtering may be combined with the phasor estimation. Among many of the filtering options, finite impulse response (FIR) filters provide adequate performances [5]. Introduction of a digital backend filter, however results in a filter group delay, G_d in seconds, given by

$$G_d = \frac{N}{2 \times N_s \times f_0} \tag{2.3}$$

In (2.3), N denotes the filter order and N_s is the ADC sampling rate specified as the samples/cycle at the base frequency. The filter order *N* is an even number so that the filter coefficients are symmetrical across the filtering window. The backend filter group delay

and other PMU processing delays due to analog input filtering and sampling can be compensated with the aid of proper timestamps, but the latency introduced to the measurements cannot be eliminated.

The derived quantities such as the frequency and the ROCOF are computed using the estimated phase angles. The estimated phasor magnitudes and phase angles roll off when the signal frequency deviates from the nominal power system frequency. The errors in magnitude/phase angle due to deviations in the frequency can be compensated by using an experimentally derived compensation factor, as described in Chapter 3 of this thesis.

2.5 Phasor Estimation Methods

2.5.1 Discrete Fourier Transform (DFT) Method

Consider a data window of $N + 1$ samples and the center of the computational time window as the reference time for the phasor estimation. In DFT phasor estimators, samples are multiplied by nominal power system frequency quadrature oscillators (sine and cosine waves) to calculate real and imaginary parts of the phasor. The estimations of the real and imaginary parts of the phasor of signal x at the n^{th} sampling point are obtained as,

$$X_R(n) = \frac{\sqrt{2}}{N} \sum_{k=-N/2}^{+N/2} x(n+k) \cdot \cos[2\pi f_0 (n+k)\Delta t] \tag{2.4}$$

$$X_I(n) = \frac{\sqrt{2}}{N} \sum_{k=-N/2}^{+N/2} x(n+k) \cdot \sin[2\pi f_0 (n+k)\Delta t] \tag{2.5}$$

where X_R and X_I are the real and imaginary parts of the phasor, Δt is the sampling interval. The performance of DFT method deteriorates at off-nominal frequencies and during power system oscillations. Hence, additional filtering is required in the form of P-class or M-class filters. In practice, filtering is performed simultaneously with DFT calculations by modifying (2.4) and (2.5) as [5]:

$$X_R(n) = \frac{\sqrt{2}}{G} \sum_{k=-N/2}^{+N/2} x(n+k) \cdot \cos[2\pi f_0 (n+k)\Delta t] \cdot W(k) \tag{2.6}$$

$$X_I(n) = \frac{\sqrt{2}}{G} \sum_{k=-N/2}^{+N/2} x(n+k) \cdot \sin[2\pi f_0 (n+k)\Delta t] \cdot W(k) \tag{2.7}$$

where $W(k)$ are the backend performance class filter coefficients, and G is the filter gain given by

$$G = \sum_{k=-N/2}^{+N/2} W(k) \tag{2.8}$$

The DFT method is one of the most extensively used algorithm for phasor estimation due to its harmonic rejection, estimation speed and recursivity property. Therefore, many PMU manufacturers adopt the DFT method to estimate phasors.

2.5.2 Basic Least Squares (LS) Method

The least squares (LS) method minimizes the sum of squares errors between the measurements and the predefined curve, which is assumed to be a time dependent sinusoidal function of known frequency of f_0 (50 or 60 Hz), but of an unknown magnitude and phase angle. Therefore, the waveform can be written as,

$$x(t) = X_m(t)\cos(2\pi f_0 t + \phi) \tag{2.9}$$

This waveform is decomposed to two orthogonal functions with unknown amplitudes $X_R(t)$ and $X_I(t)$ as,

$$x(t) = X_R(t)\cos(2\pi f_0 t) + X_I(t)\sin(2\pi f_0 t) \tag{2.10}$$

Similar to the DFT calculations, computational data window of $N+1$ samples and the center of the computational time window are considered as the reference time for the phasor estimation. For $N+1$observations:

$$\begin{bmatrix} x\left(n-\frac{N}{2}\right) \\ \vdots \\ x(n) \\ \vdots \\ x\left(n+\frac{N}{2}\right) \end{bmatrix} = \begin{bmatrix} \cos\left[2\pi f_0\left(n-\frac{N}{2}\right)\Delta t\right] & \sin\left[2\pi f_0\left(n-\frac{N}{2}\right)\Delta t\right] \\ \vdots & \vdots \\ \cos[2\pi f_0 n\Delta t] & \sin[2\pi f_0 n\Delta t] \\ \vdots & \vdots \\ \cos\left[2\pi f_0\left(n+\frac{N}{2}\right)\Delta t\right] & \sin\left[2\pi f_0\left(n+\frac{N}{2}\right)\Delta t\right] \end{bmatrix} \begin{bmatrix} X_R(n) \\ X_I(n) \end{bmatrix} + \begin{bmatrix} \varepsilon\left(n-\frac{N}{2}\right) \\ \vdots \\ \varepsilon(n) \\ \vdots \\ \varepsilon\left(n+\frac{N}{2}\right) \end{bmatrix} \tag{2.11}$$

where X_R and X_I are the real and imaginary parts of the fundamental phasor, Δt is the sampling interval, and $\varepsilon(n)$ is the estimation error or mismatch corresponding to n^{th} sample. In matrix notation, (2.11) can be written as,

$$[x]_{\{(N+1)\times 1\}} = [A]_{\{(N+1)\times 2\}}[X]_{\{2\times 1\}} + [\varepsilon]_{\{(N+1)\times 1\}} \tag{2.12}$$

Define a function for sum of squares of error terms,

$$J(X) = [\varepsilon]^T[\varepsilon] = ([x] - [A][X])^{\mathrm{T}}([x] - [A][X]) \tag{2.13}$$

The least squares solution for this system, which minimizes $J(X)$ can be written as,

$$[X]_{(2\times1)} = ([A]^{\mathrm{T}}[A])^{-1}[A]^{\mathrm{T}}[x] \tag{2.14}$$

The least square solution (2.14) exists provided that the column vectors of $[A]$ are linearly independent. Furthermore, it is assumed that the frequency is a known quantity. However, in actual power systems, frequency is no longer a known quantity even during the steady-state. The problem can be formulated to estimate the frequency as well, but the resulting nonlinear problem requires an iterative solution approach, resulting in a computationally expensive algorithm.

Advantage of the LS method over the DFT based method is that the sampling rate does not need to be an integer number of samples per cycle. However, the sampling rate needs to be proportionally adjusted when the power system frequency changes, to minimize the magnitude and angle errors introduced by frequency change.

2.5.3 Iterative Least Squares Methods

In [43], power system voltage and current waveforms are modelled as combination of fundamental, harmonics and decaying dc offset as,

$$x(t) = a_1\cos(2\pi ft + \phi_1) + a_2\cos(4\pi ft + \phi_2) + \cdots + a_m\cos(2\pi mft + \phi_m) + \mathrm{C}\,\mathrm{e}^{-\frac{t}{\tau}} \tag{2.15}$$

where a_1, a_2, …, a_m are model coefficients, f is the fundamental frequency, m is the order of harmonics, τ is the time constant of decaying dc offset. Considering computational data window of $N+1$ ($\geq 2m+2$) samples, it can be written as

$$[A]=\begin{bmatrix} \cos\left[2\pi f\left(n-\frac{N}{2}\right)\Delta t\right] & -\sin\left[2\pi f\left(n-\frac{N}{2}\right)\Delta t\right] & .. & \cos\left[2\pi fm\left(n-\frac{N}{2}\right)\Delta t\right] & -\sin\left[2\pi fm\left(n-\frac{N}{2}\right)\Delta t\right] & 1 & \left(n-\frac{N}{2}\right) \\ : & : & : & : & : & : & : \\ \cos[2\pi fn\Delta t] & -\sin\left[2\pi f\left(n-\frac{N}{2}\right)\Delta t\right] & .. & \cos[2\pi fmn\Delta t] & -\sin[2\pi fmn\Delta t] & 1 & n \\ : & : & : & : & : & : & : \\ \cos\left[2\pi f\left(n+\frac{N}{2}\right)\Delta t\right] & -\sin\left[2\pi f\left(n-\frac{N}{2}\right)\Delta t\right] & .. & \cos\left[2\pi fm\left(n+\frac{N}{2}\right)\Delta t\right] & -\sin\left[2\pi fm\left(n+\frac{N}{2}\right)\Delta t\right] & 1 & \left(n+\frac{N}{2}\right) \end{bmatrix} \tag{2.16}$$

$$\begin{bmatrix} x\left(n-\frac{N}{2}\right) \\ : \\ x(n) \\ : \\ x\left(n+\frac{N}{2}\right) \end{bmatrix} = [A]\begin{bmatrix} a_1\cos\phi_1 \\ a_1\sin\phi_1 \\ : \\ a_m\cos\phi_m \\ a_m\sin\phi_m \\ \mathrm{C} \\ -\frac{\mathrm{C}\Delta t}{\tau} \end{bmatrix} + \begin{bmatrix} \varepsilon\left(n-\frac{N}{2}\right) \\ : \\ \varepsilon(n) \\ : \\ \varepsilon\left(n+\frac{N}{2}\right) \end{bmatrix} \tag{2.17}$$

In matrix notation, (2.17) can be written as,

$$[x]_{\{(N+1)\times 1\}} = [A]_{\{(N+1)\times(2m+2)\}}[X]_{\{(2m+2)\times 1\}} + [\varepsilon]_{\{(N+1)\times 1\}} \tag{2.18}$$

The least squares solution for this system can be written as,

$$[X]_{\{(2m+2)\times 1\}} = ([A]^{\mathrm{T}}[A])^{-1}[A]^{\mathrm{T}}[x] \tag{2.19}$$

where $a_1\cos\phi_1$ and $a_1\sin\phi_1$ are the real and imaginary parts of the fundamental phasor, Δt is the sampling interval. It is noted that matrix [A] depends on the actual frequency of the signal, which is unknown. Therefore, an iterative approach is used to estimate the

actual frequency. The iterative process is started with an assumed frequency, which is usually frequency of the previous time instant. The phasors are estimated from the assumed frequency and frequency is then updated from the estimated fundamental phasor. The iteration process is terminated when the frequency update reaches within a specified tolerance.

2.6 Frequency Estimation and Measurement Reporting

2.6.1 Frequency Estimation

Once the real and imaginary components of a phasor are determined, the phase angle can be obtained as,

$$\theta(n) = \tan^{-1}\left(\frac{X_I(n)}{X_R(n)}\right) \tag{2.20}$$

As the phase angles at the previous sampling points are known the frequency deviation is estimated as [5],

$$\Delta f(n) = \frac{6[\theta(n) - \theta(n-1)] + 3[\theta(n-1) - \theta(n-2)] + [\theta(n-2) - \theta(n-3)]}{20\pi \times \Delta t} \tag{2.21}$$

where $\theta(n)$ is the phase angle of the n^{th} estimate, $\theta(n-1)$ is the phase angle of the previous estimate and so on.

2.6.2 Measurement Reporting

A new phasor is calculated at every sampling point, but all of them are not reported. The number of data points (samples) between two consecutive reportings, N_d, is dependent on the sampling rate N_s, (samples/cycle or spc), the reporting rate, F_s, (frames/s or fps) and the nominal signal frequency, f_0.

$$N_d = \frac{f_0 \times N_s}{F_s} \tag{2.22}$$

Therefore, the r^{th} phasor reported by the PMU is,

$$X_e(r) = X_e(pN_d) \qquad \text{where} \quad p = 1, 2, 3, \ldots \tag{2.23}$$

Investigations showed that if the frequency is reported as the nominal frequency plus the frequency deviation calculated using (2.21) at the reporting time, i.e. $[f_0 + \Delta f(rN_d)]$, it is difficult to achieve the frequency error (FE) limits. However, this can be rectified if the N_d frequency estimates made between the two consecutive reportings is averaged. Thus, it is proposed to report the frequency as

$$f(r) = f_0 + \frac{1}{N_d} \times \sum_{l=(p-1)N_d}^{pN_d} \Delta f(l) \tag{2.24}$$

The substitution of Δf given in (2.21) into (2.24) results in cancellation of some of the middle phasor terms in the summation in (2.24). The frequency can be estimated using only three phasor estimations near the current timestamp and three phasors near the previous timestamp as,

$$f(r) = f_0 + \frac{[6\theta r N_d + 3\theta(rN_d - 1) + \theta(rN_d - 2)]}{20\pi \times N_d \times \Delta t} - \frac{[6\theta((r-1)N_d - 1) + 3\theta((r-1)N_d - 2) + \theta((r-1)N_d - 3)]}{20\pi \times N_d \times \Delta t} \quad (2.25)$$

The IEEE synchrophasor standard [5] defines measurement reporting rates as submultiples of the nominal system frequency as listed in Table 2.1.

Table 2.1 PMU reporting rates [5]

System frequency (Hz)	50			60					
Reporting rates (fps)	10	25	50	10	12	15	20	30	60

2.7 Backend Performance Class Filters

This section briefly describes the performance class filters introduced in IEEE standard C37.118.1 [5] and its amendment [41] (i.e. IEEE Standard C37.118.1a). The backend performance class filters are finite impulse response (FIR) filters, which are better than the infinite impulse response (IIR) filters due to their linear-phase filtering. Thus, the FIR filters avoid phase distortions in phasor measurements. However, the FIR filters are relatively slower than their counterpart, the IIR filters.

2.7.1 Reference P-class Filter Model

The reference P-class filter model is a fixed length, triangular weighted, symmetric filter with length of 2 cycles of the nominal system frequency. Coefficients of the P-class reference filter as specified in [5] are calculated from

$$W(k) = 1 - \frac{2}{N+2}|k| \qquad \text{where } k = -\frac{N}{2} : +\frac{N}{2} \text{ (integers)} \tag{2.26}$$

The filter order N is related to the sampling rate N_s as

$$N = 2(N_s - 1) \tag{2.27}$$

Table 2.2 lists the filter orders and the corresponding group delays in milliseconds for P-class filters at different sampling rates. The filter orders are even numbers in order to allow the model uses an odd number of samples. This simplifies timestamp generation and phase compensation as a sample timestamp at the center of the window without adjustment.

Table 2.2 P-class filter parameters

Sampling rate (samples/cycle)	8	15*	16	32	64	96	128	256	384
Filter order (Group delay in ms)	14 (14.6)	28 (15.6)	30 (15.6)	62 (16.1)	126 (16.4)	190 (16.5)	254 (16.5)	510 (16.6)	766 (16.6)

* Sampling rate used in the P-class filter example provided in the standard [5]

Coefficients of the P-class filter calculated at 96 samples/cycle are shown in Figure 2.7 as an example. The corresponding frequency response characteristic is illustrated in Figure 2.8.

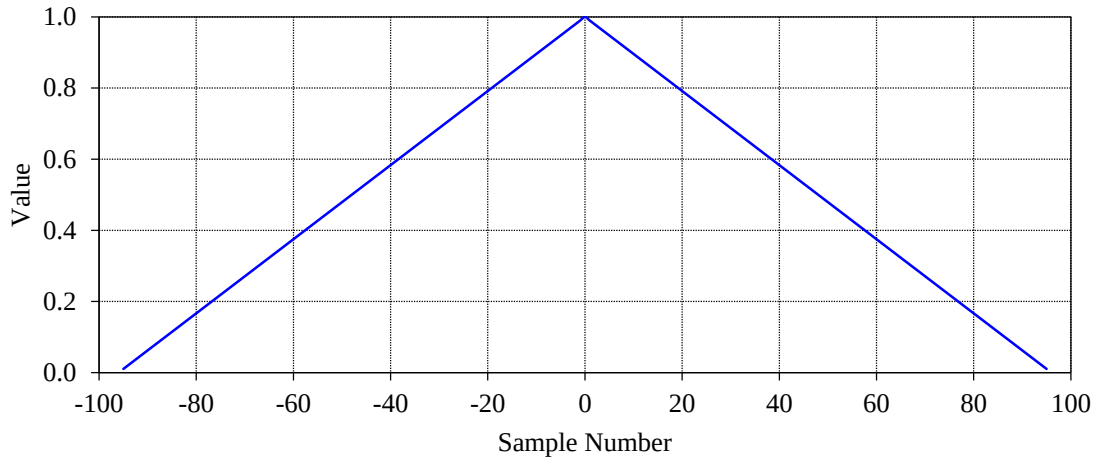

Figure 2.7 P-class filter coefficient example

(Filter order = 190)

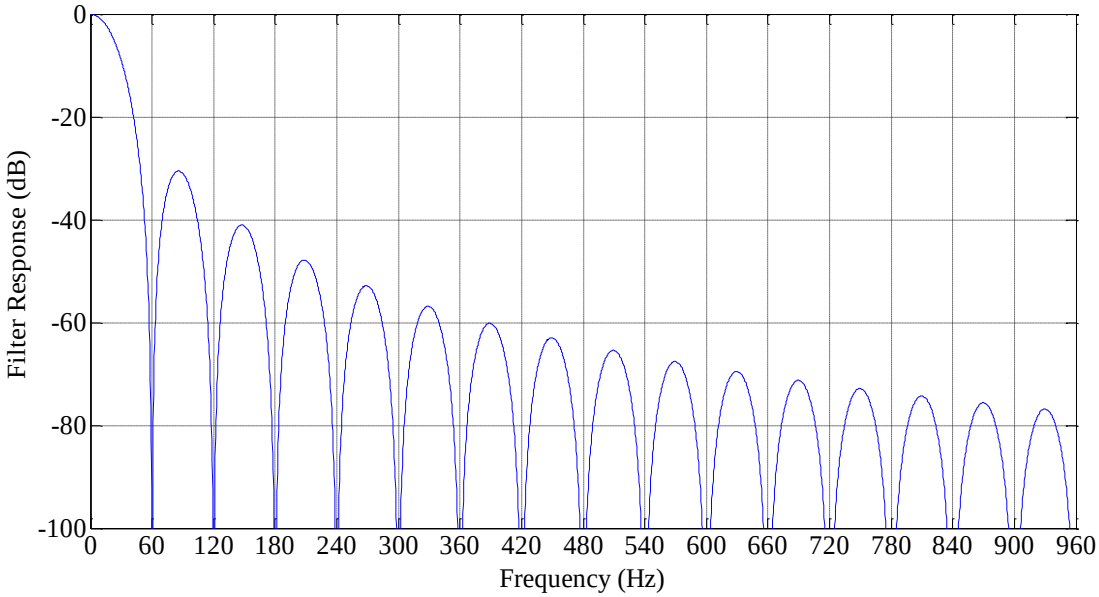

Figure 2.8 P-class filter response example in frequency domain

(Filter order = 190)

The P-class filter model performs properly at the nominal frequency where the period of estimation exactly matches the actual period of the signal. The harmonic rejection is also excellent. Under the off-nominal frequency, phase angle estimation is still accurate as the signal is centered on the estimate. However, magnitude estimates are rolled-off and

needed magnitude compensation. The magnitude of the phasor is corrected from a compensation factor, C_p given in (2.28) to compensate for the frequency deviation [5] and the magnitude of the compensated phasor is given in (2.29):

$$C_p(n) = \frac{1}{\sin\left[\pi \frac{\left(f_0 + 1.625\Delta f(n)\right)}{2f_0}\right]} \tag{2.28}$$

$$X_e(n) = C_P\sqrt{X_R(n)^2 + X_I(n)^2} \tag{2.29}$$

2.7.2 Reference M-class Filter Model

Application of M-class filter is similar to the P-class filter, however, the M-class filter has a requirement to attenuate by at least 20 dB, the signals that are above the Nyquist frequency for the given reporting rate. The standard [5] defines pass and stop bands with a frequency response mask as illustrated in Figure 2.9.

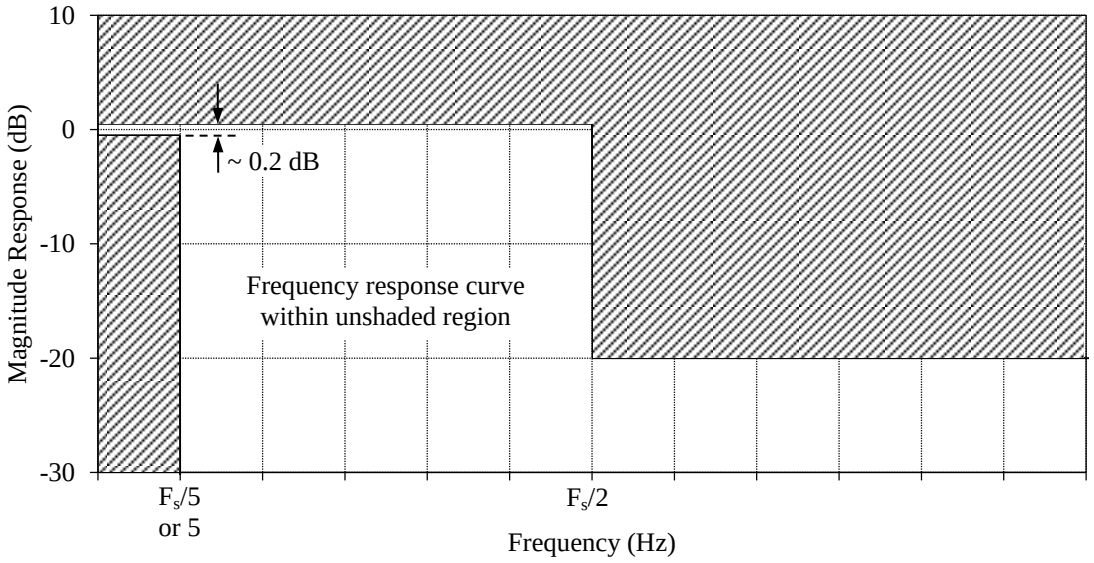

Figure 2.9 Frequency response mask specification for M-class filter [5]

The filter response curve should remain inside the unshaded region at all frequencies. The M-class filter requires more stringent filtering to meet the higher accuracy level, but it will result in longer reporting delays compared to the P-class filter.

The coefficients of the reference M-class filter given in [5] are given by

$$W(k) = sinc\left(\frac{2\pi \times 2F_{fr} \times k}{f_0 \times N_s}\right) \cdot h(k) \tag{2.30}$$

where $k = -N/2 : +N/2$ (integer values only, values of N as in Table 2.3). $F_{fr}$is the filter reference frequency from [5], $h(k)$ is Hamming function, and $W(0) = 1$. The filter order and the number of filter coefficients depend upon the sampling rate as well as the reporting rate. The filter order is adjusted to meet frequency response requirement. Table 2.3 provides the M-class filter order for different sampling and reporting rates; the values within parentheses indicate filter group delay in milliseconds. Note that the filter order increases with the sampling rate, and decreases with the reporting rate.

Table 2.3 M-class filter parameters

Sampling / Reporting	8 spc	16 spc	32 spc	64 spc	96 spc	128 spc	256 spc	384 spc
10 fps	250 (260.4)	500 (260.4)	1000 (260.4)	2000 (260.4)	3000 (260.4)	4000 (260.4)	8000 (260.4)	12000 (260.4)
12 fps	208 (216.7)	416 (216.7)	834 (217.2)	1666 (216.9)	2500 (217.0)	3334 (217.1)	6666 (217.0)	10000 (217.0)
15 fps	166 (172.9)	334 (174.0)	666 (173.4)	1334 (173.7)	2000 (173.6)	2666 (173.6)	5334 (173.6)	8000 (173.6)
20 fps	126 (131.2)	250 (130.2)	500 (130.2)	1000 (130.2)	1500 (130.2)	2000 (130.2)	4000 (130.2)	6000 (130.2)
30 fps	86 (89.6)	170 (88.5)	342 (89.1)	684 (89.1)	1026 (89.1)	1368 (89.1)	2736 (89.1)	4102 (89.0)
60 fps	46 (47.9)	94 (49.0)	186 (48.4)	372 (48.4)	558 (48.4)	744 (48.4)	1488 (48.4)	2232 (48.4)

An example of the reference M-class filter coefficients calculated for a reporting rate of 60 fps at a sampling rate of 96 samples/cycle (filter order of 558) is shown in Figure 2.10. The corresponding frequency response characteristic is illustrated in Figure 2.11 where the attenuation level beyond the Nyquist frequency of 30 Hz is greater than 20 dB.

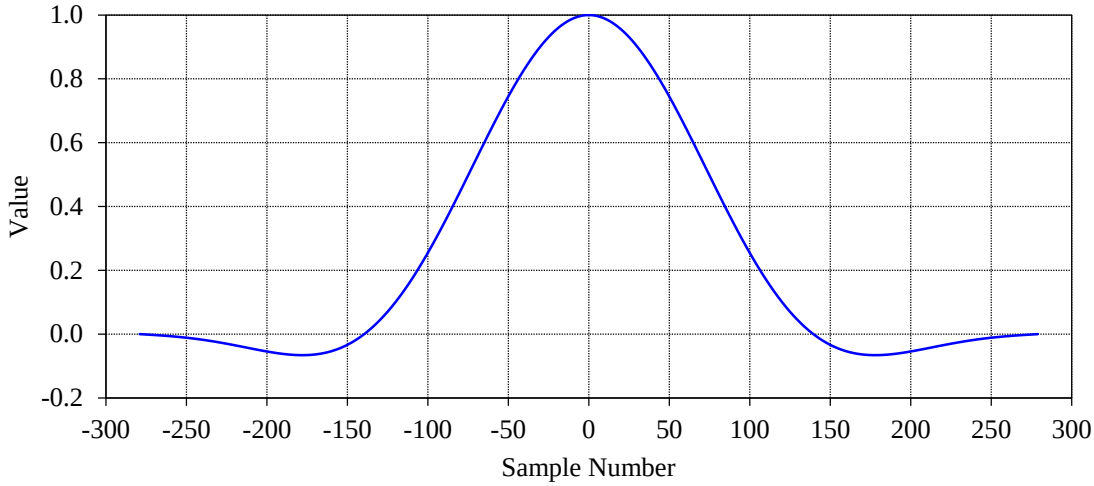

Figure 2.10 M-class filter coefficient example

(Filter order = 558 at sampling rate of 96 samples/cycle and reporting rate of 60 fps)

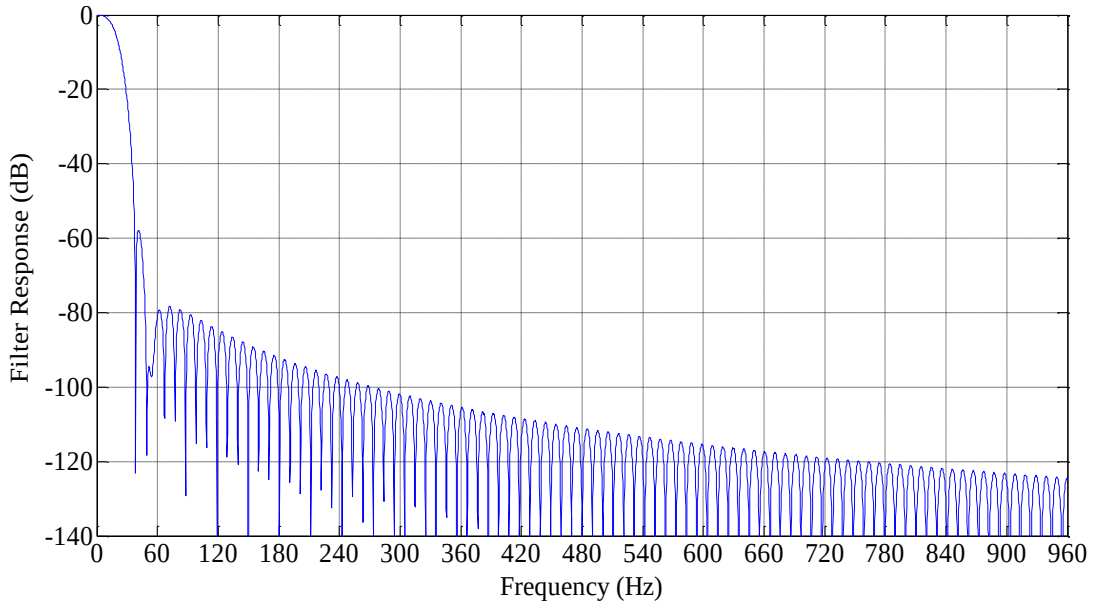

Figure 2.11 M-class filter magnitude response example in frequency domain

(Filter order = 558 at sampling rate of 96 samples/cycle and reporting rate of 60 fps)

The standard [5] does not propose a compensation factor for the reference M-class and it is found that with the uncompensated reference M-class filter given in [5], TVE exceeds 1% limit when the signal frequencies are close to 55 Hz or 65 Hz. In order to correct this, applying a compensation factor as in the case of the reference P-class is proposed in this thesis and chapter 3 will provide more details.

The issues of the reference M-class filter model are also addressed in the amendment to IEEE C37.118.1-2011 (i.e. IEEE Standard C37.118.1a [41]). It introduces a new frequency response mask characteristic as shown in Figure 2.12.

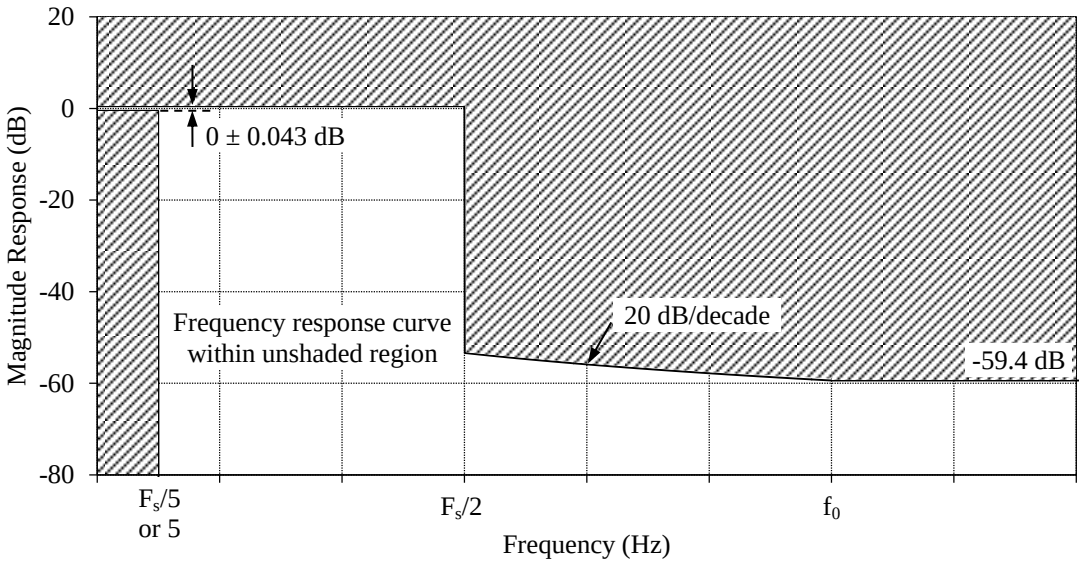

Figure 2.12 Revised frequency response mask specification for M-class filter [41]

The reference M-class filter coefficient example for the revised frequency response mask specification is shown in Figure 2.13 where the filter order is 984 at the sampling rate of 96 samples/cycle. The corresponding frequency response characteristic is illustrated in Figure 2.14 where the attenuation level beyond the Nyquist frequency of 30 Hz is greater than 50 dB, which is higher than the requirement of the original IEEE standard [5].

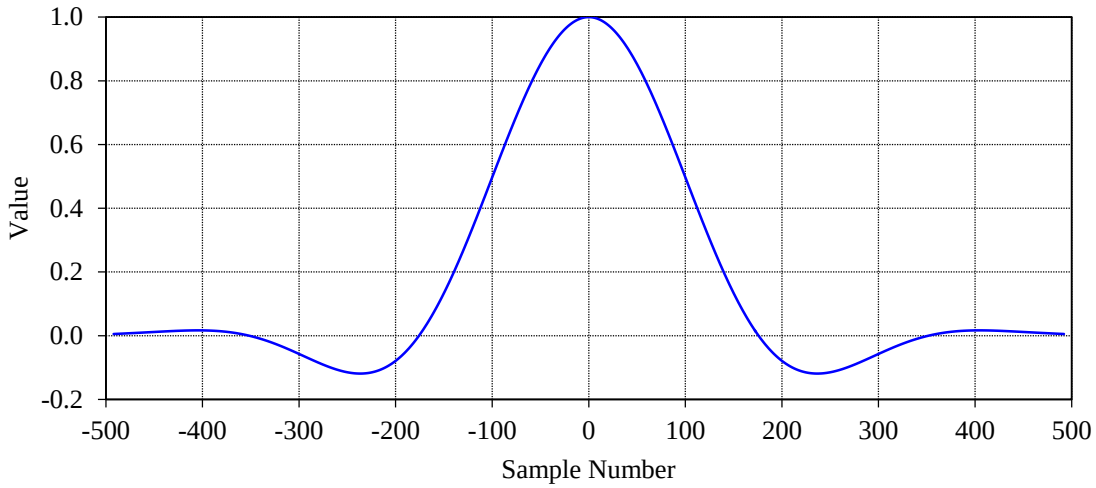

Figure 2.13 M-class filter coefficient example for revised frequency response mask
(Filter order = 984 at sampling rate of 96 samples/cycle and reporting rate of 60 fps)

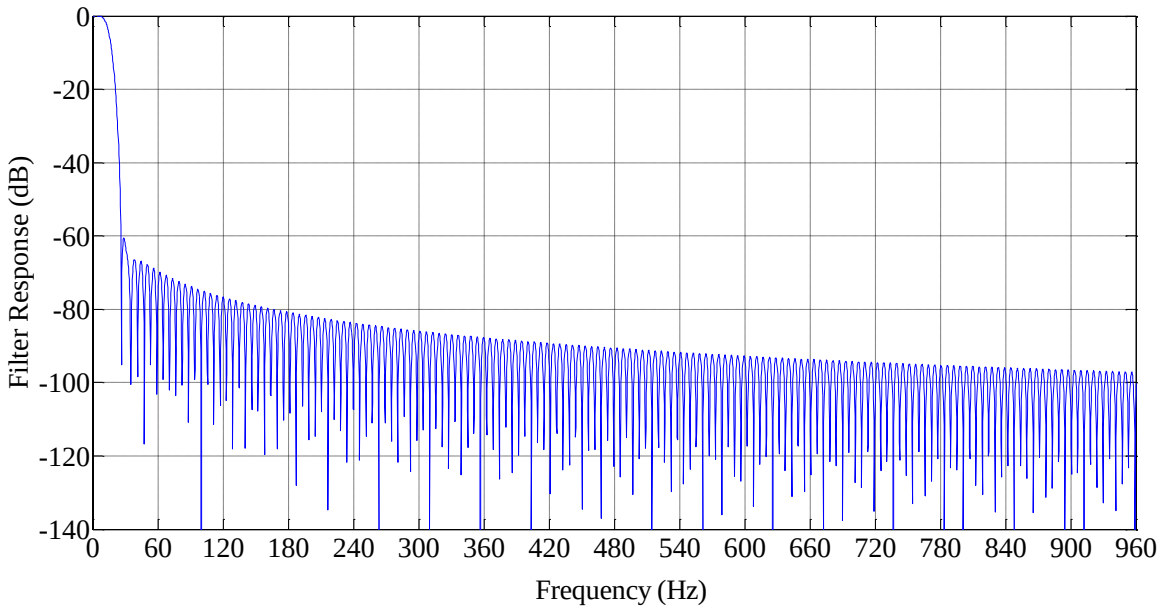

Figure 2.14 M-class filter magnitude response example for revised frequency response mask
(Filter order = 984 at sampling rate of 96 samples/cycle and reporting rate of 60 fps)

2.8 PMU Testing

Applications that rely on synchrophasor measurements to observe true power system behavior demand high accuracy and consistency under both steady-state and dynamic conditions. It is also important to establish the interoperability between PMUs from different vendors, who use different proprietary synchrophasor estimation algorithms [44]. Thus, PMU performance evaluation plays a vital role.

Even though the IEEE Standard C37.118.1-2011 [5] specifies both the steady-state and the dynamic performance requirements of synchrophasor measurements, practical implementation of PMUs compliant to the standard and conformity testing are challenging tasks. Many PMU testing efforts [4], [6], [9] consider the steady-state performance evaluation but the dynamic performance assessment and related practical issues are often neglected. Simple and repeatable PMU evaluation procedures and test setups are described in [4], [6], [9]. Generally, a known input signal is fed to the PMU with the help of a signal playback unit synchronized with the GPS clock and the PMU response is compared against the theoretical phasor.

In [45]-[49], various practical issues of PMU measurements in test environments as well as field operating conditions are assessed. Reference [45] investigates the practical concerns, such as magnitude scaling, phase-angle offsets, rise time, measurement delays, and windowing time offset in different PMUs. The responses of PMUs under transient conditions, such as oscillations, sudden system imbalances, and various switching events have been evaluated in [46]-[48]. The test results from various PMU manufacturers are presented and compared in [49], which shares experiences of testing and calibration of

PMUs in the U.S.A. and Europe. In [50], 7 commercial and 3 prototype PMUs from different vendors were assessed and test results showed that all 7 commercial PMUs fail to comply the latest synchrophasor standard [5] and its amendment [41] while 3 prototype PMUs satisfied the specifications.

2.9 Improving PMU Performance

Numerous efforts have been made to improve the accuracy of dynamic phasor estimation and the performance of PMU filtering algorithms [51]-[55]. An improved dynamic phasor estimation algorithm is proposed in [51], but the algorithm has been tested only in a simulation environment. In [52], a phase-locked loop (PLL)-based technique is applied to estimate dynamic phasors. This approach helps to prevent errors due to power system unbalances, off-nominal frequency operation and windowing issues of DFT method. It is proposed in [53] to use subspace-based techniques to estimate dynamic phasors under power system oscillations. A framework for designing PMU filtering algorithm is discussed in [54] with both simulation and actual test results. A real-time digital filter is applied in [55] to enhance PMU performances by removing the unwanted DC offset due to sudden current changes and inter-harmonics. Although these algorithms make various improvements, implementing practical PMUs fully conforming to all requirements specified in IEEE Standard C37.118.1-2011 [5] is still a challenging task [50].

2.10 Concluding Remarks

This chapter presented a brief review of the synchrophasor measurement technology. The backend performance class filters provided in the latest synchrophasor standard [5] were discussed in details. The standard phasor estimation techniques (DFT and LS methods) and a recently published phasor estimation technique [43] were presented. Recently published research related to evaluating and enhancing PMU dynamic performances was also reviewed. Many of these efforts make numerous developments; however, none of them have proven the overall performances of PMUs under dynamic conditions until the recent report published by the National Institute of Standards and Technology (NIST) in early 2016 [50]. Note that this research has been carried out prior to publish the NIST report [50].

Chapter 3

Testing and Performance Enhancement of a Phasor Measurement Unit

3.1 Introduction

This chapter examines the implementation of two performance class filters required to meet the steady-state and dynamic performances in a PMU device and associated practical issues. Furthermore, it describes a PMU test setup and the sources of errors in a PMU test environment. The investigations presented in this chapter critically examine the adequacy of reference P-class and M-class filters, and the practicality of various accuracy requirements imposed by the synchrophasor standard IEEE C37.118.1-2011 [5].

3.2 Proposed Improvements to M-Class Filter Model

3.2.1 Compensation Factor to the Reference M-Class Filter

The current IEEE synchrophasor Standard C37.118.1-2011 [5] demands TVE to be within 1% for steady-state measurements and within 3% under most dynamic test conditions. The detailed TVE requirements specified in the standard [5] are later given in Table 3.1 and Table 3.2 with the test results. As discussed in section 2.3.1, for the 1% TVE criterion, the maximum allowable magnitude error is also 1% when the error in phase angle is zero, and the maximum allowable phase angle error is 0.573^{o} with zero magnitude error. The standard [5] does not propose a compensation factor for the M-class and it is found that with the uncompensated M-class reference filter given in [5], the magnitude error exceeds the 1% limit when the signal frequencies are close to 55 Hz or 65 Hz. This results in a violation of the 1% TVE limit even though the phase angle error limit of 0.573^{o} is satisfied. It is demonstrated in Figure 3.1 by the red dashed curves which were obtained through theoretical calculations based on the PMU model described in section 2.4 (refer Figure 2.6).

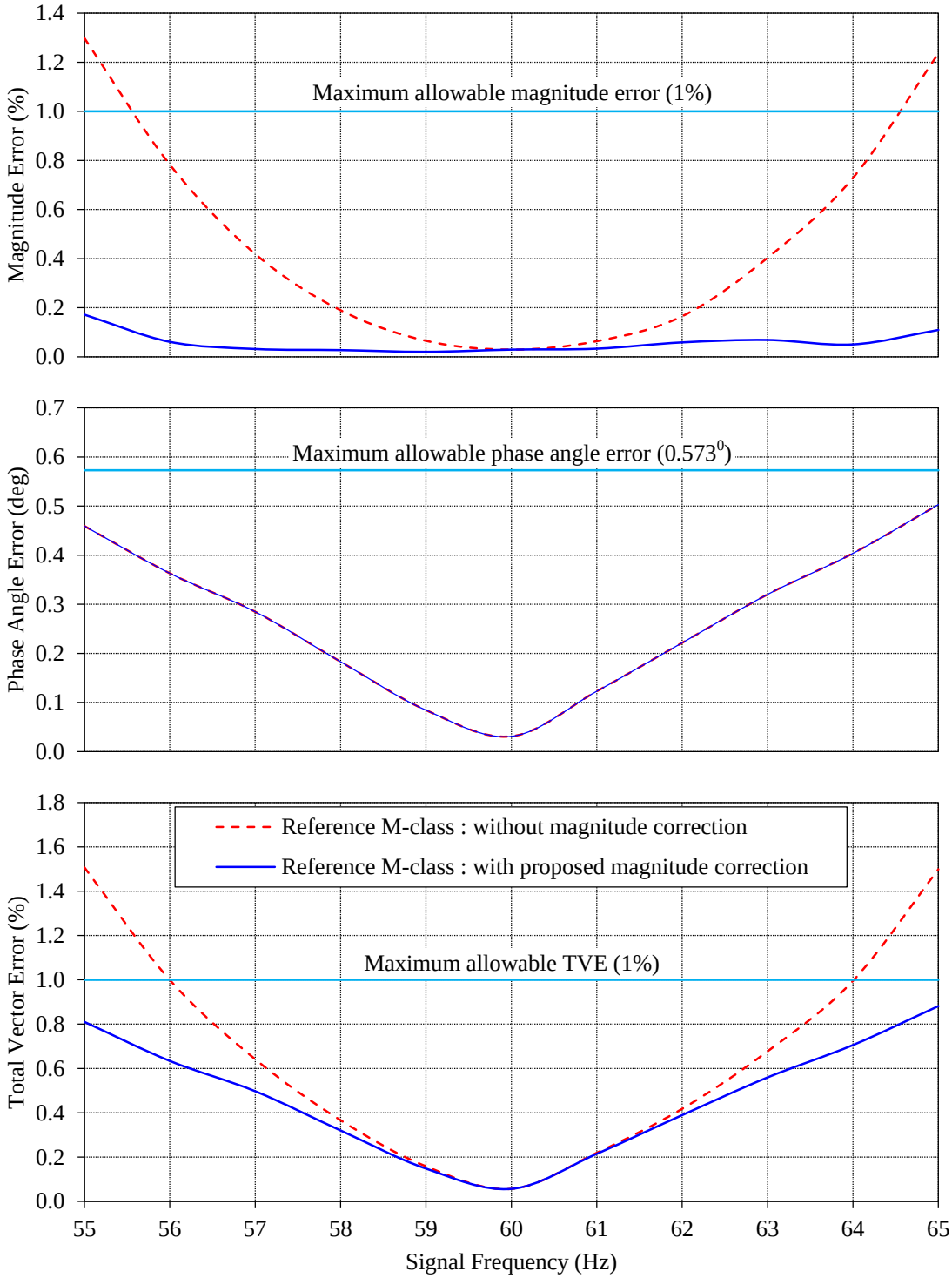

Figure 3.1 Comparison of magnitude error, phase angle error and TVE variations for reference M-class filter under signal frequency deviations with and without the compensation factor

Similar investigation showed that the PMU with reference M-Class filter fails the linear frequency ramp test [5] as well. In order to correct this, it is proposed to apply a compensation factor as in the case of P-class. The proposed correction factor, C_M is,

$$C_M(n) = \frac{1}{\sin\left[\pi \frac{\left(f_0 + 1.15\Delta f(n)\right)}{2f_0}\right]} \tag{3.1}$$

where f_0 is the nominal frequency and $\Delta f(n))$ is an offset from the nominal frequency. The factor 1.15 in (3.1) is proposed by the author based on the experiments. The blue solid curves in Figure 3.1 demonstrate that a PMU can achieve the accuracy specified in [5] for the frequency deviation test with the proposed compensation factor. The magnitude error is less than 0.2 % with the proposed compensation factor. The curves for phase angle error overlap as the proposed compensation factor is merely applied to correct the magnitude. Further testing verified that TVE requirements under all other tests [5] can also be met with the proposed compensation factor with any sampling and reporting rate combination.

3.2.2 Modified M-class Filter Model

According to Table 2.3, the order of the reference M-class filter given in the IEEE C37.118.1-2011[5] standard could be very large depending on the reporting and sampling rates. For example, at a reporting rate of 60 fps, it requires a data window of about 5.8 cycles and results in a filter group delay of about 2.9 cycles. The filters have a large number of coefficients and the implementation demands significant memory and computing resources from the real-time computing system in the PMU device. As a solution to

this drawback, a modified filter algorithm is proposed. The proposed approach approximately halves the filter lengths (filter order = $N/2$ approximated to the nearest even integer) given in Table 2.3. The filter coefficients for a particular reporting rate are then calculated by adjusting the filter reference frequency, F_{fr}, in (2.30) so that the filter satisfies the frequency response mask provided in Annex-C of the standard [5]. Coefficients of the modified M-class filter designed for a reporting rate of 60 fps at a sampling rate of 8 samples/cycle are shown in Figure 3.2 as an example. In the example, the filter order is 26 and the coefficients are calculated with $F_{fr} = 5.61$ Hz.

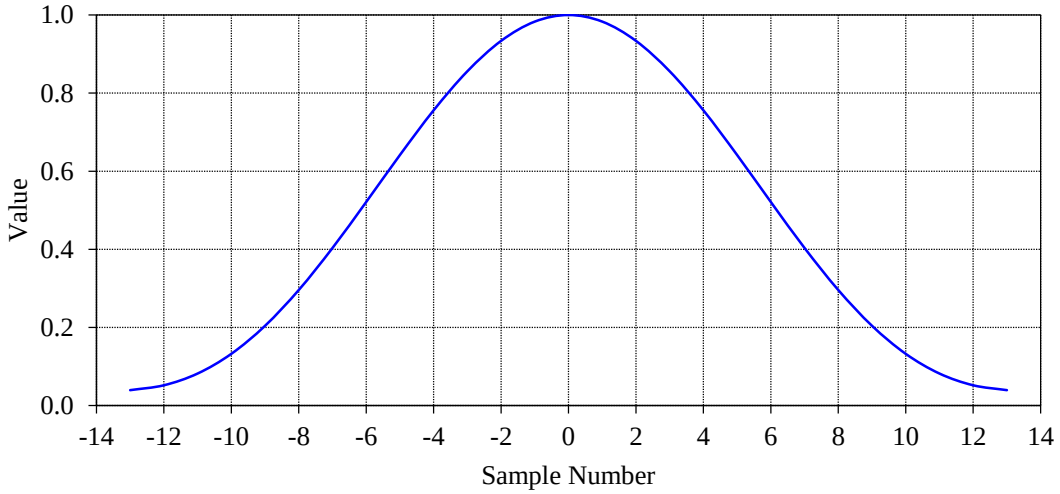

Figure 3.2 Modified M-class filter coefficient example
(Filter order = 26 at sampling rate of 8 samples/cycle and reporting rate of 60 fps)

The frequency response of the example modified M-class filter (both magnitude and phase angle) is shown in Figure 3.3. The modified M-class filter attenuates the signal frequencies that are above the Nyquist frequency by at least 20 dB for the given reporting rate and satisfies the filter frequency response mask specification of [5] as illustrated in Figure 3.3. The filter response remains outside the shaded areas at all frequencies. It is

not possible to satisfy the filter mask specification, if the M-class filter order is further reduced while keeping the basic filter structure as in (2.30).

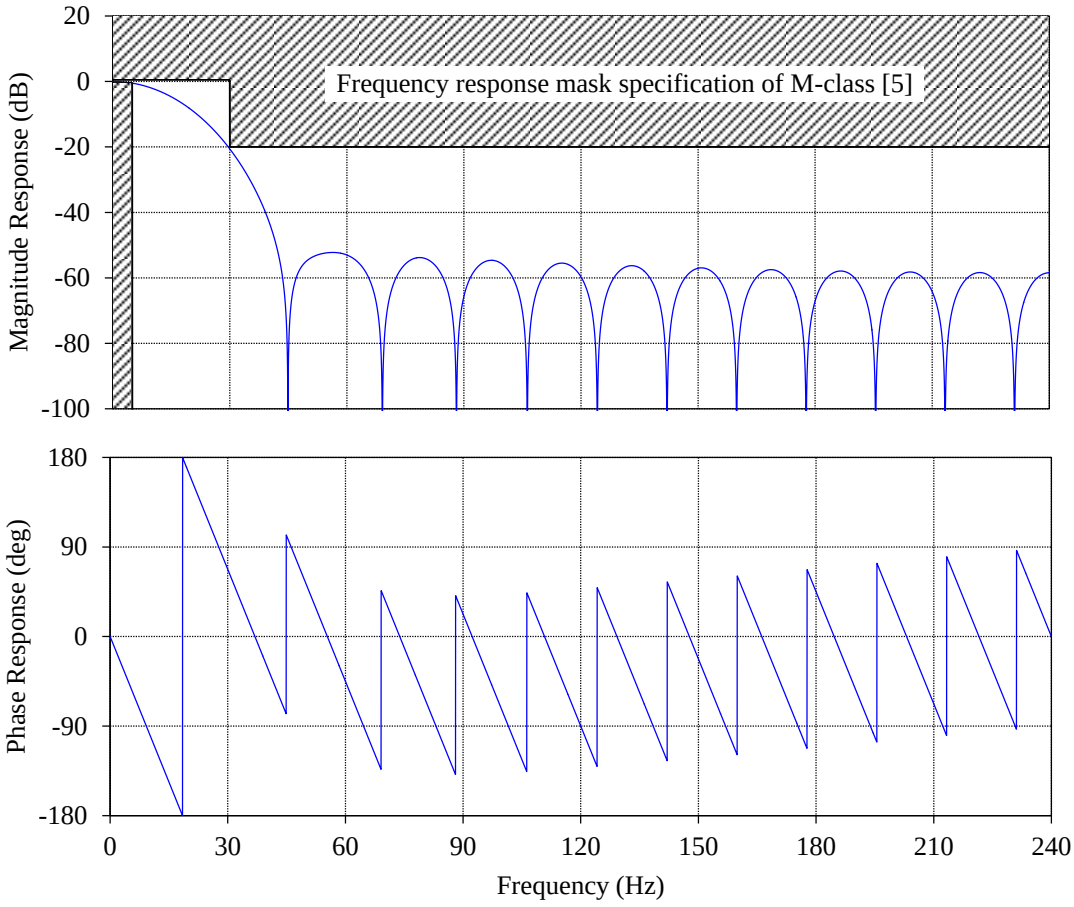

Figure 3.3 Modified M-class filter response with frequency
(Filter order = 26 at a sampling rate of 8 samples/cycle and a reporting rate of 60 fps)

The modified M-class filter will introduce some error in the measurements when the frequency deviates from the nominal value. As illustrated by the theoretical calculations presented in Figure 3.4, with the modified filter without a compensation factor, TVE exceeds 1% limit when the signal frequencies deviates more than 3.5 Hz. However, these errors can be rectified by introducing a new complex compensation factor that correct both the magnitude and phase angle for the shortened M-class filter:

$$C_{M\_New}(n) = \frac{1}{\sin\left[\pi \frac{\left(f_0 - 0.7\Delta f(n)\right)}{2f_0}\right]} \cdot \exp\left(-j\frac{\pi\Delta f(n)}{1800}\right) \tag{3.2}$$

The empirical factor –0.7 and the exponent in (3.2) were determined after numerous experiments. The phase angle correction in (3.2) was proposed based on the observation that the phase angle error increases with the frequency deviation: every 1 Hz frequency deviation results in an approximately 0.1^{o} phase angle error. With this complex compensation factor and the modified M-class filter, the PMU can meet all requirements specified in [5]. Instead of using the proposed complex correction factor, the phase angle error can also be corrected by adjusting the data window used to calculate phasors for a particular timestamp.

The blue solid curve in Figure 3.4 shows that a PMU can easily achieve the accuracy requirement specified in [5] with the modified filter, which has an approximately half the length of the original M-class reference filter, and the new compensation factor. The modified M-class filter requires only about 3 cycles with the filter group delay (latency due to filter) of about 1.5 cycles to determine phasors at a reporting rate of 60 fps but it achieves a better accuracy level than the original M-class reference filter proposed in [5], which requires 5.8 cycles long data window resulting in a group delay of 2.9 cycles. It will be shown in the following sections that a PMU with the proposed modified M-class filter and the complex correction factor can meet specified error limits during all other performance tests specified in [5].

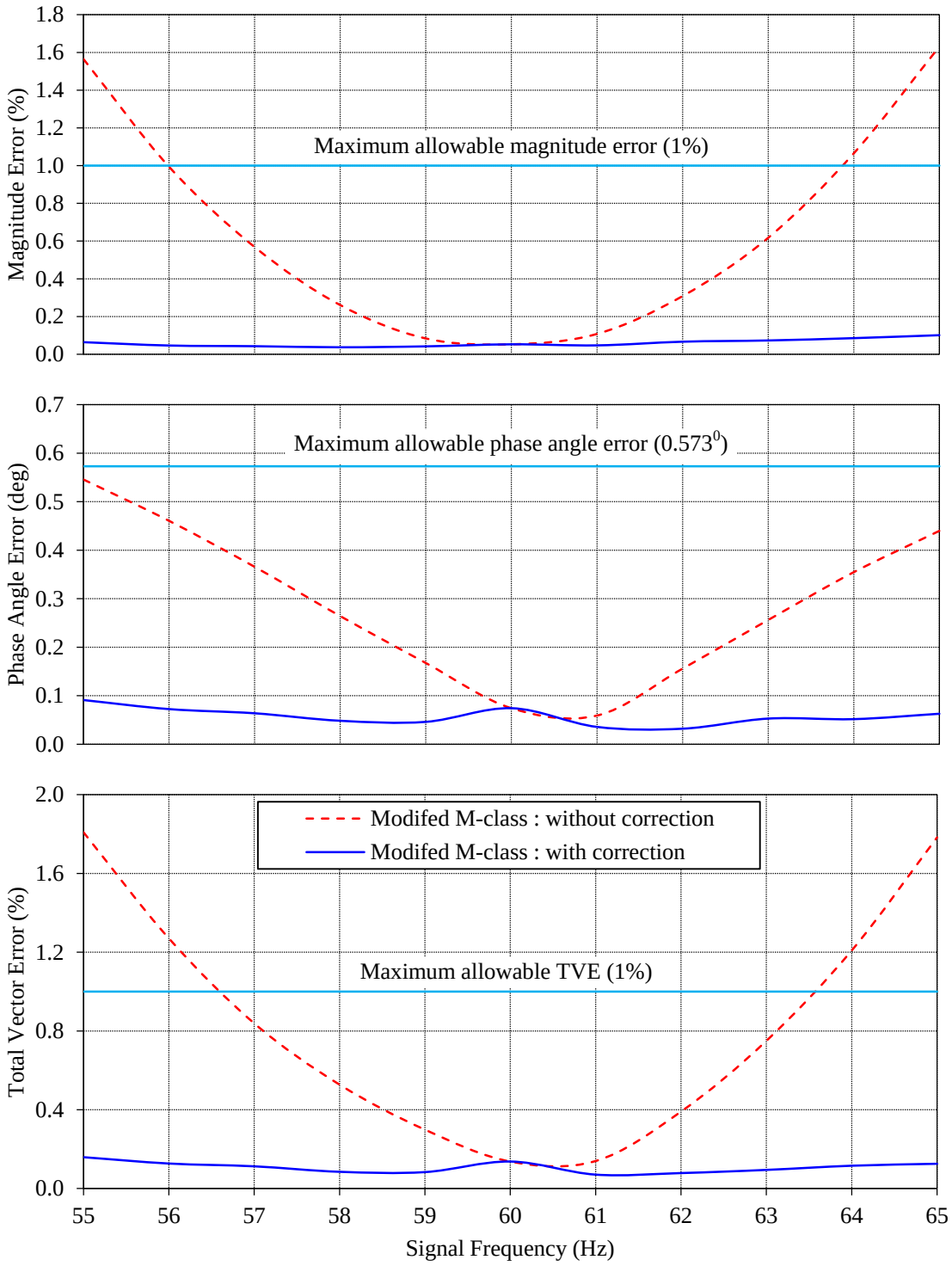

Figure 3.4 Comparison of magnitude error, phase angle error and TVE variations for the modified M-class filter under signal frequency deviations

3.3 PMU Test Setup

The PMU test setup was developed around a real-time waveform playback device (Doble^{TM} F6150) that supplies analog voltage and current signals at their appropriate levels (69 V nominal voltage and 5 A nominal current) using the recorded COMTRADE (common format for transient data exchange [56]) files. Playback signals can be precisely synchronized with a GPS clock so that the playing back of a signal file is started exactly at a specified time. [9], [57]. The GPS receiver chosen for the investigations (Tekron TTM01-E) supports an inter-range instrumentation group time code format B (IRIG-B) signal and a pulse-per-second (PPS) signal. The analog test signals generated by the playback unit are thus referenced to a known time. The test signals were generated starting from the theoretical phasors describing the test conditions as prescribed in [5]. The mathematical equations describing the time domain signals corresponding to the theoretical phasors are obtained. The COMTRADE files of the test signals were generated using the COMTRADE file recording facility of PSCAD/EMTDC^{TM} software. The playback signals are input to the PMU under test, which receives timing signals from the same GPS clock as the playback device. The phasor magnitude, phase angle, and the frequency measurements provided by the PMU were recorded and compared against the theoretical phasors corresponding to the test signals. The phasor measurement errors are quantified using the TVE as specified in the standard [5]. The operational flowchart of test setup is shown in Figure 3.5.

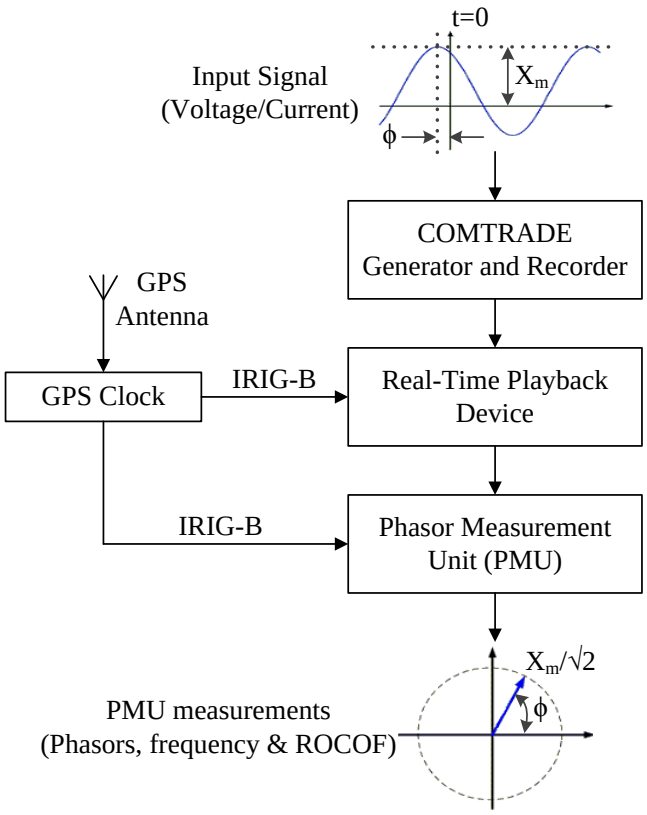

Figure 3.5 Operational flowchart of test setup

3.3.1 Sources of Errors in Testing

When evaluating the performance, it is important to understand the possible errors associated with the test setup as well as the sources of errors in a PMU device. The former includes instrumentation and operational errors including errors in the test signals generated from a mathematical signal model, playback device amplifier, GPS receiver, and playback start-up delay [9] while the later consists of errors in the GPS receiver, internal instrument transformers of PMU, ADC, time inconsistency, measurement calculations, and parasitic oscillations or processing artifacts [45].

In order to achieve high accuracy in the generated analog test signals, care must be taken right from the time of generating the COMTRADE files. The accuracy of the test signals depends upon the analog output scale and the simulation time step used in the playback device. In making the COMTRADE files, 16 bit A/D conversion resolution (65,536 levels) and a 50 μs time step were selected. The Doble F6150 signal playback device has a 16 bit digital to analog converter (DAC) and in order to supply the analog voltage and current signals with required peak-to-peak magnitudes, the appropriate precision levels must be selected. For the tests described in this research, 1 mA and 10 mV precisions were selected for currents and voltages respectively. This enabled generating current signals with peak-to-peak magnitude up to 15.56 A ($1.1\times5A\times\sqrt{2}\times2$) and voltage signals with peak-to-peak magnitudes of 214.68 V ($1.1\times69V\times\sqrt{2}\times2$).

In order to evaluate TVE, the test signal also needs to be synchronized using a GPS clock. In the tests, the same GPS clock supplied synchronizing signals to the playback instrument and the PMU under test, thereby minimizing errors due to the GPS clock. The GPS receiver chosen for the test provides 1-PPS signal which indicates the beginning of the current second of the universal coordinated time (UTC) and IRIG-B signal as shown in Figure 3.6.

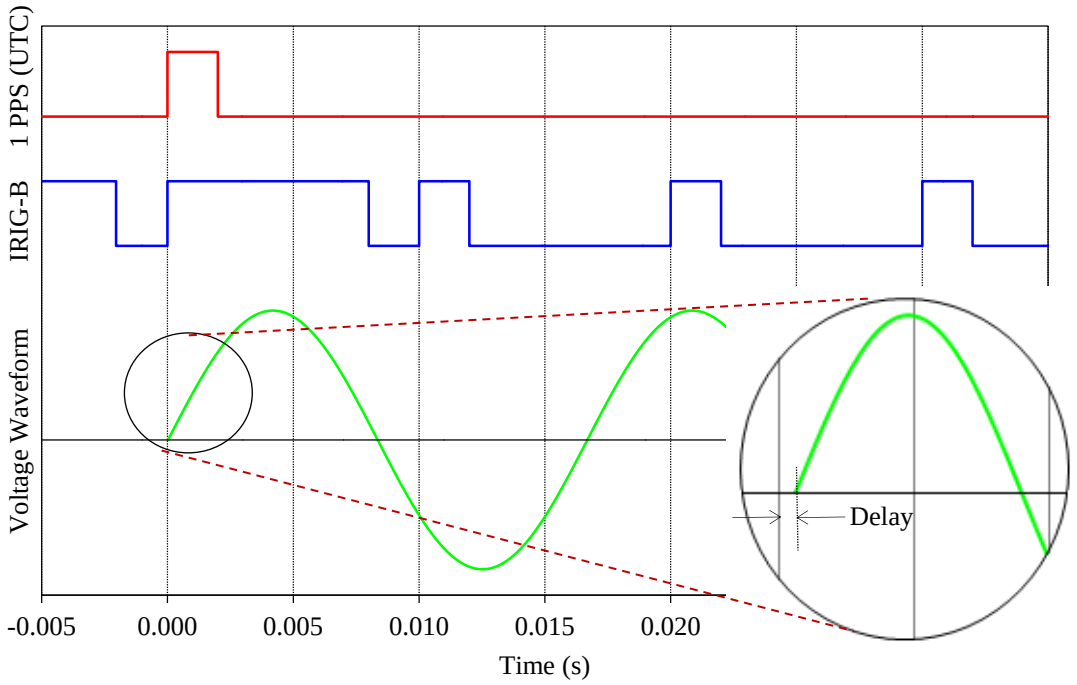

Figure 3.6 Starting delay of waveform with respect to the UTC reference

The playback system is configured to start playing a recorded signal always at the beginning of a full second, based on the UTC 1-PPS signal provided by the GPS clock. However, the actual analog signal starts to appear on the output of playback device after a certain delay (which was approximately 10 μs for the instrument used) as shown in Figure 3.6. This time needs to be compensated in the TVE calculation and evaluating other performance measures such as step response performance and latency. The signal magnitude errors can be minimized by properly calibrating the playback device using known voltage and/or current waveforms [9], [58]. In [5], it is recommended that test uncertainty be maintained less than one-fourth of the accuracy requirement. Therefore, the TVE of the test signal at the PMU input is kept below 0.25% since the required TVE from the PMU is less than 1% under most of the situations.

The sources of errors in the PMU device include those introduced by its internal instrument transformers. Actual instrument transformers always have a ratio and a phase angle correction (although small), making them a source of biased measurements if they are not properly calibrated. It is essential to calibrate both magnitudes and phase angles. The calibration is achieved by comparing the known voltage and/or current waveforms and measured values. Since accurate characteristics of commercial internal instrument transformers are essential for calibration, it is usually done by the manufacturers. The errors introduced by digitization can be minimized by using a high resolution ADC, such as 16-bit ADC. Errors could also be introduced due to calculation delays in the PMU. The phasor estimation can be viewed as an averaging or filtering process, regardless of whether the performance class filters are applied at the backend, and therefore, there is an inherent delay. However, the timestamp of a phasor reported by a PMU should correspond to the time when part of the signal used to compute the phasor appearing at the PMU input. Thus, the data window corresponding to the timestamp should be adjusted to account for the processing delays, including the frontend analog input filtering, sampling, and estimation group delay of the performance class filters [6]. A PMU calculates frequency and ROCOF by taking first and second numerical derivatives of the phase angle. Abrupt changes in angle estimates, which are data outliers, produce sharp spikes in derivatives. A better PMU output can result if the derivative spikes are amplitude limited or interpolated out of the data prior to filtering. PMU measurements may contain parasitic oscillations which are actually processing artifacts. Proper hardware design and shielding can prevent parasitic oscillation.

3.4 Test Results and Discussion

Current signal measurements are presented in this thesis since current measurements are more vulnerable for errors initiated from the current transformers. The frequency measurements shown in the thesis are derived from voltage measurements. The test results illustrate performances of the highest reporting rate of 60 fps. The maximum TVE and FE observed during the test period are reported. In the research, the errors observed without the performance class filters are test results directly obtained from an actual PMU, which has a capability to record the input signal as well. The performance class filter models are implemented in MatLAB, and the signals recorded by the PMU are applied to compare different performance class filters. The errors observed with and without the performance class filters are reported, and compliance with the performance requirements specified in [5] (summarized in Table 3.1 & Table 3.2) is analyzed. Note that the reference M-class filter performances are evaluated with the compensation factor proposed in Section 3.2.1.

3.4.1 Signal Frequency Test

The signal frequency test simulates a deviation of frequency in the power system. In this test, the frequency is varied from 55 Hz to 65 Hz with a step resolution of 1 Hz while all other quantities are kept constant (nominal frequency is 60 Hz). The test continues over 5 s of test duration. The maximum percentage TVE and the maximum FE are shown in Figure 3.7.

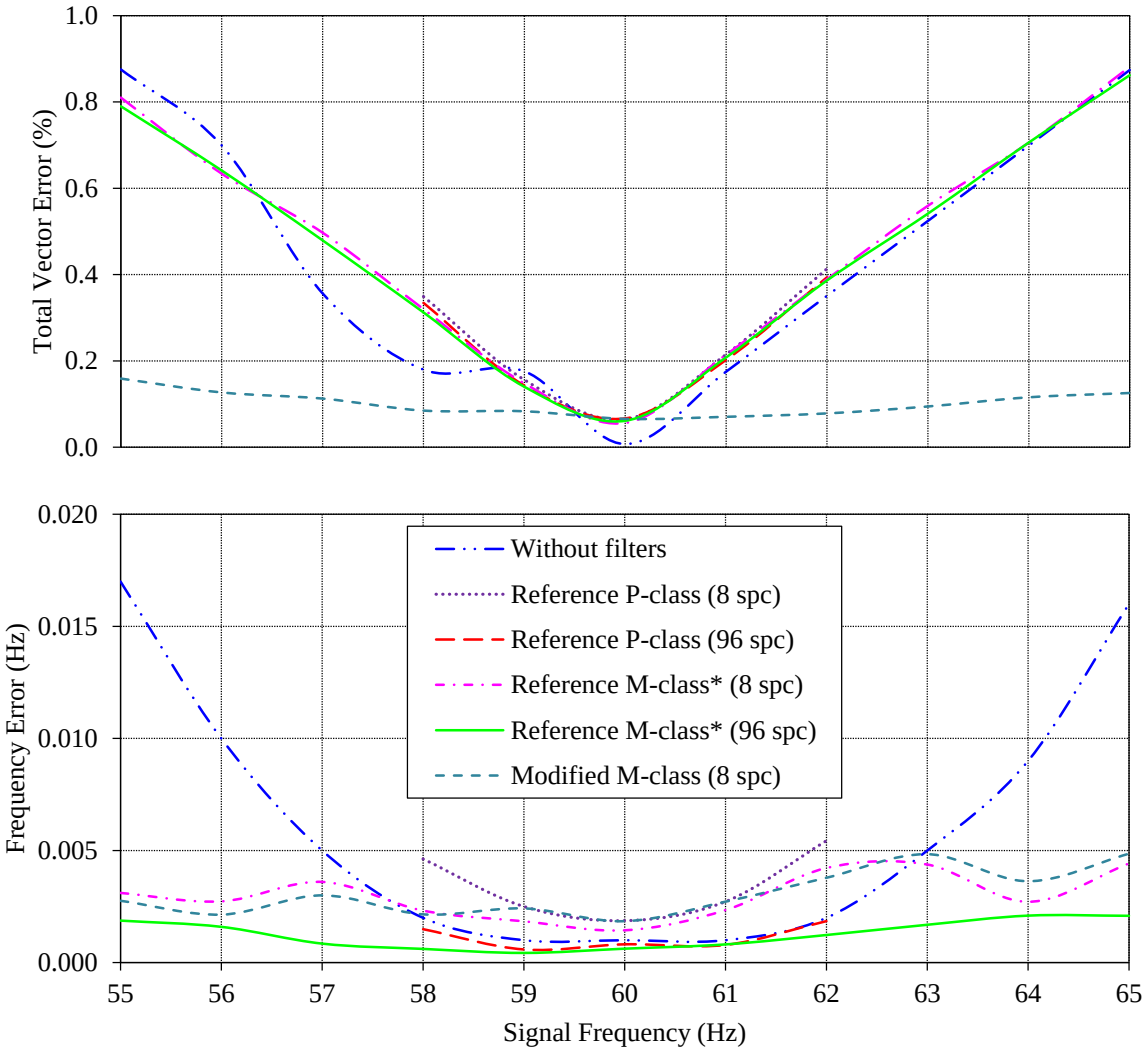

* Reference M-class filter with the proposed compensation factor

Figure 3.7 Steady-state current frequency response at 60 fps

The phasor reported by the PMU rotates with time when the signal frequency deviates from the nominal frequency. This phasor rotation should be taken into account when determining TVE. The frequency of the signal is measured in each case and FEs are determined. It is observed that the PMU satisfies the TVE requirements (< 1%) under the signal frequency test even without the performance class filters, and the filters may not significantly influence the phasor measurements under steady-state. However, the PMU

does not satisfy the FE requirement (< 0.005 Hz) without performance class filters. Note that the specified range of frequency for the P-class is only from 58-62 Hz [5].

Since ROCOF is the first numerical derivative of frequency, it should be possible to maintain ROCOF error (RFE) within the specified range if the frequency is accurately measured. However, RFE requirements specified in [5] are difficult to achieve even with the performance class filters. For example, the allowed FE of 0.005 Hz at steady-state can translate into an RFE of 0.3 Hz/s, if this frequency difference appears between two consecutive phasor reportings at 60 fps. However, the maximum RFE allowed in [5] is 0.01 Hz/s. According to Annex C in the standard [5], the ROCOF values are calculated using two consecutive sample data points. Even when these values are averaged over the reporting period, it is impossible to achieve the accuracy specification in [5]. Based on the observations of these tests, feedback was provided to the relevant IEEE working group suggesting to review the RFE specifications in [5], after considering the performance of commercial PMUs from different manufactures. The IEEE Standard C37.118.1a [41], an amendment to [5] released in early 2014, relaxes the RFE specifications where P-class and M-class limits were increased to 0.4 Hz/s and 0.1 Hz/s respectively (Note that these tests were conducted before the amendment to IEEE C37.118.1 was released).

3.4.2 Measurement Bandwidth Test

The test signals for measurement bandwidth assessment are primarily 50 or 60 Hz waveforms that are amplitude and/or phase angle modulated with a sine wave. This test simulates oscillations in a power system. The test signal is represented as,

$$x(t) = X_m[1 + k_x \cos(2\pi f_m t)] \cdot \cos[2\pi f_0 t + k_a \cos(2\pi f_m t - \pi)] \quad (3.3)$$

The magnitude modulation k_x and the phase angle modulation k_a are kept at 10% while the modulation signal frequency f_m is varied over the range 0.1 to 5 Hz. The tests at each modulation frequency step continue for at least two full cycles of modulation to allow for adequate settling time so that the modulation frequency change transient does not affecting the measurements. The variations of the maximum percentage TVE and maximum FE observed during this test are shown in Figure 3.8.

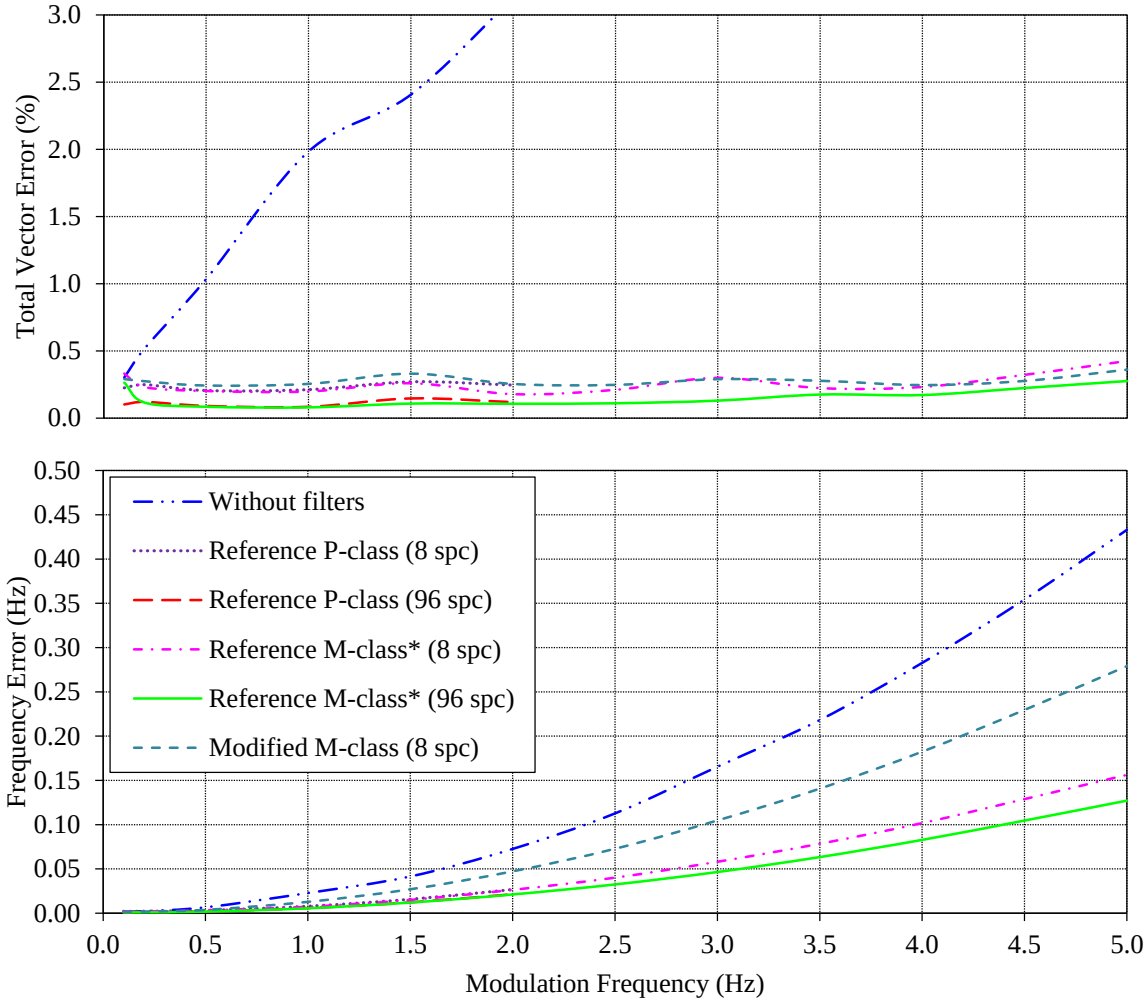

* Reference M-class filter with the proposed compensation factor

Figure 3.8 Current magnitude and phase angle modulation response at 60 fps

The PMU without performance filters can satisfy the TVE requirements only up to a modulation frequency of 2 Hz, as the maximum TVE rises above 3% beyond 2 Hz. However, once the performance class filters are applied, the TVE remains less than 1% throughout the expected modulation frequency range. In Figure 3.8, the curves for P-class and M-class TVEs overlap. The FE is also higher than the specified range (0.3 Hz) without filters but addition of performance filters rectifies the situation. The curves for P-class should be considered only up to 2 Hz because the specified range of modulation frequency for P-class is from 0.1 to 2 Hz only. Also, the specified FE limit for the P-class is 0.06 Hz. This test procedure has been slightly changed through the amendment, IEEE Standard C37.118.1a [41]; according to the new procedure the magnitude and phase angle modulations are applied separately.

3.4.3 Linear Frequency Ramp Test

In the linear frequency ramp test, the input signal frequency is changed at a constant rate starting from its nominal value, similar to what would occur in a sudden system imbalance caused by a loss of significant load or generation. The frequency ramp test signal is represented as,

$$x(t) = X_m \cos\left(2\pi f_0 t + \pi R_f t^2\right) \tag{3.4}$$

where R_f is the signal frequency ramp rate. The test is repeated for negative ramps (60 Hz - 55 Hz at rates up to −1.0 Hz/s) and positive ramps (60 Hz - 65 Hz at rates up to +1.0 Hz/s). To eliminate the effect of transients, the measurements taken during the two reporting intervals before and after a change in the frequency ramp are excluded in the cal-

culation of errors. The observed variations of the maximum percentage TVE and the maximum FE are shown in Figure 3.9.

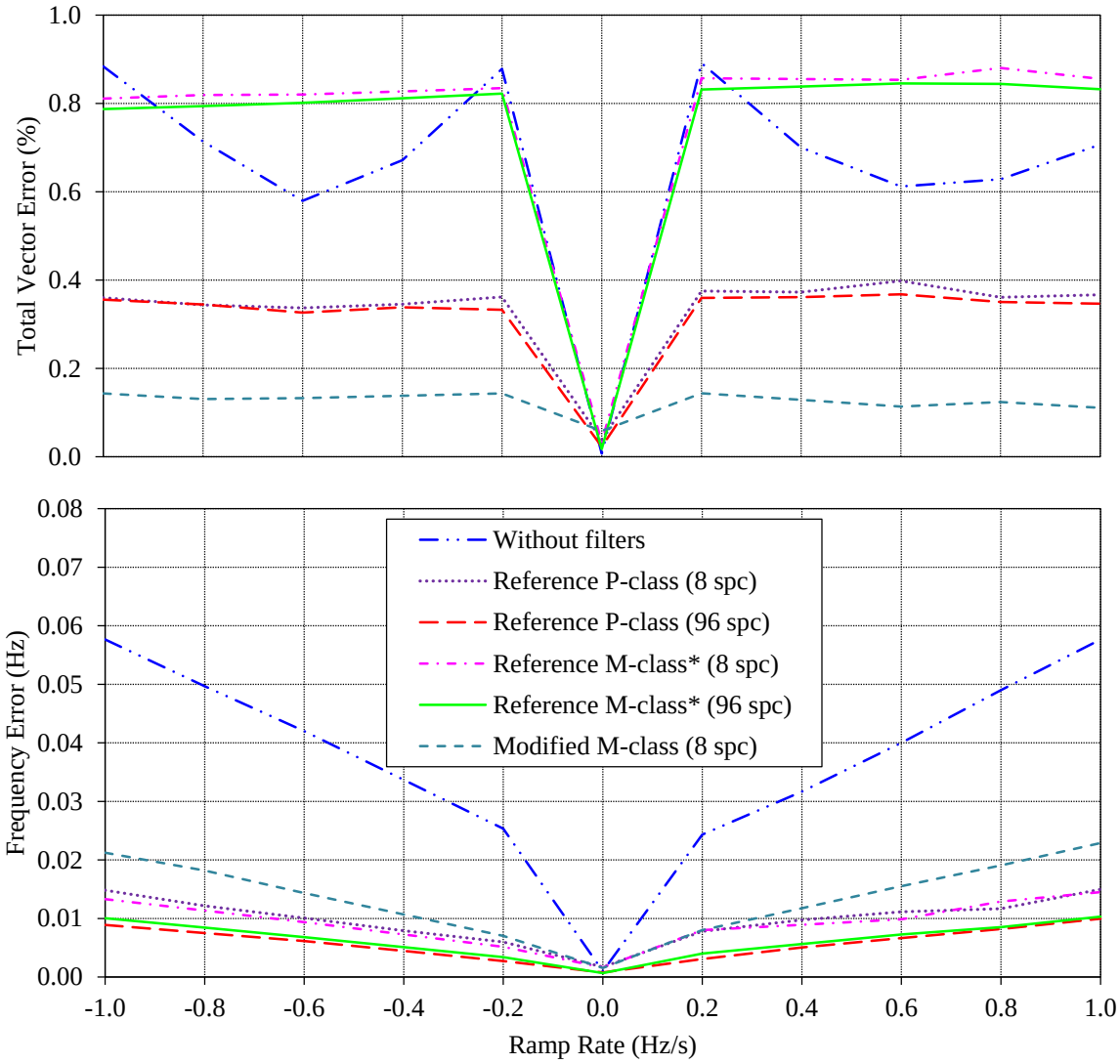

* Reference M-class filter with the proposed compensation factor

Figure 3.9 Current signal linear frequency ramp response at 60 fps

The TVE remains below the specified limit (< 1%) even without the backend filters. However, FE limits of P-class (0.01 Hz) can be satisfied only with the performance class filters. It is noted that in [5], M-class FE limit is given as 0.005 Hz, which is even lower

than the P-class FE limit and equal to the steady-state FE limit. This is a somewhat unrealistically strict limit and cannot be achieved with any of the M-class filters considered in this research. Therefore, it was suggested to review M-class FE limit of the standard [5], under the frequency ramp test. The IEEE Standard C37.118.1a [41], an amendment to [5] addressed this inconsistency and amended M-class FE limit to 0.01 Hz.

Results of the signal frequency, the measurement bandwidth, and the frequency ramp tests for P- and M-classes are summarized in Table 3.1.

Table 3.1 TVE and FE results of the P-class and M-class compliance

Influence quantity	Condition		Max TVE (%)	Max FE (Hz)
Signal frequency	Specified in [5] (P-class/M-class)		1.00/1.00	0.005/0.005
	without filter (P-class range)		0.35	0.002
	Reference P-class	(8 spc)	0.41	0.005
		(96 spc)	0.40	0.002
	without filter (M-class range)		0.88	0.017
	Reference M-class*	(8 spc)	0.88	0.004
		(96 spc)	0.83	0.002
	Modified M-class	(8 spc)	0.13	0.005
Measurement bandwidth	Specified in [5] (P-class/M-class)		3.00/3.00	0.06/0.30
	without filter (P-class range)		3.21	0.07
	Reference P-class	(8 spc)	0.18	0.03
		(96 spc)	0.15	0.02
	without filter (M-class range)		8.53	0.43
	Reference M-class*	(8 spc)	0.42	0.16
		(96 spc)	0.28	0.13
	Modified M-class	(8 spc)	0.36	0.28
Linear frequency ramp	Specified in [5] (P-class/M-class)		1.00/1.00	0.01/0.005
	without filter (P-class range)		0.89	0.060
	Reference P-class	(8 spc)	0.38	0.015
		(96 spc)	0.36	0.009
	without filter (M-class range)		0.89	0.060
	Reference M-class*	(8 spc)	0.88	0.013
		(96 spc)	0.84	0.10
	Modified M-class	(8 spc)	0.14	0.023

* Reference M-class filter with the proposed compensation factor

3.4.4 Step Response Tests

This test is used to simulate power system switching events. The test signal with a unit step function $u(t)$ is applied to the magnitude or the phase angle. The unified test signal is represented by (3.5), but step is applied only for one quantity in a given test.

$$x(t) = X_m\,[1 + k_m u(t)]\cos[2\pi f_0 t + k_a u(t)] \tag{3.5}$$

The step response tests include +10% and –10% steps in magnitude k_m, and +10° and –10° steps in phase angle k_a. The step initiates a transition between two steady-states used to determine the response time, delay time, and maximum overshoot/undershoot. Since the typical PMU response and delay times are small compared to the PMU reporting interval, it is difficult to characterize the response of a single step. Therefore, the equivalent sampling approach explained in [5], [6], [46] should be used to achieve the required measurement resolution. In this technique, at least 10 successive step tests are made, where, in each event, the time of the step is shifted within a fraction of the reporting interval. The phasors are interleaved in accordance with their timestamps relative to one timestamp. This technique achieves an equivalent measurement step response with a time resolution to derive points on the measurement curve. Figure 3.10 shows the magnitude positive step waveform example for a current input, and the corresponding magnitude, TVE, and FE responses plotted on the same time scale. The results show that high delay times observed without filters can be reduced by incorporating the performance class filters. An example waveform of the phase angle positive step test signal and the corresponding phase angle, TVE and FE responses are shown in Figure 3.11.

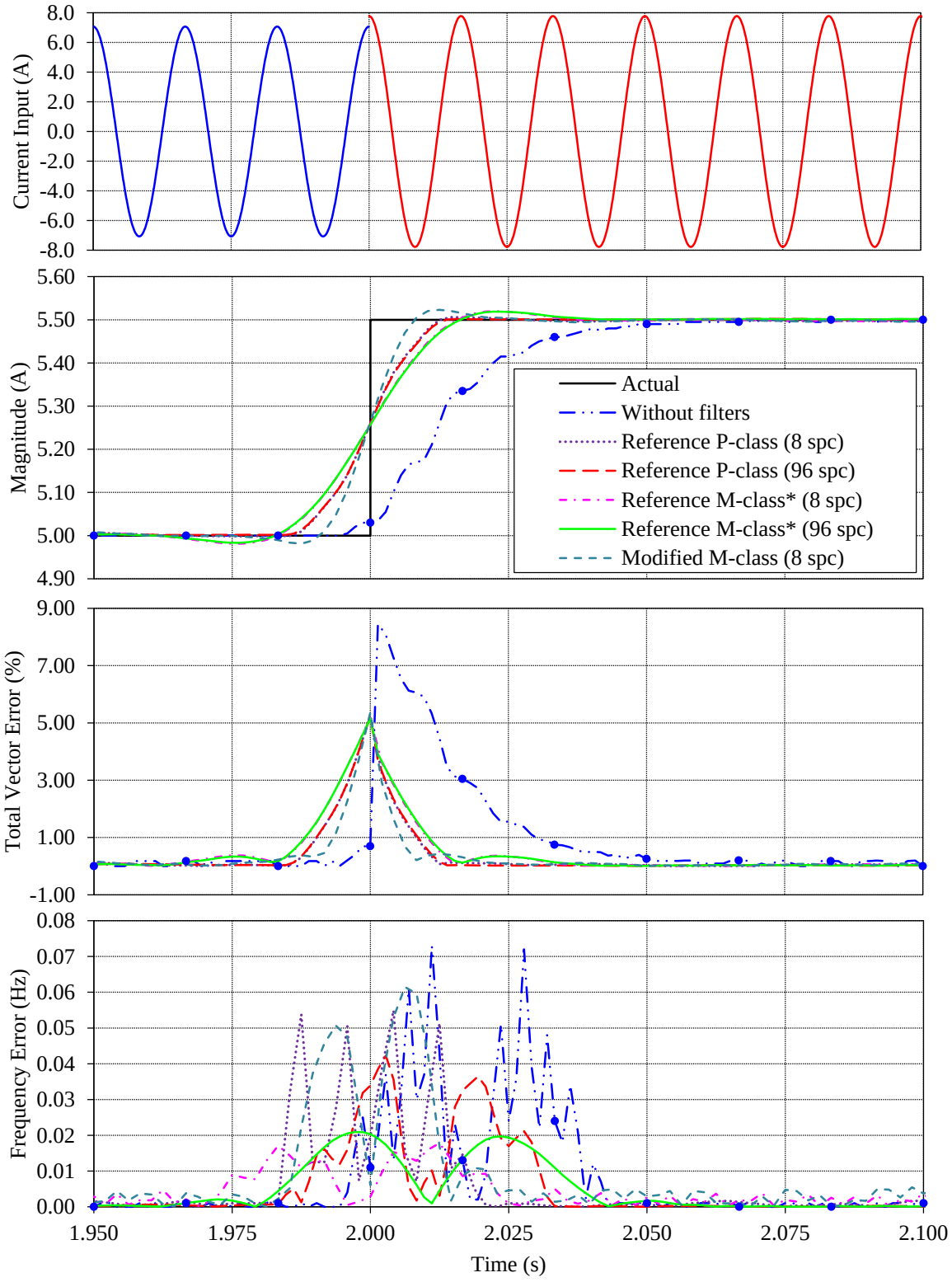

* Reference M-class filter with the proposed compensation factor

Figure 3.10 Waveforms of current magnitude positive step response at 60 fps

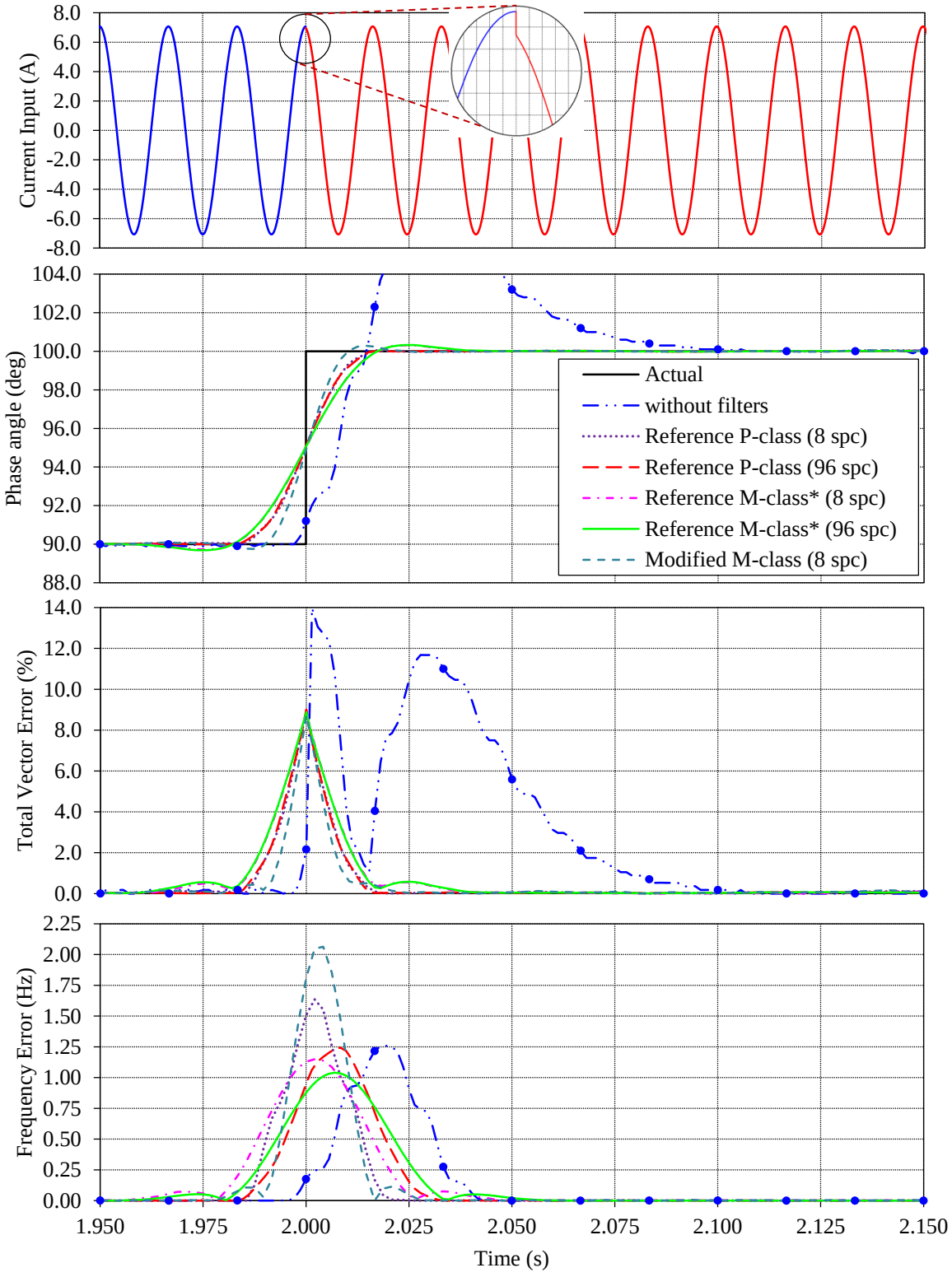

* Reference M-class filter with the proposed compensation factor

Figure 3.11 Waveforms of current phase angle positive step response at 60 fps

The TVE response time, delay time, maximum overshoot/undershoot, and frequency response time for each test case are also presented in Table 3.2.

Table 3.2 Step change performances

Influence quantity	Condition		Response time (sec.)	|Delay time| (sec.)	Max overshoot / undershoot (% of step)	Frequency Response time (sec.)
10% magnitude positive step	Specified in [5] (P-class/M-class)		0.028/ 0.079	0.004/ 0.004	5.0/10.0	0.058/ 0.120
	without filter		0.029	0.012	0.0	0.045
	Reference P-class	(8 spc)	0.018	0.001	0.4	0.035
		(96 spc)	0.018	0.001	0.0	0.043
	Reference M-class*	(8 spc)	0.021	0.001	4.2	0.048
		(96 spc)	0.022	0.001	4.2	0.054
	Modified M-class	(8 spc)	0.013	0.001	4.6	0.038
10% angle positive step	Specified in [5] (P-class/M-class)		0.028/ 0.079	0.004/ 0.004	5.0/10.0	0.058/ 0.120
	without filter		0.085	0.007	68.0	0.046
	P-class filter	(8 spc)	0.024	0.001	0.2	0.038
		(96 spc)	0.023	0.001	0.2	0.048
	Reference M-class*	(8 spc)	0.024	0.001	3.4	0.090
		(96 spc)	0.027	0.001	3.2	0.098
	Modified M-class	(8 spc)	0.015	0.001	3.3	0.067

* Reference M-class filter with the proposed compensation factor

The PMU tested can achieve the accuracy requirement specified in [5] with a sampling rate of 8 spc and at a reporting rate of 60 fps. Once the accuracy at the highest reporting rate is achieved, the same filter can be used for lower reporting rates, by decimating the data from the output stream with the aid of an additional low-pass filter similar to the M-class filter. However, such additional filtering does not require for P-class, where it can be accomplished by taking every $N_k{}^{\text{th}}$ sample; where N_k is the ratio between the highest and the required reporting rates [5]. For example, at the reporting rate of 30 fps data reduction can be accomplished by taking every other sample. The PMU accuracy

can be slightly improved with a sampling rate of 96 spc but it is computationally more expensive.

3.5 Concluding Remarks

Theoretical calculations revealed some inadequacies in the reference M-class filter given in IEEE C37.118.1-2011 standard [5], and a new compensation factor was proposed for the reference M-class filter to rectify the deficiencies. The practical difficulties in implementing the reference M-class filter [5] in real-time environment were recognized and a new modified M-class filter that significantly reduces the number of filter coefficients and the filter group delay were introduced. A simple and repeatable test setup was introduced to evaluate steady-state and dynamic performances of a PMU as per the IEEE C37.118.1-2011 standard [5]. The performance of a commercial PMU with and without performance class filters was evaluated using the proposed test setup. Furthermore, some suggestions were made to review the M-class FE and RFE requirements of the synchrophasor standard [5]. In the IEEE Standard C37.118.1a [41], the amendment to IEEE C37.118.1-2011 released in 2014, the M-class FE and RFE requirements have been relaxed. At the time of the PMU tests reported in this thesis, the test procedures were not specified, but in December 2014, a synchrophasor measurement test suite specification [42] was published by the IEEE standards association conformity assessment program.

Chapter 4

Efficient Algorithms for Real-Time Monitoring of Transmission Line Parameters

4.1 Introduction

In this chapter, a novel approach for formulating the synchrophasor based transmission line parameters monitoring problem, which leads to computationally much simpler solution algorithms than the hitherto published algorithms, is proposed. Results of the evaluation of the three new algorithms proposed in this chapter using a power system simulated in a RTDS™ real-time digital simulator are presented in comparison to the performances of few previously published line parameters monitoring algorithms. The chapter also presents validation of the algorithms using a laboratory hardware experimental setup. Finally, the application of the algorithms to estimate line parameters under real conditions is examined using actual PMU measurements obtained from a utility.

4.2 Importance of Real-Time Line Parameters Monitoring

Every electricity utility has a database of transmission line parameters, which is usually created and updated over several years. These line parameters are often based upon theoretical calculations and may not reflect minor alterations to the transmission line as well as changes due to ageing. Moreover, the actual values of the transmission line parameters vary on the loading as well as on the ambient conditions such as temperature, solar radiation, wind speed, and any ice buildup. The current carried by the conductor determines the power losses, which are converted to heat, and the ambient conditions determine the rate of heat dissipation. The temperature determined by the heat balance in turn affect the resistivity and the sag. Thus, the parameters used to model a transmission line are continuously changing to a certain extent. By monitoring the line parameters in real-time, parameters can be updated to reflect the prevailing conditions. The line parameters updated in real-time can potentially improve the accuracy of many applications including state estimation, identification of fault locations, online determination of line losses and so on. In addition, the estimated line resistance can be used to determine the closeness of the transmission line to its thermal limit.

Traditional state estimators rely upon the theoretically calculated transmission line parameters, which depend upon several assumptions and may not reflect the actual system state. In addition, errors in the theoretical values of line parameters limit the state estimator's capability to detect bad data. Therefore, the output of state estimator may not

be an accurate representation of the power system state at the given time. These drawbacks can be eliminated and the accuracy of state estimators can be improved by using the transmission line parameters that are updated in real-time.

Today, most utilities want to operate their existing transmission lines close to their operating limits due to both economic and environmental reasons, particularly due to difficulties in obtaining environmental clearances for the construction of new transmission lines. The conductor temperature, which changes with the loading and environmental conditions, should be maintained below a certain value known as the thermal limit to avoid excessive conductor sags and permanent deformation of conductors. The average temperature of a conductor can be estimated if the resistance of the transmission line is known. With accurate estimates of line resistance provided by real-time line parameter monitoring, temperature of the conductors can be continuously estimated with a known temperature coefficient of resistivity of the conductor material. Although this method does not allow monitoring of local hot spots, it provides a reasonable and economical alternative to direct monitoring of conductor temperatures.

Most of the fault location algorithms rely on accurate transmission line parameters and real-time monitoring can help to precisely identify fault locations. In addition, real-time line parameter tracking can improve the accuracy of estimating power losses in transmission lines, and hence the accuracy of loss coefficients and incremental loss factors. This helps to minimize transmission losses through optimal power flow programs.

The real-time monitored line parameters may be used for several utility applications such as operational studies and configuration of protective relays. The real-time moni-

tored line parameters can be stored and used as an offline approach to eliminate the line parameter errors in the database.

Thus, real time line parameter monitoring is useful for the applications mentioned above and others.

4.3 Real-Time Monitoring of Line Parameters

Accurate transmission line parameters are important for reliable operation of a power system. The traditional theoretical calculations and offline measurements are widely used approaches, but they do not allow tracking of parameters when they are changing with the environmental factors and load conditions. Synchrophasor based real-time transmission line parameter monitoring algorithms can track such changing parameters.

Recent literature reports a number of efforts to calculate the parameters of a transmission line using PMU measurements [19], [20], [27], [59]-[67]. In [19], line parameters are identified using the total least squares (TLS) estimation. Another approach is to obtain ABCD chain parameters of the two-port network model of a transmission line using known voltage and current phasors at the terminals [20], [27], [59], [60]. The transmission line parameters are then found from the ABCD chain parameters. However, this approach requires at least two sets of measurements taken under different operation conditions. In [61]-[63], transmission line parameters are estimated based on the distributed parameter line model using nonlinear estimation theory. A method to estimate the parameters of a transmission line in a simple laboratory scale power system test setup is proposed in [64]. In [65], transmission line parameters are estimated from phasors calculated

by the new discrete Fourier transform (DFT) filtering approach termed as smart DFT. Transmission line parameters estimation method in [67] uses PMU measurements at one end and conventional magnitude measurements available at the other end, and the line parameters are estimated using nonlinear estimation theory.

Even though synchrophasor measurements have a guaranteed accuracy, practical PMU measurements can be contaminated with noise. Therefore, most of existing approaches use multiple sets of PMU measurement for calculation. However, methods proposed in [64]-[66] use a single set of measurements for their calculations. Many of the literature on synchrophasor based line parameter estimation algorithms [20], [60]-[63], [65], [66] have been validated with simulations alone. Only few algorithms such as those proposed in [59], [64], [67] have been validated using laboratory test setups whereas only the algorithms in [19] and [27] have been evaluated with the actual field measurements. Investigation of the performance of real-time transmission line parameters monitoring algorithms with practical synchrophasor measurements is important to gain confidence before applying it in the field. However, field validation is very difficult as the actual parameter values under a given ambient condition are not known, unless a special test designed to estimate the line parameters is conducted.

Although transmission line parameter estimation using PMU measurements is discussed in several papers, only a few them address the calculation of parameters of a series compensated transmission lines [61], [68]-[70]. All these published approaches require some form of input excitation, that is at least two set of measurements under different operation conditions, to successfully estimate the parameters.

4.4 Problem of Line Parameter Estimation

The equivalent π-model of a transmission line is shown in Figure 4.1, where V_S, I_S, V_R and I_R denote voltages and currents of the sending and the receiving ends respectively.

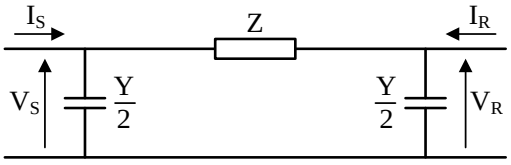

Figure 4.1 The equivalent π-equivalent model of a transmission line

Considering the measurement polarities indicated in Figure 4.1, the relationships between the currents and the voltages at the sending and the receiving ends can be expressed as,

$$V_S = V_R\left(1 + \frac{YZ}{2}\right) - I_R Z \tag{4.1}$$

$$I_S = V_R Y\left(1 + \frac{YZ}{4}\right) - I_R\left(1 + \frac{YZ}{2}\right) \tag{4.2}$$

where $Z = R + jX_L$ and $Y = jy_c$. The transmission line parameters to be found are R, X_L and y_c, which denote the series resistance, series inductive reactance and the shunt capacitive susceptance respectively. Alternatively, considering the distributed parameter model, the same relationships can be expressed as,

$$V_S = V_R\cosh(\gamma L) - I_R Z_C \sinh(\gamma L) \tag{4.3}$$

$$I_S = -I_R\cosh(\gamma L) + \frac{V_R}{Z_C}\sinh(\gamma L) \tag{4.4}$$

In this case, the parameters to be found are the characteristic impedance, Z_C, and the propagation constant γ. The length of the transmission line, L, is assumed to be known.

4.5 Review of Transmission Line Parameter Estimation Algorithms

In this section, some of the previously published line parameter estimation algorithms are briefly described. The algorithms presented here are used for the comparative assessment of the performance of the new algorithms presented later in this chapter. The particular set of algorithms were chosen because they work with similar input data and possess the ability of tracking line varying parameters under changing operating and environmental conditions.

The computational complexity of mathematical algorithms can be measured by analysing how they respond to changes in the size of input data set [71]. For instance, it is possible to analyse how the processing time of a parameter estimating algorithm change as the number of synchrophasor measurement sets or the data window size grows. As described in [71], the complexity of an algorithm can be expressed using big O notation as $O(mN^{\alpha})$, where N is the input data size, and m and α are two parameters dependent on the algorithm complexity. For example, for a linear algorithm $m = 1$ and $\alpha = 1$. The computational complexity of the proposed line parameters estimation algorithms and other exiting algorithms are analysed using this method.

4.5.1 Method A [19]

In the algorithm proposed in [19], line parameters are identified with a moving-window of PMU measurements using the total least squares (TLS) estimation. The meth-

od requires the voltage and the current phasors as well as the complex power measurements at both terminals. This algorithm is computationally expensive because it uses the singular value decomposition (SVD) technique to solve a matrix equation which could sometimes be ill-conditioned. Therefore, it is a computationally expensive algorithm where the computational complexity is $\mathrm{O}(N^2)$, where N is the number of measurements collected from PMUs (i.e. data window length)

4.5.2 Method B [20]

The method 4 in [20] formulates the problem considering the nodal equations (1) and (2) and rearranging them into four real equations as,

$$\mathrm{V}_{\mathrm{S}}^{(\mathrm{Re})} = \mathrm{V}_{\mathrm{R}}^{(\mathrm{Re})}\left(1 - \frac{X_L y_c}{2}\right) - \mathrm{V}_{\mathrm{R}}^{(\mathrm{Im})}\frac{R y_c}{2} - \mathrm{I}_{\mathrm{R}}^{(\mathrm{Re})}R + \mathrm{I}_{\mathrm{R}}^{(\mathrm{Im})}X_L \tag{4.5}$$

$$\mathrm{V}_{\mathrm{S}}^{(\mathrm{Im})} = \mathrm{V}_{\mathrm{R}}^{(\mathrm{Re})}\frac{R y_c}{2} + \mathrm{V}_{\mathrm{R}}^{(\mathrm{Im})}\left(1 - \frac{X_L y_c}{2}\right) - \mathrm{I}_{\mathrm{R}}^{(\mathrm{Re})}X_L + \mathrm{I}_{\mathrm{R}}^{(\mathrm{Im})}R \tag{4.6}$$

$$\mathrm{I}_{\mathrm{S}}^{(\mathrm{Re})} = -\mathrm{V}_{\mathrm{R}}^{(\mathrm{Re})}\frac{R {y_c}^2}{4} - \mathrm{V}_{\mathrm{R}}^{(\mathrm{Im})}y_c\left(1 - \frac{X_L y_c}{4}\right) - \mathrm{I}_{\mathrm{R}}^{(\mathrm{Re})}\left(1 - \frac{X_L y_c}{2}\right) + \mathrm{I}_{\mathrm{R}}^{(\mathrm{Im})}\frac{R y_c}{2} \tag{4.7}$$

$$\mathrm{I}_{\mathrm{S}}^{(\mathrm{Im})} = \mathrm{V}_{\mathrm{R}}^{(\mathrm{Re})}y_c\left(1 - \frac{X_L y_c}{4}\right) - \mathrm{V}_{\mathrm{R}}^{(\mathrm{Im})}\frac{R {y_c}^2}{4} - \mathrm{I}_{\mathrm{R}}^{(\mathrm{Re})}\frac{R y_c}{2} - \mathrm{I}_{\mathrm{R}}^{(\mathrm{Im})}\left(1 - \frac{X_L y_c}{2}\right) \tag{4.8}$$

where the superscripts (Re) and (Im) denotes the real and imaginary part of the complex variable, respectively. Since unknowns are direct transmission line parameters (i.e. series resistance R, series inductive reactance X_L, and shunt capacitive susceptance y_c) the problem is nonlinear. Thus, least squares (LS) based nonlinear estimation theory is employed to solve for the unknown parameters. The solution requires a computationally expensive iterative process. Therefore, the computational complexity not only depends upon the N

but also number of iterations, m. Thus, the computational complexity is $O(mN)$. The number of iterations depends on the initial condition and the tolerance specified to terminate the iterations. The initial values of the unknown parameters can be obtained using the theoretical estimations [20]. However, this problem can be linearized by rearranging equations as proposed in algorithm 1 of this thesis.

4.5.3 Method C [61]

The distributed parameter model of the line is employed for deriving the algorithm presented in [61]. Considering the voltage and the current phasors measured at the two ends, a set of complex equations for the voltage and current are derived and rearranged into a set of real equations. The algorithm looks to estimate Z_C and γ. The resulting estimation problem is nonlinear and the solution can be obtained from a technique similar to that used in method 4 in [20]. Thus, the computational complexity is also same as the method B. i.e. $O(mN)$. The drawbacks of the method B [20] are common to this method as well.

4.5.4 Method D [63]

A nonlinear optimal estimation theory based transmission line parameter estimation algorithm is proposed in [63]. The algorithm is developed considering the distributed transmission line model and a set of synchronized measurements of the voltage and current phasors at two ends. This algorithm differs from the others, and has the ability of detecting possible synchronization errors. Thus, it enhances estimation accuracy [63]. How-

ever, a large number of unknowns are necessary to be estimated during the solution, because in addition to the unknown transmission line parameters, measurements itself are optimized to obtain the solution. Also, the number of estimations required grows with the data window size. The problem is nonlinear, and therefore, an iterative Newton-Raphson method is used for obtaining the solution. Each iteration involves $(12N+1) \times (12N+1)$ matrix inversion. Therefore, the computational complexity is $O(mN^3)$ and this algorithm is obviously the computationally most expensive method..

4.5.5 Method E [20] and Method F [65]

Noise-free synchrophasor measurements are assumed in the method 1 in [20] and the approach presented in [65]. The line parameters are determined considering a single measurement set consisting of the voltage and current phasors measured at two ends. Thus, the estimated parameters are vulnerable to noise.

4.6 Proposed Transmission Line Parameters Estimation Algorithms

In this thesis, three novel transmission line parameters estimation algorithms are developed. The first two algorithms proposed in this thesis (for the lump and distributed parameter models) distinguish from the previously published algorithms [19], [20], [61]-[63], [67] by the solution approach. The algorithms developed in this thesis use computationally simpler linear LS estimation instead of nonlinear LS or iterative methods, while not requiring data at different operating points (or input excitation). This is possible

through the judicious selection of the estimation parameters to enable formulating a linear estimation problem. The last algorithm is based on nonlinear LS estimation and an iterative solution procedure distinguishes due to its ability of estimating the parameters of series compensated transmission lines.

4.6.1 Algorithm for Estimating π −Equivalent Circuit Parameters (Algorithm 1)

Letting $^1/_{\mathrm{Z}} = g + \mathrm{j}b$ and separating the real and imaginary parts of the two complex expressions (4.1) and (4.2), four real equations can be obtained as,

$$\mathrm{I}_{\mathrm{S}}^{(\mathrm{Re})} = \left(\mathrm{V}_{\mathrm{S}}^{(\mathrm{Re})} - \mathrm{V}_{\mathrm{R}}^{(\mathrm{Re})}\right)g + \left(\mathrm{V}_{\mathrm{R}}^{(\mathrm{Im})} - \mathrm{V}_{\mathrm{S}}^{(\mathrm{Im})}\right)b - \frac{\mathrm{V}_{\mathrm{S}}^{(\mathrm{Im})}}{2}y_c \tag{4.9}$$

$$\mathrm{I}_{\mathrm{S}}^{(\mathrm{Im})} = \left(\mathrm{V}_{\mathrm{S}}^{(\mathrm{Im})} - \mathrm{V}_{\mathrm{R}}^{(\mathrm{Im})}\right)g + \left(\mathrm{V}_{\mathrm{S}}^{(\mathrm{Re})} - \mathrm{V}_{\mathrm{R}}^{(\mathrm{Re})}\right)b + \frac{\mathrm{V}_{\mathrm{S}}^{(\mathrm{Re})}}{2}y_c \tag{4.10}$$

$$\mathrm{I}_{\mathrm{R}}^{(\mathrm{Re})} = \left(\mathrm{V}_{\mathrm{R}}^{(\mathrm{Re})} - \mathrm{V}_{\mathrm{S}}^{(\mathrm{Re})}\right)g + \left(\mathrm{V}_{\mathrm{S}}^{(\mathrm{Im})} - \mathrm{V}_{\mathrm{R}}^{(\mathrm{Im})}\right)b - \frac{\mathrm{V}_{\mathrm{R}}^{(\mathrm{Im})}}{2}y_c \tag{4.11}$$

$$\mathrm{I}_{\mathrm{R}}^{(\mathrm{Im})} = \left(\mathrm{V}_{\mathrm{R}}^{(\mathrm{Im})} - \mathrm{V}_{\mathrm{S}}^{(\mathrm{Im})}\right)g + \left(\mathrm{V}_{\mathrm{R}}^{(\mathrm{Re})} - \mathrm{V}_{\mathrm{S}}^{(\mathrm{Re})}\right)b - \frac{\mathrm{V}_{\mathrm{R}}^{(\mathrm{Re})}}{2}y_c \tag{4.12}$$

where the superscripts (Re) and (Im) denotes the real and imaginary part of the complex variable respectively. Considering N measurements sets collected from PMUs, the following vectors and matrices can be defined.

$$[A] = \left[\mathrm{I}_{\mathrm{S1}}^{(\mathrm{Re})} \quad \mathrm{I}_{\mathrm{S1}}^{(\mathrm{Im})} \quad \mathrm{I}_{\mathrm{R1}}^{(\mathrm{Re})} \quad \mathrm{I}_{\mathrm{R1}}^{(\mathrm{Im})} \quad \cdots \quad \cdots \quad \mathrm{I}_{\mathrm{SN}}^{(\mathrm{Re})} \quad \mathrm{I}_{\mathrm{SN}}^{(\mathrm{Im})} \quad \mathrm{I}_{\mathrm{RN}}^{(\mathrm{Re})} \quad \mathrm{I}_{\mathrm{RN}}^{(\mathrm{Re})}\right]^{\mathrm{T}} \tag{4.13}$$

$$[H] = \begin{bmatrix} V_{S1}^{(Re)} - V_{R1}^{(Re)} & V_{R1}^{(Im)} - V_{S1}^{(Im)} & -V_{S1}^{(Im)}/2 \\ V_{S1}^{(Im)} - V_{R1}^{(Im)} & V_{S1}^{(Re)} - V_{R1}^{(Re)} & V_{S1}^{(Re)}/2 \\ V_{R1}^{(Re)} - V_{S1}^{(Re)} & V_{S1}^{(Im)} - V_{R1}^{(Im)} & -V_{R1}^{(Im)}/2 \\ V_{R1}^{(Im)} - V_{S1}^{(Im)} & V_{R1}^{(Re)} - V_{S1}^{(Re)} & V_{R1}^{(Re)}/2 \\ \vdots & \vdots & \vdots \\ \vdots & \vdots & \vdots \\ V_{SN}^{(Re)} - V_{RN}^{(Re)} & V_{RN}^{(Im)} - V_{SN}^{(Im)} & -V_{SN}^{(Im)}/2 \\ V_{SN}^{(Im)} - V_{RN}^{(Im)} & V_{SN}^{(Re)} - V_{RN}^{(Re)} & V_{SN}^{(Re)}/2 \\ V_{RN}^{(Re)} - V_{SN}^{(Re)} & V_{SN}^{(Im)} - V_{RN}^{(Im)} & -V_{RN}^{(Im)}/2 \\ V_{RN}^{(Im)} - V_{SN}^{(Im)} & V_{RN}^{(Re)} - V_{SN}^{(Re)} & V_{RN}^{(Re)}/2 \end{bmatrix} \quad (4.14)$$

$$[\Psi] = [g \quad b \quad y_c]^{\mathrm{T}} \quad (4.15)$$

Using the vectors and matrices defined in (4.13)-(4.15), the measurement equation can be expressed in compact form as:

$$[A]_{(4N\times 1)} = [H]_{(4N\times 3)}[\Psi]_{(3\times 1)} \quad (4.16)$$

The least square solution of the set of equations expressed in (4.16) is given by

$$[\Psi] = ([H]^T[H])^{-1}[H]^T[A] \quad (4.17)$$

The matrix $[H]^T[H]$ is a 3×3 non-singular, real-valued, symmetrical matrix irrespective of the number of measurements and thus, its inverse can easily be obtained regardless of the number of measurements considered. This is the main advantage of the proposed method for real time transmission line parameters monitoring. The computational complexity of the algorithm is $\mathrm{O}(N)$.

4.6.2 Algorithm for Estimating Distributed Model Parameters (Algorithm 2)

The unknown complex parameters Z_C and γ in (4.3) and (4.4) can be decoupled and expressed as,

$$\sqrt{V_S^2 - V_R^2} = \sqrt{I_S^2 - I_R^2} \cdot Z_c \tag{4.18}$$

$$V_S I_S - V_R I_R = (V_R I_S - V_S I_R)\cosh(\gamma L) \tag{4.19}$$

Considering N measurements sets collected from PMUs, the following vectors can be defined.

$$[C] = \left[\sqrt{V_{S1}^2 - V_{R1}^2} \quad \cdots \quad \cdots \quad \sqrt{V_{SN}^2 - V_{RN}^2}\right]^T \tag{4.20}$$

$$[D] = \left[\sqrt{I_{S1}^2 - I_{R1}^2} \quad \cdots \quad \cdots \quad \sqrt{I_{SN}^2 - I_{RN}^2}\right]^T \tag{4.21}$$

$$[E] = [V_{S1} I_{S1} - V_{R1} I_{R1} \quad \cdots \quad \cdots \quad V_{SN} I_{SN} - V_{RN} I_{RN}]^T \tag{4.22}$$

$$[F] = [V_{R1} I_{S1} - V_{S1} I_{R1} \quad \cdots \quad \cdots \quad V_{RN} I_{SN} - V_{SN} I_{RN}]^T \tag{4.23}$$

Using the complex-valued vectors defined in (4.20)-(4.23), two decoupled measurement equations can be expressed in compact form as:

$$[C]_{(N\times 1)} = [D]_{(N\times 1)} Z_C \tag{4.24}$$

$$[E]_{(N\times 1)} = [F]_{(N\times 1)} \cosh(\gamma L) \tag{4.25}$$

The least square solution of the set of equations expressed in (4.24) and (4.25) are given by,

$$\mathrm{Z_C} = ([D]^{\mathrm{T}}[D])^{-1}[D]^{\mathrm{T}}[C] \tag{4.26}$$

$$\gamma = \frac{1}{L}\cosh^{-1}([F]^{\mathrm{T}}[F])^{-1}[F]^{\mathrm{T}}[E] \tag{4.27}$$

Since $[D]^{\mathrm{T}}[D]$ and $[F]^{\mathrm{T}}[F]$ are single element (complex-valued) matrices regardless of the number of measurements, their inverse matrices can be directly calculated by taking their reciprocals. Therefore, it is computationally efficient and appropriate for real-time applications. The computational complexity of the algorithm is also $\mathrm{O}(N)$. From the estimated $\mathrm{Z_C}$ and γ, parameters of the equivalent π-model of the transmission line can be obtained as:

$$R = \mathrm{Real}\big(\mathrm{Z_C}\sinh(\gamma L)\big) \tag{4.28}$$

$$X_L = \mathrm{Imag}\big(\mathrm{Z_C}\sinh(\gamma L)\big) \tag{4.29}$$

$$y_c = 2 \times \mathrm{Imag}\left(\frac{\tanh(\gamma L/2)}{\mathrm{Z_C}}\right) \tag{4.30}$$

4.6.3 Algorithm for Estimating Parameters of a Series Compensated Line (Algorithm 3)

A series compensated transmission line can be represented using cascaded equivalent π-models as shown in Figure 4.2.

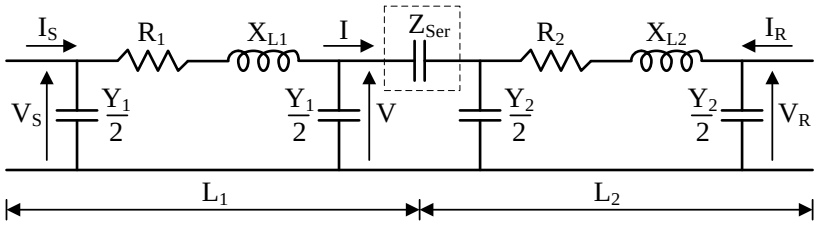

Figure 4.2 The equivalent model of a series compensated transmission line

The series compensator is located at a distance L_1 away from the sending end. The transmission line parameters can be expressed as,

$$\mathrm{Z}_1 = R_1 + \mathrm{j}X_{L1} = \mathrm{Z_C}\sinh(\gamma L_1) \tag{4.31}$$

$$\mathrm{Z}_2 = R_2 + \mathrm{j}X_{L2} = \mathrm{Z_C}\sinh(\gamma L_2) \tag{4.32}$$

$$\mathrm{Y}_1 = \mathrm{j}y_{c1} = \frac{2}{\mathrm{Z_C}}\tanh\left(\gamma\frac{L_1}{2}\right) \tag{4.33}$$

$$\mathrm{Y}_2 = \mathrm{j}y_{c2} = \frac{2}{\mathrm{Z_C}}\tanh\left(\gamma\frac{L_2}{2}\right) \tag{4.34}$$

Considering the measurement polarities indicated on Figure 4.2, expressions can be derived for the transmission line segment left to the compensation device as:

$$\mathrm{V_S} = \mathrm{V}\cosh(\gamma L_1) + \mathrm{I}\mathrm{Z_C}\sinh(\gamma L_1) \tag{4.35}$$

$$\mathrm{I_S} = \mathrm{I}\cosh(\gamma L_1) + \frac{\mathrm{V}}{\mathrm{Z_C}}\sinh(\gamma L_1) \tag{4.36}$$

Similar expressions can be derived for the transmission line segment right to the compensation device as,

$$\mathrm{V} - \mathrm{I}\mathrm{Z}_{\mathrm{Ser}} = \mathrm{V}_{\mathrm{R}}\cosh(\gamma L_2) - \mathrm{I}_{\mathrm{R}}\mathrm{Z}_{\mathrm{C}}\sinh(\gamma L_2) \tag{4.37}$$

$$\mathrm{I} = -\mathrm{I}_{\mathrm{R}}\cosh(\gamma L_2) + \frac{\mathrm{V}_{\mathrm{R}}}{\mathrm{Z}_{\mathrm{C}}}\sinh(\gamma L_2) \tag{4.38}$$

where $\mathrm{Z}_{\mathrm{Ser}} = -\mathrm{j}X_{Ser}$ and X_{Ser} depends upon the degree of compensation $k = X_{Ser}/X_L$. The series compensator can be switched either fully or partially on, or it can be completely bypassed. By eliminating V and I from (4.35)-(4.38), two equations can be obtained as:

$$f_1 = \mathrm{V}_{\mathrm{S}} - \left(\mathrm{V}_{\mathrm{R}} - \frac{\mathrm{I}_{\mathrm{R}}\mathrm{Z}_{\mathrm{Ser}}}{2}\right)\cosh(\gamma L) - \left(\frac{\mathrm{V}_{\mathrm{R}}\mathrm{Z}_{\mathrm{Ser}}}{2\mathrm{Z}_{\mathrm{C}}} - \mathrm{I}_{\mathrm{R}}\mathrm{Z}_{\mathrm{C}}\right)\sinh(\gamma L) + \frac{\mathrm{I}_{\mathrm{R}}\mathrm{Z}_{\mathrm{Ser}}}{2}\cosh(\gamma L') + \frac{\mathrm{V}_{\mathrm{R}}\mathrm{Z}_{\mathrm{Ser}}}{2\mathrm{Z}_{\mathrm{C}}}\sinh(\gamma L') = 0 \tag{4.39}$$

$$f_2 = \mathrm{I}_{\mathrm{S}} - \left(\frac{\mathrm{V}_{\mathrm{R}}\mathrm{Z}_{\mathrm{Ser}}}{2\mathrm{Z}_{\mathrm{C}}{}^2} - \mathrm{I}_{\mathrm{R}}\right)\cosh(\gamma L) - \left(\frac{\mathrm{V}_{\mathrm{R}}}{\mathrm{Z}_{\mathrm{C}}} - \frac{\mathrm{I}_{\mathrm{R}}\mathrm{Z}_{\mathrm{Ser}}}{2\mathrm{Z}_{\mathrm{C}}}\right)\sinh(\gamma L) + \frac{\mathrm{V}_{\mathrm{R}}\mathrm{Z}_{\mathrm{Ser}}}{2\mathrm{Z}_{\mathrm{C}}{}^2}\cosh(\gamma L') + \frac{\mathrm{I}_{\mathrm{R}}\mathrm{Z}_{\mathrm{Ser}}}{2\mathrm{Z}_{\mathrm{C}}}\sinh(\gamma L') = 0 \tag{4.40}$$

where $L = L_1 + L_2$ and $L' = L_1 - L_2$. Two nonlinear, complex equations (4.39) and (4.40) are functions of the measurements (V_{S}, V_{R}, I_{S} and I_{R}) and the unknown transmission line parameters (Z_{C} and γ).

Considering N measurements sets collected from PMUs, a set of equations can be written in matrix form as:

$$[F] = \begin{bmatrix} f_1^{(1)}(\mathrm{V_s},\ \mathrm{V_R},\ \mathrm{I_s},\ \mathrm{I_R},\ \mathrm{Z_C}, \gamma) \\ f_2^{(1)}(\mathrm{V_s},\ \mathrm{V_R},\ \mathrm{I_s},\ \mathrm{I_R},\ \mathrm{Z_C}, \gamma) \\ \vdots \\ \vdots \\ f_1^{(N)}(\mathrm{V_s},\ \mathrm{V_R},\ \mathrm{I_s},\ \mathrm{I_R},\ \mathrm{Z_C}, \gamma) \\ f_2^{(N)}(\mathrm{V_s},\ \mathrm{V_R},\ \mathrm{I_s},\ \mathrm{I_R},\ \mathrm{Z_C}, \gamma) \end{bmatrix} = \begin{bmatrix} 0 \\ 0 \\ \vdots \\ \vdots \\ 0 \\ 0 \end{bmatrix} \tag{4.41}$$

The set of nonlinear equations in (4.41) can be solved with the aid of nonlinear LS method. The solution is obtained through an iterative process based on the Newton method as following. First, the matrix $[H]$ is defined as:

$$[H] = \begin{bmatrix} \frac{\partial f_1^{(1)}}{\partial \mathrm{Z_C}} & \frac{\partial f_2^{(1)}}{\partial \mathrm{Z_C}} & \cdots & \frac{\partial f_1^{(N)}}{\partial \mathrm{Z_C}} & \frac{\partial f_2^{(N)}}{\partial \mathrm{Z_C}} \\ \frac{\partial f_1^{(1)}}{\partial \gamma} & \frac{\partial f_2^{(1)}}{\partial \gamma} & \cdots & \frac{\partial f_1^{(N)}}{\partial \gamma} & \frac{\partial f_2^{(N)}}{\partial \gamma} \end{bmatrix}^T \tag{4.42}$$

The derivatives for the matrix $[H]$ in (4.42) are given as:

$$\frac{\partial f_1}{\partial \mathrm{Z_C}} = \left(\frac{\mathrm{V_R Z_{Ser}}}{2\mathrm{Z_C}^2} + \mathrm{I_R}\right)\sinh(\gamma L) - \frac{\mathrm{V_R Z_{Ser}}}{2\mathrm{Z_C}^2}\sinh(\gamma L') \tag{4.43}$$

$$\frac{\partial f_1}{\partial \gamma} = L\left(\frac{\mathrm{I_R Z_{Ser}}}{2} - \mathrm{V_R}\right)\sinh(\gamma L) - L\left(\frac{\mathrm{V_R Z_{Ser}}}{2\mathrm{Z_C}} - \mathrm{I_R Z_C}\right)\cosh(\gamma L) + L'\frac{\mathrm{I_R Z_{Ser}}}{2}\sinh(\gamma L') + L'\frac{\mathrm{V_R Z_{Ser}}}{2\mathrm{Z_C}}\cosh(\gamma L') \tag{4.44}$$

$$\frac{\partial f_2}{\partial \mathrm{Z_C}} = \frac{\mathrm{V_R Z_{Ser}}}{\mathrm{Z_C}^3}\cosh(\gamma L) + \left(\frac{\mathrm{V_R}}{\mathrm{Z_C}^2} - \frac{\mathrm{I_R Z_{Ser}}}{2\mathrm{Z_C}^2}\right)\sinh(\gamma L) - \frac{\mathrm{V_R Z_{Ser}}}{\mathrm{Z_C}^3}\cosh(\gamma L') - \frac{\mathrm{I_R Z_{Ser}}}{\mathrm{Z_C}^2}\sinh(\gamma L') \quad (4.45)$$

$$\frac{\partial f_2}{\partial \gamma} = L\left(\mathrm{I_R} - \frac{\mathrm{V_R Z_{Ser}}}{2\mathrm{Z_C}^2}\right)\sinh(\gamma L) - L\left(\frac{\mathrm{V_R}}{\mathrm{Z_C}} - \frac{\mathrm{I_R Z_{Ser}}}{2\mathrm{Z_C}}\right)\cosh(\gamma L) + L'\frac{\mathrm{V_R Z_{Ser}}}{2\mathrm{Z_C}^2}\sinh(\gamma L') + L'\frac{\mathrm{I_R Z_{Ser}}}{2\mathrm{Z_C}}\cosh(\gamma L') \quad (4.46)$$

The vector $[\Psi]$ is defined as:

$$[\Psi] = [\mathrm{Z_C} \quad \gamma]^T \quad (4.47)$$

Starting from an initial guess, $[\Psi]$ can be updated iteratively. The N^{th} update is obtained as,

$$[\Psi]^{(p+1)} = [\Psi]^{(p)} + [\Delta\Psi]^{(p)} \quad (4.48)$$

where $[\Delta\Psi] = -([H]^T[H])^{-1}[H]^T[F]$. The matrix $[H]^T[H]$ is a 2×2, non-singular, complex-valued, symmetrical matrix irrespective of the number of measurements and therefore, its inverse can easily be calculated regardless of the number of measurements sets. The iteration process is terminated when the variable update reaches within a specified tolerance. The initial values of the unknown parameters can be obtained using the theoretical calculations or use typical values for the given transmission line configuration. Once $\mathrm{Z_C}$ and γ are known, final transmission line parameters can be obtained from (4.28)-(4.30) similar to the proposed algorithm 2.

Algorithm 3 can be easily modified to estimate the parameters when the series compensator is completely bypassed or the parameters of an uncompensated transmission line by substituting $Z_{Ser} = 0$ in (4.39) and (4.40).

4.6.4 Application to Other Configurations

If the series compensator is located at the receiving end of the transmission line as shown in Figure 4.3, all three proposed algorithms can be used with a modified V_R, where V_R is replaced with V'_R.

$$V'_R = V_R + I_R Z_{Ser} \tag{4.49}$$

Similar approach can be realized if the series compensator is located at the sending end.

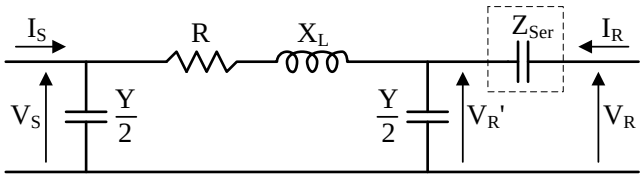

Figure 4.3 The equivalent model of a series compensator at the receiving end

If a shunt reactor is located at the receiving of the line as shown in Figure 4.4, the proposed algorithms can be applied with a modified I_R, where I_R is replaced with I'_R.

$$I'_R = I_R - I_{Sh} \tag{4.50}$$

where $I_{Sh} = V_R / Z_{Sh}$ and Z_{Sh} is the impedance of the shunt compensator.

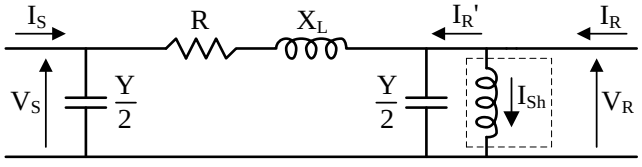

Figure 4.4 The equivalent model of a shunt reactor at the receiving end

As real time synchrophasor measurements are used to estimate the transmission line parameters, the data window is advanced with each PMU reporting. It is assumed that both the sending and the receiving end PMUs ensure the same reporting rate. All of the proposed algorithms treat parameters constant during the data window. The estimated transmission line parameters are updated each time a new PMU measurement set is reported.

4.7 Performance Validation – Simulations

The performance of the proposed transmission line parameter estimation algorithms and other existing approaches (Method A-F) was assessed under different conditions. The performance was tested through real-time simulations, hardware experiments and using the actual field data.

The two-area, four-generator benchmark power system [29] used for the study consisted of two areas connected through a tie-line as shown in Figure 4.5. It was assumed that PMUs are installed at two ends of the tie-line as indicated in Figure 4.5. The tie-line is operated at 230 kV and has a length of 220 km, and transfers 356 MW under base case conditions. The power system was simulated in a RTDS™ real-time simulator and the distributed parameter transmission line model (Bergeron) available in RTDS simulator was used to represent the transmission line under study. The RTDS transmission line module calculates the theoretical values of line parameters from the conductor data and the line geometry [72]. This detailed model considers the distributed nature of parameters, mutual coupling between phases and travel times. The synchrophasor measurements

required as inputs were obtained through the P-class PMU model available in RTDS simulator [73], at a reporting rate of 60 frames/s. The positive sequence voltage and current phasors of the sending and the receiving ends were collected using openPDC™ phasor data concentrator [74] and saved to a database. The proposed three algorithms were implemented in RTDS and thus operated in online mode. The other algorithms, which were implemented in MatLab™, used archived data as inputs.

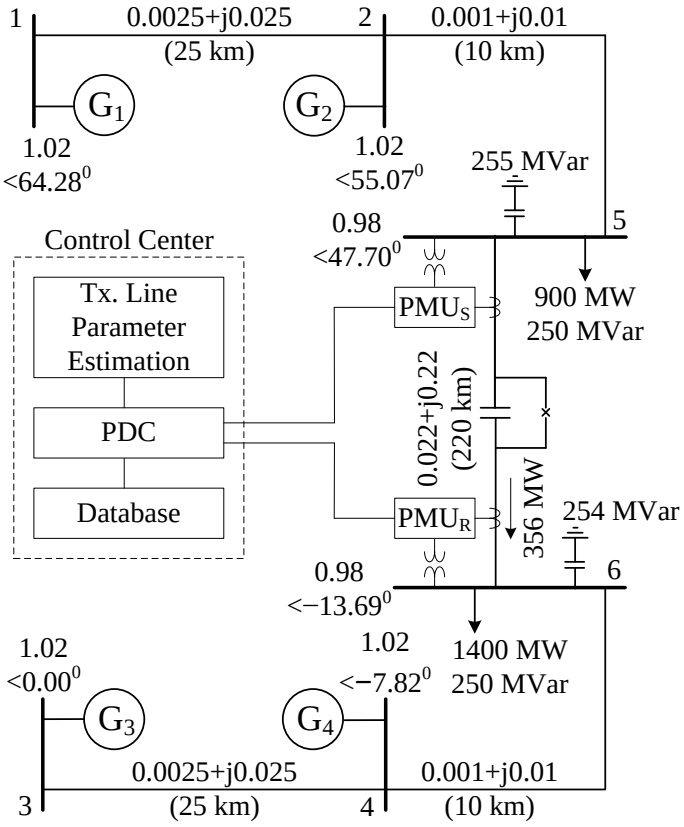

Figure 4.5 Simplified two-area four generator power system

Outputs of all algorithms estimate the series resistance, series inductive reactance and the shunt capacitive susceptance of the equivalent π-model of the transmission line. A data window of 15 synchrophasor measurements was used for estimations except for meth-

ods E and F, which were based on a single measurement. Estimations obtained under different conditions are compared with the theoretical values given by the RTDS transmission line module in Table 4.1.

Table 4.1 Theoretical transmission line parameters of the tie-line

Parameter	R (Ω)	X_L (Ω)	y_c (S)
Value	11.64	116.40	6.898×10^{-4}

4.7.1 Transmission Line Parameters under Ideal Conditions

The transmission line parameters were estimated under ideal conditions, i.e. when the transmission line was ideally transposed and the PMU measurements were noise free. The estimated parameters are shown in Table 4.2. According to the results, all algorithms perform very well under ideal conditions. The estimation errors (compared to theoretical values) are less than 1.5% for all parameters, for all algorithms. The accuracy level remained the same even for the series compensated case, where only Algorithm 3 can be applied. Algorithm 3 always converges within 10 iterations under noise free conditions.

Table 4.2 Transmission line parameters estimated by different algorithms

	R		X_L		y_c	
	Value (Ω)	Error (%)	Value (Ω)	Error (%)	Value (S)	Error (%)
Algorithm 1	11.50	1.20	114.87	1.32	6.945×10^{-4}	0.68
Algorithm 2	11.50	1.20	114.87	1.32	6.945×10^{-4}	0.68
Methods A – F *	11.50	1.20	114.87	1.32	6.945×10^{-4}	0.68
Algorithm 3 †	11.50	1.20	114.87	1.32	6.943×10^{-4}	0.66

* all yield the same estimate up to prescribed no. of significant digits

† series compensated transmission line (L_1 = 66 km, k = 50%)

4.7.2 Effect of Line Length under Ideal Conditions

The transmission line length was varied from 11 km to 440 km in steps of 11 km and the estimates of R (Ω), X_L (Ω), and y_c (S) were obtained. The variations of the estimation errors with the line length are plotted in Figure 4.6. The proposed algorithms 2 and 3, as well as other methods yielded similar results. The percentage error of the estimated resistance was high when the transmission line length was very short (<44 km), partly due to smaller magnitudes of actual resistance. However, the errors remained around 2% even when the length was over 400 km. The percentage estimation errors of X_L, and y_c remained nearly constant around 1.3% and 0.7%, respectively.

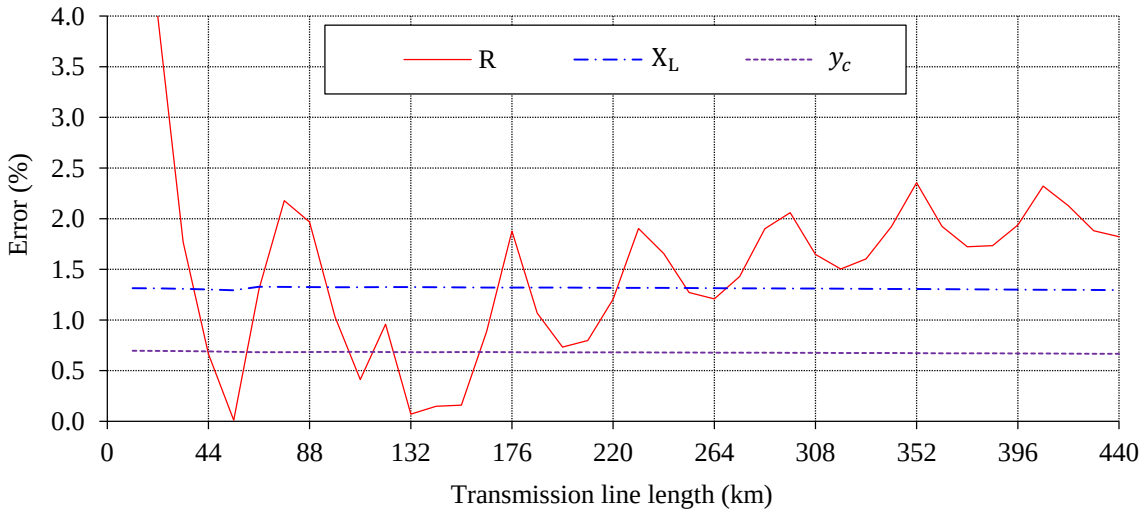

Figure 4.6 Variations of the errors with transmission line length

4.7.3 Effect of the Degree of Compensation

Algorithm 3 proposed for estimation of the parameters of series compensated transmission lines was tested under different degrees of compensation. The line length was 220 km and the series compensator was located at 66 km from the sending end. Ac-

cording to the variations of the estimation errors are shown in Figure 4.7, performance was not affected by the degree of compensation.

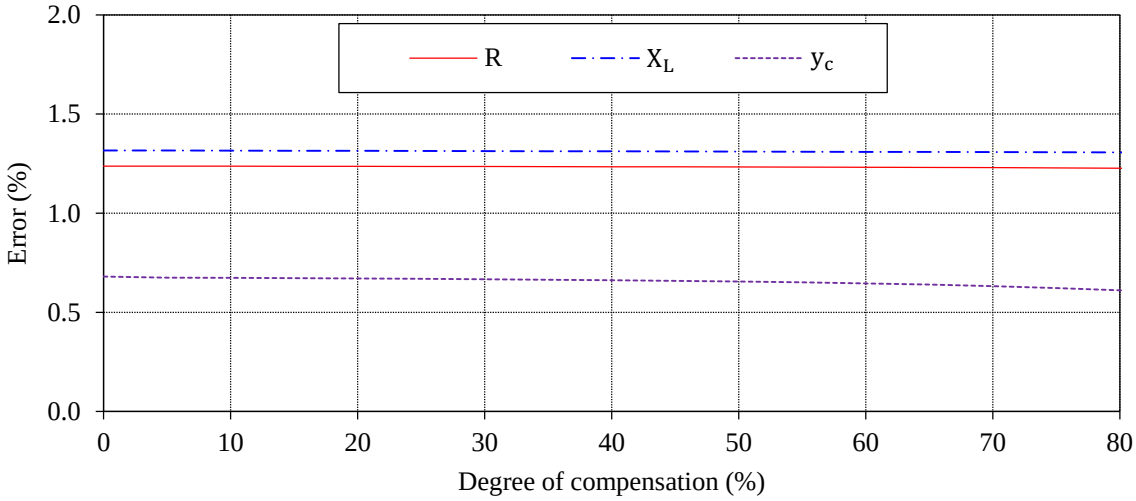

Figure 4.7 Variations of errors with the degree of compensation

4.7.4 Effect of the Location of Series Compensator

In this experiment, Algorithm 3 was used to estimate the parameters of the same series compensated transmission line, with 50% compensation. The location of the series compensator was varied from sending end to receiving end. The percentage estimation errors for R, X_L, and y_c are shown in Figure 4.8. The errors of resistance estimation seemed to increase slightly, when the series compensator was close to an end, but the errors were remained below 2% for all cases. Generally, the algorithm is not affected by the location of series compensator.

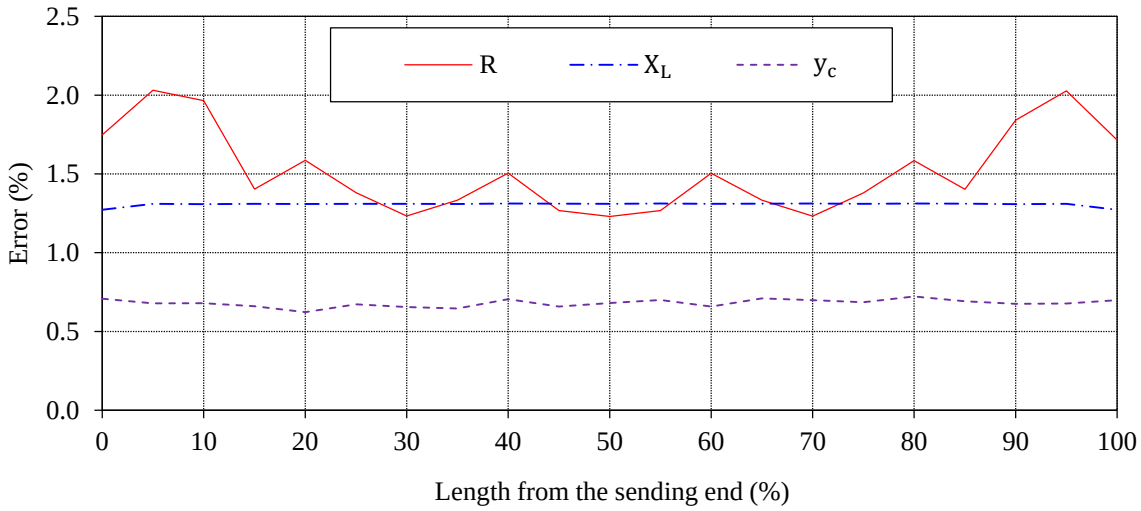

Figure 4.8. Variations of the errors with the location of the series compensator

4.7.5 Effect of Unbalance

All parameter estimation algorithms were developed based on the per-phase equivalent model of a transmission line, where balanced three-phase voltages and currents are implicitly assumed. However, in practice power systems are not ideally balanced. In order to test the performance of the algorithms under an unbalanced condition, unbalanced loads given in Table 4.3 were introduced to the simulated power system. Voltage and current waveforms observed at the sending and the receiving ends are shown in Figure 4.9.

Table 4.3 Unbalanced loads connected to bus-5 and bus-6

Load	Bus-5			Bus-6		
	Phase-A	Phase-B	Phase-C	Phase-A	Phase-B	Phase-C
Active (MW)	500	300	100	400	200	800
Reactive (MVar)	125	75	50	80	40	130

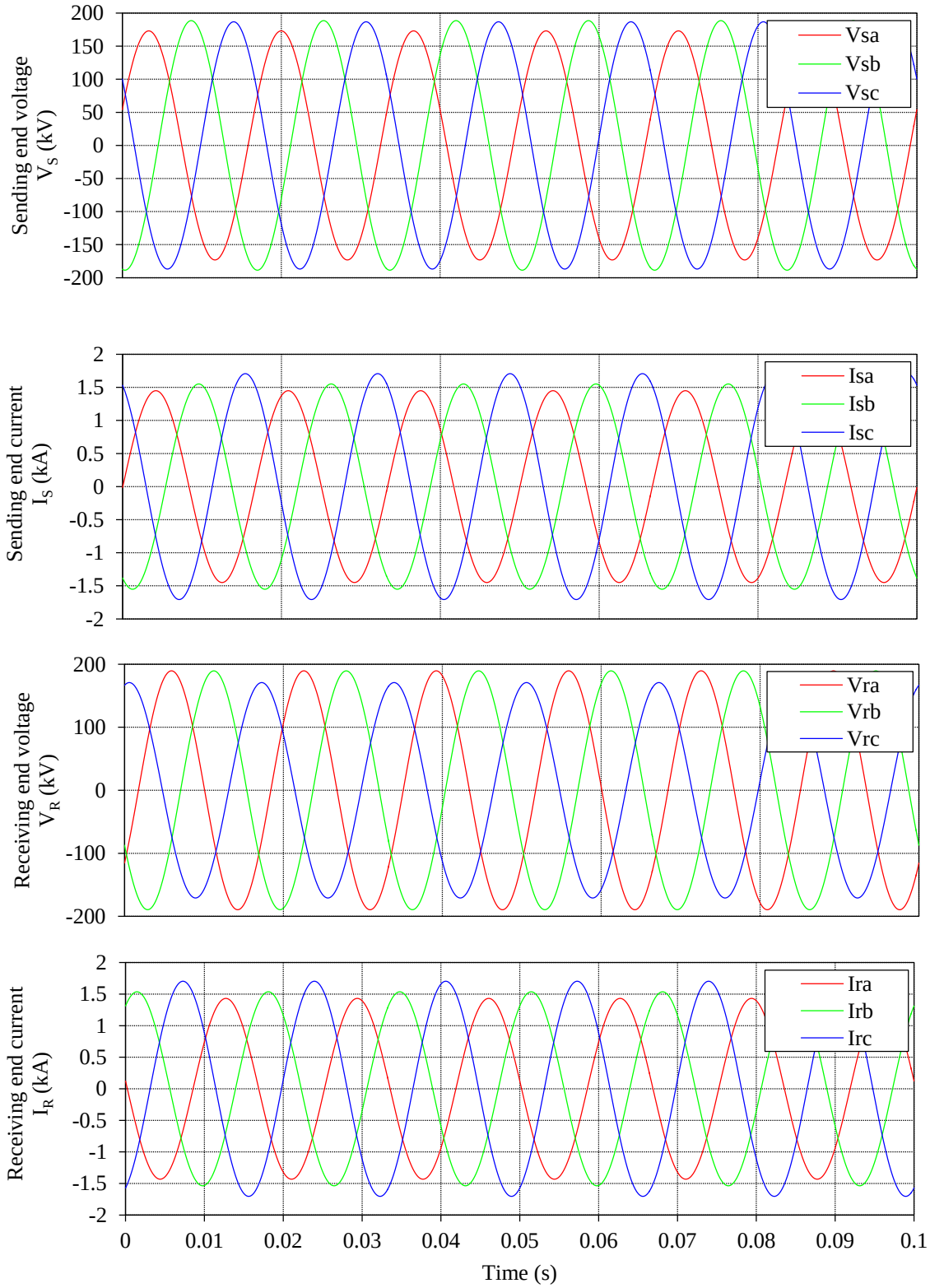

Figure 4.9. Waveforms at sending and receiving ends under unbalanced condition

The estimated transmission line parameters are compared with the theoretical values in Table 4.4. The estimated errors are less than 2% even under the unbalanced conditions. Voltage and current unbalance had minimal effect because the positive sequence phasor measurements were used in the calculations.

Table 4.4 Parameters estimated under unbalanced conditions

	R		X_L		y_c	
	Value (Ω)	Error (%)	Value (Ω)	Error (%)	Value (S)	Error (%)
Algorithm 1	11.48	1.37	114.86	1.32	6.945×10^{-4}	0.68
Algorithm 2	11.48	1.37	114.86	1.32	6.945×10^{-4}	0.68
Methods A – F *	11.48	1.37	114.86	1.32	6.945×10^{-4}	0.68
Algorithm 3 †	11.49	1.26	114.87	1.31	6.943×10^{-4}	0.66

* all yield the same estimate up to prescribed no. of significant digits

† series compensated transmission line (L_1 = 66 km, k = 50%)

Long transmission lines are usually transposed but there are cases where transmission lines are not transposed. The impact of unbalanced currents is higher when a transmission line is not transposed. Thus, the previous simulation experiment was repeated with a non-transposed line model, and the estimated transmission line parameters are compared with the theoretical values in Table 4.5. Even for this case, the estimated parameters have an error less than 2%.

Table 4.5 Estimated parameters under unbalanced, non-transposed conditions

	R		X_L		y_c	
	Value (Ω)	Error (%)	Value (Ω)	Error (%)	Value (S)	Error (%)
Algorithm 1	11.78	1.20	114.65	1.51	6.960×10^{-4}	0.90
Algorithm 2	11.78	1.20	114.65	1.51	6.960×10^{-4}	0.90
Methods A – F *	11.78	1.20	114.65	1.51	6.960×10^{-4}	0.90
Algorithm 3 †	11.54	0.82	114.66	1.49	6.952×10^{-4}	0.78

* all yield the same estimate up to prescribed no. of significant digits

† series compensated transmission line (L_1 = 66 km, k = 50%)

4.7.6 Parameter Estimation under Noisy Conditions

Phasor estimation itself is a filtering process and the anti-aliasing filters as well as additional backend filters [5] in PMUs provide good immunity against the high frequency noise in measured signals. However, it is impossible to completely eliminate the effect of noise in practice. The performance of the proposed algorithms under noisy conditions was evaluated by adding a zero mean Gaussian noise to the input voltage and current waveforms before they are fed into the PMU models. The accuracy of synchrophasor measurements is expressed in terms of total vector error (TVE) [5]. Tests showed that with this type of noise, signal-to-noise ratios (SNRs) lower than 30 dB can result in TVEs exceeding 1%, which is the acceptable limit under most steady-state and dynamic conditions [5]. Variations of the estimated values of transmission line resistance using noisy signal inputs with different SNRs are shown in Figure 4.10. These results were obtained with Algorithm 1. Similar plots can be obtained for the other transmission line parameters and other methods as well.

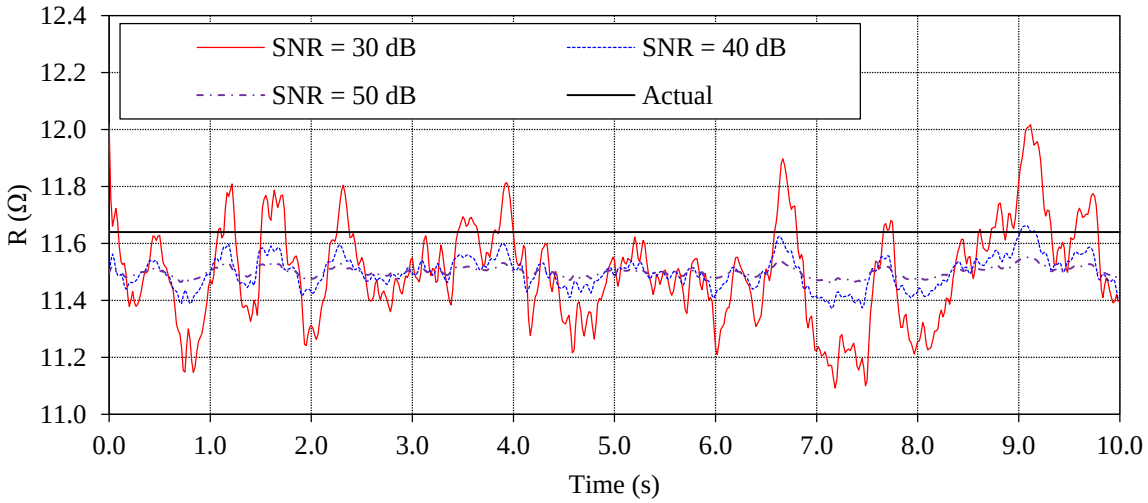

Figure 4.10 Transmission line parameters at different noisy levels (algorithm 1)

Random fluctuations in the estimated values become higher with increasing noise levels (decreasing SNR). Careful examination of the results show that (i) estimations of X_L is the least affected by the noise, (ii) estimation errors of R, and y_c start to quickly increase when SNRs drop below 40 dB. It was also observed that method B, method C and the algorithm 3 did not converge for some data points even after 50 iterations when SNRs drop below 40 dB. They were programmed to stop after 50 iterations and report the output, thus the maximum errors are slightly high for such cases. Occasional non-convergence and larger errors under noise are drawbacks of method B, method C and the algorithm 3. The maximum estimation errors observed under 35 dB noise level during a period of 10 seconds are given in Figure 4.11. Methods E & F are highly vulnerable to random noise as they use a single measurement set. All other algorithms are not much affected at this level of random noise.

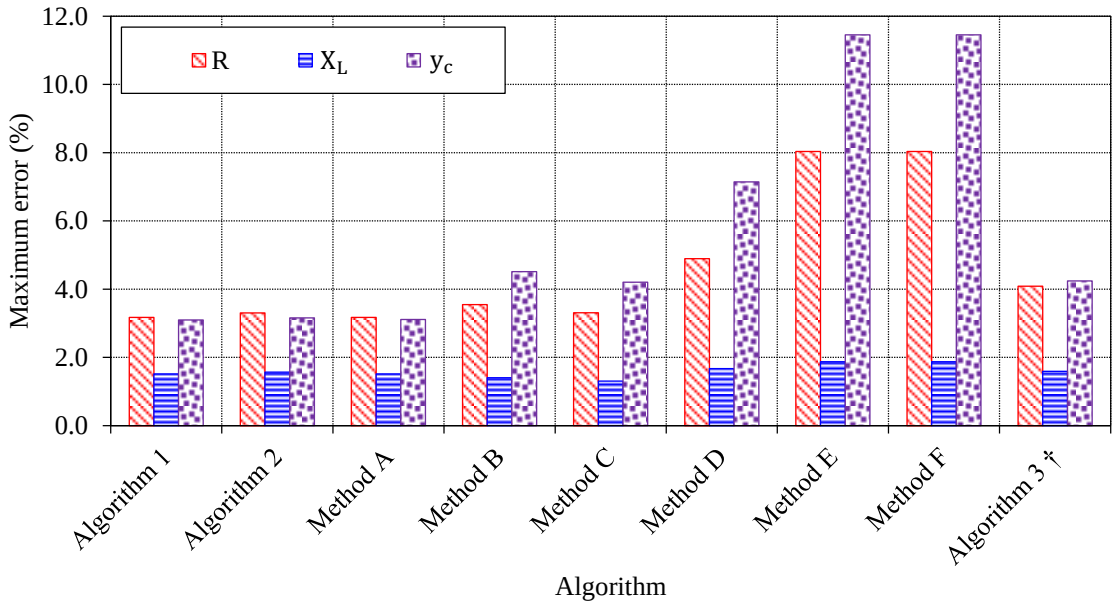

Figure 4.11 Maximum errors under noise (SNR = 35 dB)

4.7.7 Data Window Length

If PMU measurements are totally noise-free, then a single set of measurements is enough to estimate transmission line parameters. However, practical measurements are contaminated with noise from various sources and therefore, use of several measurements can help to increase the accuracy of parameter estimations. For example, the variation of line resistance R estimated with a single measurement is compared with that estimated using 15 measurements (data window size, w=15), when the SNR=35 dB in Figure 4.12.

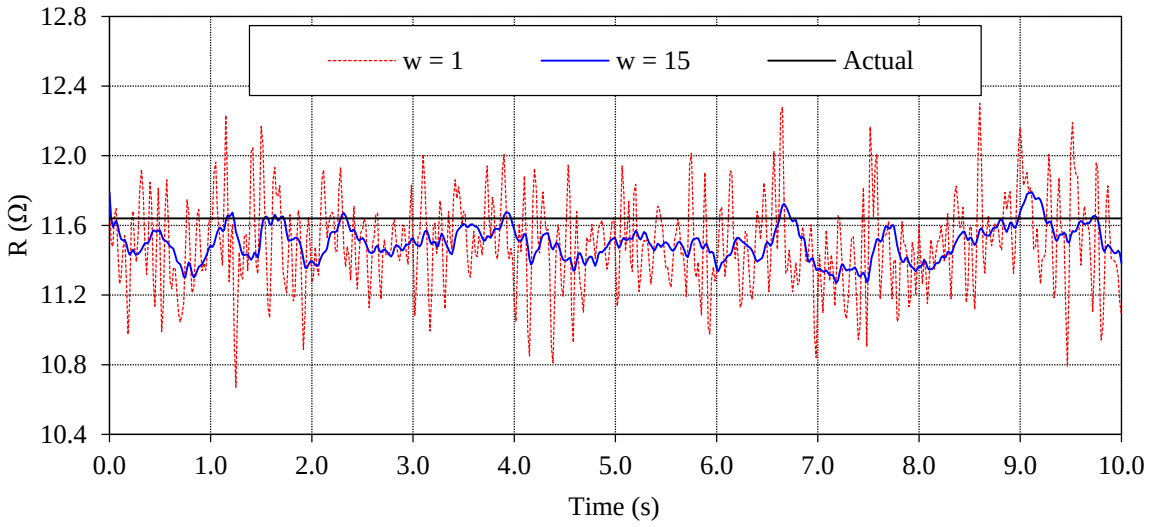

Figure 4.12 Line parameters with different data window lengths (SNR = 35 dB)

The fluctuations and the maximum error in the estimated R are higher with the single dataset compared to the estimated R with 15 datasets. The other transmission line parameters also showed similar variations. Increasing window lengths reduce the maximum error in estimated transmission line parameters, but these reductions become insignificant for data window lengths above 15 as seen in Figure 4.13, when the SNR in input analog signals is around 35 dB.

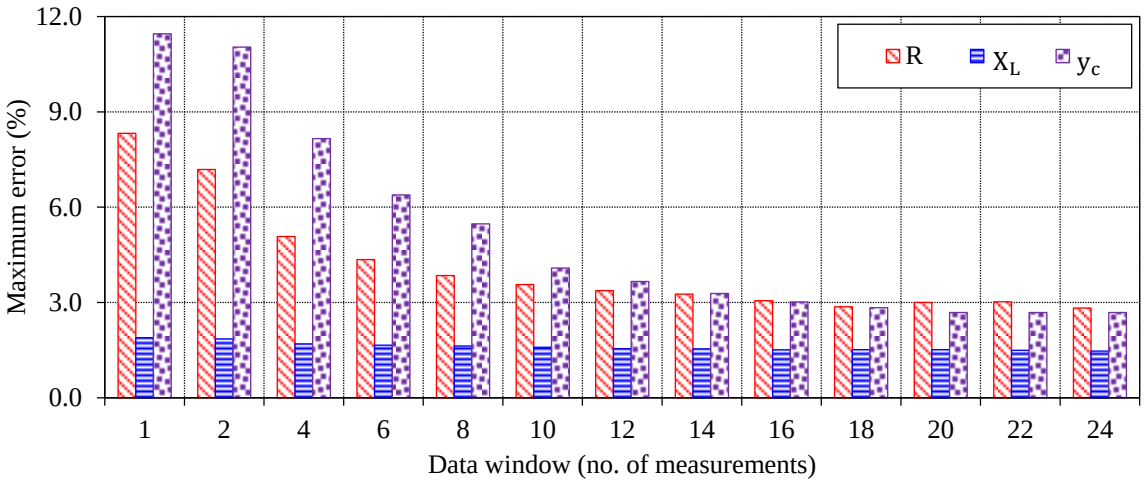

Figure 4.13 Maximum error at different data window lengths (SNR = 35 dB)

4.7.8 Comparison of Computational Efficiency

The main advantage of the proposed new line parameter estimation algorithms is the computational efficiency, especially when implementing in real-time monitoring environment. The computational complexities of the proposed algorithms and the existing methods were examined and expressed in terms of big O notation. The results are summarized in Table 4.6 for easy comparison.

Table 4.6 Computational complexities of different algorithms

Algorithm	Computational complexities	
	Big O notation	Comments
Algorithm 1	$O(N)$	Linear
Algorithm 2	$O(N)$	Linear
Method A	$O(N^2)$	Quadratic
Method B	$O(mN)$	Depends upon no. of measurements and no. of iterations
Method C	$O(mN)$	Depends upon no. of measurements and no. of iterations
Method D	$O(mN^3)$ †	Depends upon no. of measurements and no. of iterations

* Methods E and F are ignored since they are based on a single measurement

† It is assumed that the matrix inversion obtained from the Gauss–Jordan elimination method

Alternatively, the computational efficiency of different algorithms can be experimentally analysed by measuring the computational time of the algorithms for a given input data set under the same operating conditions. In order to make a fair comparison, all line parameter estimation algorithms should be implemented in the same programming language and executed on the same computer. In the test conducted, the two algorithms proposed for uncompensated line parameters estimation (algorithm 1 and algorithm 2) and the existing algorithms were all implemented in MatLAB R2015a, and one minute of PMU measurements (60 frames/s × 60 seconds = 3600 measurements) were used. The programs were run on a PC with Windows 7 OS, Intel® CoreTM i7-2600 CPU @ 3.40GHz, 4 Core Processor, and 16 GB physical memory. The data window length was selected as 15 measurements. The average computational times obtained from 25 tests are compared in Table 4.7.

Table 4.7 Computational time of different algorithms

Algorithm	Computational time (s)
Algorithm 1	0.074
Algorithm 2	0.115
Method A	0.287
Method B	2.366
Method C	2.372
Method D	31.937

From the results in Table 4.6 and Table 4.7, it is obvious that the proposed new linear LS based algorithms are significantly more efficient in terms of computational time, compared to the other existing algorithms. The computational time of Method A, which is the fastest among existing algorithms, is 387% of the computational time of Algorithm

1 (250% of the computational time of Algorithm 2). When monitoring a single transmission line, the computational time of any of the algorithms considered in Table 4.7 would not be a major issue with the capability of modern computers. However, in a situation where hundreds of transmission lines in a large power system are being monitored in real-time at a central control centre, the proposed new algorithms will provide significant advantage in terms of the required computing resources.

4.8 Performance Validation – Experimental Setup

In this section, the proposed transmission line parameter estimation algorithms, along with other methods (Method A-F), are tested in a laboratory setup. The aim of this experiment is to validate the algorithms with practical measurements. It should be noted that usefulness of field measurements for validations is limited, because the actual parameters of a transmission line cannot be established without specialized offline tests. The block diagram and the actual arrangement of the experimental setup are shown in Figure 4.14 and Figure 4.15, respectively.

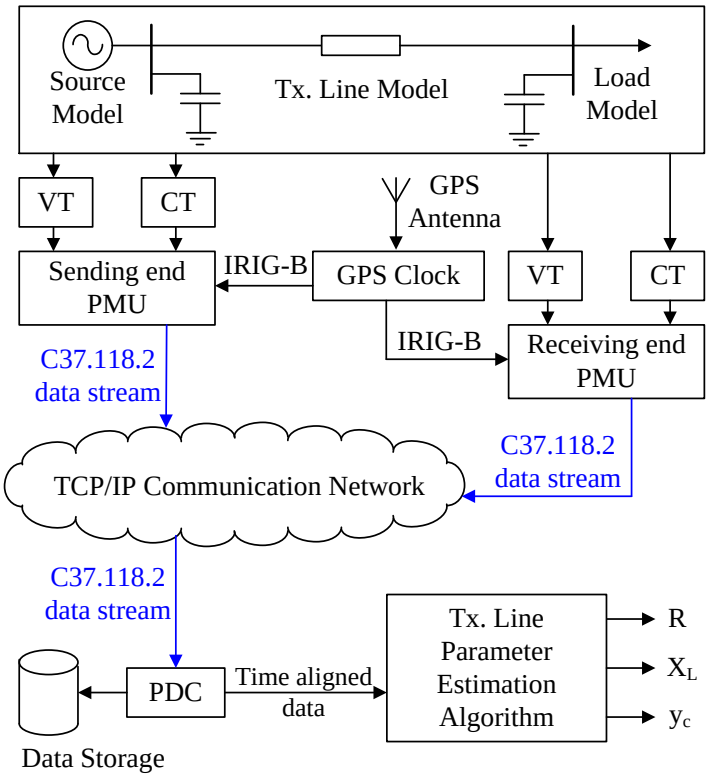

Figure 4.14 Experimental setup – Block diagram

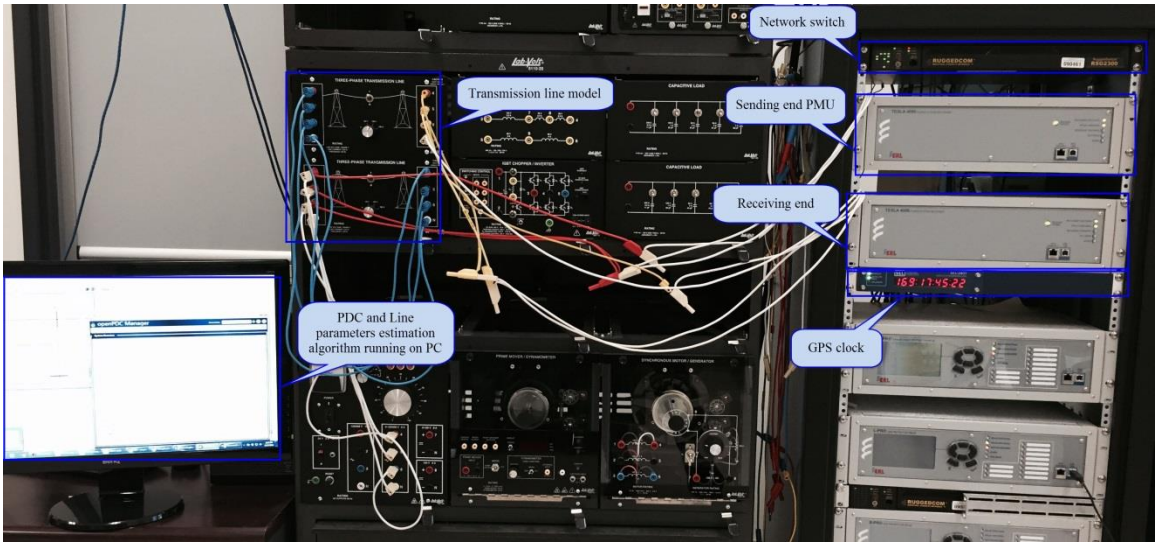

Figure 4.15 Experimental setup – Actual arrangement

The transmission line module of a LabVolt™ power system test bench [75] augmented with shunt capacitances was used to create a π-network representing a three-phase transmission line. The three-phase source and load modules of the same test bench were connected to sending and receiving ends of π-network, respectively. The voltage and current signals at two ends of the transmission line were fed to two ERL Phase™ TESLA 4000 recorders with PMU capability through instrument voltage and current transformers [76]. A SEL-2407 GPS clock [77] provided inter-range instrumentation group time code format B (IRIG-B) signal to PMUs. The PMUs in TESLA 4000 were configured to report synchrophasors at 60 frames/s to openPDC™ v2.0 [74] PDC through a TCP/IP network. The PDC, which aligned the data according to the time tags, provided data to the transmission line parameter estimation algorithms. Similar to the simulations based study, a data window of 15 reportings were used except for the methods E and F, which are based on a single measurement.

The estimations obtained under different conditions are compared with the direct measurements obtained for the LabVolt transmission line modules given in Table 4.8. The transmission line parameters are estimated under balanced conditions given in Table 4.9, and the results under unbalanced conditions (obtained using unbalanced loads) are provided in Table 4.10.

Table 4.8 Parameters for the experimental transmission line setup

Parameter	R (Ω)	X_L (Ω)	y_c (S)
Value (Uncompensated line)	19.5	120.0	5.13×10^{-4}
Value (Series compensated line)	9.2	120.0	10.25×10^{-4}

Table 4.9 Line parameters estimated under balanced condition

	R		X_L		y_c	
	Value (Ω)	Error (%)	Value (Ω)	Error (%)	Value (S)	Error (%)
Algorithm 1	19.27	1.18	120.85	0.71	5.167×10^{-4}	0.78
Algorithm 2	19.28	1.13	120.84	0.70	5.167×10^{-4}	0.78
Methods A – F *	19.27	1.18	120.85	0.71	5.167×10^{-4}	0.78
Algorithm 3 †	9.47	2.93	118.61	1.16	10.90×10^{-4}	6.32

* all yield the same estimate up to prescribed no. of significant digits

† series compensated transmission line (k = 33.5%)

Table 4.10 Line parameters estimated under unbalanced condition

	R		X_L		y_c	
	Value (Ω)	Error (%)	Value (Ω)	Error (%)	Value (S)	Error (%)
Algorithm 1	20.29	4.05	121.38	1.15	5.166×10^{-4}	0.76
Algorithm 2	20.29	4.05	121.37	1.14	5.166×10^{-4}	0.76
Methods A – F *	20.29	4.05	121.38	1.15	5.166×10^{-4}	0.76
Algorithm 3 †	9.63	4.67	118.62	1.15	10.87×10^{-4}	6.03

* all yield the same estimate up to prescribed no. of significant digits

† series compensated transmission line (k = 33.5%)

The transmission line parameters obtained under balanced conditions using practical measurements are consistent with the actual values for all algorithms; the maximum errors are less than 2% for uncompensated lines. However, the estimation error for the shunt susceptance (obtained with algorithm 3) increases to 6% in the case of series compensated transmission line. Furthermore, it is observed that the maximum errors increase under unbalanced conditions; however, they remain below 5% for R and below 2.5% for X_L, and y_c. For the series compensated transmission line, the error for y_c remains around 6% even under unbalanced conditions. It should be noted that the LabVolt transmission

line model uses iron-core reactors, and the slight waveform distortions due to core saturation, although minimized, contribute to increase the estimation errors.

4.9 Line Parameter Estimation with Field Measurements

The proposed algorithms and other existing methods were applied to evaluate parameters of an actual 226 km, 230 kV, single circuit transmission line. The estimations were obtained with three data sets obtained under three different conditions: (i) a cold day, (ii) a hot day, and (iii) a high load condition. The theoretically calculated transmission line parameters based on the line configuration at 25^0C are provided in Table 4.11.

Table 4.11 Theoretically calculated transmission line parameters (25 ^{0}C)

Parameter	R (Ω)	X_L (Ω)	y_c (S)
Value	13.89	108.03	8.143×10^{-4}

A shunt reactor was connected to the receiving end of the transmission line as in Figure 4.4 during low load conditions. Therefore, the receiving end current measurements were modified as per (4.50), when the line was shunt reactor compensated. As the weather and load conditions change, line parameters will vary, especially the value of R. Therefore, when reporting the difference between the estimated and theoretical resistance, the value of theoretical R given in Table 4.12 was adjusted using the theoretically estimated average conductor temperatures.

Table 4.12 Line parameters estimated with field data

		R		X_L		y_c	
		Value (Ω)	Diff. (%)	Value (Ω)	Diff. (%)	Value (S)	Diff. (%)
Cold day (Jan. 24, 2013)	Theoretical	11.20*	--	108.03 †	--	8.143×10^{-4} †	--
	Algorithm 1	13.23	18.16	107.35	0.67	8.380×10^{-4}	2.91
	Algorithm 2	13.23	18.17	107.35	0.67	8.380×10^{-4}	2.91
	Method A [19]	13.23	18.16	107.35	0.67	8.380×10^{-4}	2.91
	Method B [20]	13.22	18.04	107.34	0.64	8.375×10^{-4}	2.85
	Method C [61]	13.22	18.04	107.36	0.62	8.389×10^{-4}	3.02
	Method D [63]	13.23	18.17	107.35	0.63	8.380×10^{-4}	2.91
	Method E [20]	13.23	18.17	107.35	0.63	8.380×10^{-4}	2.91
	Method F [65]	13.23	18.17	107.35	0.63	8.380×10^{-4}	2.91
Hot day (Aug. 16, 2013)	Theoretical	14.31*	--	108.03 †	--	8.143×10^{-4} †	--
	Algorithm 1	16.66	16.47	106.70	1.22	8.359×10^{-4}	2.65
	Algorithm 2	16.66	16.45	106.70	1.22	8.359×10^{-4}	2.65
	Method A [19]	16.66	16.47	106.70	1.22	8.359×10^{-4}	2.65
	Method B [20]	16.63	16.26	106.64	1.28	8.358×10^{-4}	2.64
	Method C [61]	16.65	16.38	106.68	1.25	8.362×10^{-4}	2.68
	Method D [63]	16.66	16.45	106.71	1.22	8.359×10^{-4}	2.65
	Method E [20]	16.66	16.45	106.71	1.22	8.359×10^{-4}	2.65
	Method F [65]	16.66	16.45	106.71	1.22	8.359×10^{-4}	2.65
High load (Mar. 28, 2013)	Theoretical	12.56*	--	108.03 †	--	8.143×10^{-4} †	--
	Algorithm 1	13.92	10.78	107.25	0.72	8.385×10^{-4}	2.97
	Algorithm 2	13.89	10.54	107.26	0.71	8.385×10^{-4}	2.97
	Method A [19]	13.92	10.78	107.24	0.72	8.385×10^{-4}	2.97
	Method B [20]	13.88	10.45	107.25	0.72	8.379×10^{-4}	2.89
	Method C [61]	13.88	10.51	107.11	0.85	8.393×10^{-4}	3.07
	Method D [63]	13.89	10.54	107.26	0.71	8.385×10^{-4}	2.97
	Method E [20]	13.89	10.54	107.26	0.71	8.385×10^{-4}	2.97
	Method F [65]	13.89	10.54	107.26	0.71	8.385×10^{-4}	2.97

* adjusted to the conductor temperature

† change is insignificant

Average conductor temperature was calculated using the steady-state heat balance equation of the transmission line as prescribed in IEEE Standard 738-2012, the standard for calculating the current-temperature relationship of bare overhead conductors [23], [24],

$$q_c + q_r = q_s + I^2 R(T_{avg}) \tag{4.51}$$

where q_c and q_r are convective and radiated heat loss rates, q_s is the solar heat gain rate, I is the current flowing through the conductor, and $R(T_{avg})$ is the conductor resistance at the average temperature of the conductor T_{avg}. The weather data were obtained from the nearest weather stations [78] for the respective measurement periods. The methods for calculating q_c , q_s and q_r using the weather data are given in the standard.

The transmission line parameters estimated under different conditions are compared in Table 4.12. Note that the differences are not reported as errors, because there is no certainty that the theoretically calculated values are the actual values. The differences between the X_L, and y_c values obtained from the proposed algorithms and the traditional calculations remain less than 2% and 3% respectively. However, the estimated R values sometimes deviate up to 20% from the adjusted theoretical values. The estimations of the resistance are consistently higher than the theoretical values for all algorithms (except algorithm 3) considered, pointing to a possible error in the theoretically estimated resistance value. Another possible reason for deviations is the spatial and time averaging of weather data, especially the wind speed and direction (data represents averages over two-minute intervals) [78]. In the heat balance equation, the conductor temperature is highly sensitive to fluctuations in wind speed. Since it is very difficult and practically impossible

to include all contributing factors, a few assumptions were made during the theoretical calculations. For example, it was assumed that tower configuration and the soil resistivity are identical throughout the transmission line and the line is ideally transposed but it was not the reality. Furthermore, the conductor length was estimated using the length of the line and a uniform and constant sag; however, it varies with conductor expansions and contractions. In addition, any errors of instrument VTs & CTs can also contribute to the deviations.

The value of series resistance is the most uncertain estimate when using PMU measurements. In [79], a method is suggested to compensate offset errors in resistance or a conductor temperature by obtaining a reference temperature and the corresponding resistance.

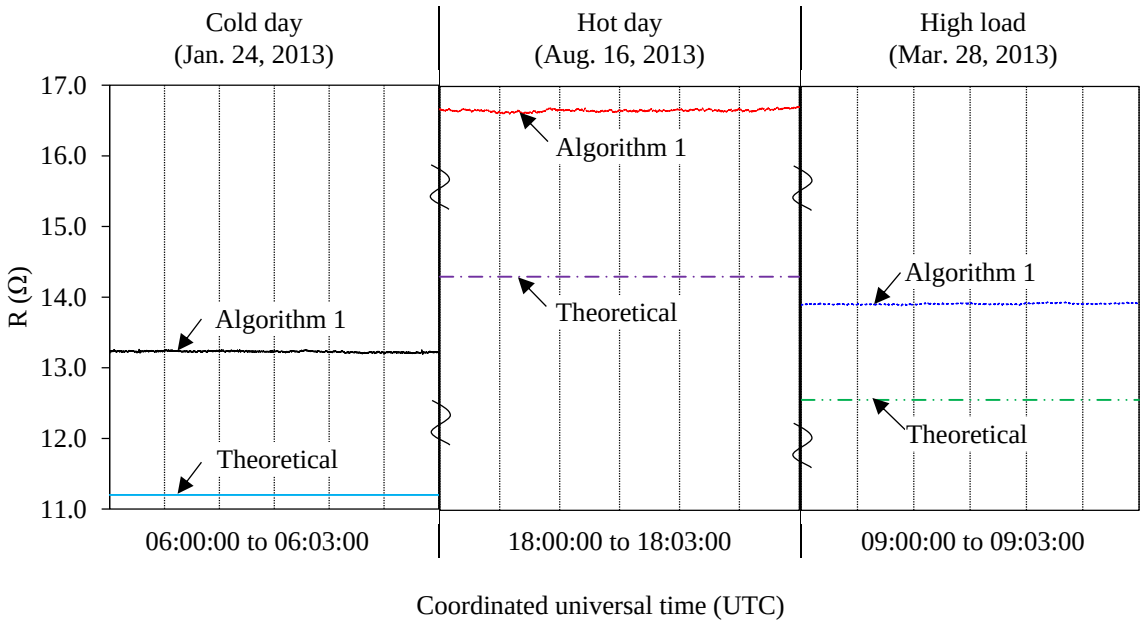

Figure 4.16 Estimations of resistances under different conditions

The variation of the transmission line resistance values estimated with Algorithm 1 during a period of 3 minutes is shown in Figure 4.16. The estimations show that the noise in the field measurements is minimal.

4.10 Sensitivity of Estimated Parameters to Measurement Errors

The errors in the estimated transmission line parameters due to random noise can be largely eliminated by using the proposed algorithms with a properly sized data window. However, if the PMU measurements are biased, it is difficult to estimate the transmission line parameters accurately. The CTs and PTs usually introduce magnitude and phase angle errors. In addition, timing errors of the GPS clock cause phase angle errors in the PMU measurements.

To investigate the sensitivity of the proposed algorithm 1 to such errors in measurements, bias-errors were introduced to the magnitudes and the phase angles of phasor measurements separately. It is assumed that the line is balanced and measurements are free of random noise. The magnitude bias-errors were varied from −1% to +1% while the phase angle bias-errors are changed from -1^0 to $+1^0$. The resulting errors in the estimated transmission line parameters are plotted in Figure 4.17 and Figure 4.18. Each curve is obtained by introducing a bias-error to the measurement given in the legend.

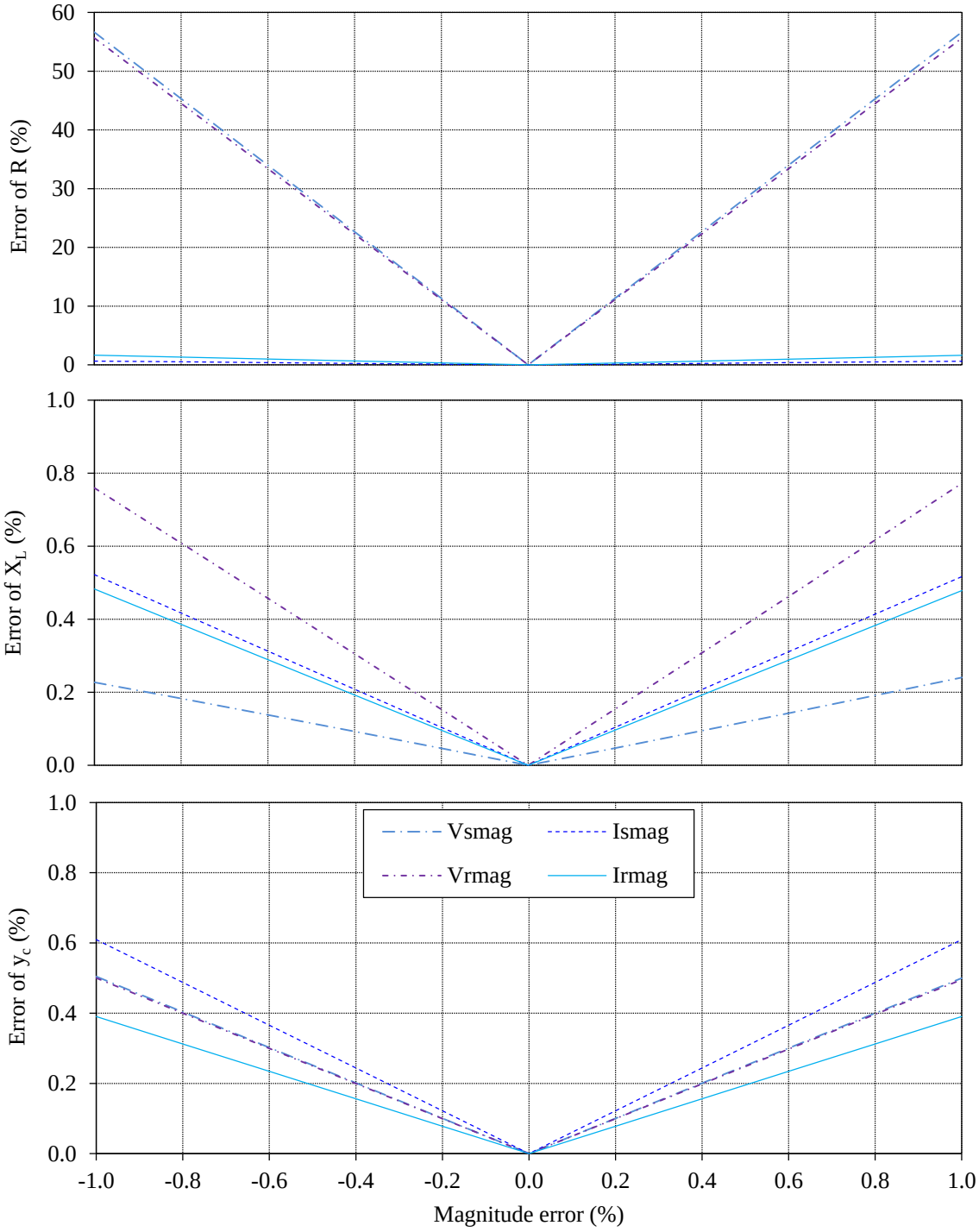

Figure 4.17 Errors in transmission line parameters with bias-errors in magnitude

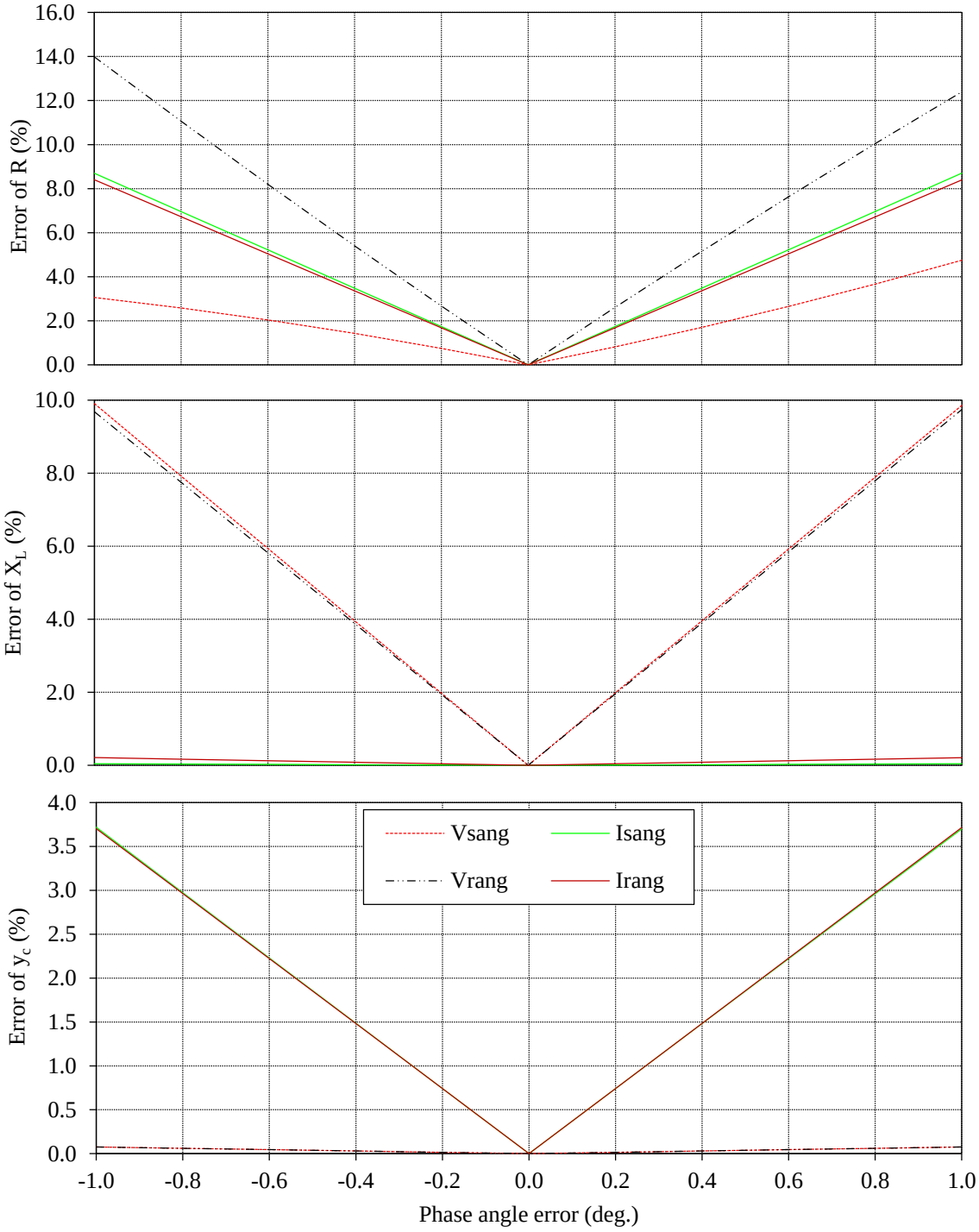

Figure 4.18 Errors in transmission line parameters with bias-errors in phase angle

It is found that R is very sensitive to the bias errors in the voltage magnitudes; a ±1% error in a voltage magnitude causes over 50% error in the R estimate. The estimations of X_L are more sensitive to voltage angle errors; a $\pm 1^0$ error in a voltage angle causes about 10% error in X_L. Also, $\pm 1^0$ error in a current angle causes about 4% error in the estimated y_c. Very similar relationships could be observed for the other algorithms. The series resistance is much more sensitive to measurement errors compared to the others.

In addition, it was found that the estimation errors of R due to voltage magnitude bias-errors depend upon the X/R ratio of the transmission line. At high X/R ratios, R is more sensitive to voltage magnitude errors as demonstrated in Figure 4.19.

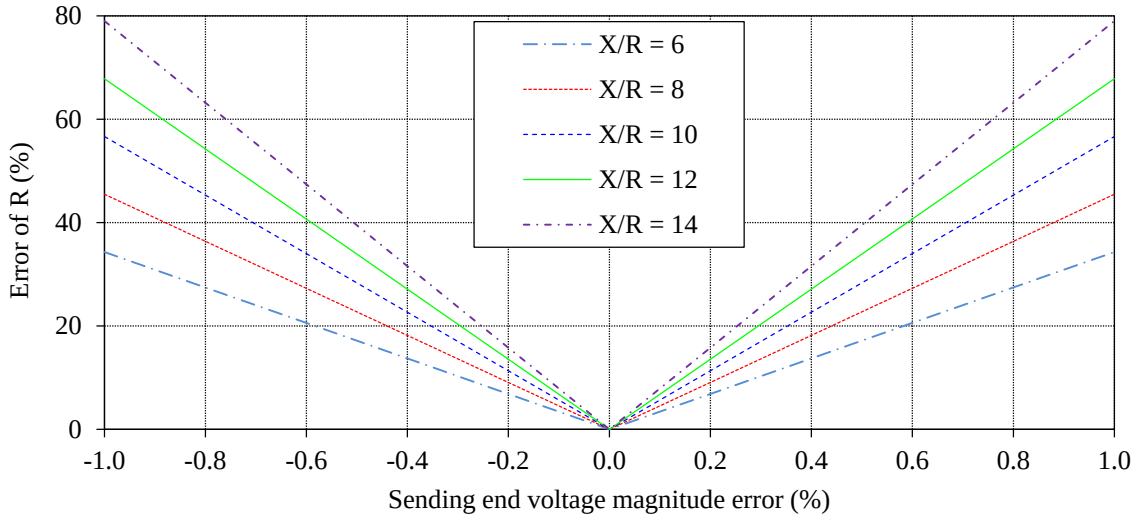

Figure 4.19 Variations of the error of estimated R at different X/R ratios

4.11 Concluding Remarks

Three synchrophasor measurements based transmission line parameter monitoring algorithms were derived as a simple synchrophasor application. The accuracy of the new

algorithms were evaluated and compared with the existing algorithms through a series of simulation and laboratory experiments. Despite the computational simplicity, performance of the proposed new algorithms 1 and 2 are always comparable or better than the existing algorithms under noisy, unbalanced, and practical measurement conditions. The proposed algorithm 3 demonstrated its ability of estimating line parameters of a series compensated transmission line without input excitation. Investigation of the sensitivity of the estimated parameter values to bias-errors in measurements revealed that the series resistance is highly sensitive to errors in the measured voltage magnitudes, the series reactance is most sensitive to the errors in voltage phase angles, and the shunt susceptance is most sensitive to errors in the current phase angles.

Chapter 5

Transient Stability Status Prediction in Power Systems

5.1 Introduction

In this chapter, a novel method to predict the transient stability status of a power system is proposed. First, a brief background of transient stability is given and the problem of transient stability prediction is defined. Then a review of the existing transient stability status prediction approaches with their advantages and disadvantages is presented. Finally, the concept for a new transient stability status prediction method is introduced with the aid of a single machine to infinite bus (SMIB) system. Application of the proposed method to a multi-machine system and implementation issues will be discussed in the next chapter.

5.2 Power System Transient Stability

A power system is a dynamic system that can be modeled by a set of differential and algebraic equations (DAEs) [28]-[30], [80], [81] given by,

$$\dot{x}(t) = f\big(t, x(t)\big) \tag{5.1}$$

$$0 = \mathrm{g}\big(t, x(t)\big) \tag{5.2}$$

where x is the state vector and its entries are state variables. Time is denoted by t and the derivative of a state variable x with respect to time is denoted by $\dot{x}$. The set of differential equations that model the generators, motors, their controls, and dynamics of other devices [82] are represented in (5.1), which is sufficiently differentiable and its domain includes the origin [18]. The state vector x may comprise of physical quantities in a system such as generator rotor angles, angular speeds, field voltages, damping winding currents, and state variables associated with other devices such as HVDC converters and flexible alternative current transmission system (FACTS) devices, or abstract mathematical variables associated with the differential equations [29]. The set of algebraic equations in (5.2) includes the equations of the network and static loads [82].

The power system has a stable equilibrium point (SEP) x_0 at time $t = t_0$ and must satisfy the equation,

$$f(t, x_0) = 0 \;\; ; \quad \forall \quad t \geq t_0 \tag{5.3}$$

The power system is referred to as stable, if as time $t \to \infty$, the trajectories of the state variables remain within the vicinity of the equilibrium point when subjected to a disturbance. This is also referred to as stability in the sense of Liapunov [81]. A special case

where the trajectories return to the original SEP as time $t \to \infty$, is referred to as asymptotically stable system.

The transition of a power system after subjecting to a disturbance or a fault is described by three sets of differential equations;

$$\dot{x}(t) = f^{pre}\big(t, x(t)\big) \qquad -\infty < t \leq 0 \tag{5.4}$$

$$\dot{x}(t) = f^{fault}\big(t, x(t)\big) \qquad 0 < t \leq t_{cl} \tag{5.5}$$

$$\dot{x}(t) = f^{post}\big(t, x(t)\big) \qquad t_{cl} < t < \infty \tag{5.6}$$

The pre-disturbance or the initial steady-state is expressed in (5.4) when the power system is settled at a SEP. The initial condition can be obtained from the classical power flow solution. At $t = 0$, a disturbance or a fault occurs and the system dynamics change. During $0 < t \leq t_{cl}$, the so called disturbance state or the faulty state, a number of switching events may occur due to the action of the protection and control devices, which remove the faulty elements from the network. Each switching event may change the network structure and giving rise to a different set of dynamic equations to represent each event. However, for simplicity it is assumed that there are no structural changes during $0 < t \leq t_{cl}$ and all switching events arise at $t = t_{cl}$. Therefore, only a single set of differential equations given in (5.5) is sufficient to represent the faulty state. When the disturbance or the fault is cleared the system is referred to as the post-disturbance or the final steady-state, where the system state is governed by (5.6).

The possible initial conditions for (5.6) can be obtained from the solution of (5.5) at each instant of time [83]. Thus, the initial condition depends upon the disturbance clearing time t_{cl}. Let us assume that the power system has a post-disturbance SEP x_p (i.e. is a

stable solution to (5.6)). The post-disturbance system is stable if the trajectories of (5.6) with the initial condition obtained from the solution of (5.5) at $t = t_{cl}$ will converge to x_p as $t \to \infty$. The largest value of t_{cl}, which satisfies the above criterion, is known as the critical clearing time [83].

The problem of predicting the transient stability, as used in this thesis, is to forecast whether the system will find a SEP or not, after a disturbance ($t > 0$) using the measurements of power system variables made during the disturbance state and post-disturbance state. Ideally, predictions should be made sufficiently before the power system becomes unstable, in order to allow time for activating emergency controls. It should be noted that this is quite different from the online-dynamic security assessment.

5.3 Previous Approaches for Transient Stability Prediction

In literature, there are a few basic approaches to predict the transient stability status of a power system: 1) time-domain simulations, 2) equal-area criterion and its extensions, 3) transient energy function (TEF) methods, 4) curve-fitting techniques, and 5) machine-learning based classification techniques.

5.3.1 Time-Domain Simulations

The time-domain simulation is the most straightforward routine where a set of DAEs given by (5.1) and (5.2) are solved using step-by-step numerical integration for a given

initial condition, and the trajectories of state variables along the time axis are obtained. In transient stability, variations of the generator rotor angles are the key concern. The simulation duration is normally limited to about 3 to 5 seconds following the disturbance [18], [28].

There are two approaches to solve DAEs: 1) the sequential approach, in which the system of DAEs are solved sequentially, and 2) the simultaneous approach, in which the differential equations in (5.1) are transformed into a set of algebraic equations, which is thereafter solved simultaneously with the algebraic equations in (5.2) [28].

The numerical integration methods are categorized into two, namely, explicit methods and implicit methods. The explicit methods such as Euler, predictor-corrector, Runge-Kutta (R-K) methods compute the state variables for the next integration step at the end of the previous integration step in terms of their values at the beginning of the integration step [28]. It is essential to consider the propagation of error in the application of explicit numerical integration techniques as minor errors made early in the integration process tend to be magnified at later steps [29]. If the propagation error is significant, the explicit methods are numerically unstable. Therefore, it is required to set an integration step smaller than the lowest time constant of the system and the accuracy depends on the size of the integration step. Implicit methods such as trapezoidal rule determine the state variables at the end of the current integration step in terms of both the values at the beginning of the previous integration step and the actual values of the current integration step [28]. Implicit methods are more numerically stable than explicit methods because the integration step size is less important.

Time-domain simulation is the standard tool for offline transient stability studies as the modern commercial transient stability simulation tools not only handle power systems with a large number of generators, but also include detailed models to represent the power system devices. However, time-domain simulations have not been widely used for real-time applications since the simulation speed is usually slower than real-time. In [84]-[86], post-disturbance rotor angle trajectories are obtained faster than real-time with the aid of several tools and techniques including high-speed computers, specialized parallel processing techniques, reduced-order generator models, piecewise constant-current load equivalents, piecewise constant transfer admittance equivalents, and an implicitly decoupled PQ integration technique. This approach requires specialized computing resources and is hard to implement for large power systems. However, the biggest drawback is the need for an accurate network configuration during and after a disturbance that is difficult to obtain in real-time without a specialized scheme similar to those of SPSs.

5.3.2 Equal-Area Criterion and Its Extensions

The equal-area criterion (EAC) is a popular graphical method, which is helpful to understand the basic factors that influence the transient stability of a power system [29]. The concept of EAC was developed by considering a single machine connected to an infinite bus through a transmission line. The machine is represented by a classical model (constant voltage source behind a transient reactance). The electrical output P_e at the generator terminal is expressed as,

$$P_e = P_{max} \sin \delta \tag{5.7}$$

where P_{max} is the maximum possible electrical power output and δ is the generator rotor angle measured with respect to the voltage angle of the infinite bus. The equation of motion or the swing equation for the single machine infinite bus (SMIB) system is,

$$\frac{2H}{\omega_s}\frac{d^2\delta}{dt^2} = P_m - P_e \tag{5.8}$$

where P_m is the mechanical power input, H is the inertia constant and ω_s is the synchronous speed (rad/s). Multiplying both sides by $2d\delta/dt$ and integrating gives,

$$\left[\frac{d\delta}{dt}\right]^2 = \int_{\delta_0}^{\delta_m} \frac{\omega_s(P_m - P_e)}{H} d\delta \tag{5.9}$$

where δ_0 is the initial rotor angle at the pre-disturbance SEP and δ_m is the maximum rotor angle. The criterion for stability is given by [29],

$$\left[\frac{d\delta}{dt}\right]^2 = \int_{\delta_0}^{\delta_m} \frac{\omega_s(P_m - P_e)}{H} d\delta = 0 \tag{5.10}$$

The power-angle curves for the three different conditions: a) pre-disturbance, b) during the disturbance, and c) post-disturbance are shown in Figure 5.1.

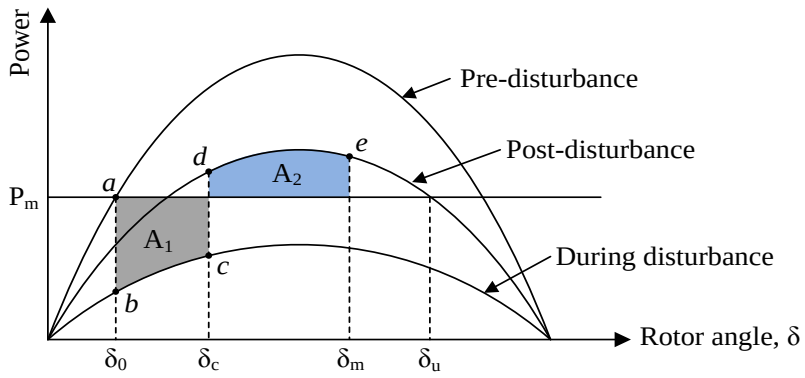

Figure 5.1 Power-angle curves for the three different conditions and areas defined in EAC

Initially, the power system operates at a SEP such that $P_m = P_e$ and $\delta = \delta_0$ (point *a*). The operating point instantaneously jumps from *a* to *b* when the disturbance occurs. Since $P_m > P_e$ the rotor accelerates until reaching the operating point at *c*. The energy gained by the rotor during the acceleration (δ changes from δ_0 to δ_c) is equal to area A_1 and is given by,

$$\text{Area } A_1 = \int_{\delta_0}^{\delta_c} (P_m - P_e)\, d\delta \tag{5.11}$$

Once the disturbance is cleared the operating point suddenly jumps from *c* to *d*. The rotor decelerates as $P_e > P_m$ and the operating point moves from *d* to *e*. The energy loss during the deceleration (δ changes from δ_c to δ_m) is equal to area A_2 and is expressed as,

$$\text{Area } A_2 = \int_{\delta_c}^{\delta_m} (P_e - P_m)\, d\delta \tag{5.12}$$

If the energy gain is equal to the energy lost (i.e. $A_1 = A_2$), then the post-disturbance system is stable. This is the basis for the EAC. The disturbance clearing angle δ_c can be increased such that $\delta_m = \delta_u$. This clearing angle is known as critical clearing angle and the corresponding time is known as the critical clearing time. Further increase of δ_c causes the post-disturbance system to become unstable because the resulting acceleration area is greater than that of the deceleration area (i.e. $A_1 > A_2$).

The major drawback of EAC is that the method cannot be directly applied to multi-machine systems with detailed generator models as it overlooks behaviours of speed governors and voltage regulators. Therefore, the concept of the EAC is extended to multi-machine systems in [87]-[90], and it is then referred to as extended EAC (EEAC). In this

approach, the multi-machine system is decomposed into two clusters, namely, the critical cluster and the remaining cluster. As its name implies the critical cluster is comprised with critical machines and their dynamic behaviour is represented as a single machine. The non-critical machines belonging to the remaining cluster are also modeled as a single machine. Thus, the dynamic behaviour of the multi-machine system is reduced to a two-machine system, which is further simplified to a SMIB system. The conventional EAC can then be applied to the reduced SMIB system, however, errors due to ignorance of the detailed dynamics are still inevitable.

5.3.3 Transient Energy Function Methods

Transient energy function (TEF) methods are based on the direct method of the Lyapunov stability principle, which allows one to determining the stability of a system without explicitly integrating the differential equations [81]. The principle behind this method is a generalization of the energy concepts associated with a system and its stability. If the total mechanical energy in a system decreases all the time, the system is stable and eventually settles down to an equilibrium point. The stability assessment is done by constructing an energy function, the so called Lyapunov function and to observe whether or not it declines [91].

Once a disturbance occurs in the power system, the electrical power outputs of nearby generators decrease, but their mechanical power inputs remain unchanged. The rotors of the generators absorb the excess mechanical power and accelerate; this results in an increase in the kinetic energy (KE) of the generators. When the disturbance is cleared, the kinetic energy is then converted into potential energy (PE), and power system tries to

absorb this energy to bring the system back to a new SEP. The ability of the energy absorption depends on the configuration of the post-disturbance network. There is an upper bound on the transient energy (critical energy level) that a given post-disturbance network configuration can absorb. Therefore, the power system stability assessment is done by constructing a Lyapunov function, which contains the kinetic and potential energy, and comparing with the critical energy level for a given disturbance [83].

As illustrated in Figure 5.2, the potential energy of the system is zero at the initial SEP, and the system gains kinetic and potential energy during the disturbance. The disturbance is then cleared at $\delta = \delta_c$ and the kinetic energy starts to transform into potential energy. The criterion for the stability is given as,

$$PE(\delta_c) + KE(\delta_c) \leq PE(\delta_u) \tag{5.13}$$

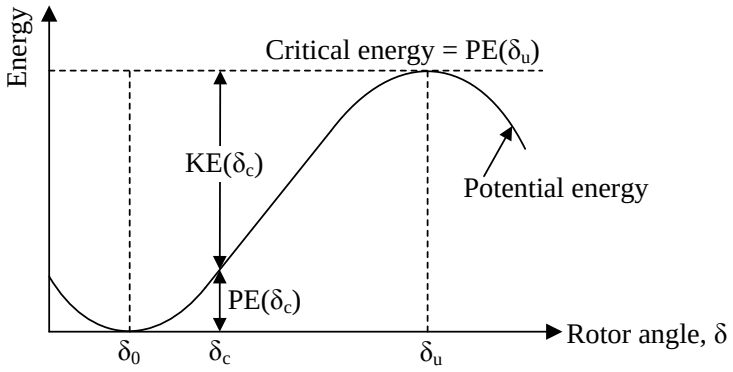

Figure 5.2 Energy-angle relationship [29]

Even though the TEF method has the ability to predict the stability status of the system immediately after the clearance point, it is often difficult to construct an accurate Lyapunov function and to determine the levels of kinetic and potential energy under cer-

tain disturbances for a given practical power system. Furthermore, determination of critical energy level is a major handicap when applying to relatively large power systems.

5.3.4 Curve-Fitting Techniques

Application of curve-fitting techniques to predict the future behavior of post-disturbance trajectories, especially of the rotor angles and generator speeds, are approaches used for predicting transient instabilities [92]- [97].

5.3.4.1. Prediction of Rotor Angle Trajectory

Reference [92] shows that the post-disturbance rotor angle (absolute angle) of a generator can be expressed in terms of Taylor series expansion as,

$$\delta(t_1) = a_0 + a_1 t_1 + a_2 t_1^2 + a_3 t_1^3 + \cdots \tag{5.14}$$

where it is assumed that the disturbance is cleared at $t = t_c$ and $t_1 = t - t_c$. The coefficients of (5.14) can be determined by substituting quantities including, but not limited to, angle, speed, and power of the post-disturbance system to the expressions that are given in [92]. The generator is first-swing stable if there exists a peak (or a valley) for the rotor angle expression (5.14). The existence of a peak is checked by observing the roots of the time derivative of (5.14), given by.

$$\dot{\delta}(t_1) = a_1 + 2a_2 t_1 + 3a_3 t_1^2 + \cdots = 0 \tag{5.15}$$

If (5.15) has a real positive root, the generator is declared as first-swing stable. However, if there is no real root or all the roots are negative, it implies that the generator is first-swing unstable. This procedure is repeated for all generators in order to observe the first-

swing stability status of the entire system. The authors claim that a third or fourth-order expansion is sufficient to obtain accurate estimates [92].

It is practically difficult to measure the rotor angle and the speed of a generator without special sensors. In [93], [94], rotor angle trajectory of a generator is predicted by only measuring the output power of the generator. The discrete format of the swing equation given in (5.8) can be written as,

$$t_{k+1} = t_k + \Delta t \tag{5.16}$$

$$\Delta\omega(t_{k+1}) = \frac{\omega_s}{2H}(P(t_k) - P_0)\Delta t \tag{5.17}$$

$$\delta(t_{k+1}) = \delta(t_k) + 0.5\Delta\omega(t_{k+1})\Delta t \tag{5.18}$$

where the disturbance occurs at $t = t_k$, Δt is the sampling period, P_0 is the electrical power output before the disturbance, $P(t_k)$ is the electrical power output measured after the disturbance. The absolute rotor angle is expressed as a 4th order polynomial function since a high-order polynomial becomes unstable in some cases [93], [94].

$$\delta(t) = a_0 + a_1 t + a_2 t^2 + a_3 t^3 + a_4 t^4 \tag{5.19}$$

Considering n (≥ 5) iterations of (5.16)-(5.18), the estimation vector for the rotor angle can be written as,

$$[X]_{(n\times 1)} = [\delta(0) \quad \delta(\Delta t) \quad \delta(2\Delta t) \quad \ldots \quad \delta(n\Delta t)]^T \tag{5.20}$$

The prediction model can be represented as,

$$[X]_{(n\times 1)} = [H]_{(n\times 5)} \times [A]_{(5\times 1)} \tag{5.21}$$

where,

$$[H]_{(n\times 5)} = \begin{bmatrix} 1 & 0 & 0 & 0 & 0 \\ 1 & \Delta t & (\Delta t)^2 & (\Delta t)^3 & (\Delta t)^4 \\ : & : & : & : & : \\ : & : & : & : & : \\ 1 & n\Delta t & (n\Delta t)^2 & (n\Delta t)^3 & (n\Delta t)^4 \end{bmatrix} \tag{5.22}$$

$$[A]_{(5\times 1)} = [a_0 \quad a_1 \quad a_2 \quad a_3 \quad a_4]^T \tag{5.23}$$

The parameter vector $[A]$ can be determined by using the least squares solution as,

$$[A] = ([H]^T[H])^{-1}[H]^T[Y] \tag{5.24}$$

The absolute rotor angle trajectories are predicted for each generator and then, relative rotor angle trajectories are determined with respect to a reference generator. If the predicted relative rotor angle of a generator is greater than 180^0, the system is expected to be unstable.

In literature, other approaches such as the grey Verhulst model, trigonometric function model, and auto regression prediction method [95], [96] are reported in predicting rotor angle trajectories based on the trend characteristics in post-disturbance period.

5.3.4.2. Prediction of Speed Trajectory

In [97], the speed of a generator is predicted as a truncated n^{th} order polynomial function. If $\widehat{\omega}(t)$ is the predicted value of speed at time t, it can be expressed as,

$$\widehat{\omega}(t) = a_0 + a_1 t + a_2 t^2 + \cdots + a_n t^n \tag{5.25}$$

Let Δt be the sampling period and considering N $(\geq n+1)$ measurements sets, the observation vector for the generator speed can be written as,

$$[Y]_{(N\times 1)} = [\omega(0) \quad \omega(\Delta t) \quad \omega(2\Delta t) \quad \dots \quad \omega(N\Delta t)]^T \tag{5.26}$$

The prediction model can be represented as,

$$[Y]_{(N\times 1)} = [H]_{(N\times n)} \times [A]_{(n\times 1)} \tag{5.27}$$

where,

$$[H]_{(N\times n)} = \begin{bmatrix} 1 & 0 & 0 & 0 & 0 \\ 1 & \Delta t & (\Delta t)^2 & \dots & (\Delta t)^n \\ : & : & : & : & : \\ : & : & : & : & : \\ 1 & N\Delta t & (N\Delta t)^2 & \dots & (N\Delta t)^n \end{bmatrix} \tag{5.28}$$

$$[A]_{(n\times 1)} = [a_0 \quad a_1 \quad a_2 \quad \dots \quad a_n]^T \tag{5.29}$$

The parameter vector $[A]$ can be determined by using the least squares solution as,

$$[A] = ([H]^T[H])^{-1}[H]^T[Y] \tag{5.30}$$

After estimating the model parameters, the predicted value for the speed can be obtained by,

$$\hat{\omega}(k\Delta t) = a_0 + a_1 k\Delta t + a_2(k\Delta t)^2 + \cdots + a_n(k\Delta t)^n \tag{5.31}$$

Once a new measurements set is available, the data window is advanced to obtain the updated model parameters. i.e.

$$[A_{new}] = ([H]^T[H])^{-1}[H]^T[Y_{new}] \tag{5.32}$$

If the trajectory of generator speed has a zero crossing, the generator is declared as first-swing stable. The zero crossings can be tested either by observing the change of sign, or by checking the availability of a positive real root. If the predicted speed trajectory does not have a zero crossing, then the system is first-swing unstable. This procedure is followed for all generators in order to observe their first-swing stabilities and ultimate-

ly the entire system stability status can be declared. It is recommended in [97] that second or third order polynomial models with 6 to 10 measurements set are adequate to obtain accurate prediction results.

Even though the curve-fitting methods do not require knowledge of the network configuration and parameters of power system, they are sensitive to the start-up time of the prediction and the sampling periods, thus prediction accuracy is poor.

5.3.5 Swing Center Voltage Method

Swing center voltage (SCV) is defined as the voltage at the location of a two machine equivalent system where the voltage value is zero when the internal angles between the two machines are 180^0 apart [98].

Consider a two machine system as shown in Figure 5.3. The left source represents a machine and its internal voltage angle, δ will advance during a power swing. The right source represents an infinite bus and its angle remains zero and unchanged with time.

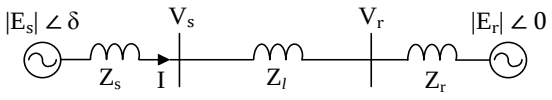

Figure 5.3 Two machine system

The voltage phasor diagram of a two machine system is shown in Figure 5.4. The phasor OO′ represents the SCV.

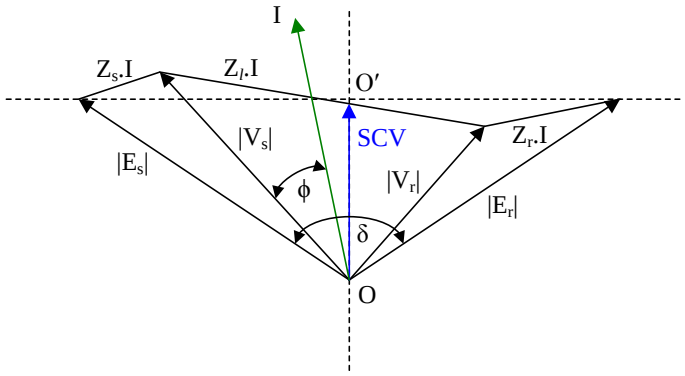

Figure 5.4 Voltage phasor diagram of a two machine system

If it is assumed an equal source magnitude, $E = |E_s| = |E_r|$, the SCV can be written as [99],

$$\mathrm{SCV}(t) = \sqrt{2}E \sin\left(\omega t + \frac{\delta(t)}{2}\right)\cos\left(\frac{\delta(t)}{2}\right) \tag{5.33}$$

This is a typical magnitude modulated sinusoidal waveform. Figure 5.5 shows the positive sequence SCV for a 60 Hz power system with a constant slip frequency of 5 Hz, for an example. The magnitude of the SCV changes between 0 and 1 pu and the voltage magnitude is forced to zero in every 0.2 seconds since the slip frequency is 5 Hz.

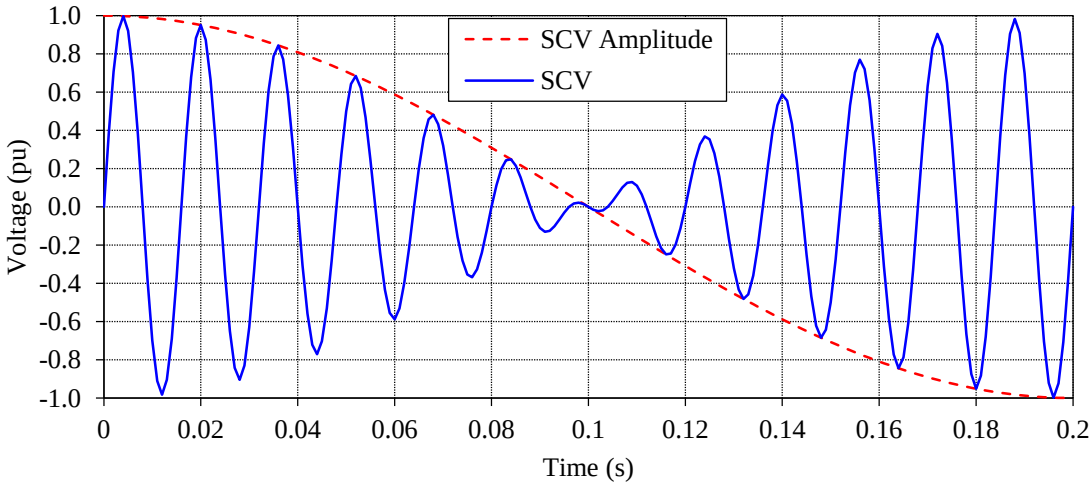

Figure 5.5 SCV during a power swing

If the system impedance, Z_l is assumed as a pure inductance, the voltage phasor diagram shown in Figure 5.5 can be redrawn. The projection of V_s onto the axis of the current, I is shown in Figure 5.6.

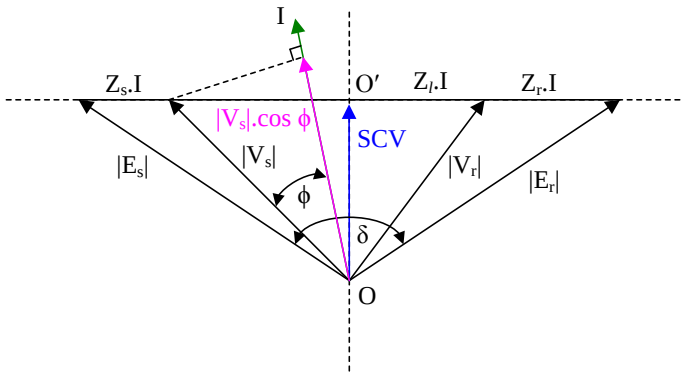

Figure 5.6 Projection of V_s onto the axis of current, I

The projection $|V_s| \cos \phi$ approximates well with the SCV. i.e.

$$SCV \approx |V_s| \cos \phi \tag{5.34}$$

where ϕ is phase angle between voltage and current. Thus, the SCV can be practically obtained from the terminal voltage and current measurements [100].

Considering an equal source magnitude and positive sequence quantities, a simple relation for the positive sequence SCV_1 and δ can be written as,

$$SCV_1 = E_1 \cos\left(\frac{\delta}{2}\right) \tag{5.35}$$

where E_1 is the positive sequence equal source magnitude. The time derivative of SCV_1 can be written as,

$$\frac{d}{dt}(SCV_1) = -E_1 \sin\left(\frac{\delta}{2}\right)\frac{d\delta}{dt} \tag{5.36}$$

The expression (5.36) represents the rate of change of positive sequence SCV and the slip frequency. The derivative of the SCV is independent from the network impedance and reaches its minimum when the angle between two machines is 180^0. Stable and unstable power swings can be detected by looking the rate of change of positive sequence SCV. The positive sequence SCV and its rate of change for a two machine system with a constant slip frequency of 5 Hz is shown in Figure 5.7, as an example.

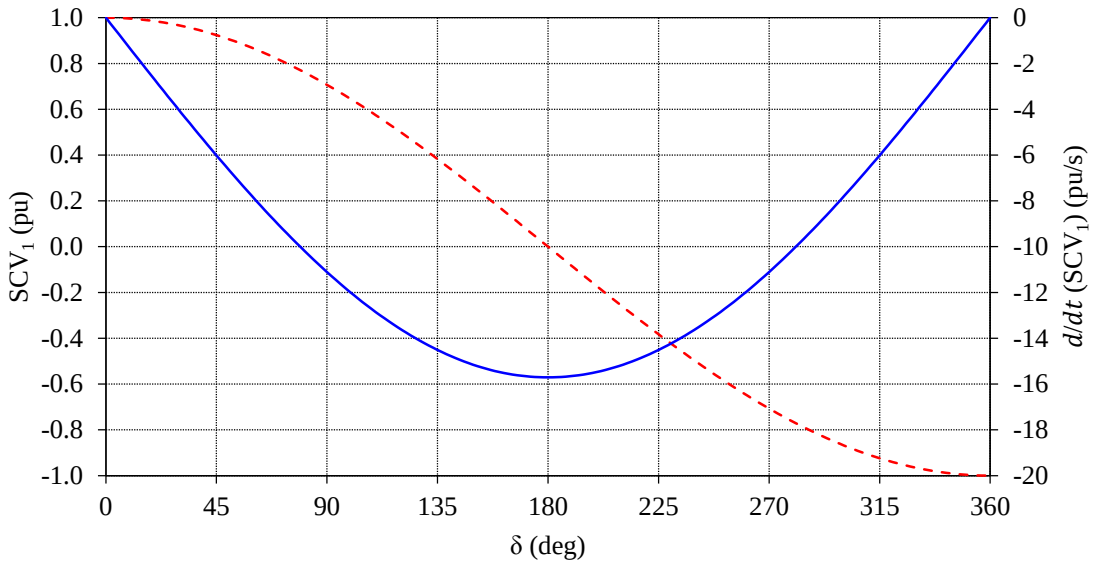

Figure 5.7 Positive sequence SCV and its derivative

The SCV method has several advantages such as the SCV is independent of the system source and line impedances and it is bounded with a lower limit zero and an upper limit of 1 pu. Therefore, the SCV method does not require power system studies in order to determine threshold values to detect a power swing. However, power swing detection is slower due to the slow rate of change of the SCV [99].

5.3.6 Machine Learning Techniques

The transient instability can be predicted with post-fault power system variables such as voltages, phase angles, active and reactive power injections by using classifiers trained with various machine learning techniques such as artificial neural networks (ANN), decision trees (DT), fuzzy logic, and support vector machines (SVM) [34], [36], [101]-[112].

5.3.5.1. Artificial Neural Networks

Artificial neural networks (ANNs) are used for fast pattern recognition and classification as well as function approximation. In general, the model of an ANN depends upon the neural network topology, the method of training, and the selection of outputs and inputs [101], [102]. It is one of the earliest machine learning based techniques, which is employed to assess the security status of power system.

In [101], ANN is applied to estimate the critical clearing time (CCT) of a multi-machine power system, where generators are described by the classical model. For each generator, rotor angles relative to the center of inertia (COI) angle at the instant of disturbance, the rotor angle deviations at the instant of disturbance clearing relative to their pre-disturbance values, and the acceleration energy of during the disturbance are provided as input features. The authors claim the CCTs estimated by the ANN model agree with the analytical results [101]. However, the biggest drawback is every single topology change requires a completely new set of discrimination rules.

Power system vulnerability assessment is done in [102], where ANN is employed as a classifier. The energy margin of the system and unstable equilibrium point (UEP) angles of the advanced generators are used as input features. The ANN output is a vulnerability

status of the system (vulnerable or non-vulnerable). The ANN model produces promising results even for previously unseen cases. However, there is no evidence that the ANN model yields satisfactory performances under topology changes without retraining.

An adaptive ANN application proposed in [103] addresses the major drawback of earlier approaches [101], [102], where the stability status can precisely be declared under different network configurations without retraining the ANN model. Furthermore, feature selection and data extraction techniques are also introduced to reduce the number of inputs and enhance model performances. However, inherent limitations of ANN based methods such as the possibility of having many local solutions and the slow rate of convergence during the training are still inevitable.

5.3.5.2. Decision Trees

In literature, decision trees (DT) have been employed to predict/assess transient stability status of power systems [104]-[107]. DT sequentially classifies a set of training data in a tree style, in terms of features associated with the data. It starts from a root node and each node is divided into sub branches (usually two) according to the possible answers for its question. DT construction is usually an offline process whereas the constructed DT can classify unseen testing data in real-time. It is significantly easy and fast to construct a DT and it performs well for the applications that require a small number of outputs, such as transient stability status of power system (either stable or unstable).

It is essential to identify appropriate features for DT applications as performances highly depend upon the attributes. For instance, pre-disturbance system parameters such as regional load level, voltage set-points and active generations of units, and the topolog-

ical variables are considered as candidate features [104]. In [107], mechanical input power the kinetic energy deviation, the average acceleration, the electrical output power at the moment of the fault clearing, and the fault duration are considered as input features.

Although DT has several benefits, the main drawback is the lack of accuracy due to the non-optimized techniques applied for training the classifiers. Furthermore, it is heavily time consuming to generate databases with credible contingencies during the training phase.

5.3.5.3. Support Vector Machines

Support vector machines (SVMs) were introduced in 1995 as a novel classification technique [108]. SVM construct a hyperplane from given a set of training examples, each are labelled in one of two or more categories. Then the hyperplane can assign new examples into one category or another. As the generalization capability of SVM is less affected by the number of input features it provides high performances under variations in the input signals. This feature essentially attracts SVMs for power system applications where input measurements are often varied due to changes in operating conditions and network topologies.

In literature, SVM are successfully applied to assess and predict transient stability of power system [34], [36], [109]-[112]. The studies reported in [34], [36], [109] achieved satisfactory classification accuracy for large actual power systems. However, training of robust classifiers applicable to all operating conditions is a time consuming task and needs experts well versed in both power system behavior and machine learning tech-

niques. Power industry is generally reluctant to apply black-box type machine learning solutions, especially in real time control and protection applications.

5.4 Transient Stability Status Prediction using Voltage Magnitude Measurements

Rotor angles of generators are the direct indicators of transient stability status of a power system as the energy imbalance in a generator due to a perturbation causes the rotor angle variations [18]. Generator terminal voltage magnitudes are also affected due to a perturbation. Although the terminal voltage of a generator does not directly indicate its stability status, the terminal voltage dip during a fault and a slow rate of voltage recovery after clearing the fault restricts the generator electrical power output during the transient period. Thus, the generator terminal voltage magnitudes have a critical impact on the transient stability following a fault, and can be used as an indicator of the transient stability status of a power system [31], [34], [36].

The relationship between the rotor angle and the terminal voltage magnitude can be derived for the single machine to infinite bus (SMIB) equivalent circuit shown as in Figure 5.8.

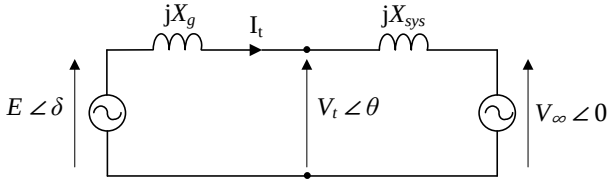

Figure 5.8 SMIB equivalent circuit

It is assumed that the system resistance is negligible compared to the system inductance, and the generator is modelled as a classical model, where the machine is represented as a constant voltage (so called internal voltage) behind the impedance.

The terminal current, $\mathrm{I_t}$ can then be expressed as,

$$\mathrm{I_t} = \frac{E\angle\delta - V_\infty\angle 0}{\mathrm{j}X_g + \mathrm{j}X_{sys}} \tag{5.37}$$

where $E\angle\delta$ is the internal voltage of the machine, $V_\infty\angle 0$ is the infinity bus voltage, $\mathrm{j}X_g$ is the synchronous reactance of the machine, and $\mathrm{j}X_{sys}$ is the system impedance. Thus, the generator terminal voltage can be written as,

$$V_t\angle\theta = E\angle\delta - \mathrm{j}X_g.\mathrm{I_t} \tag{5.38}$$

From (5.37) and (5.38) it can be written as,

$$V_t\angle\theta = E\angle\delta - \mathrm{j}X_g.\left(\frac{E\angle\delta - V_\infty\angle 0}{\mathrm{j}X_g + \mathrm{j}X_{sys}}\right) \tag{5.39}$$

By simplifying the expression (5.39) the generator terminal voltage magnitude can be written as,

$$V_t{}^2 = \frac{2EV_\infty X_g X_{sys}\cos\delta + E^2 X_{sys}{}^2 + V_\infty{}^2 X_g{}^2}{\left(X_g + X_{sys}\right)^2} \tag{5.40}$$

Since E, V_∞, X_g, and X_{sys} remain constant the terminal voltage magnitude, V_t can be written as a function of the rotor angle δ as,

$$V_t = \sqrt{\frac{k_1\cos\delta + k_2}{k_3}} \tag{5.41}$$

where $k_1 = 2EV_\infty X_g X_{sys}$, $k_2 = E^2 X_{sys}{}^2 + V_\infty{}^2 X_g{}^2$, and $k_3 = \left(X_g + X_{sys}\right)^2$.

Thus, the generator terminal voltage magnitude also provides similar transient stability information as the rotor angles.

As a transient stability status indictor, terminal voltage magnitudes have several advantages over the rotor angles. Time tagged voltage magnitude measurements can directly be obtained through PMUs installed at the generator terminals. In contrast, the rotor angle of a generator needs to be derived from other indirect measurements or measured with a specially deployed optical or magnetic sensor [5]. The rotor angles should be expressed relative to a common reference such as the COI angle in order to be meaningful. The COI angle requires to be updated in each measurement instant, and this calculation requires the connectivity status of all generators. The voltage magnitudes do not need such a reference, except for normalizing to a per unit (pu) quantity [31], [36].

In [34] and [36], post-disturbance recovery voltage magnitude measurements have been successfully used to predict the rotor angle instability status using SVM classifiers. In [34], the measured bus voltages are compared with a set of pre-identified voltage variation trajectory templates to evaluate a fuzzy membership that indicate the similarity between the measured voltage variations and the templates. The similarity values are input to the trained SVM to make the classification. In contrast, the SVM in [36] directly uses a sequence of sampled values of the post-disturbance voltages measured at selected buses. The work in these two references establishes that the post-disturbance recovery voltage magnitude measurements have a strong relationship with the post-disturbance transient stability status [34], [36]. Based on that premise, a new approach that does not rely on machine learning is developed in this thesis for early prediction of the transient stability status of power system. The proposed technique monitors the loci of the post-disturbance

voltage magnitudes on rate of change of voltage vs. voltage deviation (ROCOV–ΔV) plane, and declares instability condition if it crosses a predefined boundary. The voltage measurements are obtained from PMUs. This method is simple to implement and capable of predicting first-swing transient instabilities as well as multi-swing transient instabilities of a power system following a severe disturbance. In addition, the proposed new method can recognize the unstable generator(s), which is vital for initiating emergency control actions. The proposed approach could be implemented as the basis for a response-based WAPaC scheme against transient instability.

5.5 Transient Stability Status Prediction Using Post-disturbance Loci on ROCOV–ΔV Plane

In order to examine the use of generator terminal voltage magnitudes as an indicator of the post-disturbance transient instability of a power system, consider the SMIB system shown in Figure 5.9.

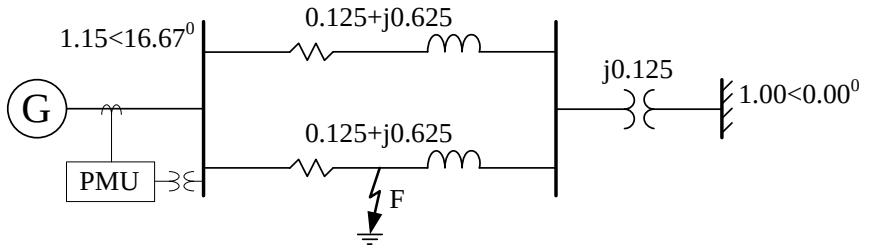

Figure 5.9 SMIB system with the initial steady-state power flow solution

It is simulated in PSCAD/EMTDC^{TM} software with the 555 MVA, 24 kV, 60 Hz, three-phase, 2-pole synchronous generator given in [29]. The parameters of the generator, its

excitation system with automatic voltage regulator (AVR) and power system stabilizer (PSS) are given in Appendix A. When the generator delivers 500 MVA at 0.9 power factor (lagging) the initial steady-state power flow solution provides the generator terminal voltage as $1.15\angle 16.67^0$ pu. At 1.0 s, a three-phase-to-ground fault is applied at the midpoint (location F) of one of the parallel transmission lines and the fault is cleared by removing the faulted line.

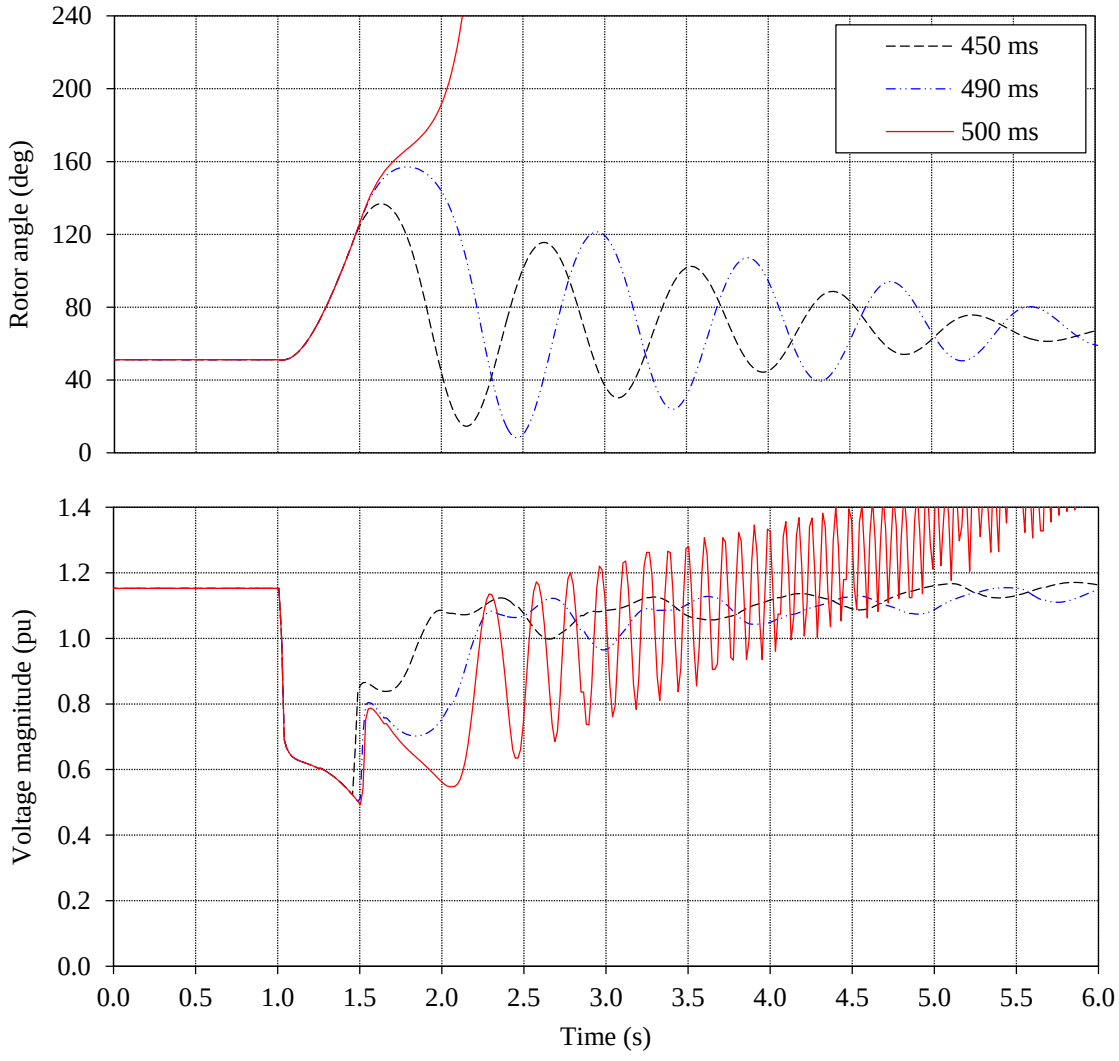

Figure 5.10 Variations of rotor angle and voltage magnitude following a fault

Figure 5.10 shows the variations of the rotor angle and the terminal voltage magnitude obtained for different fault durations. It is observed that the power system is stable when the fault duration is less than 490 ms, whereas the power system is unstable when it is 500 ms.

Two transient stability indicators investigated in this thesis are the generator terminal voltage deviation ΔV and the rate of change of ΔV after clearing a fault. They are calculated as:

$$\Delta V = Vmag - 1.0 \tag{5.42}$$

$$\frac{d}{dt}\Delta V = \frac{d}{dt}Vmag = \text{ROCOV} \tag{5.43}$$

where $Vmag$ is the measured voltage magnitude in pu, and ROCOV is rate of change of voltage (pu/s). With time synchronized measurements from PMUs, ΔV and ROCOV can be easily determined. At the n^{th} measurement:

$$\text{ROCOV}(n) = \big(Vmag(n) - Vmag(n-1)\big) \cdot F_s \tag{5.44}$$

where F_s is the PMU reporting rate given as frame/s or fps. The post-disturbance trajectories of the operating point on ROCOV–ΔV plane are shown in Figure 5.11. When the system is stable, the operating point takes a spiral trajectory and converges to a point on the ΔV axis. When the power system is unstable, the trajectory diverges; the operating point moves away from the origin farther into the 2nd, 3rd or 4th quadrant of the ROCOV–ΔV plane. From the simulation experiments, it was evident that a stability boundary can be defined as shown in Figure 5.11. A detail procedure to determine the stability boundary will be provided in Section 6.2.2.

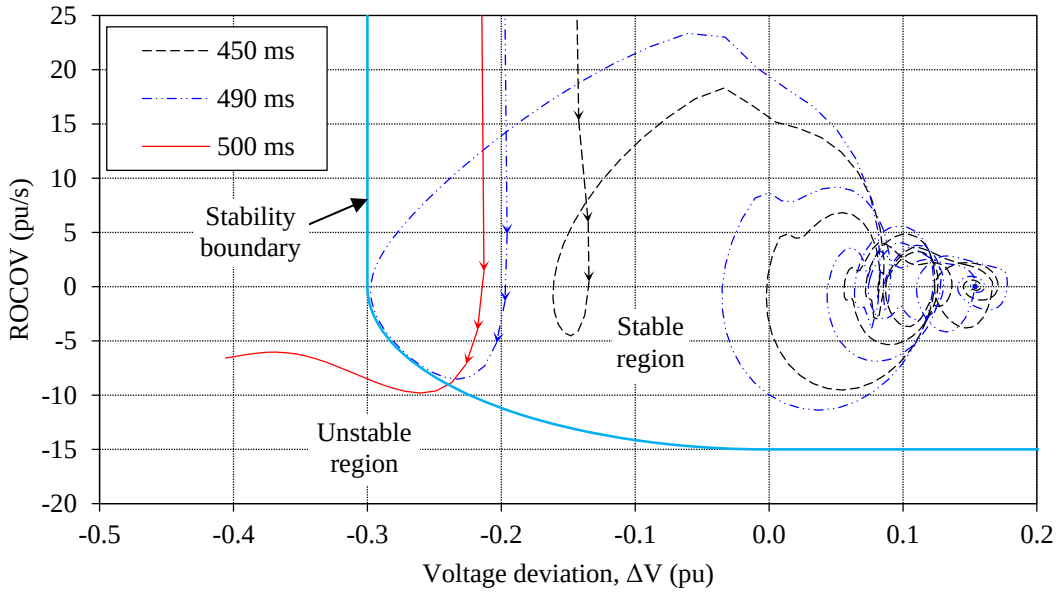

Figure 5.11 Plot of ROCOV vs. ΔV

If a post-disturbance operating point (i.e. operating point after clearing the fault) trajectory crosses the stability boundary from stable region to unstable region, the power system can be declared as unstable with good certainty.

The proposed method of determining the transient instability is useful only if the stability status can be predicted sufficiently in advance to enable automatic emergency control actions. The instant at which a multi-machine power system become unstable can be identified using the transient stability index η, calculated from the generator rotor angles [113]:

$$\eta = \frac{360^0 - |\Delta\delta|_{max}}{360^0 + |\Delta\delta|_{max}} \tag{5.45}$$

where $|\Delta\delta|_{max}$ is the maximum angle separation between any two generators during the post-disturbance. When the transient stability index $\eta > 0$, the power system is considered as stable; otherwise the power system is transiently unstable. Thus, this index is di-

rectly proportional to the maximum rotor angle separation and declares the power system as transiently unstable when $|\Delta\delta|_{max} > 360^0$. If this criterion is applied to the SMIB system, considering the rotor angle of the infinite bus remains at zero, the system is declared unstable at $t = 2.259$ s. In this simple SMIB system, out-of-step condition can directly be determined using the trajectory of impedance (measured at the generator terminal) on R-X plane. This method predicts occurrence of pole slipping at 2.023 s. In the approach proposed in this thesis, the operating point trajectory crosses the stability boundary on ROCOV–ΔV plane at 1.632 s. This is about 390 ms earlier than the other methods could predict, which is an important advantage in deploying automatic emergency control against transient instability. As each individual generator in a multi-machine system also subjected to terminal voltage dip during a fault more or less similar to a machine connected to an infinite bus, the above method can be extended to a multi-machine system.

5.6 Concluding Remarks

This chapter reviewed the background literature related to the transient stability status prediction in power systems. The existing approaches were categorized into five basic groups and their advantages and limitations were discussed. The previous research work that used generator terminal voltage magnitudes as a transient stability status prediction indicators were reviewed, and the advantages of this approach are highlighted. Finally, the concept of the proposed transient stability status prediction approach was illustrated with a simple SMIB system.

Chapter 6

Prediction of Post-Disturbance Transient Stability Status of Multi-Machine Power Systems Using Synchrophasor Measurements

6.1 Introduction

In the previous chapter, a novel method to predict the transient stability status a power system after being subjected to a severe disturbance was presented. The proposed technique is based on the ROCOV–ΔV characteristics of the post-disturbance voltage magnitudes obtained from synchrophasor measurements. This chapter is devoted to describe the method of implementation for a multi-machine power system and to thoroughly validate the proposed algorithm.

6.2 Procedure for Implementing the Proposed Algorithm for a Multi-machine System

In multi-machine systems, the post-disturbance trajectories of each generator can be plotted on the ROCOV vs. ΔV plane for the marginally stable and unstable cases, similar to the plot shown in Figure 5.11. Investigations showed that each generator has a distinct boundary on the ROCOV vs. ΔV plane, which separates stable swings from the unstable swings. It is assumed that time synchronized generator terminal bus voltage measurements are available from PMUs, and the measurements are sent to a central location such as a load dispatch center (LDC) through a dedicated telecommunication infrastructure. At the LDC, the data is collected by a PDC which then time aligns, does the quality checks and feeds the processed measurements to the transient stability status prediction algorithm.

The development of the proposed transient stability status prediction scheme for a multi-machine system involves three-steps:

1. Identification of contingencies that makes each generator marginally unstable through dynamic simulations
2. Determination of stability boundary for each generator
3. Detection of severe disturbances to trigger the transient stability status prediction algorithm

6.2.1 Identification of Marginally Critical Contingencies

It is important to identify marginally stable/unstable contingencies for each generator considering credible contingencies. The easiest way is to apply a three-phase bolted fault at the generator terminal bus and increase the fault duration until the generator becomes unstable. This routine works for most generators; however, occasionally the neighboring generators can become unstable before the generator under consideration. This happens when the generator being considered is much stronger than the neighboring generators. In such cases, the pre-disturbance operating conditions can be modified, for example, by increasing the load on the strong generator while reducing the load on the neighboring weak generators. Identification of the marginally stable/unstable cases need to be performed by the study engineers well familiar with the particular power system, especially when the power system has HVDC infeeds and FACTS devices.

6.2.2 Determination of Stability Boundary

Determination of the stability boundary for each generator involves the following steps:

a) Apply a three-phase short circuit fault at the generator terminal bus and increase the fault duration until the generator becomes unstable. It is appropriate to increase the fault duration in one cycle steps as the highest standard PMU reporting rate is 50 fps for a 50 Hz system and 60 fps for a 60 Hz system [5]. Establish the marginally stable case by reducing the fault duration by one cycle. A suitable dy-

namic simulation program with accurate system model can be used for this purpose.

b) Plot the trajectory of marginally stable case on the ROCOV–ΔV plane.

c) Locate point B (x_1, y_1) shown in Figure 6.1 just outside (to the left) of the left most point of the trajectory. Draw the left side vertical line AB parallel to the ROCOV axis. The stable post-disturbance trajectories are always located to the right of this vertical line AB, which is the first segment of the stability boundary on the ROCOV–ΔV plane shown in Figure 6.1.

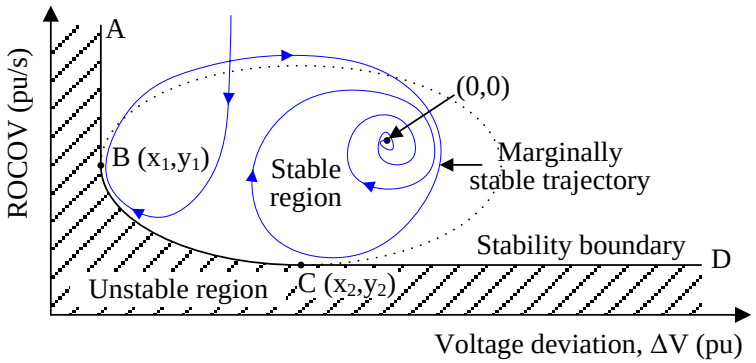

Figure 6.1 Stability boundary on ROCOV–ΔV plane

d) Locate point C (x_2, y_2) shown in Figure 6.1, just below the lowest point of the marginally stable trajectory. Draw the horizontal line segment CD parallel to the ΔV axis. The stable trajectories are always located above the line CD, and it is the third segment of the stability boundary.

e) Draw an ellipse that passes through B and C in such a way that the left most point of ellipse coincides with point B and the bottom most point of ellipse passes through point C. The elliptical segment BC is the second segment of the stability

boundary, and it is the most important segment because the trajectory often crosses the boundary through that segment.

Thus, the stability boundary is a combination of 3 piecewise continuous functions and are defined as:

$$\begin{cases} \Delta V = x_1 & ; \text{ROCOV} \geq y_1 \\ \left(\dfrac{\Delta V - x_2}{x_1 - x_2}\right)^2 + \left(\dfrac{\text{ROCOV} - y_1}{y_1 - y_2}\right)^2 = 1 & ; x_1 < \Delta V < x_2 \text{ and } y_2 < \text{ROCOV} < y_1 \\ \text{ROCOV} = y_2 & ; \Delta V \geq x_2 \end{cases} \quad (6.1)$$

This procedure is followed for each generator in order to find their stability boundaries.

6.2.3 Detection of Disturbances

When implemented as a real-time system, the proposed scheme continuously monitors generator voltage magnitudes and calculates the respective ROCOV values, but the status prediction algorithm is launched only after detecting a severe disturbance (fault). The disturbance detection logic used in this thesis is shown in Figure 6.2 where $Vmag_G^{(i)}(t)$ is the voltage magnitude of the i^{th} generator at time t, $\text{ROCOV}_G^{(i)}(t)$ is the rate of change of voltage of i^{th} generator at time t, F_s is the PMU reporting rate in fps and n_g is number of generators. The time difference between two consecutive reportings, Δt is given as

$$\Delta t = \frac{1}{F_s} \quad (6.2)$$

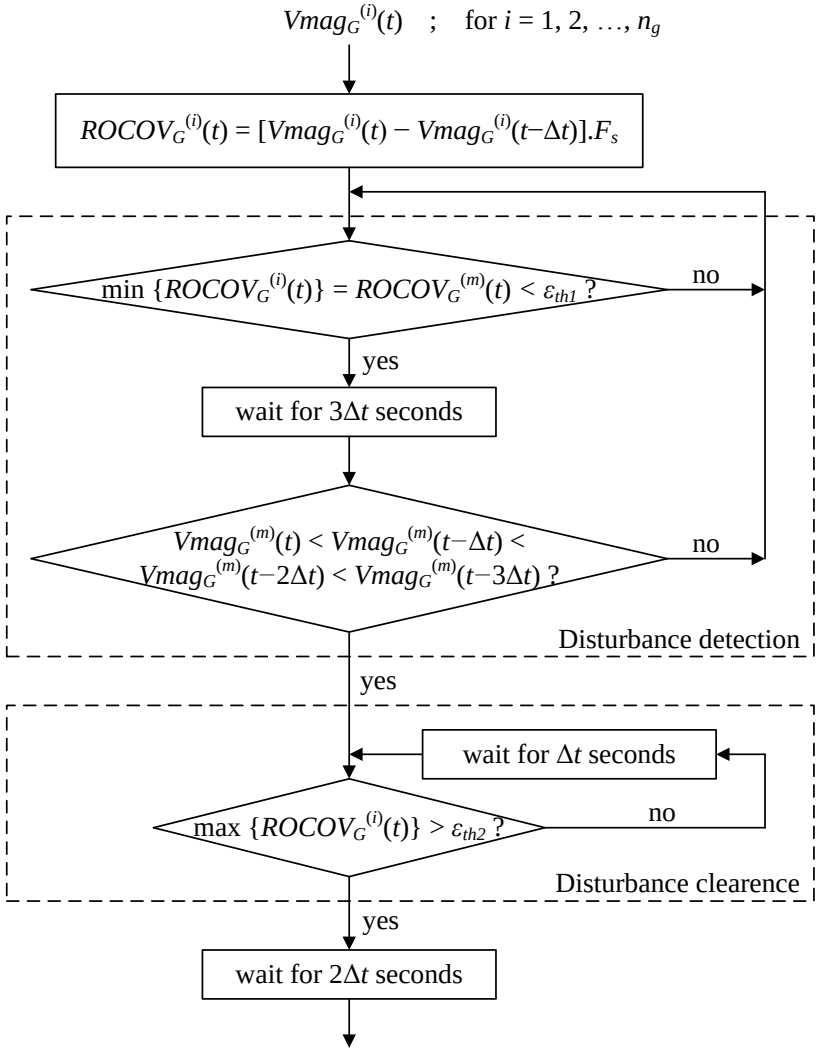

Figure 6.2 Severe disturbance detection logic

After a severe fault, the voltage magnitudes measured at the buses close to the fault depress with a sudden drop in the ROCOV values. If the minimum ROCOV value of any generator bus (say generator m) drops below a pre-specified threshold ε_{th1} and the voltage magnitude of that generator bus (i.e. generator m) continues to decrease for two consecutive measurement intervals, a severe disturbance is declared. Once, the faulty element is isolated, the voltage starts to recover. At that instance, a sudden change in ROCOV values

in the positive direction can be experienced. If the maximum ROCOV value of any generator bus rises above a pre-specified threshold ε_{th2}, it is assumed that the fault is cleared. The transient stability prediction algorithm is triggered after receiving two measurements following the clearance of the disturbance to ensure that the post-disturbance trajectories on ROCOV–ΔV plane start from the stable region.

6.3 Testing with TSAT Simulations

The IEEE 39-bus test system (New England power system) [83] was used to demonstrate and validate the proposed transient stability prediction approach, as it has been popularly used for evaluating transient stability related applications. This test system comprises 39 buses, 10 generators, 19 loads and 34 transmission lines. The generator at bus-39 represents the aggregation of a large system. Thus, the bus-39 was used as a reference bus and rotor angles of other generators were measured with respect to the rotor angle of this reference generator. The system parameters are given in the Appendix B.

The proposed method was first validated using the simulations performed in commercial software TSAT™, which is a phasor-domain simulation tool [113]. TSAT was first used to identify the transient stability boundary for all nine generators (the 10^{th} generator at bus 39 represents an equivalent system) following the procedure described in Section 6.2 and stability boundaries for each generator (points B and C) are given in Table 6.1. TSAT has a capability to simulate numerous contingencies in batch mode. This facility was utilized to evaluate the performance of the proposed method for a variety of credible contingencies under different operating conditions.

Table 6.1 Stability boundaries for each generator

Generator	B (x_1, y_1)	C (x_2, y_2)
Gen.-30	(-0.11, 0.00)	(-0.04, -0.35)
Gen.-31	(-0.30, 0.00)	(-0.17, -0.55)
Gen.-32	(-0.30, 0.00)	(-0.20, -0.57)
Gen.-33	(-0.29, 0.00)	(-0.20, -0.68)
Gen.-34	(-0.36, 0.00)	(-0.20, -0.60)
Gen.-35	(-0.25, 0.00)	(-0.15, -0.49)
Gen.-36	(-0.23, 0.00)	(-0.17, -0.72)
Gen.-37	(-0.32, 0.00)	(-0.20, -0.38)
Gen.-38	(-0.43, 0.00)	(-0.21, -0.93)

6.3.1 Base Case

The contingencies considered in the experiment included three-phase-to-ground faults on the buses and five different locations on the transmission lines (at 5%, 25%, 50%, 75% and 95% of the length). It was assumed that line faults were cleared after the standard fault duration of 6 cycles (100 ms) by removing the faulted line. Bus faults were assumed as temporary faults. This gave 209 simulation cases, of which 186 were stable and 23 are unstable. Additional 418 (2 × 209) simulation cases were obtained by repeating the same contingencies with fault durations of 5 cycles (83.33 ms) and 7 cycles (116.67 ms). Of the new simulation cases, 372 (196 + 176) were stable and 46 (13 + 33) were unstable.

In this thesis, two performance measures are considered: (i) the prediction accuracy and (ii) the early prediction advantage. The early prediction advantage is defined as the difference between the time when the proposed method predicts an unstable condition and the time when the instability is declared when applied the criterion given in (5.45). When implementing a practical WAPaC scheme, early prediction advantage can be con-

sidered as the total time available for communication, data processing in PDCs and application program, and taking any control action.

Performances of the proposed transient stability status prediction observed in this simulation experiment are shown in Table 6.2. The prediction accuracy was always 100% for the contingencies that result in transient instability. The overall accuracy was more than 99%. Out of 558 stable contingencies, only one stable contingency was wrongly predicted as unstable. The average early prediction time advantage was around 700 ms. Furthermore, the proposed technique was able to accurately identify the generator(s) that lose(s) the synchronism.

Table 6.2 Prediction accuracy : Base case

Fault duration	Condition	Predicted as stable	Predicted as unstable	Early prediction advantage* (ms)	Overall accuracy (%)
5 cycles	Stable case	196/196	0/196	n/a	100.00
	Unstable case	0/13	13/13	712	
6 cycles	Stable case	185/186	1/186	n/a	99.52
	Unstable case	0/23	23/23	680	
7 cycles	Stable case	176/176	0/176	n/a	100.00
	Unstable case	0/33	33/33	713	

* Mean values of early prediction time advantage are compared w. r. t. (5.45)

6.3.2 Cases with Random Load/Generation Variations

After the proposed transient stability status prediction method showed satisfactory performances with the base case load and generation, its robustness was next tested for new cases obtained by randomly changing the pre-disturbance generations and loads

around the base case [114], [115]. For the n^{th} pre-disturbance operating point, active power injection and voltage at the i^{th} generator bus were calculated as [114]

$$P_G^{(i)}(n) = P_{Gbase}^{(i)}\left[1 + 2\Delta P^{(i)}\left(0.5 - \varepsilon_{PG}^{(i)}(n)\right)\right] \tag{6.3}$$

$$V_G^{(i)}(n) = V_{Gbase}^{(i)}\left[1 + 2\Delta V^{(i)}\left(0.5 - \varepsilon_{VG}^{(i)}(n)\right)\right] \tag{6.4}$$

where $P_{Gbase}^{(i)}$ and $V_{Gbase}^{(i)}$ are the active power and voltage at the i^{th} generator in the base case, $\Delta P^{(i)}$ and $\Delta V^{(i)}$ are fractional perturbation of active power and voltage allowed at the i^{th} generator bus and $\varepsilon_{PG}^{(i)}$ and $\varepsilon_{VG}^{(i)}$ are uniform independent random variables between 0 and 1. Similarly, for the n^{th} pre-disturbance operating point, active and reactive power consumption at the j^{th} load bus were computed as [115]

$$P_L^{(j)}(n) = P_{Lbase}^{(j)}\left[1 + 2\Delta P^{(j)}\left(0.5 - \varepsilon_{PL}^{(j)}(n)\right)\right] \tag{6.5}$$

$$Q_L^{(j)}(n) = Q_{Lbase}^{(j)}\left[1 + 2\Delta Q^{(j)}\left(0.5 - \varepsilon_{QL}^{(j)}(n)\right)\right] \tag{6.6}$$

where $P_{Lbase}^{(j)}$ and $Q_{Lbase}^{(j)}$ are the real and imaginary power at the j^{th} load in the base case, $\Delta P^{(j)}$ and $\Delta Q^{(j)}$ are fractional perturbation of real and imaginary powers allowed at the j^{th} load bus and $\varepsilon_{PL}^{(j)}$ and $\varepsilon_{QL}^{(j)}$ are uniform independent random variables between 0 and 1. In this thesis, maximum random changes, $\Delta P^{(i)}$, $\Delta P^{(j)}$, and $\Delta Q^{(j)}$ were set to 10% while the maximum random changes for $\Delta V^{(i)}$ was set to 2%. Each randomly generated pre-disturbance operating condition was screened by running a load flow study and discarding the case if it violates the ± 5% voltage limit.

Using the above method, 10 random operating conditions were generated. The same 627 contingencies applied to the base case were repeated for each random pre-disturbance condition. The most important feature of this test is that the same stability boundaries determined for the base case were used to predict the stability status under different pre-disturbance operating conditions. Table 6.3 summarizes the results. The performances were similar to those of the base case results: the overall accuracy is over 99% and the average early prediction time advantage is around 700 ms. Transient instability prediction accuracy is again 100% (625/625) for unstable contingencies. This confirmed the robustness of the proposed method. Only 31 out of 5645 stable contingencies were predicted as unstable. Careful analysis of these false detections showed that they all are marginally stable contingencies. Experiments showed that these misclassifications could be reduced by adjusting the transient stability boundary; however, it then reduced the early prediction time advantage. The selection of the transient stability boundary is a trade-off between the accuracy and the early prediction time advantage.

Table 6.3 Prediction accuracy : Random cases

Fault duration	Condition	Predicted as stable	Predicted as unstable	Early prediction advantage* (ms)	Overall accuracy (%)
5 cycles	Stable case	1962/1967	5/1967	n/a	99.76
	Unstable case	0/123	123/123	698	
6 cycles	Stable case	1883/1889	6/1889	n/a	99.71
	Unstable case	0/201	201/201	727	
7 cycles	Stable case	1769/1789	20/1789	n/a	99.04
	Unstable case	0/301	301/301	710	

* Mean values of early prediction time advantage are compared w. r. t. (5.45)

6.4 Validation with an Experimental Setup based on Real-Time Simulations

Having tested the proposed concept through offline phasor-domain dynamic simulations in TSAT, the transient stability status prediction algorithm was evaluated with the aid of real-time simulations and a laboratory scale synchrophasor network consisting of a single PDC. This enabled to demonstrate the practicality of the proposed approach with actual PMU measurements. The arrangement of the experimental setup is shown in Figure 6.3. The 39-bus test system was implemented in the RTDS™ simulator. The real-time simulation model was cross-validated against the phasor-domain model used in TSAT to ensure accuracy. The RTDS simulator used in this experiment was equipped with a GTNET™ hardware board which can emulate 24 PMUs reporting positive sequence phasor measurements [73]. The voltage and current signals at the generator buses in the simulated power system were input (internally) to the PMU modules. The P-class PMU model was selected as it is preferred for the applications requiring fast response [5]. A SEL-2407 GPS clock [77] was used to provide IRIG-B time signal to the RTDS simulator via a GTSYNC™ card. All PMU modules use this signal for time synchronized sampling and timestamping. The PMUs in the RTDS were configured to report synchrophasors at 60 fps through a TCP/IP network. The synchrophasor data were collected by the openPDC v2.0 [74] PDC, and provided to the transient stability status prediction algorithm. The same transient stability boundaries determined using TSAT simulations

were applied to predict the transient stability status of the power system in this real-time system.

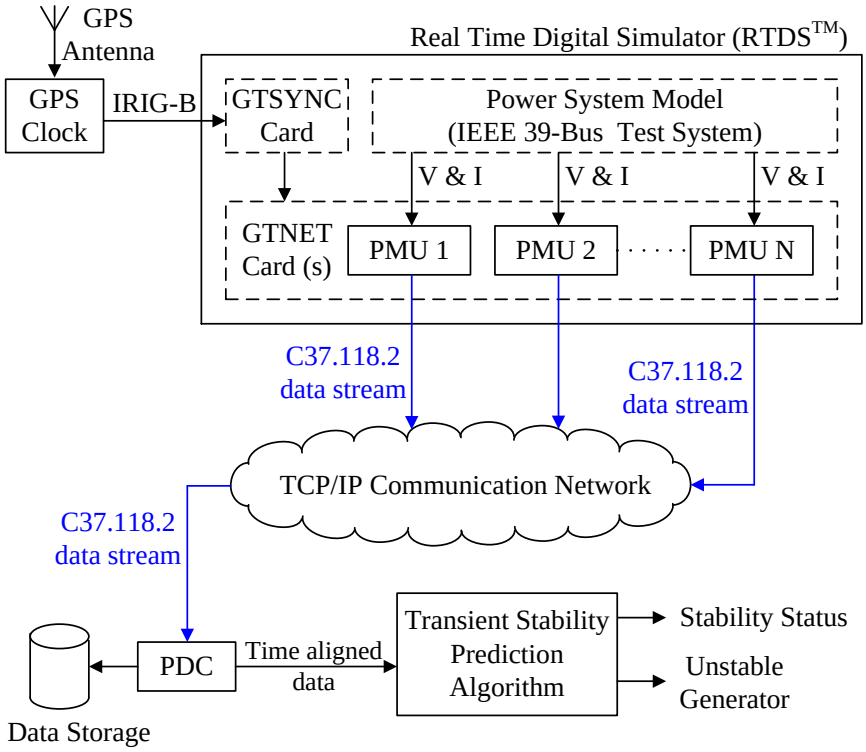

Figure 6.3 RTDS and laboratory scale synchrophasor network

6.4.1 Disturbance Detection

The results shown in Figure 6.4 validate the disturbance detection logic described in Section 6.2.3. The thresholds ε_{th1} and ε_{th2} of the detection logic were selected considering 5% voltage drop/rise within two consecutive PMU reportings (i.e. $\varepsilon_{th1} = -0.05 \times 60 = -0.3$ pu/s and $\varepsilon_{th2} = 0.05 \times 60 = +0.3$ pu/s at 60 fps reporting rate). In the presented case, a three-phase-to-ground fault was applied at 50% of Line 2-25 and the fault was cleared by removing the line after 6 cycles. The fault was applied when the UTC is around 21:22:47.833 and it was cleared when UTC is around 21:22:47.933. The

variations of the generator bus voltage magnitudes as reported by the PMUs and the ROCOV values computed from the reported measurements are shown in Figure 6.4. The dots on the curves represent the instants at which the PMUs reported new synchrophasors.

It can be observed that the minimum value of ROCOV at 21:22:47.850 (the first reporting followed by the fault) was less than −3 pu/s threshold and it was reported by the PMU at the generator at bus 37. Thus the disturbance must be close to bus 37. During the two consecutive reporting periods after the fault, the voltage magnitude measured at generator bus 37 is decreasing. It takes two reporting intervals to observe the impact of a fault on the voltage magnitude due to the P-class filter used in PMUs. Based on the observations, the proposed disturbance detection logic concludes that it detected a fault at 21:22:47.850. Then the detection logic looks for a sudden change in ROCOV in positive direction. At 21:22:47.950 (the first reporting interval followed by fault clearance), the maximum observed ROCOV exceeded the threshold +3 pu/s and thus, the disturbance detection logic concluded that the fault was cleared at 21:22:47.950. After the assigned delay of two reporting periods, the transient stability prediction algorithm was launched at 21:22:47.983. During the experiments, the proposed disturbance detection logic recognized all faults accurately.

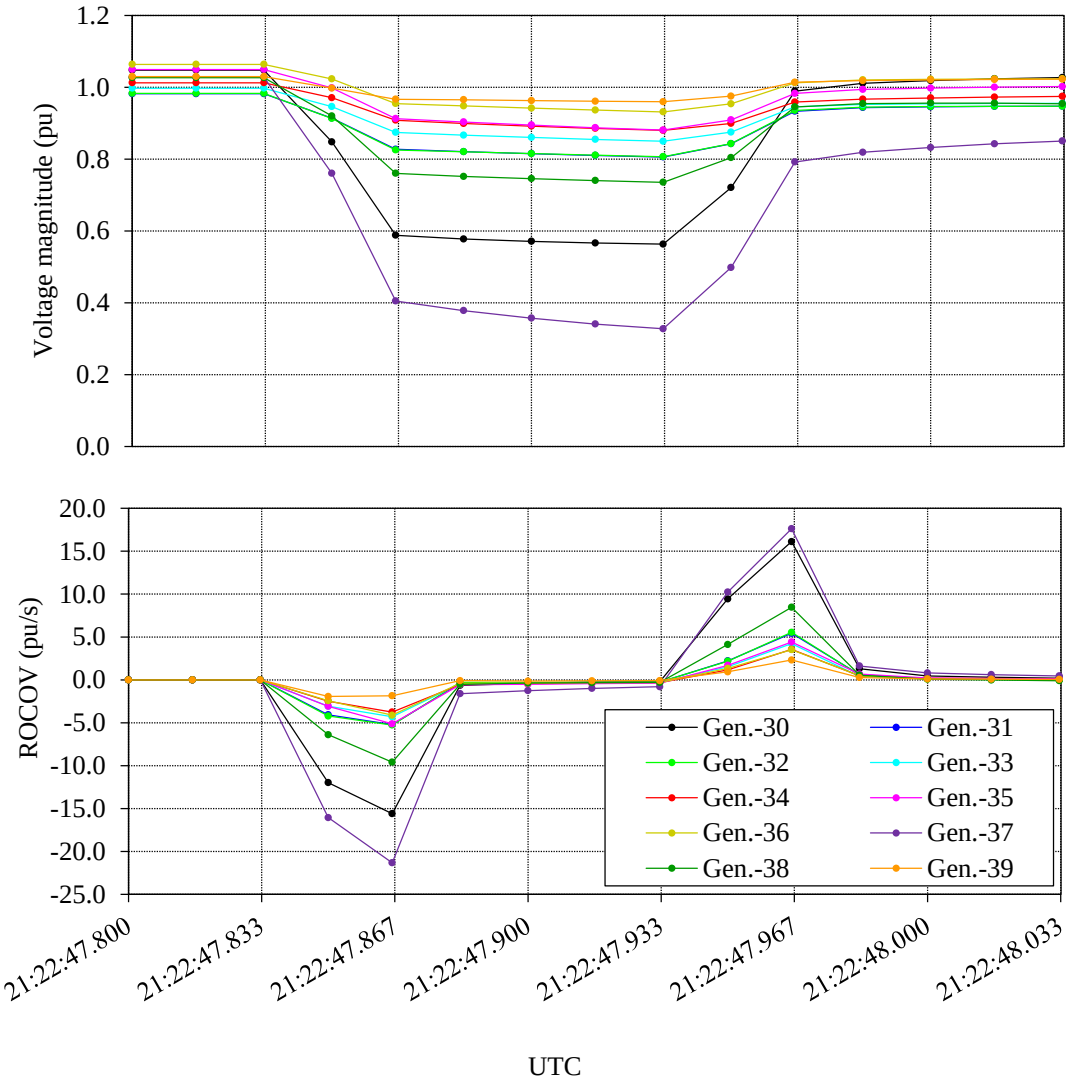

Figure 6.4 Variations of voltage magnitude and ROCOV of 6 cycles fault

6.4.2 Performance under Symmetrical Faults

The effectiveness of the proposed transient stability status prediction method was validated with 25 selected three-phase-to-ground contingencies, of which 18 were stable and 7 were unstable. The overall accuracy was 100% and the average early prediction time advantage was around 700 ms (minimum 300 ms, maximum 1100 ms).

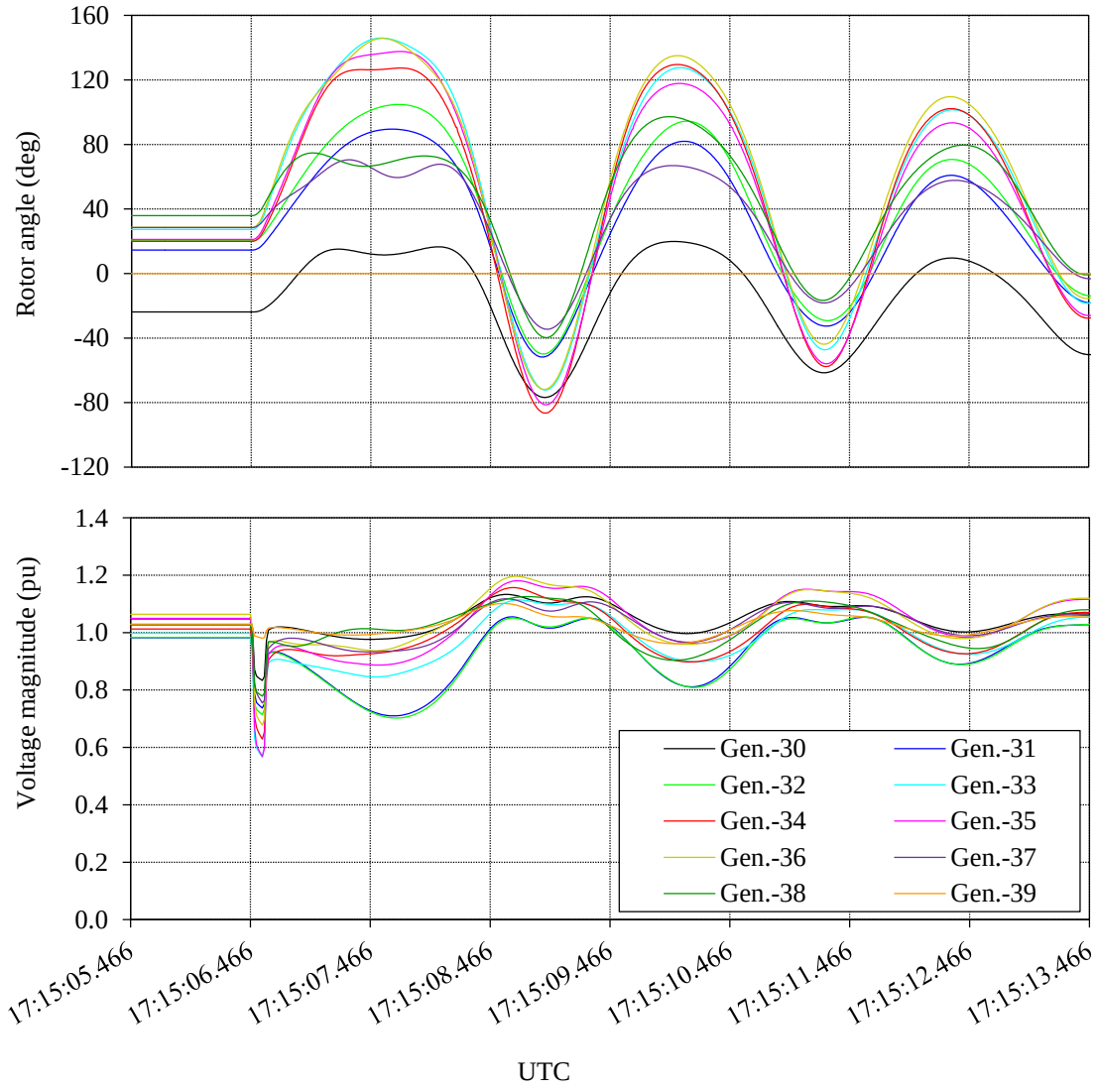

Figure 6.5 Variations of rotor angle and voltage magnitude for a fault on line 16-17 (25% of the length) cleared by removing the line after 6 cycles

In order to examine the detailed working of the algorithm, consider the case of three-phase to ground fault applied on Line 16-17 (at 25% of the length from bus 16). The fault was cleared by removing the line after 6 cycles. The corresponding variations of the rotor angle and the voltage magnitudes are shown in Figure 6.5. The power system was transiently stable after this contingency. The post-disturbance trajectories of generators on ROCOV–ΔV plane are shown in Figure 6.6. The trajectories of all nine generators re-

mained within the stable region. Therefore, the proposed transient stability prediction algorithm declared the power system as stable.

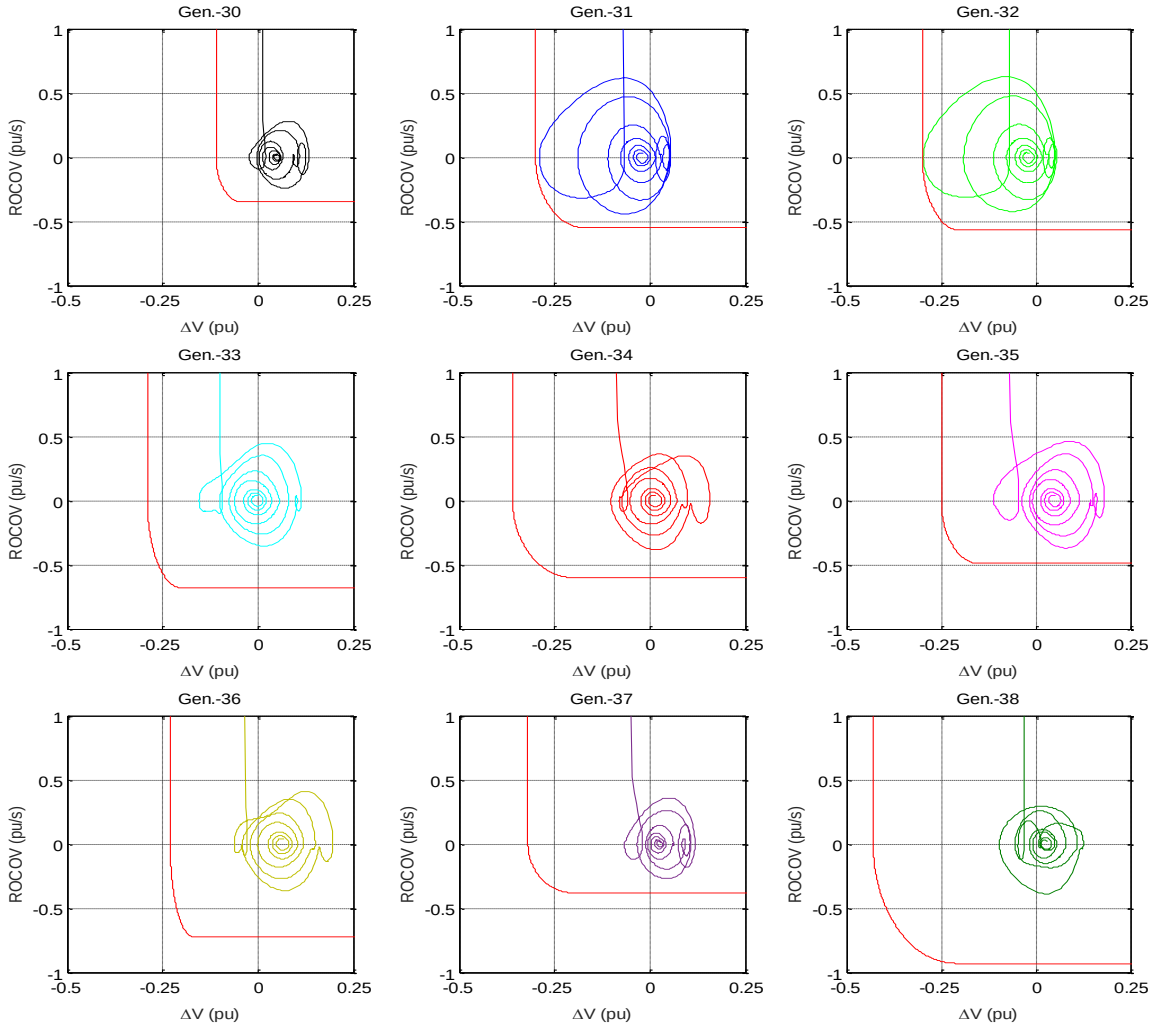

Figure 6.6 ROCOV vs. voltage deviation for a fault on line 16-17 (25% of the length) cleared by removing the line after 6 cycles

In the second example, a three-phase-to-ground fault was applied on line 26-29 (at 25% of the length from bus 26) when UTC is 19:06:00.166 and cleared by removing the line after 6 cycles. Following the fault, the generator at bus 38 became unstable as can be seen in Figure 6.7.

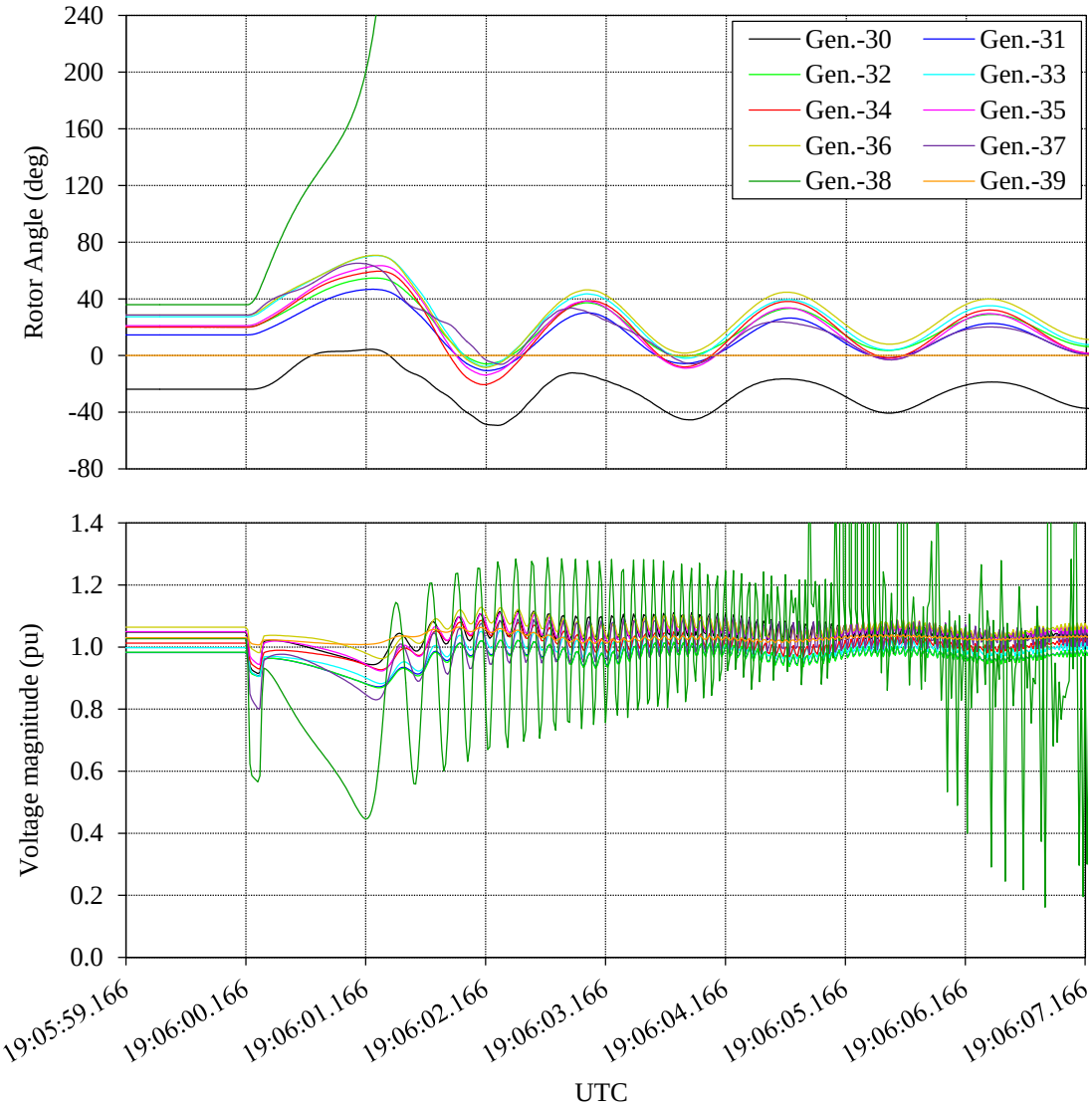

Figure 6.7 Variations of rotor angle and voltage magnitude for a fault on line 26-29 (25% of the length) cleared by removing the line after 6 cycles

This is a first-swing instability and the proposed transient stability status prediction algorithm declared the power system as unstable at UTC of 19:06:00.883, and identified generator at bus 38 as the unstable generator. The corresponding post-disturbance trajectories of the generators on ROCOV–ΔV plane are shown in Figure 6.8. When the rotor angle separation criterion given in (5.45) was applied, instability was declared at

19:06:01.383 (UTC). Therefore, in this case, the proposed approach has an early prediction time advantage of 500 ms.

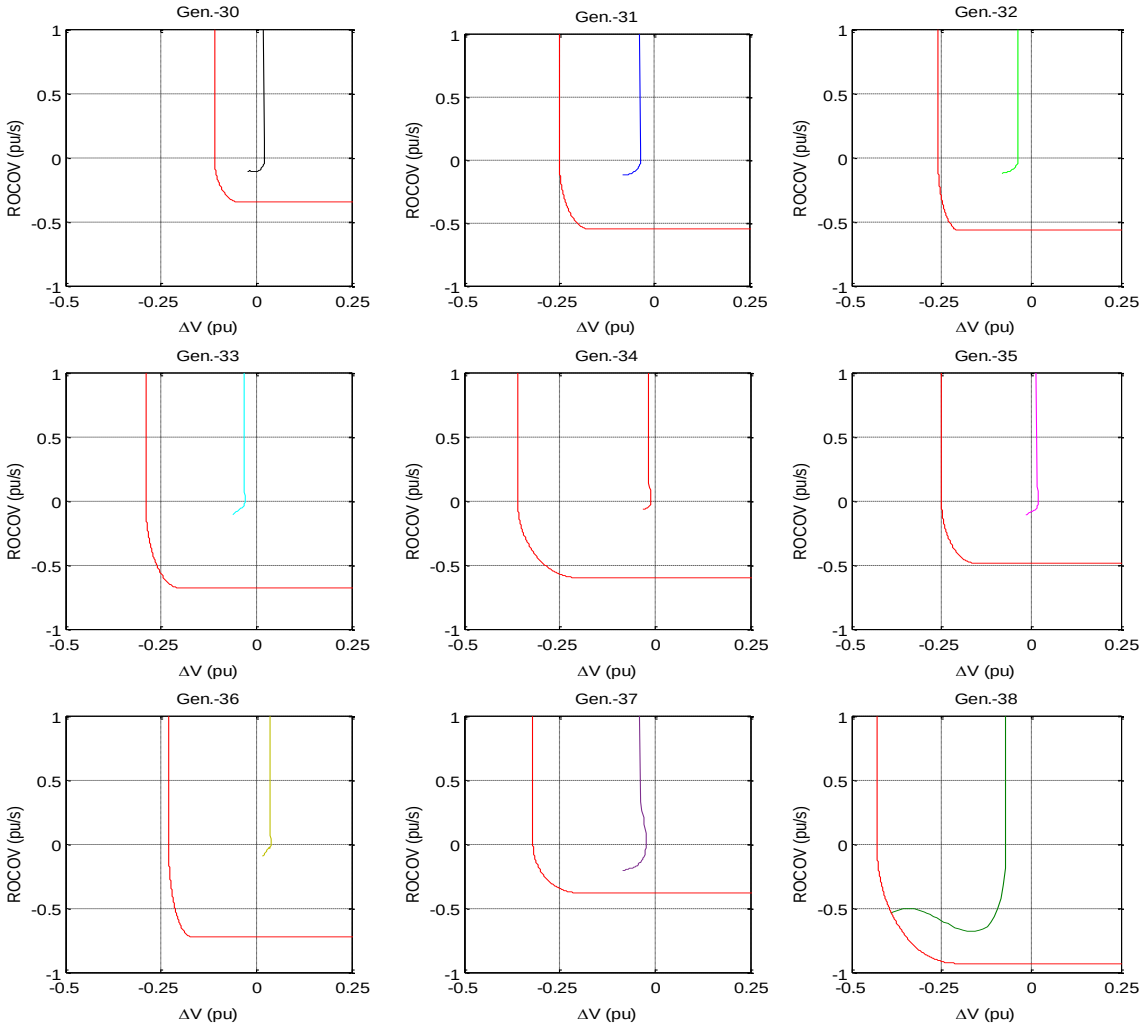

Figure 6.8 ROCOV vs. voltage deviation for a fault on line 26-29 (25% of the length) cleared by removing the line after 6 cycles

In the third example, a three-phase to ground fault was applied on line 2-25 (at 50% of the length from bus 2) when UTC is 21:22:47.833 and cleared by removing the line after 6 cycles. Following the fault, the generators at bus 37 and bus 38 became unstable as can be seen in Figure 6.9.

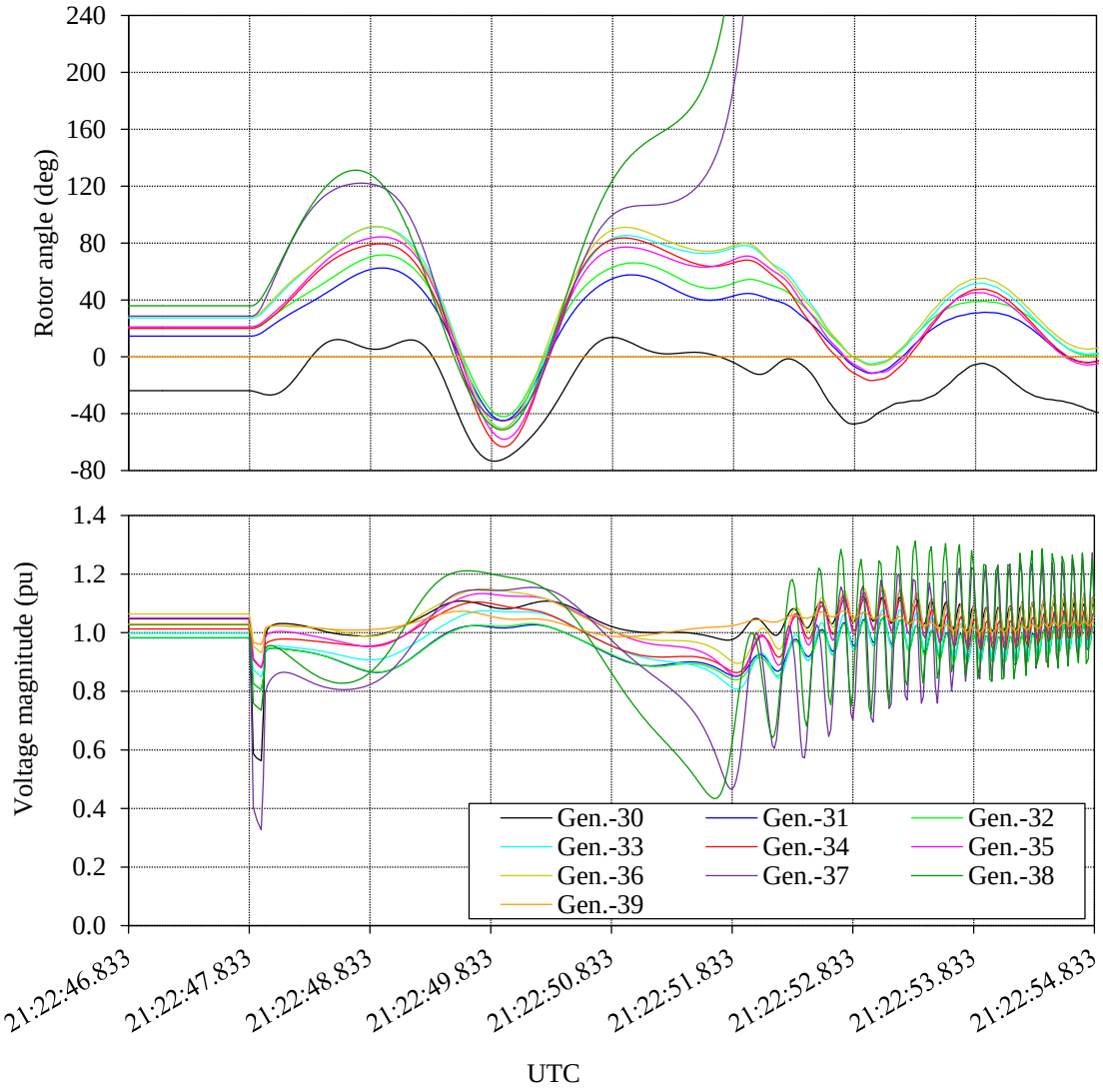

Figure 6.9 Variations of rotor angle and voltage magnitude for fault on line 2-25 (50% of the length) cleared by removing the line after 6 cycles

This is a multi-swing instability, the generators do not become unstable during the first swing. The proposed transient stability status prediction algorithm declared the power system as unstable at UTC of 21:22:50.616, and identified generator at bus 37 as the unstable generator. The corresponding post-disturbance trajectories of the generators on ROCOV–ΔV plane are shown in Figure 6.10. It can be seen from these plots that the trajectory of generator at bus 38 also approaching the stability boundary. When the rotor

angle separation criterion given in (5.45) was applied, instability was declared at 21:22:51.916 (UTC). Therefore, for this case, the proposed approach has an early prediction time advantage of 1300 ms.

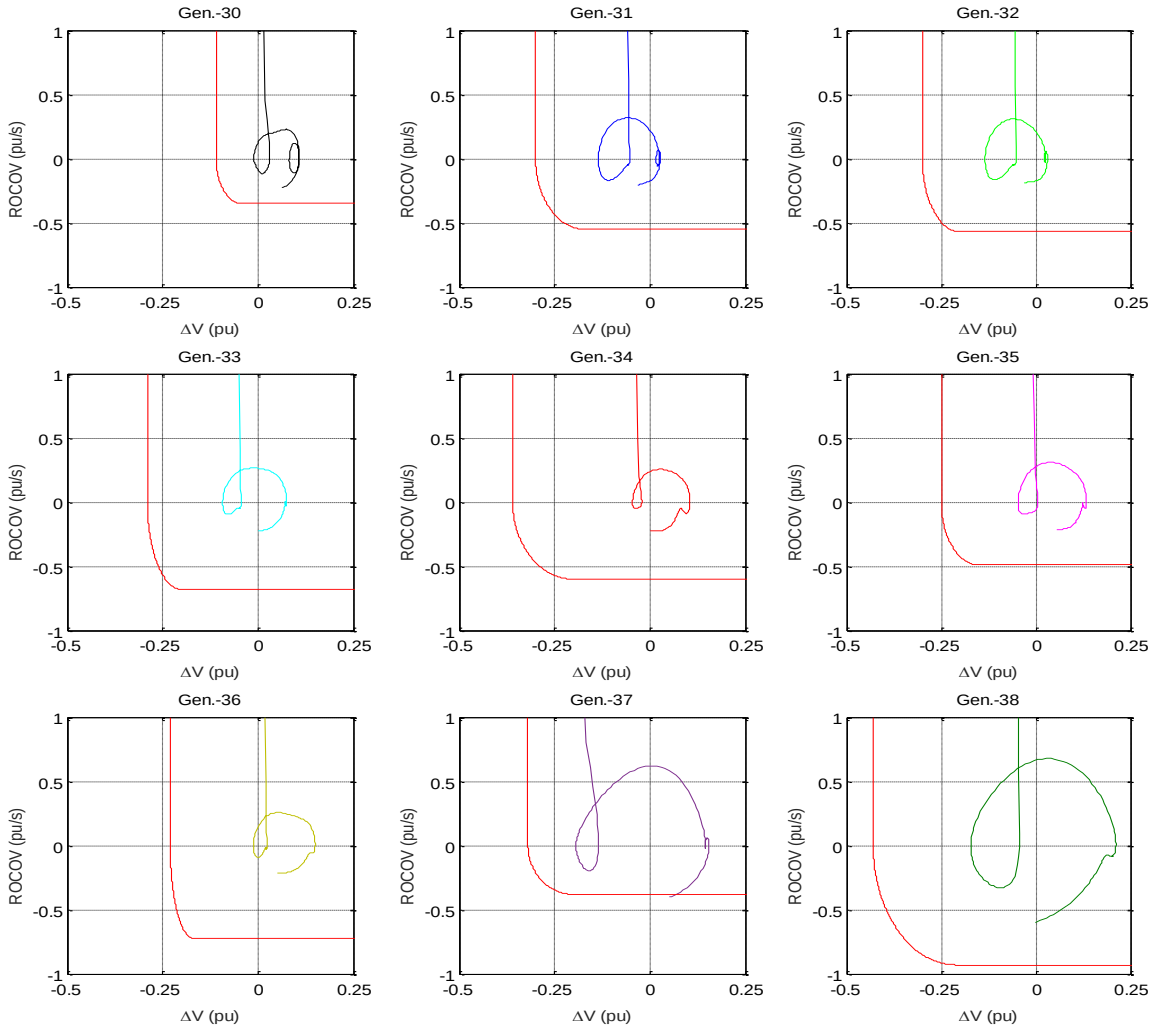

Figure 6.10 ROCOV vs. voltage deviation for a fault on line 2-25 (50% of the length) cleared by removing the line after 6 cycles

In the last illustrative example, a three-phase-to-ground fault was applied on line 16-17 (at 95% of the length from bus 16) when UTC is 17:02:41.433 and cleared by remov-

ing the line after 6 cycles. The entire power system became unstable following the fault as can be seen in Figure 6.11.

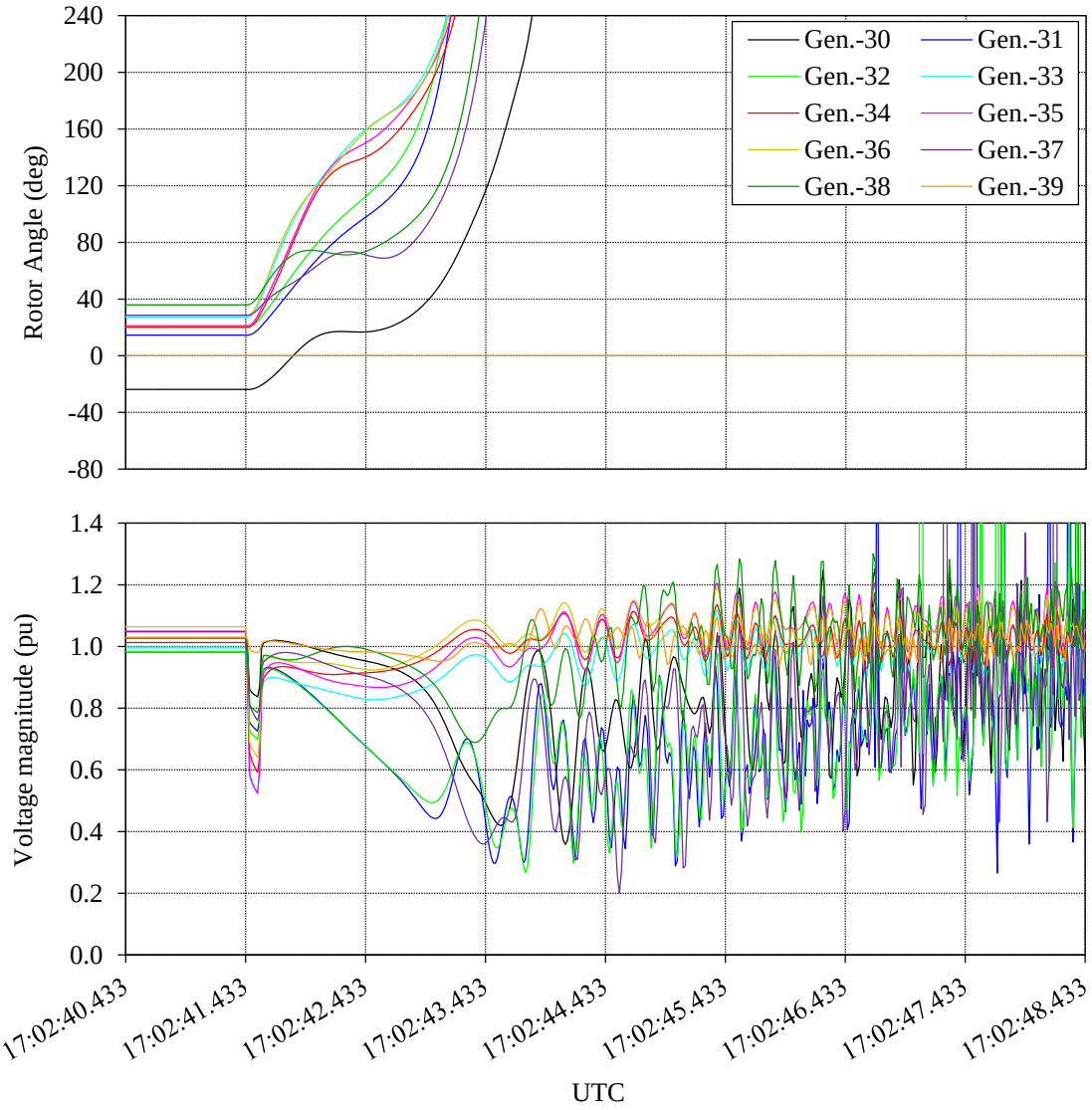

Figure 6.11 Variations of rotor angle and voltage magnitude for fault on line 16-17 (95% of the length) cleared by removing the line after 6 cycles

The proposed transient stability status prediction algorithm declared the power system as unstable at UTC of 17:02:42.200, and identified generators at bus 31 and bus 32 as the unstable generators. The corresponding post-disturbance trajectories of the generators on

ROCOV–ΔV plane are shown in Figure 6.12. When the rotor angle separation criterion given in (5.45) was applied, instability was declared at 17:02:43.216 (UTC). Therefore, in this case, the proposed approach has an early prediction time advantage of 1016 ms.

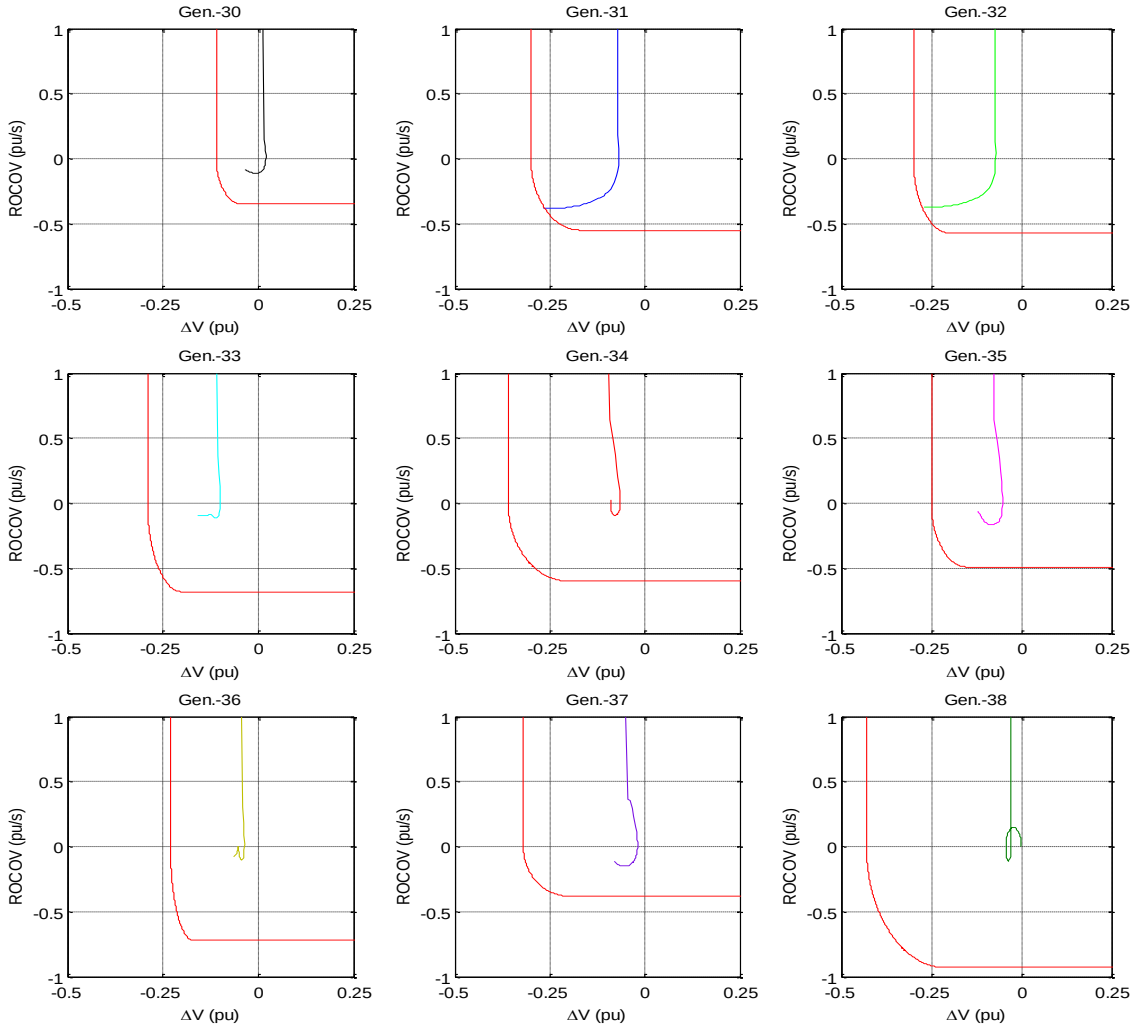

Figure 6.12 ROCOV vs. voltage deviation for fault on line 16-17 (95% of the length) cleared by removing the line after 6 cycles

6.4.3 Performance under Asymmetrical Faults

It is important to investigate how the proposed transient stability status prediction algorithm performs under asymmetrical faults, which are less severe in nature, but more probable in power systems. Initial investigations showed that positive sequence voltages were sufficient to predict the stability status under all types of faults:

i. Single-phase-to-ground faults
ii. Phase-to-phase faults
iii. Phase-to-phase-to-ground faults
iv. Three-phase-to-ground faults

In the test, 225 contingencies were created for each fault type and the fault durations were varied in the range of six to ten cycles. In total, 900 cases were created in RTDS. The results of this test are summarized in Table 6.4. It can be observed that the overall accuracy is over 99% for all fault types. The average early prediction time advantage varies in the range of 600-700 ms.

Despite the filtering provided by PMUs, if a voltage transient with significant magnitude (~ 1 pu) occurs during a post-disturbance period where the transient stability status prediction algorithm is in-operation, the ROCOV–ΔV trajectory can temporary enter the unstable region for a duration of two to three reporting intervals. Declaration of false instability condition due to such transients can be avoided by delaying the decision for several consecutive reporting periods, but at the expense of reduction in the early prediction time advantage. In future, it will be possible to stream PMU data at high reporting rates (more than 50 fps or 60 fps) with the infrastructure developments. This will help to main-

tain or even to increase the early prediction time advantage when several additional consecutive reporting periods are considered for the status prediction process.

Table 6.4 Prediction accuracy for different types of faults

Fault duration	Condition	Predicted as stable	Predicted as unstable	Early prediction advantage* (ms)	Overall accuracy (%)
i	Stable case	219/219	0/219	n/a	100.00
	Unstable case	0/6	6/6	619	
ii	Stable case	200/200	0/200	n/a	100.00
	Unstable case	0/25	25/25	601	
iii	Stable case	176/177	1/177	n/a	99.55
	Unstable case	0/48	48/48	705	
iv	Stable case	106/108	2/108	n/a	99.11
	Unstable case	0/117	117/117	653	

* Mean values of early prediction time advantage are compared w. r. t. (5.45)

6.4.4 Impact of the Topology Changes

The robustness of the proposed transient stability prediction algorithm was tested by evaluating its performance under three different topology variations from the base case. The topology changes considered were:

i. Line 5-8 out of service

ii. Line 22-23 out of service

iii. Line 25-26 out of service

These topology changes altered the pre-fault operation conditions and thus, the post-disturbance trajectories. In total, 300 contingencies including both symmetrical and asymmetrical faults with different fault durations in the range of 6-10 cycles were simulated for each topology change. The results of the test are summarized in Table 6.5.

Table 6.5 Prediction accuracy under topology changes

Fault duration	Condition	Predicted as stable	Predicted as unstable	Early prediction advantage* (ms)	Overall accuracy (%)
i	Stable case	230/231	1/231	n/a	99.67
	Unstable case	0/69	69/69	717	
ii	Stable case	256/258	2/258	n/a	99.33
	Unstable case	0/42	42/42	630	
iii	Stable case	215/215	0/215	n/a	100.00
	Unstable case	0/85	85/85	603	

* Mean values of early prediction time advantage are compared w. r. t. (5.45)

It can be observed that the overall accuracy remains over 99% for all three scenarios, despite the use of original stability boundaries determined using TSAT simulations under base case scenario. The average early prediction time advantage varied in the range of 600-700 ms. This test further proves that the proposed method is capable of predicting the transient stability status even when the network topology is altered from that used for determining the stability boundaries.

6.5 Concluding Remarks

In this chapter, the method of implementation of the proposed transient stability status prediction algorithm was described and the algorithm was thoroughly validated using an offline simulations and an experimental setup based on real-time simulations. Based on the results of numerous experiments, it can be concluded that using the post-disturbance trajectories of generator terminal buses on ROCOV–ΔV plane, the stability status of the system can be determined. The proposed technique is capable of early predicting the first-swing as well as multi-swing transient instabilities. Furthermore, the proposed method

pinpoints the unstable generator, which is very important in determining emergency control actions. A synchrophasor based mitigation approach against transient instabilities based on early prediction will be presented in the next chapter.

Chapter 7

A Synchrophasor based Emergency Control Scheme for Mitigating Transient Instabilities

7.1 Introduction

A simple emergency control scheme to mitigate transient instabilities is proposed in this chapter to demonstrate the utility of the transient stability status prediction algorithm described in Chapter 6. The proposed method can be recognized as a response based wide area protection and control system. It trips unstable generators and sheds loads based on frequency measurements to mitigate possible transient instabilities with the aid of post-disturbance voltage magnitudes and frequencies obtained from PMUs installed at the generator terminals and the load centers. The effectiveness of the proposed approach was evaluated using the same RTDS^{TM} based test setup described in section 6.4, however, was augmented by adding a path to convey the control actions to close the control loop.

7.2 Wide Area Transient Stability Control

Wide area transient stability control is applied to prevent imminent blackouts, and involves coordinated emergency activities such as load shedding to control the power system dynamics in real-time [116], [117]. Transient instability is a rapid phenomenon and therefore, such a control scheme should respond within a couple of hundreds of milliseconds. Clearly, under this type of a scenario, there is no time for human operator intervention [118].

In literature, there are diverse approaches for wide area transient stability control; however, the selective tripping of unstable generators for transmission line outages has been applied extensively to improve stability [119]. When a power system is unstable, identification of coherent clusters of generators helps to make the intelligent choice of a control strategy [120]. Coherent clusters of generators swing together after a severe disturbance. Rotor angle and phase angle at the generator terminal voltage are often used in literature to recognize generator coherency [120]-[122]. The philosophy behind this idea is that the early generator acceleration is only the initial information about the swing [120]. As discussed in Section 5.4, the terminal voltage magnitude dip during a fault and a slow rate of recovery during the post-disturbance restrict electrical power output resulting in an early generator acceleration. Thus, post-disturbance terminal voltage magnitude has direct impact on the stability of a generator and be indicative of its acceleration (or deceleration) after a disturbance. Therefore, the generator terminal voltage magnitudes should also be applied to approximately identify the coherent clusters, especially when the system is going to be transiently unstable. The critical cluster comprises unstable gen-

erator(s), which can be recognized with the aid of a transient stability status prediction algorithm. If the critical cluster of generators is identified, it is possible to trip all generators in that coherent cluster to mitigate potential transient instabilities.

Tripping of generators consequently causes the system frequency to drop due to generation-load imbalance. Thus, it is essential to follow up generator shedding with a load shedding procedure. The transient stability control scheme proposed in this thesis is activated upon prediction of potential instability by the scheme proposed in Chapter 6, trips a selected set of generators to prevent potential out of step conditions and then activates a simple frequency based load shedding scheme.

The proposed scheme is centralized and therefore, it is possible to trip unstable cluster of generators immediately. If the out-of-step protection based local control scheme is used, unstable generators should be tripped individually as the local control schemes do not aware about the overall situation of the power system. Experiments showed that such an approach causes total system collapse under number of contingencies. Further, it is easy to implement the frequency based load shedding as a centralized scheme.

7.3 Generator and Load Shedding Scheme

The overall structure of transient stability status prediction and emergency control system is shown in Figure 7.1. As discussed in Chapter 6, the transient stability status prediction algorithm classifies the transient swings in the post-disturbance stage as stable or unstable, based on rate of change of voltage vs. voltage deviation characteristics of the

post-disturbance voltage magnitudes obtained from PMUs installed at the generator terminals.

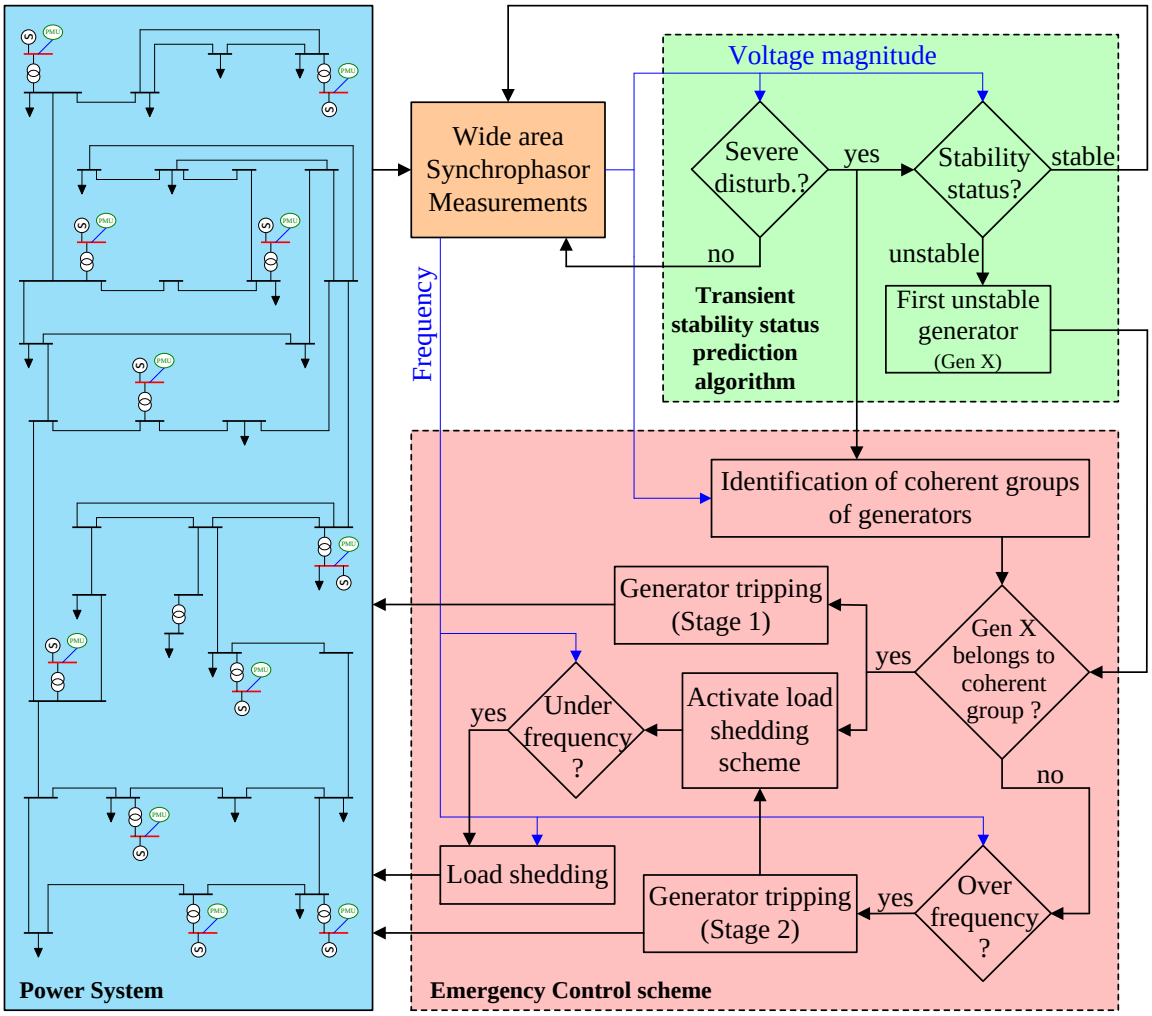

Figure 7.1 Overall structure of the proposed transient stability status prediction and emergency control system

When the disturbance detection logic identifies a severe disturbance, it triggers the coherency recognition technique with the aid of the post-disturbance voltage magnitudes. If the system is declared as unstable, and the generator that becomes unstable first will be notified by the transient instability prediction algorithm. Then the control signals are is-

sued to trip all generators belong to the cluster that includes the generator that becomes unstable first. Then the frequency based load shedding scheme is launched to retain generation-load equilibrium of the rescued portion of power system. While the load shedding scheme is in operation, frequencies at the healthy generator terminals are monitored through PMUs and trip these generators if their frequencies exceed the over frequency setting. As the proposed scheme is centralized and time-critical, it is assumed that a dedicated communication network is available for sending signals to trip generators and loads.

7.3.1 Recognition of Coherent Clusters of Generators

The idea behind the proposed coherent cluster recognition technique is similar to the philosophy of the proposed transient stability status prediction algorithm where the slow rate of voltage recovery during the premature post-disturbance restricts the generator electrical power output. This tends some generators initially accelerate and swing together. Therefore, early post-disturbance voltage magnitudes obtained from PMUs at the generator terminals comprise the initial information about the coherency and support identification of the critical cluster that includes the generator(s) predicted to be unstable soon. As per the author's knowledge this is the first time that voltage magnitudes are used for finding coherent generators.

In order to determine coherent groups, generator terminal voltage magnitudes in an observation data window of K consecutive measurements are collected for each generator in the system. The distance between the trajectories of the post disturbance terminal voltages of two generators can be measured by

$$I_{ij} = \sum_{k=1}^{K} \left[Vmag_G^{(i)}(t_{cl} + k\Delta t) - Vmag_G^{(j)}(t_{cl} + k\Delta t) \right]^2 \quad ; \quad \text{for } i, j = 1, 2, \ldots, n_g \qquad (7.1)$$

where $Vmag_G^{(i)}(t_{cl} + k\Delta t)$ and $Vmag_G^{(j)}(t_{cl} + k\Delta t)$ are the voltage magnitudes of i^{th} and j^{th} generators at time $t_{cl} + k\Delta t$, Δt is the PMU reporting interval given in (6.2) and n_g is number of generators.

A matrix of I_{ij}values can be computed considering different generator pairs, and be used to identify the coherent swing groups. Suppose the generators i and j belong to the same coherent cluster while the generator k belongs to a different cluster. Then the distance I_{ij} will be smaller than the distance I_{ik}. The distances between trajectories can be used to group them into coherent clusters using the routine described in [120]. Note that the algorithm given in [120] is based on rotor angles.

As shown in Figure 7.2 the distance values of each unclassified generator is compared with a pre-specified threshold ε_I. If the distance from generator i to all other generator is greater than the threshold, the generator i is classified into a new cluster; otherwise the closest generator (say generator j') to the generator i is identified. If the generator j' is already classified into a cluster, then the generator i is classified into the same cluster as generatorj'. If generator j' is unclassified, both generators i and j' are classified into a new cluster. This routine is continued until all the generators are classified. After the classification, if I_{ij} value between any two generators in the same cluster is greater than the threshold ε_I (say for generator k) then it is considered to be included in a different cluster which yields more I_{ik} values that are smaller than the threshold ε_I. This is continued until the optimum clustering is obtained.

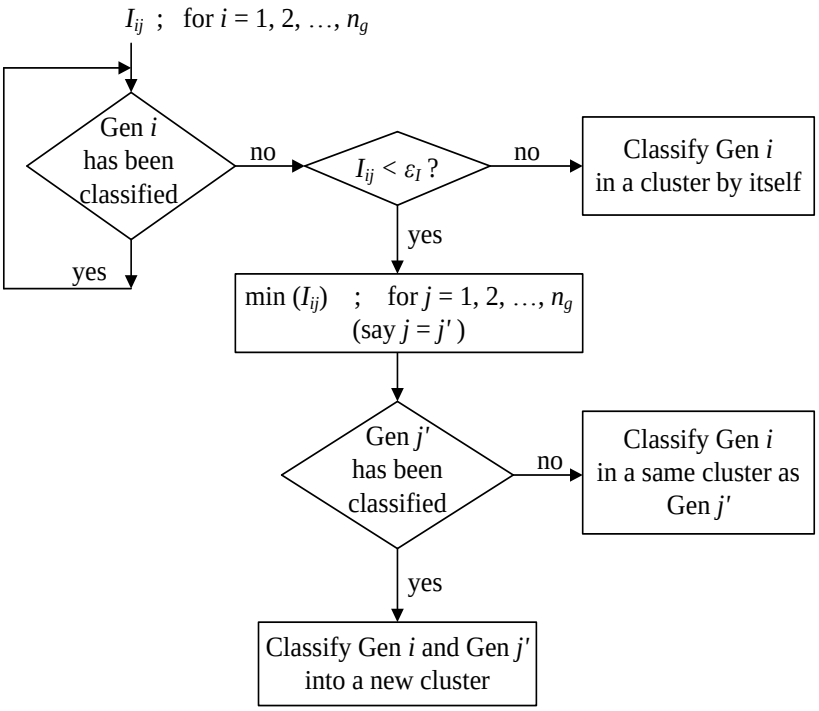

Figure 7.2 Coherency cluster recognition routine (adapted from [120])

7.3.2 Frequency based Load Shedding

The simple frequency based load shedding scheme proposed in this study relies only on the healthy generator and the load center frequencies. It is not attempted to optimally determine the exact location and the precise amount of load shedding, but it is assumed that load shedding locations have been preselected by the study engineers well familiar with the particular power system. Furthermore, it is assumed that PMUs are installed at all load shedding locations. The schematic diagram of the proposed load shedding scheme is shown in Figure 7.3. Tripping of unstable generators trigger the load shedding scheme to retain the generation-load equilibrium.

The average frequency, $\bar{f}_{sys}$, of the rescued portion of the power system is determined from the frequency measurements obtained from the PMUs located at the generator terminals as

$$\bar{f}_{sys} = \frac{1}{n_g{}'} \sum_{k=1}^{n_g{}'} f_k(t) \tag{7.2}$$

where $f_k(t)$ is frequency of the k^{th} stable generator in the rescued system at time t and $n_g{}'$ is the number of stable generators in the system. In Figure 7.3, $f_p(t)$ represents frequency at the p^{th} unshed load at time t and n_p* is the number of unshed loads in the system.

In the proposed approach, three frequency settings are defined such that $f_{set1} < f_{set2} < f_{set3}$. If the average system frequency is less than f_{set1}, the three unshed loads at lowest frequency locations will be shed. Then the duration of t_{set1} seconds is waited before further load shedding so that the power system has enough time to response. When the average system frequency is less than f_{set2} or f_{set3} the next two loads or a single load, respectively, will be selected based on frequency measurements. The waiting-times corresponding the settings f_{set2} and f_{set3} are t_{set2} and t_{set3} seconds respectively.

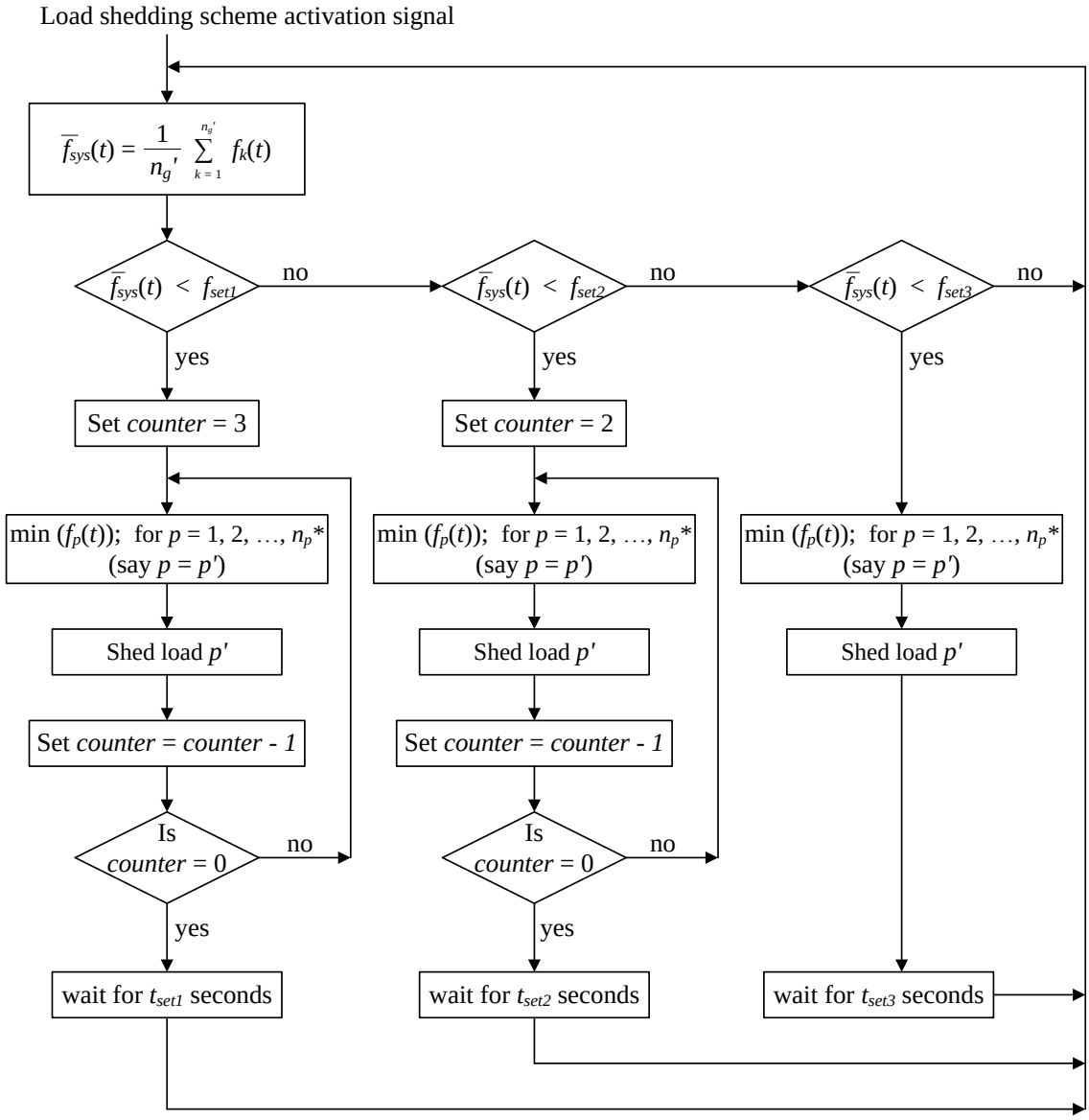

Figure 7.3 Proposed load shedding scheme

7.4 Experimental Setup for Validation

The effectiveness of the proposed approach was evaluated using the test setup consisting of a real-time digital simulator (RTDS™) and a laboratory scale communication

network described in Section 6.4. This test setup was augmented to accommodate emergency control signals (going from the emergency controller to the actuators in the simulated power system) as shown in Figure 7.4.

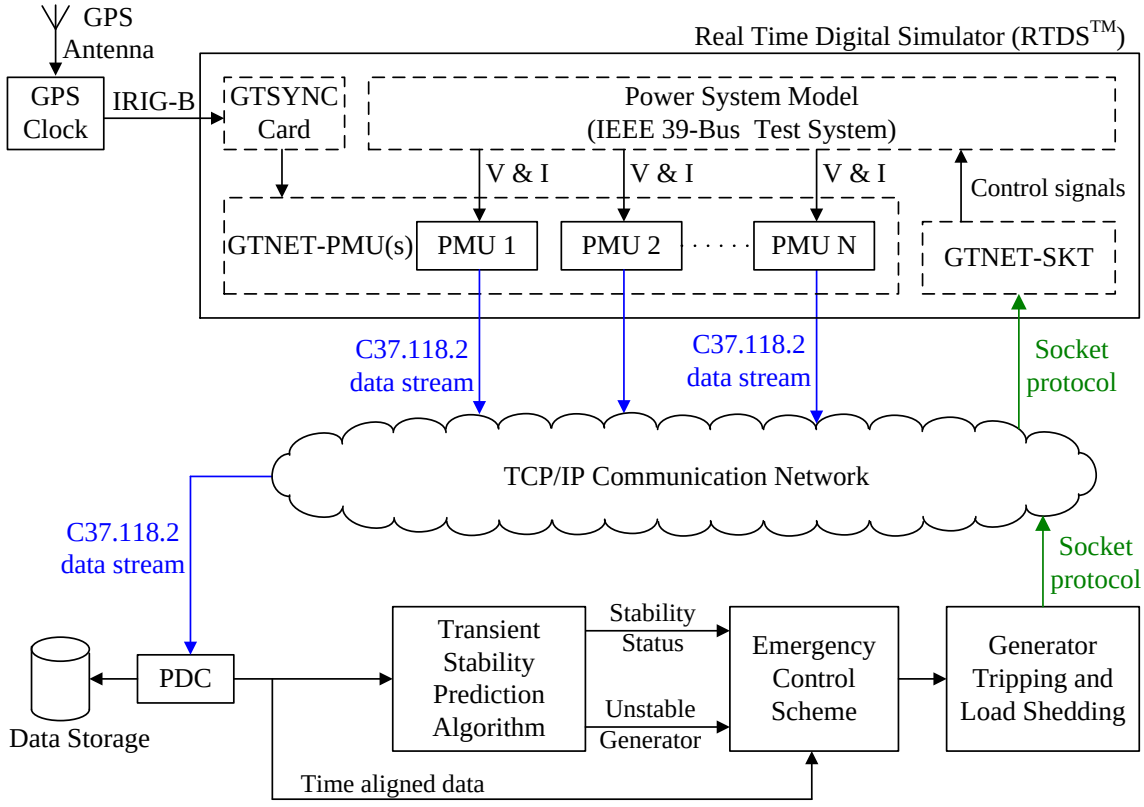

Figure 7.4 Test setup for validating the synchrophasor based emergency control scheme

The GTNET-SKT™ (SocKeT) protocol was used to communicate control signals to the RTDS using a TCP/IP network [123]. Both integers and 32-bit floating point numbers defined in the IEEE 754 format can be transmit/receive using the SKT protocol. Data points are stored in big endian format and the size of the packets is a multiple of 4 bytes. The maximum possible data update rate is 5000 Hz [123].

The latency of the laboratory communication network used for transferring both measurements and control signals was minimal. Therefore, to emulate more realistic sce-

nario, the PDC waiting time was set as 200 ms and additional 50 ms delay was added to control signals so that the simulated results to be more realistic. The generator clustering was based on the synchrophasor data gathered during the first 20 cycles (333 ms) following the clearance of the disturbance. This is because the long time intervals may mislead the clustering process [120]. The threshold ε_I was selected as 0.16 based on trial and error. The New England 39-bus system was used as the test network. Ten load shedding locations were identified after some initial off-line simulation studies, which are given in Table 7.1.

Table 7.1 Load shedding locations

Location	Active power (MW)	Reactive power (MVar)
Bus 3	322.0	2.4
Bus 4	500.0	184.0
Bus 8	522.0	176.0
Bus 15	320.0	153.0
Bus 20	628.0	103.0
Bus 21	274.0	115.0
Bus 24	308.6	-92.0
Bus 25	224.0	47.2
Bus 26	139.0	17.0
Bus 27	281.0	75.5

The load shedding scheme was design to activate 6 cycles following the generator tripping. Frequency settings and the corresponding waiting times of the load shedding scheme are given in Table 7.2. The settings were determined after some off-line simulation studies, but not much emphasis was placed on optimizing the load shedding scheme. The main purpose is to demonstrate the emergency control scheme.

Table 7.2 Frequency settings and waiting times

Setting	Frequency setting, f_{set}(Hz)	Waiting time, t_{set}(ms)
1	59.3	800
2	59.0	500
3	58.5	300

In order to examine the detailed working of the proposed transient instability prediction and emergency control scheme, the same examples illustrated in Section 6.4 (where a single generator or multiple generators become unstable) were revisited.

7.4.1 Example 1 : Fault on line 26-29 (25% of the length)

In the first example, a three-phase to ground fault was applied on Line 26-29 (at 25% of the length from bus 26) when the UTC is around 6:31:53.333. The fault was cleared by removing the line after 6 cycles. The corresponding distance matrix elements, I_{ij}were calculated and given in Table 7.3. The proposed coherency cluster recognition technique recognized two clusters: the first cluster comprised only the generator at bus 38, and the second coherency cluster consisted of the remaining eight generators (the 10^{th} generator at bus 39 represents an equivalent system). The transient stability status prediction algorithm declared the system as unstable at 6:31:54:316 and the generator at bus 38 was identified as the generator that will become out-of-step first. Therefore, a trip signal was issued immediately (around 6:31:54:316), which tripped the generator at bus 38 around 6:31:54:366. The corresponding variations of the rotor angle, the voltage magnitudes and generator trip signals at the LDC are shown in Figure 7.5.

Table 7.3 Distance matrix elements – Example 1

	Gen-30	Gen-31	Gen-32	Gen-33	Gen-34	Gen-35	Gen-36	Gen-37	Gen-38 †	Gen-39
Gen-30	0	0.071	0.069	0.052	0.018	0.000	0.009	0.044	0.704	0.001
Gen-31	0.071	0	0.000	0.002	0.019	0.071	0.128	0.004	0.351	0.085
Gen-32	0.069	0.000	0	0.001	0.018	0.070	0.127	0.004	0.353	0.083
Gen-33	0.052	0.002	0.001	0	0.010	0.052	0.102	0.001	0.398	0.064
Gen-34	0.018	0.019	0.018	0.010	0	0.017	0.049	0.006	0.526	0.024
Gen-35	0.000	0.071	0.070	0.052	0.017	0	0.009	0.043	0.711	0.001
Gen-36	0.009	0.128	0.127	0.102	0.049	0.009	0	0.090	0.868	0.005
Gen-37	0.044	0.004	0.004	0.001	0.006	0.043	0.090	0	0.429	0.054
Gen-38 †	0.704	0.351	0.353	0.398	0.526	0.711	0.868	0.429	0	0.752
Gen-39	0.001	0.085	0.083	0.064	0.024	0.001	0.005	0.054	0.752	0

† unstable coherency cluster

As a result of generator tripping, the system will lose its power balance and the system frequency tends to drop as shown in Figure 7.6(a) without the load shedding scheme. In the next set of graphs shown in Figure 7.6(b), variations of the frequency measurements after activating the simple frequency based load shedding scheme described in Section 7.3.2 are shown. At 6:31:59.366 it was sensed that the system frequency dropped below 59.3 Hz and consequently, a signal was issued to trip the load at bus 3. During the waiting time, it was observed that the system frequency tended to rise; however, it still below 59.3 Hz at 6:32:00:183 causing the controller to issue another signal to trip the load at bus 25. As the system frequency did not recover, the controller trips the load at bus 26 at 6:32:01:016. After shedding the third load the power system became stable and system frequency returned close to the nominal value as shown in Figure 7.6(b).

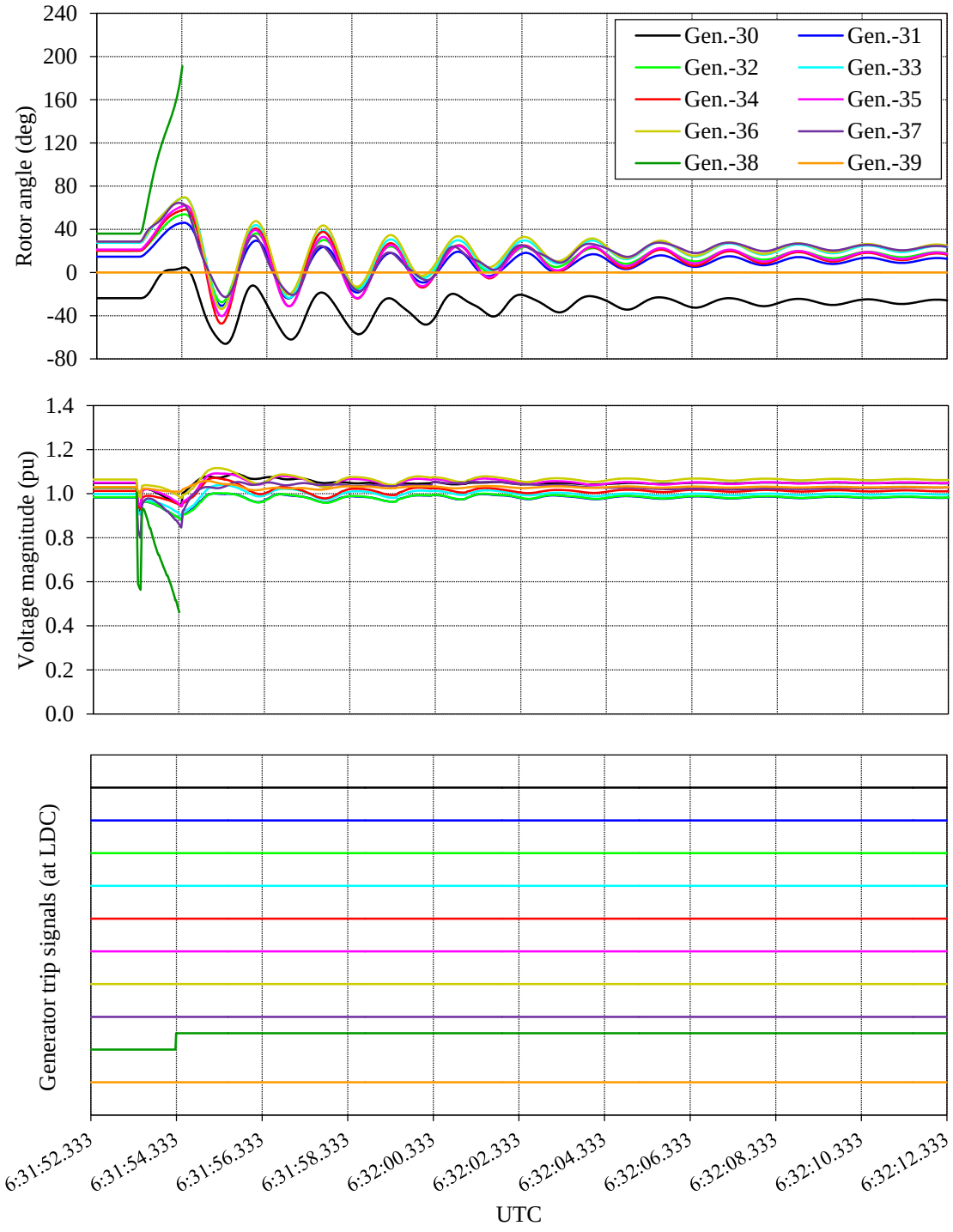

Figure 7.5 Example 1 : Variations of rotor angle, voltage magnitude and generator trip signals with the emergency control scheme

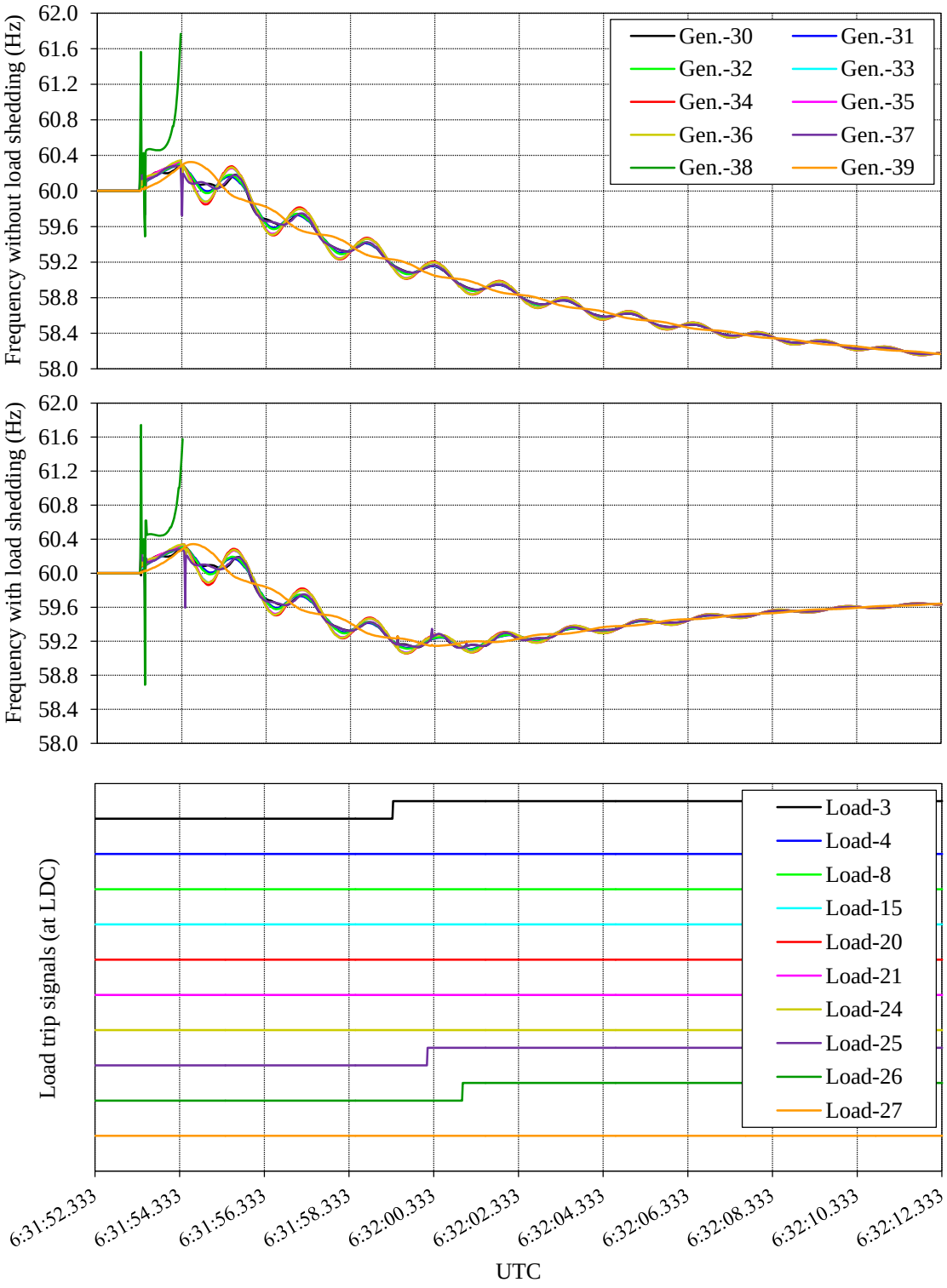

Figure 7.6 Example 1 : Comparison of frequency variations with and without load shedding scheme and load trip signals

7.4.2 Example 2 : Fault on line 2-25 (50% of the length)

In the second example, a three-phase to ground fault was applied on line 2-25 (at 50% of the length) when UTC is 6:35:56.833 and cleared by removing the line after 6 cycles. The distance matrix elements, I_{ij} are given in Table 7.4. Following the fault clearance, the proposed coherency cluster recognition technique recognized two clusters where the first coherency cluster comprised generators at bus 37 and bus 38 and the second coherency cluster comprised of the remaining seven generators. The transient stability status prediction algorithm declared the system as unstable and the generator at bus 37 was recognized as the generator that will become out-of-step first. This generator belonged to the first coherency cluster, and therefore, this coherency cluster was categorized as the critical cluster.

Table 7.4 Distance matrix elements – Example 2

	Gen-30	Gen-31	Gen-32	Gen-33	Gen-34	Gen-35	Gen-36	Gen-37 †	Gen-38 †	Gen-39
Gen-30	0	0.150	0.152	0.120	0.054	0.015	0.001	0.642	0.249	0.001
Gen-31	0.150	0	0.000	0.002	0.024	0.070	0.132	0.175	0.161	0.134
Gen-32	0.152	0.000	0	0.002	0.025	0.071	0.134	0.173	0.150	0.136
Gen-33	0.120	0.002	0.002	0	0.013	0.050	0.105	0.210	0.143	0.106
Gen-34	0.054	0.024	0.025	0.013	0	0.012	0.044	0.325	0.179	0.045
Gen-35	0.015	0.070	0.071	0.050	0.012	0	0.010	0.463	0.164	0.010
Gen-36	0.001	0.132	0.134	0.105	0.044	0.010	0	0.609	0.226	0.000
Gen-37 †	0.642	0.175	0.173	0.210	0.325	0.463	0.609	0	0.120	0.611
Gen-38 †	0.249	0.161	0.150	0.143	0.179	0.164	0.226	0.120	0	0.228
Gen-39	0.001	0.134	0.136	0.106	0.045	0.010	0.000	0.611	0.228	0

† unstable coherency cluster

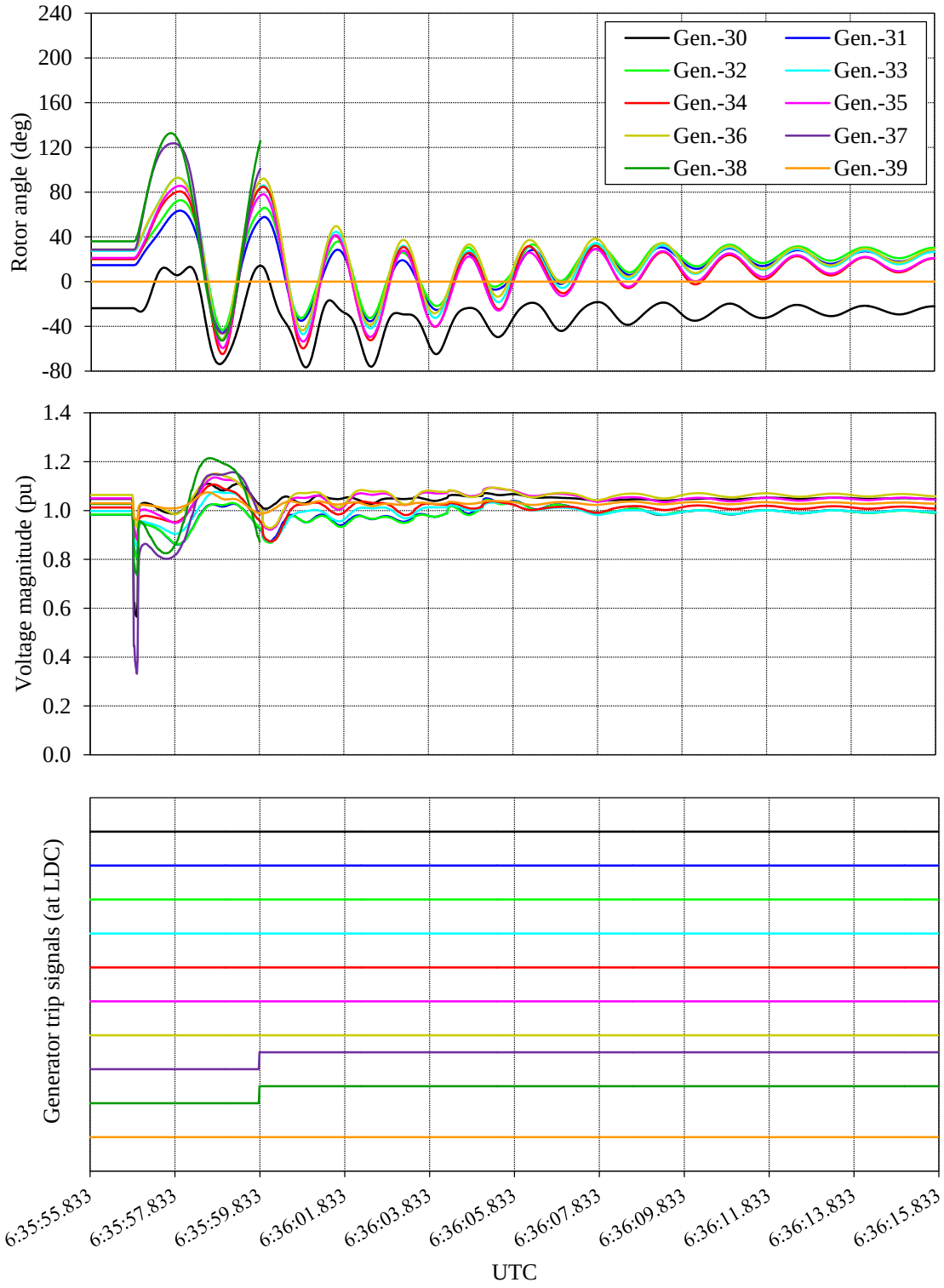

Figure 7.7 Example 2 : Variations of rotor angle, voltage magnitude and generator trip signals with the emergency control scheme

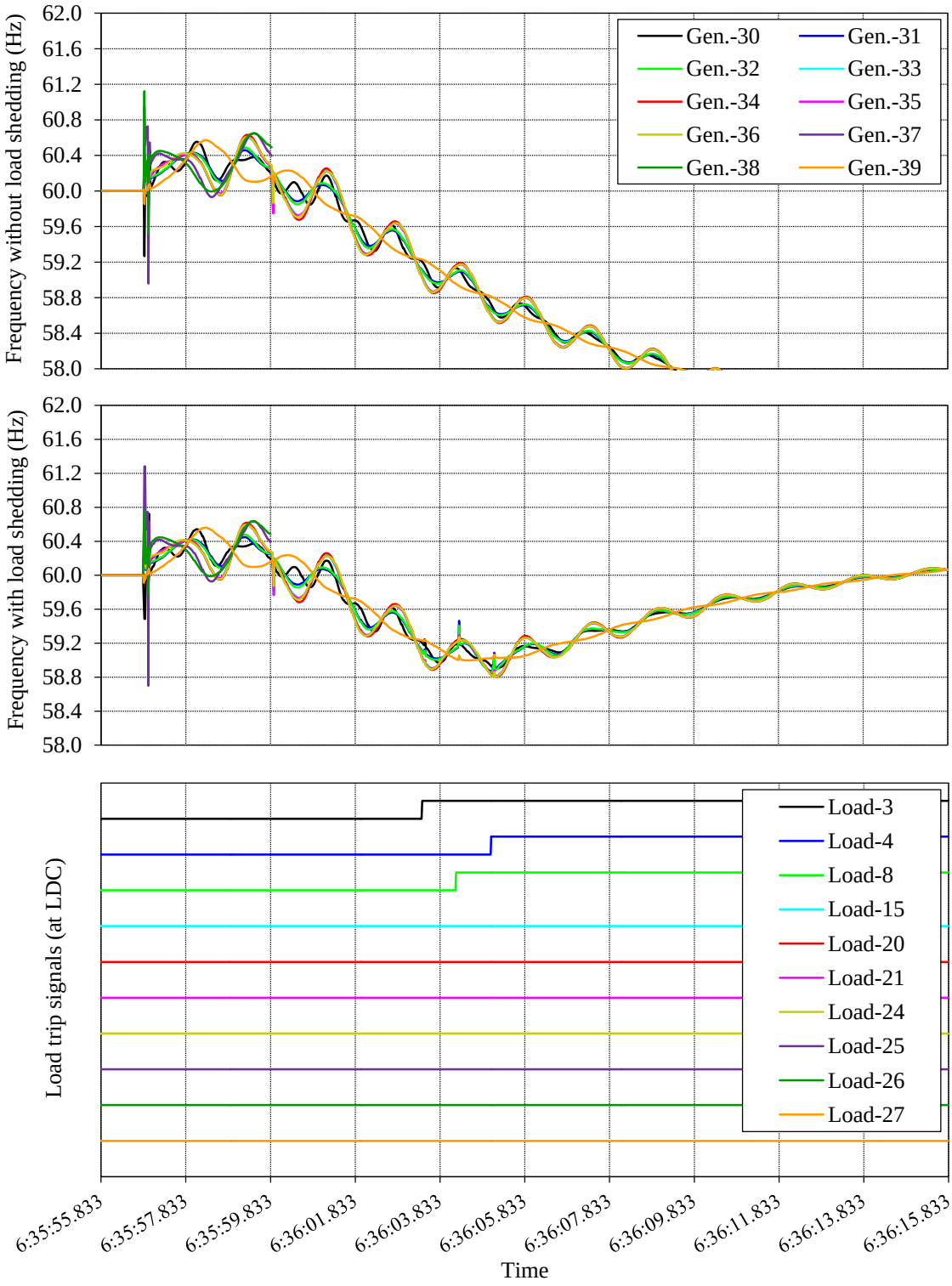

Figure 7.8 Example 2 : Comparison of frequency variations with and without load shedding scheme and load trip signals

Commands were issued around 6:35:59.833 to trip both generators (generators at bus 37 and bus 38) in the critical cluster. The generators at bus 37 and bus 38 were tripped around 6:35:59:883 due to the additional delay introduced to the control signals. The corresponding variations of the rotor angle, the voltage magnitudes and generator trip signals at the LDC are shown in Figure 7.7.

At 6:36:03.416, it was detected that the system frequency dropped below 59.3 Hz and consequently, a signal was issued to trip the load at bus 3. During the waiting time, it was monitored that the system frequency was still below 59.3 Hz; hence, a signal was issued around 6:36:04.216 to trip the load at bus 8. As the system frequency did not improve the third signal was issued around 6:36:05.050 to trip the load at bus 4. After shedding the third load it was observed that the power system was frequency stable as shown in Figure 7.8.

7.4.3 Example 3 : Fault on line 16-17 (95% of the length)

In the last example, a three-phase-to-ground fault was applied on line 16-17 (at 95% of the length) when UTC is 5:49:34.333 and cleared by removing the line after 6 cycles. The distance matrix elements, I_{ij} are given in Table 7.5 and the coherency cluster recognition technique identified two clusters. The first coherency cluster comprised generators at bus 31, bus 32, bus 33 and bus 34. The rest of the generators belonged to the second coherency cluster. The transient stability status prediction algorithm declared the system as unstable and identified generators at bus 31 and bus 32 as the unstable generators, which belonged to the first coherency cluster. Therefore, this coherency cluster was cate-

gorized as a critical cluster and trip signals were issued around 5:49:35.400 to trip all generators (generators at bus 31, bus 32, bus 33 and bus 34) in the critical cluster. It was observed that generators at bus 35 and bus 36 exceeded over frequency setting of 61.0 Hz. Therefore, these two generators were tripped (stage 2) around 5:49:35.683. The corresponding variations of the rotor angle, the voltage magnitudes and generator trip signals at the LDC are shown in Figure 7.9.

Table 7.5 Distance matrix elements – Example 3

	Gen-30	Gen-31 †	Gen-32 †	Gen-33 †	Gen-34 †	Gen-35	Gen-36	Gen-37	Gen-38	Gen-39
Gen-30	0	0.242	0.261	0.327	0.163	0.127	0.073	0.037	0.058	0.000
Gen-31 †	0.242	0	0.000	0.011	0.020	0.155	0.182	0.232	0.199	0.234
Gen-32 †	0.261	0.000	0	0.009	0.025	0.150	0.190	0.244	0.208	0.251
Gen-33 †	0.327	0.011	0.009	0	0.032	0.178	0.221	0.280	0.242	0.317
Gen-34 †	0.163	0.020	0.025	0.032	0	0.133	0.150	0.175	0.140	0.167
Gen-35	0.127	0.155	0.150	0.178	0.133	0	0.009	0.029	0.017	0.122
Gen-36	0.073	0.182	0.190	0.221	0.150	0.009	0	0.009	0.002	0.069
Gen-37	0.037	0.232	0.244	0.280	0.175	0.029	0.009	0	0.006	0.035
Gen-38	0.058	0.199	0.208	0.242	0.140	0.017	0.002	0.006	0	0.053
Gen-39	0.000	0.234	0.251	0.317	0.167	0.122	0.069	0.035	0.053	0

† unstable coherency cluster

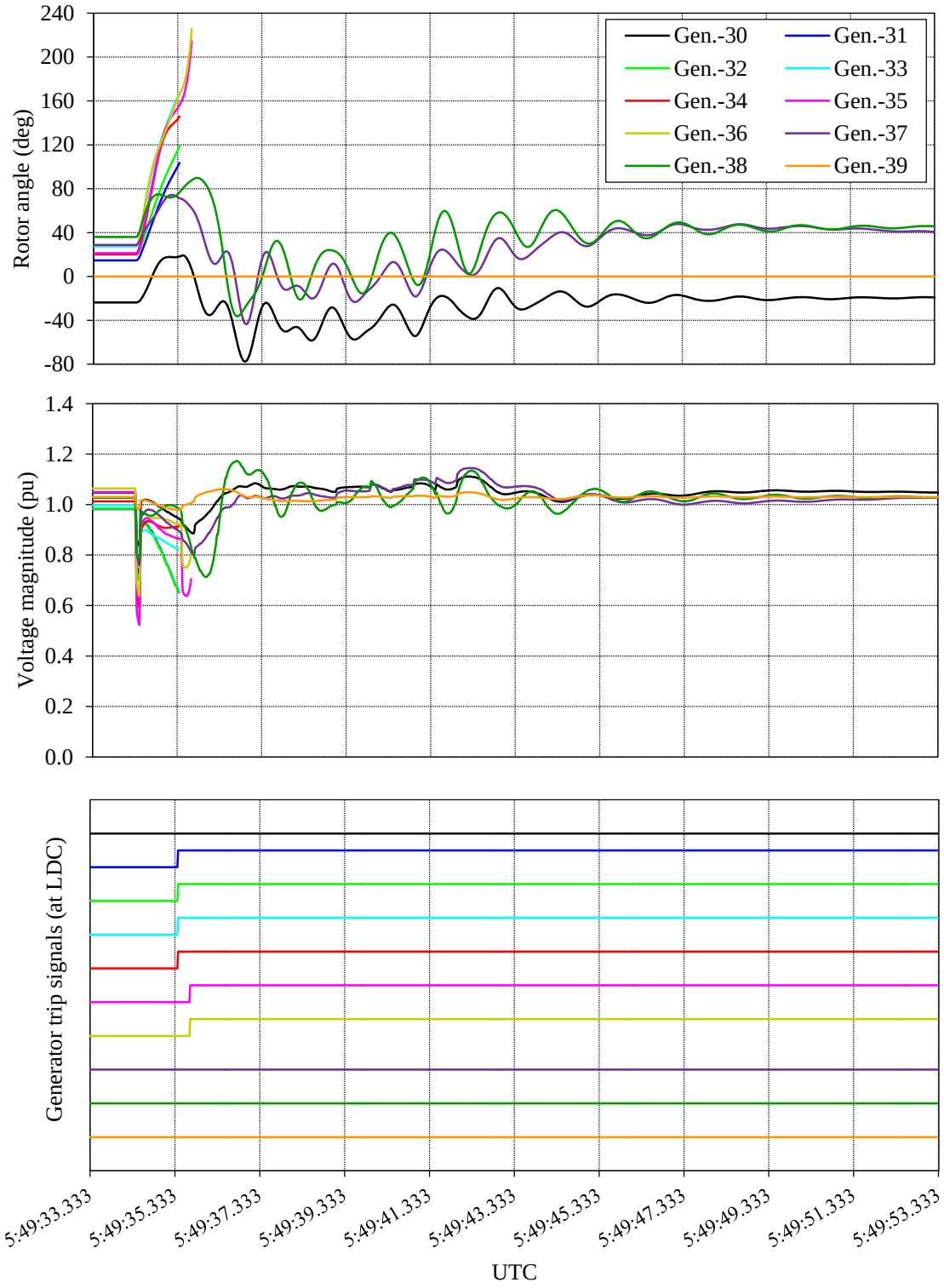

Figure 7.9 Example 3 : Variations of rotor angle, voltage magnitude and generator trip signals with the emergency control scheme

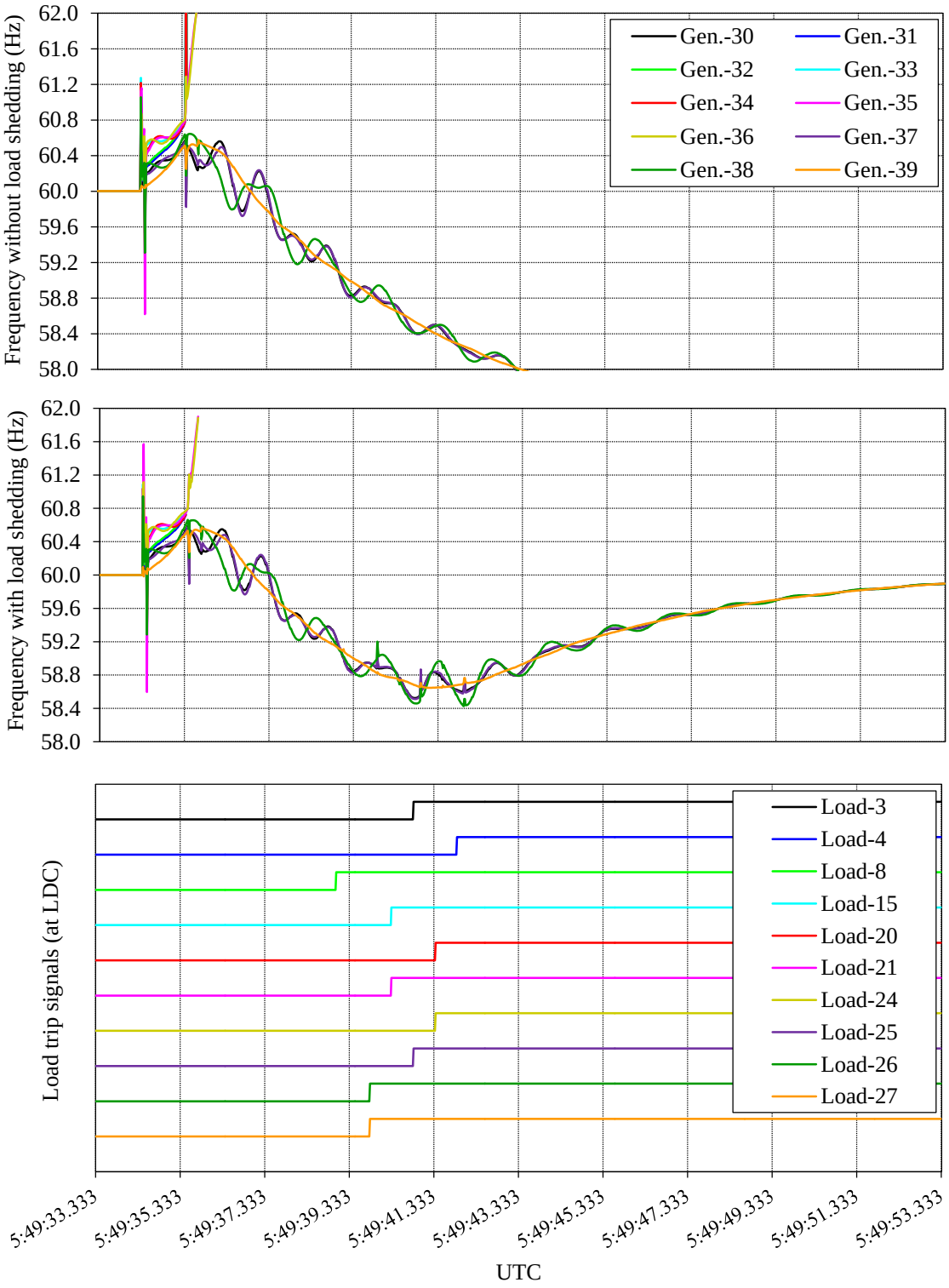

Figure 7.10 Example 3 : Comparison of frequency variations with and without load shedding scheme and load trip signals

The system frequency rapidly dropped as the power imbalance was rather significant due to loss of six generators. At 5:49:39.016 it was detected that the system frequency dropped below 59.3 Hz and consequently, a signal was issued to trip the load at bus 8. During the waiting time, it was monitored that the system frequency further dropped below 59.0 Hz; hence, signals were issued around 5:49:39:833 to trip the loads at bus 26 and bus 27. As the system frequency did not improve the load shedding process continued until all 10 loads in the load shedding scheme had been tripped. After shedding all ten loads it was observed that the saved portion of the power system was stable as shown in Figure 7.10. This is a very severe disturbance and restoration of the system need to be followed after the generator and load shedding.

7.5 Real-World Implementation Issues

In this thesis, the proposed transient instability prediction and emergency control scheme was thoroughly validated for the IEEE 39-bus test system using the real-time simulator and a laboratory scale test setup. A next possible step is to confirm the performance of the proposed scheme on the field as a pilot project, which will help to reveal more practical concerns.

The proposed emergency control scheme trips the unstable cluster of generators immediately after the system is predicted as unstable. However, it may not be advisable to open generator circuit breakers immediately due to possible high transient recovery voltage (TRV) that may be damaging to the breaker. If the circuit breaker of a generator is opened when the voltages across the circuit breaker contacts are 180^0 out-of-phase during

interruption [98], the resulting TRV may exceed the breaker capability. Therefore, it may be necessary to apply local supervision to check and delay if necessary, the operation of the generator circuit breakers.

Today, most utilities already have PMUs at their important substations such as large generator stations and load centers with dedicated communication channels to the LDC. Therefore, the emergency control scheme proposed in this thesis can be easily installed at the LDC without adding significant infrastructure facilities. However, it may be necessary to reconfigure existing PMUs and PDCs to satisfy the requirements of the proposed scheme. In addition, it is essential to study the impact data quality and communication network related issues, such as cyber security. A detailed study of such aspects is beyond the scope to this thesis.

Since the emergency control scheme proposed in this thesis is simple and more generic, it can be applied to most of real power systems. However, the emergency control actions are system specific: if available, options such as fast control of HVDC converters or FACTs devices, controlled islanding, etc. can be devised as means of controlling the instability. Therefore, it is possible to develop more sophisticated schemes in real power system depends on the availability of resources.

7.6 Concluding Remarks

In this chapter, a response based emergency control scheme was described as an emergency control strategy to alleviate potential transient instabilities. A technique was proposed to approximately identify coherent clusters of generators based on the post-

disturbance voltage magnitudes, which is a novel approach. The unstable coherent cluster was recognized from the generator that would become out-of-step first as identified by the transient instability prediction algorithm described in Chapter 6. A simple frequency based load shedding scheme was introduced to maintain the generation-load equilibrium after tripping of generators belong to the unstable coherent cluster. The proposed scheme was implemented in a real-time environment and tested using a setup consisting of a real-time simulator and laboratory scale communication network. The studies carried out for the IEEE 39-bus test system demonstrated effectiveness of the proposed approach.

Chapter 8

Conclusions and Contributions

This chapter presents the conclusions of the research, summarizes the main contributions, and proposes directions for future research in the area of wide area synchrophasor applications in particular transmission line parameters estimation, and transient stability status prediction and emergency control.

8.1 Conclusions

In this thesis, application of wide area synchrophasor measurements for improved real-time monitoring and control of power systems was investigated. The three specific areas investigated are: (i) steady-state and dynamic performances of PMUs, (ii) real-time tracking of transmission line parameters, and (iii) transient stability status prediction and emergency control for transient instability mitigation.

In Chapter 2, literature on the synchrophasor technology and the synchrophasor standards with special focus on the phasor, frequency and ROCOF estimation methods, reference P-class and M-class filters described in the synchrophasor standard [5], and the

existing approaches to evaluate and improve performances of PMUs were reviewed in detail. Based on the literature survey, it can be concluded that it is mandatory to implement P-class and M-class filters in a PMU to achieve adequate steady-state and dynamic performance requirements specified in the latest synchrophasor standard [5], and the test procedures for performance evaluation are not well defined.

Addressing one of the issues identified in Chapter 2, a PMU performance evaluation setup was developed in Chapter 3. The test setup plays back the test signals that are mathematically generated from signal models into the PMU under test through a real-time playback device with precise GPS synchronization, and the PMU outputs are compared against the theoretical phasor values of the respective test signals to calculate the errors. The PMU performance evaluation approach proposed in this thesis is simple, repeatable, and meets the test equipment accuracy limits specified in the standard.

Using the developed test setup, the steady-state and dynamic performance of a commercial PMU, which was originally designed according to the old synchrophasor standard [39], was evaluated. The test results showed that incorporation of the P-class reference filter and magnitude correction factor proposed in the latest synchrophasor standard IEEE C37.118.1-2011 [5] enabled this PMU to satisfy the dynamic performance requirements of P-class PMUs. However, the PMU failed to satisfy some of the M-class performance requirements with the reference M-class filter provided in the standard [5]. In order to rectify this problem, a magnitude compensation factor was proposed. In order to overcome the practical difficulties in implementing the reference M-class filter in real-time environments, a modified M-class filter with a significantly less number of filter coefficients and a new complex compensation factor was proposed. This new lower order

filter significantly eases the computing resources required to implements the M-class PMUs, reduces the measurement latency at all reporting rates, and realizes an accuracy level better than the reference M-class filter proposed in IEEE C37.118.1-2011 standard [5]. The test results also revealed certain unrealistic FE and RFE requirements imposed on the M-class PMUs in the IEEE C37.118.1-2011 standard [5]. The suggestions made in this research to relax the FE and RFE requirements of M-class PMUs are reflected in the recently released amendment (IEEE C37.118.1a-2014 [41]) to the synchrophasor standard [5].

The problem of real-time estimation of transmission line parameters using synchrophasors was investigated in Chapter 4. Two new computationally efficient and stable transmission line parameter estimation algorithms were derived. It was shown that through appropriate selection of parameters to be estimated, the transmission line parameter estimation problem can be formulated as a linear least square estimation problem. The first algorithm (Algorithm-1) requires inversion of only a non-singular, real-valued, 3×3 symmetrical matrix irrespective of the number of measurements in the data window. The second algorithm (Algorithm-2) requires only to invert single element complex matrices regardless of the number of measurement. Thus, the proposed algorithms are computationally more efficient compared to the previously published line parameter estimation algorithms which require use of iterative nonlinear estimation routines or input excitation. In addition to the above two, a new algorithm (Algorithm-3) was proposed to estimate the parameters of a series compensated line. This iterative, non-linear LS estimation-based algorithm requires inversion of a 2×2 complex-valued matrix in each iteration

irrespective of the number of measurements. All of the proposed algorithms require voltage and current phasors of the sending and the receiving ends of the transmission line and the estimated line parameters are updated with each PMU reporting. The proposed algorithms were tested using the practical synchrophasors produced by (i) a RTDS simulator and (ii) a laboratory scale hardware setup. Tests were conducted under noisy and unbalanced conditions, and the accuracy levels of the proposed algorithms were better or comparable with the existing computationally more demanding algorithms. When tested with a set of field measurements obtained from a utility for an uncompensated transmission line, all line parameter estimation algorithms provided similarly accurate estimations. Analysis of the sensitivity of the estimations to bias-errors in the measurements showed that transmission line resistance is highly sensitive to the errors in voltage magnitudes and, the sensitivity is higher at the larger X/R ratios.

A novel approach for transient stability status prediction was introduced in Chapter 5. A thorough review of the previously proposed methods and their limitations was presented. Based on the literature review, post-disturbance recovery voltage magnitudes measured at the generator terminals was recognized as a good indicator to identify potential transient instabilities. It was shown that a transient stability boundary can be drawn on the ROCOV–ΔV plane and a generator will become transiently unstable soon after its post-disturbance trajectory crosses this boundary. The proposed approach does not rely on machine learning techniques as in the case of previously reported voltage magnitude based transient stability prediction algorithms.

In Chapter 6, a practical methodology for implementation of the proposed transient stability prediction algorithm for a large multi-generator power system was developed.

The implementation involves three steps: for each generator, identification of a contingency that makes the generator marginally stable, determination of the stability boundary of each generator using the post-disturbance recovery voltages measured during the marginally stable contingency, and design of a disturbance detection methodology. It was shown that phasor-domain dynamic simulations can be used to determine stability boundaries and design the disturbance detection logic. The so determined boundaries are generally valid for range of operating conditions and under normal topology variations.

The proposed transient stability status prediction approach was first validated using offline simulations done in TSAT for the IEEE 39-bus test system. Then, the proposed approach was validated using the practical synchrophasors obtained from the IEEE 39-bus test system simulated in a RTDS real-time simulator. A laboratory scale synchrophasor network with a single network switch and a PDC was included in the experimental setup. Both offline simulations and real-time experimental studies showed over 99% overall prediction accuracy under all types of faults. The proposed method could predict potential instabilities on average 600 ms earlier compared to the conventional rotor angle separation methods, allowing a reasonable time to take an appropriate emergency control action. The experiments showed that the proposed technique is capable of early predicting the first-swing as well as the multi-swing transient instabilities. Furthermore, the proposed algorithm correctly determines the generator that will become unstable first, which is a major advantage when determining the emergency control actions. The proposed transient instability prediction technique is computationally simple, transparent, does not require machine learning methods, and can be designed using a readily available phasor

domain dynamic model of the power system. Thus the proposed method is more acceptable to the industry.

In order to demonstrate the utility of the transient stability prediction algorithm, an emergency control scheme for transient instability mitigation was introduced in Chapter 7. If a potential instability is detected by the transient stability status prediction algorithm presented in Chapter 6, it enables the emergency control and indicates the generator that will become out-of-step first. The proposed emergency control scheme, designed for the IEEE 39-bus test system, comprised a method to identify coherent clusters of generators and a frequency deviation based load shedding scheme. A novel method was proposed to recognize the coherent clusters of generators where the post-disturbance generator voltage magnitudes are used as inputs, in contrast to the traditionally used generator rotor angles. Generator voltages are the same inputs used in the transient stability status prediction algorithm. The cluster of generators, which includes the generator that is predicted to be unstable first is categorized as the unstable cluster, and the proposed emergency controller immediately trips all generators in the unstable cluster. In order to preserve the load-generator balance, a simple frequency deviation based load shedding scheme was proposed. The load shedding scheme is based on the post-disturbance frequencies obtained from the same PMUs, which provide voltage magnitudes to the prediction algorithm. The entire system response based transient instability prediction and emergency control scheme was implemented and validated using real-time simulations conducted in RTDS and laboratory scale communication network. The studies carried out for the IEEE 39-bus test system demonstrated effectiveness of the emergency controller for a variety of contingencies.

8.2 Contributions

The main contributions of the research work presented in this thesis are:

1. Development of a simple and repeatable PMU evaluation procedure and a test setup. Test results and various TVE and FE curves, which can serve as a good reference for PMU manufacturers and users.
2. Revelation of some inadequacies of the reference M-class filter algorithm proposed in the IEEE synchrophasor standard C37.118.1-2011 [5]. Proposal for applying a new compensation factor for the reference M-class filter to rectify the problem.
3. Reduced order modified M-class filter, which can significantly reduce the number of filter coefficients and the filter group delay. This finding reduces measurement latency, and eases the real-time computing resources requirements of the PMUs on microprocessor devices.
4. Suggestions to relax some inconsistent error limits imposed by the IEEE synchrophasor standard C37.118.1-2011 [5]. These findings were shared with the IEEE synchrophasor working group, which subsequently developed the amendment [41] to the original standard.
5. Computationally more efficient novel transmission line parameters estimation algorithms, which are comparable or better than the existing algorithms in terms of accuracy, under practical measurement conditions. Validation of the proposed transmission line parameters estimation algorithms using a hardware test setup, a real-time simulation based test setup and actual field measurements.

6. A new algorithm for predicting the transient stability status of a power system after being subjected to a severe disturbance based on rate of change of voltage vs. voltage deviation characteristics of the post-disturbance voltage magnitudes obtained from synchrophasor measurements. The proposed algorithm is computationally simple, transparent, can be designed with the aid of conventional dynamic simulation tools, and identifies the generator that becomes unstable first.
7. Validation of the performance of the proposed transient stability status prediction algorithm using both offline simulations and real-time simulations with practical synchrophasor data. Examination of the sensitivity of the proposed transient stability status prediction algorithm to variety of circumstances such as change of operating conditions, asymmetrical faults, and network topology changes.
8. Development and demonstration of a response based wide area emergency control scheme to mitigate possible transient instabilities by tripping the unstable cluster of generators followed by load shedding.

These contributions have led to the following publications in journals and conferences:

Journal Papers:

- **D. R. Gurusinghe**, A. D. Rajapakse, and K. Narendra, "Testing and enhancement of the dynamic performance of a phasor measurement unit", *IEEE Transactions on Power Delivery*, vol. 5, no. 4, pp. 1551- 1560, Aug. 2014.
- **D. R. Gurusinghe** and A. D. Rajapakse, "Post-disturbance transient stability status prediction using synchrophasor measurements", *IEEE Transactions on Power Systems*, vol. 31, no. 5, pp. 3656- 3664, Sep. 2016.

- **D. R. Gurusinghe**, S. Menike, A. Konara, A. D. Rajapakse, P. Yahampath, U. D. Annakkage, B. Archer, and T. Weekes, "Co-simulation of power system and synchrophasor communication network on a single simulation platform", *Technology and Economics of Smart Grids and Sustainable Energy*, (2016) 1:6, pp. 1-14, Mar. 2016.
- **D. R. Gurusinghe** and A. D. Rajapakse, "Efficient algorithms for real-time monitoring of transmission line parameters and their performance with practical synchrophasors", accepted for *IET Generation, Transmission & Distribution*, Nov. 2016.

One more manuscript is under review:

- **D. R. Gurusinghe** and A. D. Rajapakse, "A Synchrophasor based Emergency Control Scheme for Mitigating Transient Instabilities," submitted to *Electric Power Systems Research*, Nov. 2016.

Conference Papers/Presentations:

- **D. R. Gurusinghe**, A. D. Rajapakse, and K. Narendra, "Evaluation of steady-state and dynamic performance of a synchronized phasor measurement unit," in *proceedings of The Electrical Power and Energy Conference (EPEC 2012)*, London, Ontario, Canada, Oct. 2012.
- K. Narendra, **D. R. Gurusinghe**, and A. D. Rajapakse, "Dynamic performance evaluation and testing of phasor measurement unit (PMU) as per IEEE C37.118.1 standard", presented at *The Doble Client Committee Meetings & International Protection Testing Users Group (PTUG 2012)*, Chicago, Illinois, USA, Oct. 2012.

- **D. R. Gurusinghe**, A. D. Rajapakse, and D. Muthumuni, "Modeling of a synchrophasor measurement unit in an electromagnetic transient simulation program", in *proceedings of The International Conference on Power Systems Transients (IPST 2013)*, Vancouver, British Columbia, Canada, July 2013.
- **D. R. Gurusinghe**, A. D. Rajapakse, D. Ouellette, and R. Kuffel, "An application of wide area synchrophasor based transient stability status prediction" presented at *The North American SynchroPhasor Initiative (NASPI 2015)*, San Mateo, California, USA, Mar. 2015.
- **D. R. Gurusinghe**, A. D. Rajapakse, D. Ouellette, and R. Kuffel, "Real-time monitoring of series compensated transmission line parameters using practical synchrophasor measurements," in *proceedings of Protection, Automation & Control World Conference (PAC World 2015)*, Glasgow, UK, June 2015.
- **D. R. Gurusinghe**, A. D. Rajapakse, and K. Narendra, "Testing and enhancement of the dynamic performance of a phasor measurement unit", presented at *The IEEE PES General Meeting (PES GM 2015)*, Denver, Colorado, USA, July 2015.
- **D. R. Gurusinghe**, Yaojie Cai, and A. D. Rajapakse, "A Software Tool for Real-Time Prediction of Potential Transient Instabilities using Synchrophasor Measurements" presented at *International Synchrophasor Symposium*, Atlanta, Georgia, USA, Mar. 2016.
- **D. R. Gurusinghe** and A. D. Rajapakse, "Post-disturbance transient stability status prediction using synchrophasor measurements", presented at *The IEEE PES General Meeting (PES GM 2016)*, Boston, Massachusetts, USA, July 2016.

8.3 Suggestions for future research

In this thesis, a new modified M-class filter with less number of filter coefficients was introduced by keeping the basic filter structure given in the synchrophasor standard [5] to obtain better PMU performances. However, there is a room to introduce completely new backend filters, which can achieve similar or better performances. In addition, new phasor estimation algorithms such as smart DFT (SDFT) may realize better performances even without performance class filters. Therefore, it is worth to investigate possibilities to develop, implement, and validate new phasor estimation algorithms and new backend filters in PMUs to enhance their steady-state and dynamic performances.

The real power systems not only comprise transmission lines, but also underground cables. Estimation of underground cable parameters using synchrophasor measurements would be very beneficial to the electrical utilities. However, the estimation of the underground cable capacitance is a very challenging task and would be an interesting topic for future research.

The transient instability prediction and mitigation scheme proposed in this thesis was implemented and validated for practical synchrophasor measurements obtained from the real-time simulator and laboratory scale test setup; thus, the impact of the communication network is minimal. However, the performances of the communication network play a vital role especially for the time critical synchrophasor applications. Therefore, future researches are necessary to analysis issues in the synchrophasor communication system such as bandwidth, communication latency, measurement errors, data packet losses, and

cyber security issues in order to diagnose application specific issues and investigate appropriate solutions.

Appendix A

Single Machine to Infinite Bus (SMIB) Test System

A.1 Synchronous Generator Parameters

The synchronous generator is represented by an equivalent circuit whose parameters in per unit on 555 MVA base [29].

$K_D = 0$	$H = 3.5$		
$L_{ad} = 1.66$	$L_{aq} = 1.61$	$L_l = 0.15$	$R_a = 0.003$
$L_{fd} = 0.165$	$R_{fd} = 0.0006$	$L_{1d} = 0.1713$	$R_{1d} = 0.0284$
$L_{1q} = 0.7252$	$R_{1q} = 0.00619$	$L_{2q} = 0.125$	$R_{2q} = 0.02368$

A.2 Excitation System

The excitation system model with AVR and PSS in [29] is replicated in this thesis.

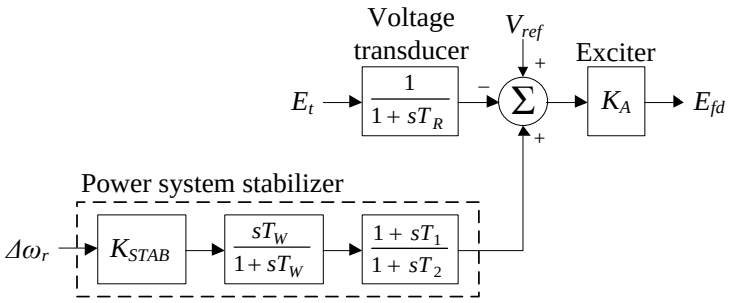

Figure A.1 Excitation system model with AVR and PSS

K_A = 200 T_R = 0.02s

K_{STAB} = 9.5 T_W = 1.4s T_1 = 0.154s T_2 = 0.033s

Appendix B

IEEE 39-bus Test System

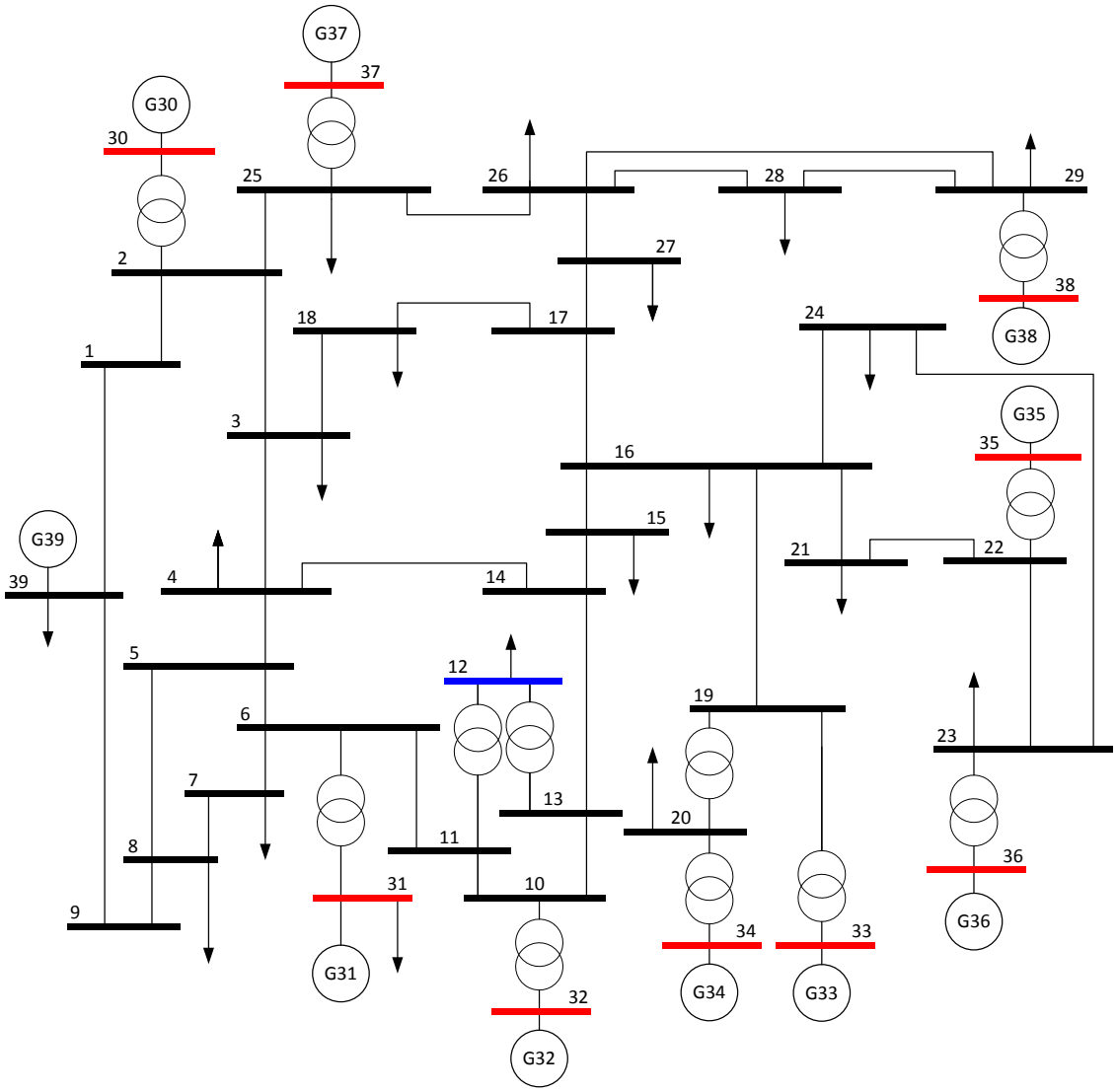

Figure A.2 IEEE 39-bus Test System [83]

B.1 Generator Parameters

The synchronous generators are represented by the two-axis model whose parameters are given on the system base of 100 MVA.

Gen No	R_a (pu)	X_l (pu)	X_d (pu)	X_q (pu)	X_d' (pu)	X_q' (pu)	X_q'' (pu)	X_q'' (pu)	H (s)	T_{do}'(s)	T_{qo}'(s)	T_{do}'' (s)	T_{qo}''(s)
30	0.00125	0.0125	0.1	0.069	0.031	0.028	0.025	0.025	42.0	10.2	1.5	0.05	0.06
31	0.00125	0.035	0.295	0.282	0.0697	0.170	0.05	0.05	30.2	6.56	1.5	0.05	0.06
32	0.00125	0.0304	0.2495	0.237	0.0531	0.0876	0.045	0.045	35.8	5.7	1.5	0.05	0.06
33	0.00125	0.0295	0.262	0.258	0.0436	0.166	0.035	0.035	28.6	5.69	1.5	0.05	0.06
34	0.00125	0.027	0.67	0.62	0.132	0.166	0.05	0.05	26.0	5.4	0.44	0.05	0.06
35	0.00125	0.0224	0.254	0.241	0.05	0.0814	0.04	0.04	34.8	7.3	0.4	0.05	0.06
36	0.00125	0.0322	0.295	0.292	0.049	0.186	0.04	0.04	26.4	5.66	1.5	0.05	0.06
37	0.00125	0.028	0.290	0.280	0.057	0.0911	0.045	0.045	24.3	6.7	0.41	0.05	0.06
38	0.00125	0.0298	0.2106	0.205	0.057	0.0587	0.045	0.045	34.5	4.79	1.96	0.05	0.06
39	0.00125	0.003	0.02	0.019	0.006	0.008	0.05	0.05	500.0	7.0	0.7	0.05	0.06

B.2 Exciter Parameters

Gen No	T_R	K_A	T_A	V_{RMAX}	V_{RMIN}	K_E	T_E	K_F	T_F	E_1	$S_E(E_1)$	E_2	$S_E(E_2)$
30	0	5	0.06	1	-1	0	0.25	0.04	1	3.54	0.08	4.728	0.26
31	0	6.2	0.05	1	-1	0	0.405	0.057	0.5	3.036	0.66	4.049	0.88
32	0	5	0.06	1	-1	0	0.5	0.08	1	2.342	0.13	3.123	0.34
33	0	5	0.06	1	-1	0	0.5	0.08	1	2.868	0.08	3.824	0.314
34	0	40	0.02	10	-10	1	0.785	0.03	1	3.927	0.07	5.236	0.91
35	0	5	0.02	1	-1	0	0.471	0.075	1.2	3.587	0.064	4.782	0.251
36	0	40	0.02	6.5	-6.5	1	0.73	0.03	1	2.8	0.53	3.8	0.74
37	0	5	0.02	1	-1	0	0.528	0.085	1.26	3.191	0.072	4.255	0.282
38	0	40	0.02	10.5	-10.5	1	1.4	0.03	1	4.257	0.62	5.676	0.85

B.3 Transmission Line Parameters

The transmission line parameters for the IEEE 39-bus test system are given on the system base of 100 MVA.

From Bus	To Bus	R (pu)	X (pu)	B (pu)	From Bus	To Bus	R (pu)	X (pu)	B (pu)
1	2	0.0035	0.0411	0.6987	13	14	0.0009	0.0101	0.1723
1	39	0.0010	0.0250	0.7500	14	15	0.0018	0.0217	0.3660
2	3	0.0013	0.0151	0.2572	15	16	0.0009	0.0094	0.1710
2	25	0.0070	0.0086	0.1460	16	17	0.0007	0.0089	0.1342
3	4	0.0013	0.0213	0.2214	16	19	0.0016	0.0195	0.3040
3	18	0.0011	0.0133	0.2138	16	21	0.0008	0.0135	0.2548
4	5	0.0008	0.0128	0.1342	16	24	0.0003	0.0059	0.0680
4	14	0.0008	0.0129	0.1382	17	18	0.0007	0.0082	0.1319
5	6	0.0002	0.0026	0.0434	17	27	0.0013	0.0173	0.3216
5	8	0.0008	0.0112	0.1476	21	22	0.0008	0.0140	0.2565
6	7	0.0006	0.0092	0.1130	22	23	0.0006	0.0096	0.1846
6	11	0.0007	0.0082	0.1389	23	24	0.0022	0.0350	0.3610
7	8	0.0004	0.0046	0.0780	25	26	0.0032	0.0323	0.5130
8	9	0.0023	0.0363	0.3804	26	27	0.0014	0.0147	0.2396
9	39	0.0010	0.0250	1.2000	26	28	0.0043	0.0474	0.7802
10	11	0.0004	0.0043	0.0729	26	29	0.0057	0.0625	1.0290
10	13	0.0004	0.0043	0.0729	28	29	0.0014	0.0151	0.2490

B.4 Transformer Parameters

The transformer parameters for the IEEE 39-bus test system are given on the system base of 100 MVA.

From Bus	To Bus	R (pu)	X (pu)	B (pu)	Transformer Tap	
					Magnitude	Angle
12	11	0.0016	0.0435	0.0000	1.006	0.00
12	13	0.0016	0.0435	0.0000	1.006	0.00
6	31	0.0000	0.0250	0.0000	1.070	0.00
10	32	0.0000	0.0200	0.0000	1.070	0.00
19	33	0.0007	0.0142	0.0000	1.070	0.00
20	34	0.0009	0.0180	0.0000	1.009	0.00
22	35	0.0000	0.0143	0.0000	1.025	0.00
23	36	0.0005	0.0272	0.0000	1.000	0.00
25	37	0.0006	0.0232	0.0000	1.025	0.00
2	30	0.0000	0.0181	0.0000	1.025	0.00
29	38	0.0008	0.0156	0.0000	1.025	0.00
19	20	0.0007	0.0138	0.0000	1.060	0.00

B.5 Power Flow Data

Bus	Type	Voltage (pu)	Load		Generator	
			(MW)	(MVar)	(MW)	(MVar)
1	PQ	–	0.0	0.0	0.0	0.0
2	PQ	–	0.0	0.0	0.0	0.0
3	PQ	–	322.0	2.4	0.0	0.0
4	PQ	–	500.0	184.0	0.0	0.0
5	PQ	–	0.0	0.0	0.0	0.0
6	PQ	–	0.0	0.0	0.0	0.0
7	PQ	–	233.8	84.0	0.0	0.0
8	PQ	–	522.0	176.0	0.0	0.0
9	PQ	–	0.0	0.0	0.0	0.0
10	PQ	–	0.0	0.0	0.0	0.0
11	PQ	–	0.0	0.0	0.0	0.0
12	PQ	–	7.5	88.0	0.0	0.0
13	PQ	–	0.0	0.0	0.0	0.0
14	PQ	–	0.0	0.0	0.0	0.0
15	PQ	–	320.0	153.0	0.0	0.0
16	PQ	–	329.0	32.3	0.0	0.0
17	PQ	–	0.0	0.0	0.0	0.0
18	PQ	–	158.0	30.0	0.0	0.0
19	PQ	–	0.0	0.0	0.0	0.0
20	PQ	–	628.0	103.0	0.0	0.0
21	PQ	–	274.0	115.0	0.0	0.0
22	PQ	–	0.0	0.0	0.0	0.0
23	PQ	–	247.5	84.6	0.0	0.0
24	PQ	–	308.6	-92.0	0.0	0.0
25	PQ	–	224.0	47.2	0.0	0.0
26	PQ	–	139.0	17.0	0.0	0.0
27	PQ	–	281.0	75.5	0.0	0.0
28	PQ	–	206.0	27.6	0.0	0.0
29	PQ	–	283.5	26.9	0.0	0.0
30	PV	1.0475	0.0	0.0	250.0	–
31	PV	0.9820	9.2	4.6	521.0	–
32	PV	0.9831	0.0	0.0	650.0	–
33	PV	0.9972	0.0	0.0	632.0	–
34	PV	1.0123	0.0	0.0	508.0	–
35	PV	1.0493	0.0	0.0	650.0	–
36	PV	1.0635	0.0	0.0	560.0	–
37	PV	1.0278	0.0	0.0	540.0	–
38	PV	1.0265	0.0	0.0	830.0	–
39	PV	1.0300	1104.0	250.0	1000.0	–

References

[1] U.S.-Canada Power System Task Force, Final Report on the August 14, 2003 Blackout in the United State and Canada: Causes and Recommendations, April 2004. [Online] Available: https://reports.energy.gov.

[2] A. G. Phadke, J. S. Thorp, and M. G. Adamiak, "A new measurement technique for tracking voltage phasors, local system frequency, and rate of change of frequency," *IEEE Transactions on Power Engineering Review*, vol. PER-3, pp. 23, May 1983.

[3] A. G. Phadke, "Synchronized phasor measurements in power systems," *IEEE Computer Applications in Power*, pp. 10-15, Apr. 1993.

[4] Z. Huang, B. Kasztenny, V. Madani, K. Martin, S. Meliopoulos, D. Novosel, and J. Stenbakken, "Performance evaluation of phasor measurement systems," in *Proceeding of IEEE Power Engineering Society General Meeting*, Pittsburgh, PA, USA, July 2008, pp. 1-7.

[5] *IEEE standard for synchrophasor measurements for power systems*, IEEE Standard C37.118.1-2011, Dec. 2011.

[6] K. Martin, T. Faris, and J. Hauer, "Standardized testing of phasor measurement units," in *Proceeding of Fault and Disturbance Analysis Conference*, Georgia Tech, Atlanta, GA, USA, 2006, pp. 1-21.

[7] K. E. Martin, G. Brunello, M. G. Adamiak, G. Antonova, M. Begovic, G. Benmouyal, P. D. Bui, H. Falk, V. Gharpure, A. Goldstein, Y. Hu, C. Huntley, T. Kase, M. Kezunovic, A. Kulshrestha, Y. Lu, R. Midence, J. Murphy, M. Patel, F. Rahmatian, V. Skendzic, B. Vandiver, and A. Zahid, "An overview of the IEEE Standard C37.118.2 – Synchrophasor data transfer for Power systems," *IEEE Transactions on Smart Grid*, vol. 5, no. 4, pp. 1980-1984, July 2014.

[8] A. Guzman, S. Samineni, and M. Bryson, "Protective relay synchrophasor measurements during fault conditions," in *Proceeding of Power Systems Conference: Advanced Metering, Protection, Control, Communication, and Distributed Resources*, Clemson, SC, USA, 2006, pp. 83-95.

[9] D. R. Gurusinghe, A. D. Rajapakse, and K. Narendra, "Evaluation of steady-state and dynamic performance of a synchronized phasor measurement unit," in *Proceeding of Electrical Power and Energy Conference*, London, ON, Canada, Oct. 2012, pp. 57-62.

[10] G. Benmouyal, E. O. Schweitzer III, and A Guzman, "Synchronized phasor measurement in protective relays for protection, control, and analysis of electric power systems," in *Proceeding of 29th Annual Western Protective Relay Conference*, Spokane, WA, USA, 2002, pp. 419-450.

[11] *IEEE guide for phasor data concentrator requirements for power system protection, control, and monitoring*, IEEE Standard C37.244-2013, May 2013.

[12] R. O. Burnett, M. M. Butts, T. W. Cease, V. Centeno, G. Michel, R. J. Murphy, and A. G. Phadke, "Synchronized phasor measurement of a power system event," *IEEE Transactions on Power Systems*, vol. 9, no. 3, pp. 1643-1650, Aug. 1994.

[13] J. D. L. Ree, V. Centeno, J. S. Thorp, and A. G. Phadke, "Synchronized phasor measurement applications in power systems," *IEEE Transactions on Smart Grid*, vol. 1, no. 1, pp. 20-27, June 2010.

[14] North American Electric Reliability Corporation, "Real-time application of synchrophasors for improving reliability," Oct. 2010. [Online]. Available: http://www.nerc.com/docs/oc/rapirtf/RAPIR%20final%20101710.pdf.

[15] M. Adamiak, W. Premerlani, and B. Kasztenny, "Synchrophasors: definition, measurement, and application," [Online]. Available: https://www.ece.cmu.edu/~electricityconference/2006/Adamiak_Premerlani_Kasztenny%20SynchroPhasors.pdf

[16] S. H. Horowitz and A. G. Phadke, "Third zone revisited," *IEEE Transactions on Power Delivery*, vol. 21, no. 1, pp. 23-29, Jan. 2006.

[17] Z. Zhong, C. Xu, B. J. Billian, L. Zhang, S.-J. S. Tsai, R. W. Conners, V. Centeno, A. G. Phadke, and Y. Liu, "Power system frequency monitoring network (FNET) implementation," *IEEE Transactions on Power Systems*, vol. 20, no. 4, pp. 1914-1921, Nov. 2005.

[18] P. Kundur, J. Paserba, V. Ajjarapu, G. Andersson, A. Bose, C. Canizares, N. Hatziargyriou, D. Hill, A. Stankovic, C. Taylor, T. Cutsem, and V. Vittal, "Definition and classification of power system stability," *IEEE Transactions on Power Systems*, vol. 19, pp. 1387-1401, May 2004.

[19] D. Lan, B. Tianshul and Z. Daonong, "Transmission line parameters identification based on moving-window TLS and PMU data," in *Proceeding of International Conference on Advanced Power System Automation and Protection (APAP)*, Beijing, China, 2011, pp. 2187-2191.

[20] D. Shi, D.J. Tylavsky, N. Logic, and K.M. Koellner, "Identification of short transmission-line parameters from synchrophasor measurements," in *Proceeding of 40th North American Power Symposium, NAPS '08*, Calgary, AB, Canada, Sep. 2008, pp.1-8.

[21] R. E. A. Bonnin, "Development of a laboratory synchrophasor network and an application to estimate transmission line parameters in real time," M.Sc. thesis, Dept. Electrical & Computer Engineering, University of Manitoba, Winnipeg, MB, Canada, 2013.

[22] M. Bockarjova and G. Andersson, "Transmission line conductor temperature impact on state estimation accuracy," in Proceeding of 2007 IEEE Power Tech, Lausanne, 2007, pp. 701-706.

[23] *IEEE standard for calculating the current-temperature relationship of bare overhead conductors*, IEEE Standard 738-2012, Dec. 2013.

[24] CIGRE Working Group B2.12, "Thermal behaviour of overhead conductors," *Technical Brochure 207*, Aug. 2002.

[25] Z. Huang, B. Kasztenny, V. Madani, K. Martin, S. Meliopoulos, D. Novosel and J. Stenbakken, "Performance evaluation of phasor measurement systems," *in Proceeding of 2008 Power and Energy Society General Meeting*, Pittsburgh, PA, USA, July 2008, pp. 1-7.

[26] A. G. Phadke and J. S. Thorp, *Synchronized Phasor Measurements and Their Applications*, New York: Springer, 2008.

[27] R. E. Wilson, G. A. Zevenbergen and D. L. Mah, "Calculation of transmission line parameters from synchronized measurements," *Electric Machines and Power Systems*, vol. 27, no. 12, pp. 1269-1278, Dec. 1999.

[28] M. Eremia and M. Shahidehpour, *Handbook of electrical power system dynamics : modeling, stability, and control*, John Wiley & Sons Inc., Hoboken, New Jersey, 2013.

[29] P. Kundur, *Power System Stability and Control*, McGraw-Hill International Book Company, 1994.

[30] L. L. Grigsby, *Power System Stability and Control*. Second Edition, CRC Press Taylor and Francis Group, 2006.

[31] C. W. Taylor, D. C. Erickson, K. Martin, R. E.Wilson, and V. Venkatasubramanian, "WACS—wide-area stability and voltage control system: R&D and online demonstration," *Proceedings of the IEEE*, vol. 93, no. 5 , pp. 892-906, May 2005.

[32] M. Begovic, D. Novosel, D. Karlsson, C. Henville, and G. Nichel, "Wide-area protection and emergency control," *Proceedings of the IEEE*, vol. 93, no. 5 , pp. 876-891, May 2005.

[33] D. Hu and V. Venkatasubramanian, "New wide-area algorithms for detecting angle stability using synchrophasors," in *Proceeding of Western Protective Relay Conference*, Spokane, WA, USA, 2006, pp.1-37.

[34] A. D. Rajapakse, F. R. Gomez, K. Nanayakkara, P. A Crossley, and V. T. Terzija, " Rotor angle instability prediction using post-disturbance voltage trajectories," *IEEE Transactions on Power systems*, vol. 25, pp. 947 - 956, 2010.

[35] D. Karlsson and S. Lindahl, "Wide area protection and emergency control," in *Proceeding of IEEE Power Engineering Society General Meeting*, vol. 1, 2004, pp. 5.

[36] F. R. Gomez, A. D. Rajapakse, U. D. Annakkage, and I. T. Fernando, "Support vector machine-based algorithm for post-fault transient stability status prediction using synchronized measurements," *IEEE Transactions on Power systems*, vol. 26, pp. 1474-1483, 2011.

[37] F. R. Gomez, "Prediction and control of transient instability using wide area phasor measurements," Thesis Doctor of Philosophy, Department of Electrical and Computer Engineering, University of Manitoba, Canada, 2011.

[38] *IEEE standard for synchrophasors for power systems*, IEEE Standard 1344-1995, Dec. 1995.

[39] *IEEE standard for synchrophasors for power systems*, IEEE Standard C37.118-2005, Mar. 2006.

[40] *IEEE standard for synchrophasor data transfer for power systems*, IEEE Standard C37.118.2-2011, Dec. 2011.

[41] *IEEE standard for synchrophasor measurements for power systems (Amendment 1: Modification of selected performance requirements)*, IEEE Standard C37.118.1a-2014, Apr. 2014.

[42] *IEEE synchrophasor measurement test suite specification*, IEEE Standards Association, Dec. 2014.

[43] S. Das and T. Sidhu, "A simple synchrophasor estimation algorithm considering IEEE Standard C37.118.1-2011 and protection requirements," *IEEE Transactions on Instrumentation and Measurements*, vol. 62, No. 10, pp. 2704-2715, Oct. 2013.

[44] K. E. Martin, J. F. Hauer, and T. J. Faris, "PMU testing and installation considerations at the Bonneville Power Administration," in *Proceeding of IEEE Power Engineering Society General Meeting,* Tampa, FL, USA, June 2007, pp.1-6.

[45] Z. Huang, J. F. Hauer, and K. M. Martin, " Evaluation of PMU dynamic performance in both lab environments and under field operating conditions", in *Proceeding of IEEE Power Engineering Society General Meeting,* Tampa, FL, USA, 2007, pp. 1-6.

[46] J. Ren, M. Kezunovic, and G. Stenbakken, "Dynamic characterization of PMUs using step signals", in *Proceeding of IEEE Power Engineering Society General Meeting,* Calgory, AB, Canada, 2009, pp. 1-6.

[47] A. G. Phadke and B. Kasztenny, "Synchronized phasor and frequency measurmeent under transient conditions," *IEEE Transactions on Power Delivery,* vol. 24, no. 1, pp. 89-95, Jan. 2009.

[48] M. Balabin, K. Görner, Y. Li, I. Naumkin, and C. Rehtanz, "Evaluation of PMU performance during transients," in *Proceeding of Power Systems Technology, Hangzhou,* China, 2010, pp. 1-8.

[49] P. Komarnicki, C. Dzienis, Z. A. Styczynski, J. Blumschein, and V. Centeno, "Practical experience with PMU system testing and calibration requirements," in *Proceeding of IEEE Power Engineering Society General Meeting,* Pittsburgh, PA, USA, 2008, pp. 1-5.

[50] A. Goldstein, "2014 NIST assessment of phasor measurement unit performance - NISTIR 8106", National Institute of Standards and Technology, U. S. Department of Commerce, Feb. 2016 [Online] Available: http://nvlpubs.nist.gov/nistpubs/ir/2016/NIST.IR.8106.pdf.

[51] R. K. Mai, Z. Y. He, L. Fu, B. Kirby, and Z. Q. Bo, "A dynamic synchrophasor estimation algorithm for online application," *IEEE Transactions on Power Delivery*, vol. 25, no. 2, pp. 570-578, Apr. 2010.

[52] M. Karimi-Ghartemani, Boon-Teck Ooi, and A. Bakhshai, "Application of enhanced phase-looked loop system to the computation of synchrophasor," *IEEE Transaction on Power Delivery*, vol. 26, no. 1, pp. 22-32, Jan. 2011.

[53] P. Banerjee and S. C. Srivastava, "A subspace-based dynamic phasor estimation for synchrophasor application," *IEEE Transactions on Instrumentation and Measurements*, vol. 61, no. 9, pp. 2436-2445, Sep. 2012.

[54] I. Kamwa, A. K. Pradhan, and G. Joos, "Adaptive phasor and frequency-tracking schemes for wide-area protection and control," *IEEE Transactions on Power Delivery*, vol. 26, no. 2, pp. 744-753, Apr. 2011.

[55] A. Ouadi, H. Bentarzi, and J. C. Maun, "Phasor measurement unit reliability enhancement using real-time digital filter," *International Journal of Circuits, Systems and Signal Processing*, vol. 5, no. 1, pp. 1-8, 2011.

[56] *IEEE standard for common format for transient data exchange (COMTRADE) for power systems*, IEEE Standard C37.111, Oct. 1999.

[57] J. Gosalia and D. Tierney, "Tutorial: using COMTRADE files for relay testing", Doble Engineering Company, Watertown, MA, USA. [Online]. Available: http://sistemaselectricos.com/cpe_box/comtrade.htm

[58] G. Stenbakken and T. Nelson, "Static calibration and dynamic characterization of PMUs at NIST," in *Proceeding of 2007 IEEE Power Engineering Society General Meeting*, Tampa, FL, USA, pp. 1-4.

[59] I. D. Kim, J. R. Lee, Y. J. Ko, and Y. T. Jin, "A study on the condition monitoring of transmission line by on-line circuit parameter measurement," *World Academy of Science, Engineering and Technology*, vol. 80 pp. 107-111, 2013

[60] I. D. Kim, R. K. Aggarwal, "A study on the on-line measurement of transmission line impedances for improved relaying protection," *Electrical Power and Energy Systems*, vol. 28, no. 6, pp.359-366, July 2006.

[61] Y. Du and Y. Liao, "Online estimation of power transmission line parameters, temperature and sag," in *Proceeding of North American Power Symposium, NAPS '11*, Boston, MA, USA, Aug. 2011, pp.1-6.

[62] Y. Liao and M. Kezunovic, "Optimal estimate of transmission line fault location considering measurement errors," *IEEE Transactions on Power Delivery*, vol. 22, pp. 1335-1341, July 2007.

[63] Y. Liao and M. Kezunovic, "Online optimal transmission line parameter estimation for relaying applications," *IEEE Transactions on Power Delivery*, vol. 24, no. 1, pp. 486-493, January 2009.

[64] V. Salehi, A. Mazloomzadeh and O. Mohammed, "Development and implementation of a phasor measurement unit for real-time monitoring, control and protection of power systems," in *Proceeding of 2011 IEEE Power Engineering Society General Meeting*, San Diego, CA, USA, July 2011, pp.1-7.

[65] J. Jiang, J. Yang, Y. Lin, C. Liu, and J. Ma, "An adaptive PMU based fault detection/location technique for transmission lines part I: theory and algorithms," *IEEE Transactions on Power Delivery*, vol. 15, no. 2, pp. 96-102, Apr. 2000.

[66] G. Sivanagaraju, S. Chakrabarti, and S. C. Srivastava, "Uncertainty in transmission line parameters: estimation and impact on line current differential protection," *IEEE Transactions on Instrumentation and Measurements*, vol. 63, no. 6, pp. 1496-1504, June 2014.

[67] S. S. Mousavi-Seyedi, F. Aminifar, and S. Afsharnia, "Parameter estimation of multi-terminal transmission lines using joint PMU and SCADA data," *IEEE Transactions on Power Delivery*, vol. 30, no. 3, pp. 1077-1085, June 2015.

[68] Y. Liao, "Some algorithms for transmission line parameter estimation," in *Proceeding of 41st Southeastern Symposium on System Theory*, Tullahoma, TN, USA, Mar. 2009, pp. 127-132.

[69] Y. Du and Y. Liao, "Parameter estimation for series compensated transmission line," *International Journal of Emerging Electric Power Systems*, vol. 12: iss. 3, article 1, pp. 1-20, 2011.

[70] L. Józsa, I. Petrović and V. Angebrandt, "Analysis of possibilities of using series compensation for consequences elimination of driving long transmission lines," *Technical Gazette*, vol. 17, no. 4, pp. 529-535, 2010.

[71] A. Mohr, "Quantum computing in complexity theory and theory of computation", [Online]. Available: http://www.austinmohr.com/Work_files/complexity.pdf.

[72] Real-Time Digital Simulator (RTDS) Power system user's manual, RTDS Technologies, Winnipeg, MB, Canada, pp. 5.1-5.23, Dec. 2012.

[73] Real-Time Digital Simulator (RTDS) Controls library manual, GTNET Components – GTNET PMU24, RTDS Technologies, Winnipeg, MB, Canada, pp. 7Fa.1-7Fa.11, Rev. 0.4: May 2015.

[74] OpenPDC, Grid Protection Alliance [Online]. Available: http:// openpdc.codeplex.com.

[75] Lab-Volt Electric power transmission line device model 8329 [Online]. Available: https://www.labvolt.com/downloads/dsa8329.pdf

[76] TESLA 4000 user manual, ERLPhase Power Technologies Ltd, Winnipeg, MB, Canada, pp. 15.1-15.15, version 2.4 rev 0, 2013.

[77] SEL-2407 Satellite-Synchronized Clock Instruction Manual, SEL Inc., Pullman, WA, USA, pp. 1-40, 2013.

[78] Climate, the government of Canada (environment Canada) [Online]. Available: http://climate.weather.gc.ca.

[79] M. Weibel, W. Sattinger, U. Steinegger, M. Zima and G. Biedenbach, "Overhead line temperature monitoring pilot project," in *Proceeding of 2006 CIGRÉ Session B2-311*, Aug. 2006, pp.1-8.

[80] P. M. Anderson and A. A. Fouad, *Power system control and stability*. 2nd edition Piscataway, NJ: IEEE, 2003.

[81] M. A. Pai, *Power system stability : Analysis by the direct method of Lyapunov*. North-Holland publishing company, Amsterdam/New York/Oxford, 1981.

[82] M. Pavella, D. Ernst, and D. Ruizvega, *Transient stability of power systems - a unified approach to assessment and control*. Kluwer Academic Publishers, Boston/Dordrecht/London.

[83] M. A. Pai, *Energy function analysis for power system stability*. Kluwer academic publishers, Boston/Dordrecht/London, 1989.

[84] C. W. Liu and J. Thorp, "Application of synchronized phasor measurements to real-time transient stability prediction," *IEE Proceeding of Generation, Transmission and Distribution*, vol. 142, no.4, pp. 355-360, 1995.

[85] S. Rovnyak, C. W. Liu, J. Lu, W. Ma, and J. Thorp, "Predicting future behavior of transient events rapidly enough to evaluate remedial control options in real-time," *IEEE Transactions on Power Systems*, vol. 10, no. 3, pp. 1195-1203, Aug. 1995.

[86] C. W. Liu and J. S. Thorp, "New methods for computing power system dynamic response for real-time transient stability prediction," *IEEE Transactions on Circuits and Systems I: Fundamental Theory and Applications*, vol. 47, no. 2, pp. 324-337, Mar. 2000.

[87] A. Rahimi and G. Schaffer, "Power System Transient Stability Indexes for On-Line Analysis of "Worst-Case" Dynamic Contingencies," *IEEE Power Engineering Review*, vol. PER-7, pp. 44-45, 1987.

[88] Y. Xue, T. Van Cutsem, and M. Ribbens-Pavella, "A simple direct method for fast transient stability assessment of large power systems," *IEEE Transactions on Power Systems*, vol. 3, pp. 400-412, 1988.

[89] Y. Xue, T. Van Custem, and M. Ribbens-Pavella, "Extended equal area criterion justifications, generalizations, applications," *IEEE Transactions on Power Systems*, vol. 4, pp. 44-52, 1989.

[90] V. Centeno, A. Phadke, A. Edris, J. Benton, M. Gaudi, and G. Michel, "An adaptive out-of-step relay," *IEEE Transactions on Power Delivery*, vol. 12, no. 1, pp. 61-71, 1997.

[91] J. E. Slotine and W. Li, *Applied nonlinear control*. Prentice Hall, 1991.

[92] M. H. Haque and A. H. M. A. Rahim, "Determination of first swing stability limit of multi-machine power systems through Taylor series expansions," *IEE Proceeding of Generation, Transmission and Distribution*, vol. 136, no.6, pp. 373-379, 1989.

[93] K. Matsuzawa, K. Yanagihashi, J. Tsukita, M. Sato, T. Nakamura, and A. Takeuchi, " Stabilizing control system preventing loss of synchronism from extension and its actual operating experience," *IEEE Transactions on Power Systems*, vol. 10, no. 3, pp. 1606-1613, Aug. 1995.

[94] G. G. Karady and J. Gu, "A hybrid method for generator tripping," *IEEE Transactions on Power Systems*, vol. 17, no. 4, pp. 1102-1107, Nov. 2002.

[95] H. Deng, J. Zhao, Y. Liu and X. Wu, "A real-time generator-angle prediction method based on the modified grey verhulst model," *in Proceeding of 2011 International Electric Utility Deregulation and Restructuring and Power Technologies Conference*, Weihai, China, 2011, pp. 179-184.

[96] K. Men, P. Xu, J. Zhao, X. Wu, and C. Hong, “Comparison of methods for the perturbed trajectory prediction based on wide area measurements,” *in Proceeding of 2011 IEEE Power Engineering and Automation Conference (PEAM)*, Wuhan, China, Sep. 2011, pp. 321-325.

[97] J. H. Sun and K. L. Lo, "Transient stability real-time prediction for multi-machine power systems by using observation," *in Proceeding of 1993 Computer, Communication, Control and Power Engineering Conference*, Beijing, China, vol. 5, pp. 217-221.

[98] Power swing and out-of-step considerations on transmission lines, Working Group D6, IEEE PES Power System Relaying Committee, IEEE Power Engineering Society, Jul. 2005.

[99] N. Fischer, G. Benmouyal, D. Hou, D. Tziouvaras, J. B. Finley, and B. Smyth, "Tutorial on power swing blocking and out-of-step tripping," *in Proceeding of 39th Annual Western Protective Relay Conference*, Spokane, WA, USA, Oct. 2012, pp. 1-20.

[100] F. Ilar, “Innovations in the detection of power swings in electrical networks,” Brown Boveri Publication CH-ES 35-30.10E, 1997.

[101] D. J. Sobajic and Y. H. Pao, “Artificial neural-net based dynamic security assessment for electric power systems,” *IEEE Transactions on Power Systems*, vol. 4, no. 1, pp. 220-228, Feb. 1989.

[102] Z. Qin, J. Davidson and A. A. Fouad, “Application of artificial neural networks in power system security and vulnerability assessment,” *IEEE Transactions on Power Systems*, vol. 9, No. 1, pp. 525-532, Feb. 1994.

[103] A. N. Al-Masri, M. Z. A. Ab Kadir, H. Hizam, and N. Mariun, "A novel implementation for generator rotor angle stability prediction using an adaptive artificial neural network application for dynamic security assessment," *IEEE Transactions on Power Systems*, vol. 28, no. 3, pp. 2516-2525, Aug. 2013.

[104] L. Wehenkel, M. Pavella, E. Euxibie and B. Heilbronn, "Decision tree based transient stability method a case study," *IEEE Transactions on Power Systems*, vol. 9, no. 1, pp. 459-469, Feb. 1994.

[105] S. Rovnyak, S. Kretsinger, J. Thorp, and D. Brown, "Decision trees for real-time transient stability prediction," *IEEE Transactions on Power Systems*, vol. 9, no. 3, pp. 1417-1426, Aug. 1994.

[106] K. Sun, S. Likhate, V. Vittal, V. S. Kolluri, and S. Mandal, "An online dynamic security assessment scheme using phasor measurements and decision trees," *IEEE Transactions on Power Systems*, vol. 22, no. 4, pp. 1935-1943, Nov. 2007.

[107] T. Amraee and S. Ranjbar, "Transient instability prediction using decision tree technique," *IEEE Transactions on Power Systems*, vol. 28, no. 3, pp. 3028-3037, Aug. 2013.

[108] C. J. C. Burges, "A tutorial on Support Vector Machines for Pattern Recognition," *Kluwer Academic Publishers*, 1998.

[109] L. S. Moulin, A. P. A. da Silva, M. A. El-Sharkawi and R. J. Marks, " Support vector machines for transient stability analysis of large-scale power systems," *IEEE Transactions on Power systems*, vol. 19, no. 2, pp. 818-825, May 2004.

[110] A. E. Gavoyiannis, D. G. Vogiatzis, D. R. Georgiadis, and N. D. Hatziargyriou, "Combined support vector classifiers using fuzzy clustering for dynamic security assessment," in *Proceeding of IEEE Power Engineering Society Summer Meeting*, Vancouver, BC, Canada, vol. 2, pp. 1281-1286, 2001.

[111] X. Wang, S. Wu, Q. Li, and X. Wang, "v-SVM for transient stability assessment in power systems," in *Proceeding of Autonomous Decentralized Systems*, Apr. 2005, pp. 356-363.

[112] D. You, K. Wang, , L. Ye, J. Wu, and R. Huang, "Transient stability assessment of power system using support vector machine with generator combinatorial trajectories inputs," *International Journal of Electrical Power & Energy Systems*, vol. 44, Issue 1, pp. 318-325, Jan. 2013.

[113] TSAT (Transient Security Assessment Tool) Manual, Powertech Labs Inc., 2004.

[114] B. Jayasekara and U. D. Annakkage, "Derivation of an accurate polynomial representation of the transient stability boundary," *IEEE Transactions on Power Systems*, vol. 21, no. 4, pp. 1856-1863, Nov. 2006.

[115] S. Weerasuriya, "Application of neural networks for classification and identification in power systems," Ph.D. dissertation, Univ. Washington, Seattle, USA, 1992.

[116] Final Report on wide area protection and emergency control, Working Group C-6, System Protection Subcommittee, IEEE PES Power System Relaying Committee, IEEE Power Engineering Society, Jan. 2003.

[117] S. A. Siddiqui, K. Verma, K. R. Niazi and M. Fozdar, "Wide area synchrophasor measurements based transient stability assessment and emergency control", in *Proceeding of IEEE Power Engineering Society Conference & Exposition*, National Harbor, MD, USA, 2014, pp. 1-5.

[118] D. A. Pierre, "A perspective on adaptive control of power systems," *IEEE Transactions on Power Systems*, vol. 2, no. 2, pp. 387-395, May 1987.

[119] L. H. Fink, "Emergency control practices : A report prepared for the System Control Subcommittee of the Power System Engineering Committee by the Task Force on Emergency Control," *IEEE Power Engineering Review*, vol. PER-5, pp. 29-30, 1985.

[120] A. G. Phadke and J. S. Thorp, "Monitoring and simulating real-time electric power system operation with phasor measurements," Virginia Polytechnic Institute and State Univ., Blacksburg, VA, USA, Jan. 1995.

[121] H. You, V. Vittal, and X. Wang, "Slow coherency based islanding," *IEEE Transactions on Power Systems*, vol. 19, no. 1, pp. 483–491, Feb. 2004.

[122] F. Hashiesh, H. E. Mostafa, A. R. Khatib, I. Helal, and M. M. Mansour, "An intelligent wide area synchrophasor based system for predicting and mitigating transient instabilities," *IEEE Transactions on Smart Grid*, vol. 3, no. 2, pp. 645-652, June 2012.

[123] Real-Time Digital Simulator (RTDS) Controls library manual, GTNET Components – GTNET SKT, RTDS Technologies, Winnipeg, MB, Canada, pp. 7H.1-7H.13, Mar. 2015.